Coherent π^0 Photoproduction on Nuclei

Claire M. Tarbert

School of Physics

University of Edinburgh

A thesis submitted for the degree of

Doctor of Philosophy

August 2007

For Mum, Dad, Andrew and Angela

Acknowledgements

First off I'd like to thank Dan Watts, supervisor-extraordinaire and self proclaimed 'handsome polymath', for his guidance on everything from data analysis to thesis writing over the past three and a bit years. It was a leap of faith letting me near his coherent π^0 experiment and I appreciate the opportunity.

I'd like to express my gratitude to all the members of the Edinburgh Nuclear Physics group past and present who have helped me out during my time here. In particular, Derek Branford, who gave me the opportunity to work in Edinburgh in the first instance, and Derek Glazier, for many helpful conversations about my data analysis, not to mention going above and beyond the call of duty in proof reading my thesis. Klaus Föhl has answered numerous physics questions and Ewan Roche spent far too much time helping me with computers when I first started - thankyou!

I would be remiss without mentioning my office mates: accomplices in seemingly endless (but always entertaining) tea breaks, as well as being the unwitting victims of my post segmentation fault rage. To name and shame them: Alexis (purveyor of high quality lunch time chat), Daria (mad as a banshee and all the better for it), Cham (the Chamster), Steve (none more zen), Gavin (a gent), and the latest office additions, Emma and Tom.

I'd like to extend my thanks to Bob Owens and Cameron McGeorge of Glasgow University. Both Bob and Cameron generously took the time to share some of their intimidating knowledge of physics with me and my data analysis has benefitted greatly from their input.

The data presented in this thesis is ultimately the result of many years work by a large group of people - the A2/CB@MAMI collaboration. I am indebted to the collaboration as a whole and I gratefully acknowledge their contribution. I'd particularly like to mention the collaboration members from Glasgow University - John Annand, Ken Livingston, Douglas MacGregor - especially for the computing assistance they have provided me

with. The experiment would also not have been possible without the logistical support provided by the collaboration members based at the Institüt fur Kernphysik itself in Mainz. I should mention the other CB students as well (shift worker comrades), in particular Evie Downie and Richard Codling, who also somehow managed to survive the endless hours in Hahn and Prestwick airport.

Furthermore I'd like to to acknowledge Sabit Kamalov for providing the theory code used in this work and Bernd Krusche for making his data available to me. I am also grateful for the financial support afforded me by EPSRC as well as the travel funds supplied by the European Union for travel to and from Mainz.

Finally, this work would not have been possible without the support of my family. They have been a constant source of encouragement over the past few years and I dedicate this thesis to them.

Abstract

The coherent nuclear π^0 photoproduction reaction is sensitive to the nuclear matter form factor i.e. the distribution of matter within the nucleus. Accurate measurements of the nuclear matter distribution as charaterised by the r.m.s. radius are important for applications to nuclear theories, neutron stars, atomic parity non-conservation and heavy ion collisions.

This thesis presents the results from a new experiment to measure coherent π^0 photoproduction on ^{208}Pb, ^{40}Ca, ^{16}O and ^{12}C. The ultimate goal of the research programme is to make a high precision measurement of the nature of the neutron skin of ^{208}Pb. The first major step in this direction is to achieve an accurate data set of coherent pion photoproduction which is presented in this thesis.

The experiment was performed in the A2 hall of the MAMI electron accelerator facility at the Institüt fur Kernphysik, Mainz, Germany. An 883 MeV beam of electrons was directed on to a 10μm nickel radiator producing a Bremsstrahlung photon beam which was then 'tagged' with a resolution of 2 MeV using the Glasgow Photon Tagging Spectrometer. The photon beam was incident on one of the 4 experimental targets inducing the reaction A(γ,π^0)A. The neutral π^0s were then detected via their two photon decay in the newly installed 4π Crystal Ball and TAPS detector systems.

The results from all four targets are presented as differential and total cross sections covering the energy range E_γ=(135-300) MeV and covering the full 180° of the pion polar angle. Comparisons have been made with previous data and with the latest theoretical calculations of Dreschel et. al. which employ detailed pion optical potentials in describing the pion-nucleus final state interaction. It is concluded that the ^{208}Pb cross sections show good agreement with the calculations indicating that the pion-nucleus FSI distortions are well accounted for by the model. A pleasing reduction in statistical and systematic uncertainties from previous measurements is also observed. While the ^{208}Pb cross sections are finalised it is suggested that the ^{12}C and ^{16}O data would benefit from a further analysis utilising the

coincident detection of nuclear decay photons to isolate incoherent events and allow a more detailed comparison with theory.

A first comparison of the theoretical model with the new high quality data gives first indications of a neutron skin on ^{208}Pb. A future scheme for the full detailed extraction of the matter distribution from the new data set is also suggested.

Declaration

The data presented in this thesis was obtained in experiments carried out by the CB@MAMI collaboration in the A2 hall of the Institüt fur Kernphysik at the University of Mainz, Germany. I played a major role in the preparation and execution of the experiment and the data analysis and interpretation is entirely my own work. Any contributions from colleagues in the CB@MAMI collaboration such as diagrams or calibrations are explicitly referenced in the text. This thesis was written by myself and the work presented in it has not been submitted in support of another degree or qualification from this or any other university or institute of learning.

Claire Tarbert

Contents

List of Figures

Chapter 1

Overview

1.1 Introduction and Overview

The size and shape of a nucleus are among its most fundamental properties. Since the discovery of the atomic nucleus at the beginning of the 20th century, investigations of these quantities have formed the basis of one of the most active areas of research in physics. The distribution of protons (charge) within the nucleus is now established to accuracies of ∼0.01%, thanks to a series of experiments including electron scattering, muonic x-rays and optical and x-ray isotope shifts[1,2]. However, none of these techniques provide information on the distribution of neutrons within the nucleus. In fact, an accurate measurement of the nuclear matter distribution (both protons and neutrons) has so far proven to be elusive. This can largely be attributed to the significant uncertainties associated with the theoretical description of the strongly interacting probes which are generally used to give sensitivity to the neutron distribution.

For light, stable nuclei, where the number of protons is similar to the number of neutrons, little difference between the r.m.s. charge and matter radii are predicted. For heavier nuclei, such as ^{208}Pb (N=126, Z=82), where the number of neutrons greatly exceeds the number of protons, theories predict the neutrons form a skin of thickness $\sim$ 0.1 - 0.3 fm. The neutron skin thickness is defined as:

$$\Delta R \;=\; r_n - r_p \tag{1.1}$$

where r_n and r_p are the r.m.s. neutron and proton radii respectively e.g.

$$r_p^2 \;=\; \frac{4\pi}{Z}\int_0^\infty \rho_(r) r^4 dr \tag{1.2}$$

ρ(r) is the charge density distribution and Z is the atomic number. Most modern nuclear theories give predictions for ΔR and as a result, this experimental observable can act as a powerful test of nuclear models. A first accurate determination of the

neutron skin thickness of ^{208}Pb, will however have a much wider reaching impact with applications in the study of parity violating electron transitions in atoms, heavy ion collisions, the nuclear equation of state in the neutron rich region and predictions of the properties of low mass neutron stars. It is extraordinary that one measurement can have importance to such a wide range of fields.

Coherent π^0 photoproduction provides a novel and elegant means of probing the matter distribution within a nucleus, although in the past, experimental difficulties have limited the success of this technique. Nuclear π^0 photoproduction takes place when a high energy photon couples to the electromagnetic current of a nucleon and emits a neutral pion. The process is termed coherent when the target nucleus is left in the ground state following the reaction and incoherent when this is not the case. The experiment described in this thesis builds on the experiences of previous measurements and uses the recent advances in photon beam quality and the availability of 4π detector systems to make measurements of the differential and total coherent π^0 cross sections on ^{208}Pb, ^{40}Ca, ^{16}O and ^{12}C. The first major step in using this reaction to measure the matter distribution is to obtain a high quality data set which is presented here. A preliminary value for the r.m.s matter radius of Pb is presented and an outline for the extraction of the matter distribution and more accurate r.m.s. radius determination is described.

This thesis continues in chapter 2 with a description of coherent pion photoproduction including details of a theoretical description and a summary of previous measurements. Chapter 3 is given over to a brief review of the impact accurate neutron skin measurements will have, particularly those of ^{208}Pb, and a summary of our present knowledge of the matter distribution. The experiment and data analysis are detailed in Chapters 4 and 5. The experimental results and conclusions are presented in Chapters 6 and 7.

Chapter 2

Coherent π^0 Photoproduction

2.1 The Photon Nucleus Interaction

The mechanism of nuclear photon absorption is strongly dependent on the energy (i.e. wavelength) of the incident photon. Consider figure 2.1(a) showing the total photoabsorption cross section. Below E_γ ~100 MeV ($\frac{\lambda}{2\pi}$ ~2 fm), the nucleons are seen to act with collective motion producing the giant nuclear resonances. At E_γ ~300 MeV the photon wavelength is comparable to the size of the nucleon ($\frac{\lambda}{2\pi}$ ~0.65 fm) and hence nucleon resonances dominate the cross section. The peak in the cross sections at ~300 MeV corresponds to the first nucleon resonance - the $\Delta(1232)$. The peaks at higher energies correspond to further Δ and N^* resonances and at higher energies still, the many overlapping resonances form a continuum. This work uses photon energies within the region E_γ = 135-300 MeV, for which only the excitation of the Δ plays an important role. The total photoabsorption cross section of course includes contributions from meson photoproduction as well as single and double nucleon knock out reactions. Below E_γ = 500 MeV however the cross section is dominated by single pion production (figure 2.1(b)).

2.2 Overview of Coherent π^0 Photoproduction

The pion occupies a unique position in nuclear and particle physics being the mediator of the long range part of the nucleon-nucleon force. In addition it has been used extensively in pion scattering experiments as a nuclear probe. Yukawa first proposed the existence of a meson with a mass of ~100MeV as the mediating particle of the strong internucleon force in 1935. This was confirmed in 1947 when the charged pions were detected in the photographic emulsion plates of cosmic ray experiments. It is by far the lightest hadron at only ~100MeV compared to the ~1GeV mass scale of the

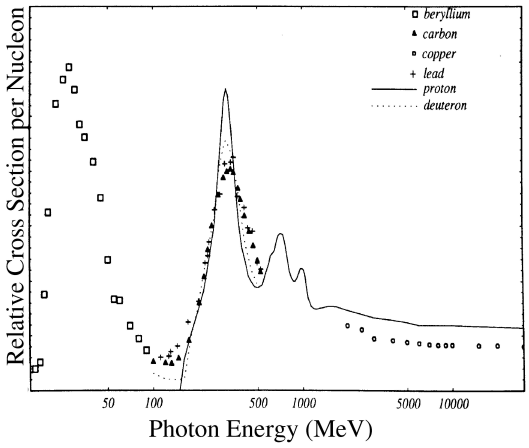

(a) Total photon absorption cross section on different nuclei. Taken from reference 4.

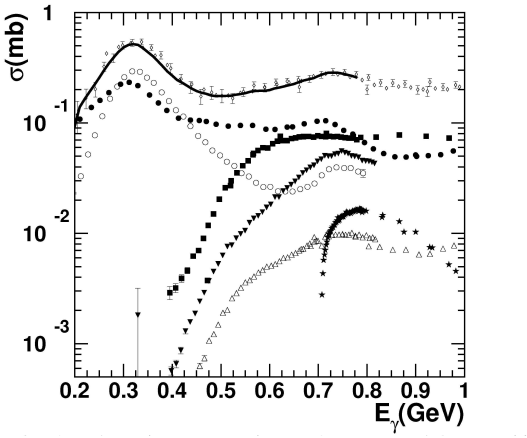

(b) Photoabsorption cross section on the proton and decomposition into meson production channels. Small open circles: photoabsorption from all meson production channels. Solid circles: single π^+ production. Open circles: π^0 production. Solid squares: $\pi^+\pi^-$ production. Downward solid triangles: $\pi^+\pi^0$ production. Upward open triangles: $\pi^0\pi^0$ production. Taken from reference 3.

Figure 2.1: Photoabsorption on the nucleon and on the nucleus.

nucleon and has 3 charge states: π^0 , π^+ and π^-. Collectively, they can be thought of as a single isotriplet state, i.e. one particle (the pion) under rotation in isopin-space. Further pion properties are listed in table B.1 [5].

Pion photoproduction on the nucleon takes place when a high energy photon couples to the electromagnetic current of a nucleon causing it to radiate pions. The reaction can proceed via 4 channels:

$$\gamma + p \rightarrow p + \pi^0 \tag{2.1}$$
$$\gamma + p \rightarrow n + \pi^+ \tag{2.2}$$
$$\gamma + n \rightarrow p + \pi^- \tag{2.3}$$
$$\gamma + n \rightarrow n + \pi^0 \tag{2.4}$$

Nuclear pion photoproduction takes place when the nucleon is embedded within a nucleus. The nuclear process can take place coherently, when the target nucleus is left in its ground state, A(γ,π)A, or incoherently when the final state differs, A(γ,π)A*. Charge conservation rules out the possibility of the coherent production of a single charged pion (consider p(γ,π^+)n or n(γ,π^-)p), leaving only coherent π^0 production. The neutral pion photoproduction process takes place with similar probability on neutrons and protons alike (figure 2.6). In the case of coherent production from a nucleus the amplitudes from all nucleons add coherently. The resulting differential cross section scales with the square of the mass number (A) and the matter form factor as a function of the momentum transferred to the nucleus (F$_m$(q)) i.e.

$$A(\gamma,\pi^0)A : \frac{d\sigma}{d\Omega} \propto A^2 F_m^2(q) \tag{2.5}$$

The matter form factor is the fourier transform of the matter density distribution and its presence leads to a diffraction pattern in the differential cross section. In this way the reaction is analagous to elastic scattering experiments, in particular elastic electron scattering where:

$$A(e,e)A : \frac{d\sigma}{d\Omega} \propto Z^2 F_c^2(q) \tag{2.6}$$

and F$_c$(q) is the charge form factor as a function of momentum transfer to the nucleus and Z is the atomic number. Indeed, the coherent channel can be thought of as the elastic π^0 production channel.

The use of the electromagnetic probe (real or virtual photons) in nuclear studies offers several advantages over strongly interacting probes, namely:

- The electromagnetic interaction is well understood via the formalism of Quantum Electrodynamics (QED).

- The photon is weakly interacting - only single interactions in the nucleus need to be considered for the reactions studied here i.e. it does not suffer from initial state interactions (ISI).
- The mean free path of the photon (both for real and virtual photons) is large i.e. it probes the entire nuclear volume as opposed to strong probes which are predominantly absorbed at the nuclear surface.

It should be noted that the weak strength of the photon-nucleus interaction results in the typically small photonuclear cross sections. One of the main challenges in this field over the past 50 years has been to provide photon and electron beams of sufficient quality and intensity to make these experiments feasible.

Although nuclear pion photoproduction experiments are not complicated by ISI, the produced pion is strongly interacting and therefore can suffer final state interactions with the nucleus (FSI). These effects manifest themselves as shifts in the pion emission angle to smaller angles and a reduction in the outgoing flux. However, the strength of the FSI is highly dependent on the pion energy. The pion-nucleus scattering cross section is dominated by the excitation of the $\Delta(1232)$ resonance which is at its maximum for pion energies of T_π $\sim$165 MeV (figure 2.2). Low energy pions have a much smaller probability of interacting with the nucleus following their production. The implication for coherent π^0 experiments where the aim is to extract the matter form factor, is that low energy measurements ($E\gamma < 300$MeV i.e. below the $\Delta(1232)$ resonance) where the FSI effects are reduced, are most important.

As mentioned, the $\Delta(1232)$ resonance plays an important role in the π-nucleus interaction as the pion energy increases. The modelling of pion photoproduction in the Δ region is further complicated by the strong interaction of the Δ resonance itself as it propagates through the nucleus. Simpler models assume that the properties of the resonance taking part in the pion production process are the same as those of the free Δ. However, strong evidence exists to suggest that the interaction of the Δ with the nuclear medium alters both its width and effective mass [6].

While the presence of final state interactions complicate the extraction of the matter distribution, they present a unique opportunity to study the π-nucleus interaction itself. The majority of data on this topic are the result of charged pion scattering experiments which predominantly sample the nuclear surface. Because of the pions short lifetime, it is not possible to scatter pions with $T_\pi < 30$MeV. With coherent π^0 production, the interaction can in principle be sampled throughout the entire nuclear volume and for pion kinetic energies approaching 0 MeV. The modification of Δ properties of nuclear resonances when embedded in the nuclear medium can also be constrained by comparison with high energy data.

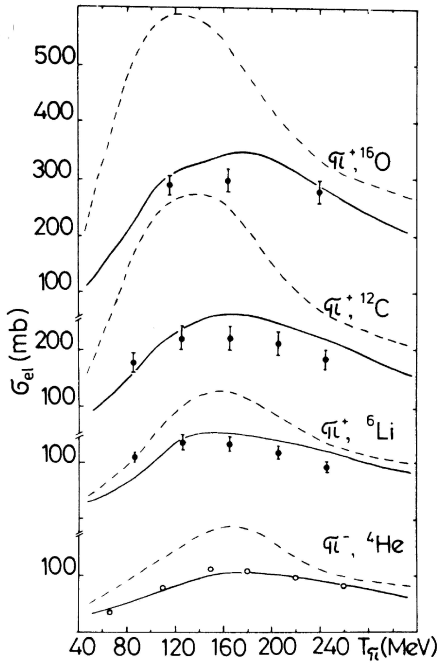

Figure 2.2: Cross section for elastic π^+ scattering on the nucleus. The data are overlayed with two theoretical calculations. The solid line contains a correction for the pion-nucleus FSI, the dashed line does not. From reference [7].

Given the varied applications of pion photoproduction it has been the subject of many theoretical investigations over the past 50 years. The elementary amplitude for pion photoproduction can be separated into a spin-dependent and spin-independent part (section B.2). In the case of coherent π^0 production from closed shell nuclei, no spin information is carried to the final state since the nucleus is spin-0 and the pion is pseudoscalar ($J^\pi = 0^-$). As a result, this process is only sensitive to the spin-independent part of the amplitude and the theoretical description is therefore greatly simplified [4]. The coherent process is therefore an important test of this specific part of the amplitude.

The motivation to study coherent nuclear pion photoproduction can be summarised thus:

- To investigate the matter distribution of nuclei.
- As a precise test of the spin independent part of the elementary pion production amplitudes.
- As a probe of π-nucleus interaction.

The primary motivation of the experiment described in this thesis is to investigate coherent π^0 production as a tool for probing the nuclear matter distribution, the importance of which is presented in Chapter 3. The remainder of this chapter will be devoted to a discussion of the available theoretical models of the coherent π^0 process as well as a summary of previous measurements.

2.3 Theoretical Description of Nuclear Pion Photoproduction

As the energy scale changes and the photon becomes sensitive to different degrees of freedom, the theoretical models used to describe the interaction of the photon with the nucleus must also adapt. The structure of hadrons (bound states of quarks) at their fundamental level is governed by the theory of Quantum Chromo Dynamics (QCD). QCD describes strongly interacting particles in terms of quarks and gluons, however, the wavelengths associated with this work are too large to resolve the internal quark structure of the nucleons. Here the internal structure is included via the pion and nucleon form factors. Instead of the quarks and gluons of QCD, the appropriate degrees of freedom for the theoretical models are pions and nucleons and models are formulated explicitly in terms of pions, nucleons and nucleon resonances [6]. QCD is not completely forgotten however, the underlying symmetries of that theory are still applicable and any theory of hadron interactions must inherit the symmetries of QCD.

The construction of a model to describe nuclear pion photoproduction is almost universally approached as follows:

1. Construct the elementary pion photoproduction amplitude on the nucleon.

2. Adapt the single nucleon case to the nucleus via the impulse approximation.

3. Include terms to account for the pion-nucleus FSI and the medium modification of the $\Delta(1232)$ resonance.

A brief desciption of each of these ingredients now follows with particular emphasis on the techniques used in the model of Dreschel et. al. [8,9]. Dreschel's model will be used in Chapter 6 as a comparison to the new experimental data and as a means of making some preliminary conclusions regarding the matter distribution of ^{208}Pb.

2.3.1 π^0 photoproduction on the nucleon

Formalism

A schematic of the pion photoproduction process is shown in figure 2.3. The nucleon is considered to be an isodoublet i.e. one particle with two isospin states (p,n) and the pion an isotriplet $(\pi^{\pm}, \pi^0)$. The transition matrix element for pion photoproduction,

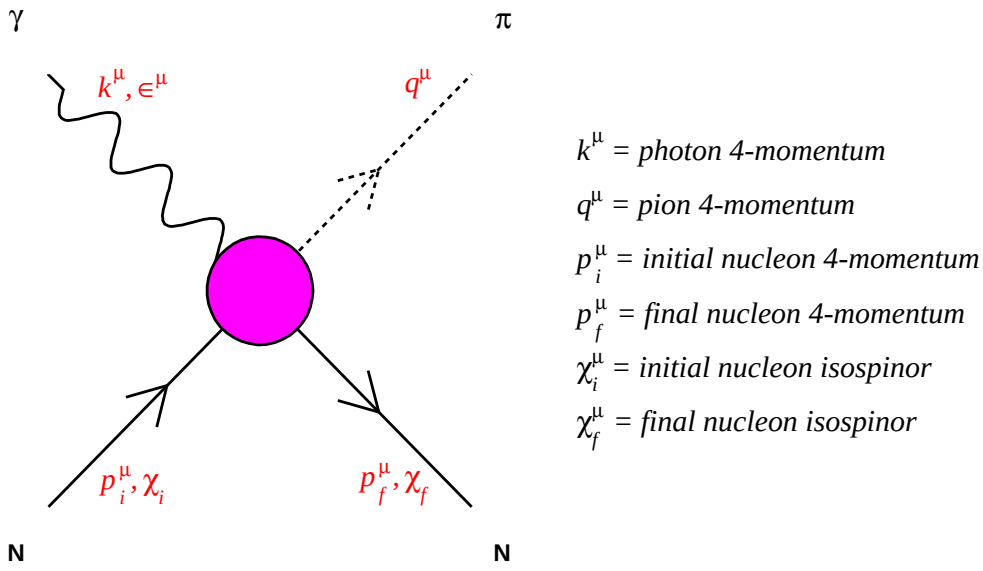

Figure 2.3: Single pion production on the nucleon.

T_{fi}, has the form:

$$T_{fi} = \epsilon_\mu J^\mu \tag{2.7}$$

$$J^\mu = u_f(p_f, s_f) j^\mu u_i(p_i, s_i) \tag{2.8}$$

The nucleon electromagnetic current is given by j_μ and u_i and u_f are the nucleon Dirac spinors. ϵ is the photon polarisation vector. The transition operator in its most general form is a linear combination of scalar amplitudes A_i and all independent Lorentz invariants, M_i (listed in appendix B.2):

$$T = \sum_i A_i M_i \tag{2.9}$$

and the matrix element becomes:

$$T_{fi} = u_f(p_f, s_f) \epsilon_\mu j^\mu u_i(p_i, s_i) \tag{2.10}$$

$$= \sum_j A_j u_f(p_f, s_f) M_j u_i(p_i, s_i) \tag{2.11}$$

This can also be expressed as:

$$T_{fi} = \langle f | \sum_{l=1}^{N} F_i \theta_i | i \rangle \tag{2.12}$$

where the amplitudes F_i are linear combinations of A_i. Furthermore, F_i can be expanded in contributions from channels with oribital angular momentum l and total angular momentum J. The result is a multipole expansion in terms of energy dependent multipoles $M_{l\pm}$ and $E_{l\pm}$ (appendix B.2). This decomposition allows greater physical insight into the reaction process. For example, the M_{1+} multipole corresponds to a magnetic transition to an intermediate state with total angular momentum J=$\frac{3}{2}$ i.e. the $\Delta(1232)$ resonance would have a strong contribution in this partial wave.

The differential cross section is calculated as a sum of the transition matrix elements over all polarisation states [4]:

$$\frac{d\sigma}{d\Omega} = \frac{q}{k} \left(\frac{m_N}{4\pi W} \right)^2 \frac{1}{4} \sum_{\epsilon} \sum_{m_i, m_f} |T_{fi}|^2 \tag{2.13}$$

The simplest calculations of the pion photoproduction amplitudes are made using the Born approximation where only the lowest order Feynman diagrams are considered. That is, only processes with single particles in the intermediate state and no excited states or loops. These are shown in figure 2.4. For π^0 photoproduction, the Kroll-Ruderman term (figure 2.4(d)) does not contribute since the photon can not couple directly to the π^0 and diagrams 2.4(a) and 2.4(b) have opposite signs and almost cancel. Therefore diagram 2.4(c) dominates the neutral pion production channel in the Born approximation. Although calculations of this sort have been shown to agree well with experimental data at photon energies close to pion threshold, the predictions, as may be expected, completely break down towards the first resonance region. The Born approach is not wrong as such; all theories agree on the structure of the Born amplitudes, it is however incomplete. To successfully describe pion photoproduction at higher photon energies requires treatment of the higher order diagrams (e.g. the diagrams of figure 2.5), in particular those involving the excitation of the Δ.

The calculation of photoproduction amplitudes beyond the Born approximation can be broadly split into two categories:

- Dispersion Theoretical Models.
- Field Theoretical Models.

Chew et. al. [10] constructed the first set of amplitudes of note in 1957 by extending the Born approximation via the application of dispersion integrals, a technique pioneered

by Kronig and Kramers in their work on optics. This method exploits the intrinsic relationship between pion photoproduction and pion scattering expressed in Watson's theorem [11]. Conservation of flux demands that the scattering matrix (S-matrix) must be unitary i.e.

$$SS^{\intercal} = 1 \tag{2.14}$$

Because of unitarity (i.e. conservation of flux), pion photoproduction is related to pion scattering, compton scattering of photons on nucleons and to radiative pion capture. The scattering matrices of the individual processes should therefore be considered as part of an enlarged S-matrix.

$$S = \begin{pmatrix} S_{\gamma\gamma} & S_{\gamma\pi} \\ S_{\pi\gamma} & S_{\pi\pi} \end{pmatrix} \tag{2.15}$$

Watson's theorem can be derived from the unitarity of this S-matrix and the result is that the multipole amplitude phase for pion photoproduction matches that of pion scattering. Further references to unitarity reflect the requirement that the multipole amplitudes be of the correct phase.

Berends et. al. [12] continued the work of Chew et. al. in 1967 performing similar calculations but in far greater detail. The dispersion integrals approach is most successful for $E_\gamma < 500$ MeV and becomes increasingly difficult at higher energies. A complication arises when using the dispersion relations for nuclear calculations. Because of the Fermi momentum of the nucleons within the nucleus, the amplitudes must be transformed to an invariant form causing mathematical complexities and a loss of physical information.

In 1977 Blomqvist and Laget [13] introduced a field theoretical model based on the use of an effective Lagrangian. This involves the explicit evalutation of the Born Feynman diagrams as well as those of higher order processes. In this way, different processes, such as the excitation of the Δ resonance can be included in an ad hoc fashion. This technique is also heavily reliant on input from π-scattering, for example the coupling constants for the interaction vertices are taken from fits to pion scattering data. The effective lagrangian approach can be extended beyond E_γ >500 MeV by the addition of further diagrams including higher order N^* and Δ resonances. Furthermore it can be directly applied to any frame of reference.

2.3.2 Unitary Isobar Model of Dreschel et. al.

The unitary isobar model of Dreschel et al. [9] is based on the construction of an effective Lagrangian to model pion photo- and electroproduction i.e. it is a field theoretical

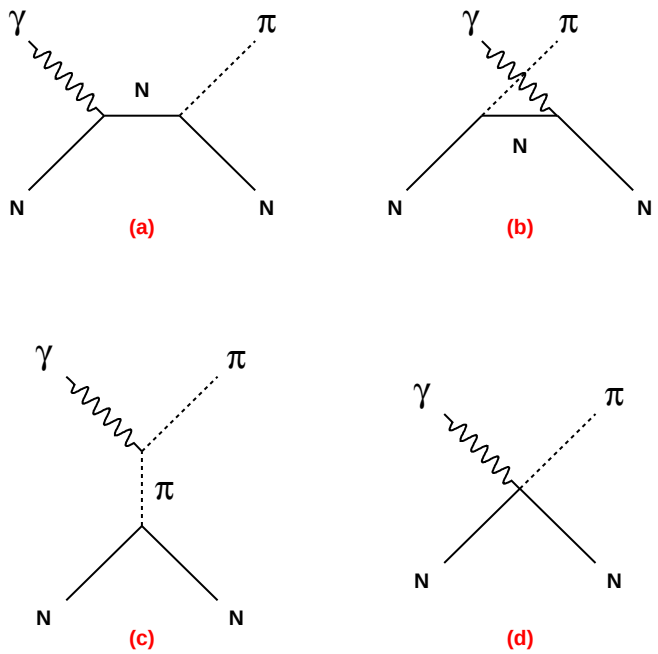

Figure 2.4: Diagrams (a)-(c) are the Born terms for pion photoproduction, (d) is the Kroll-Ruderman or seagull diagram.

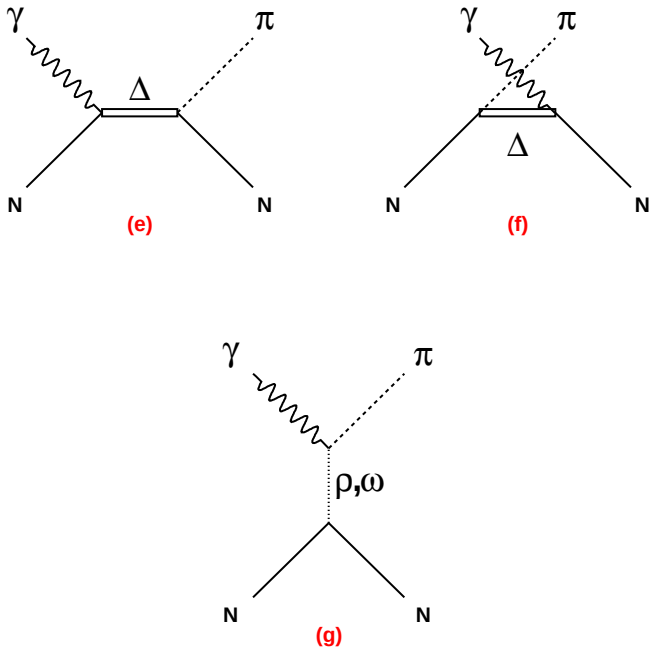

Figure 2.5: Feynman diagrams of resonant and heavy meson pion production mechanisms.

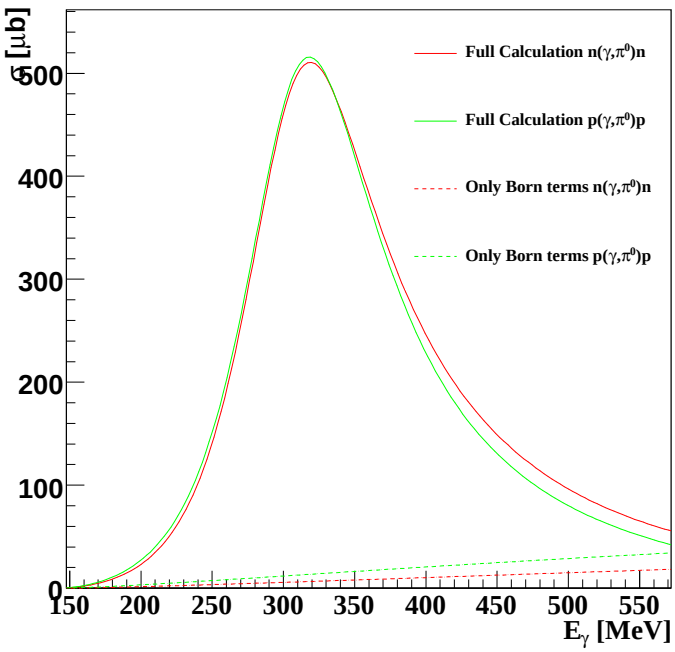

Figure 2.6: MAID calculations of π^0 photoproduction on the nucleon [9].

model. The model was designed with nuclear applications in mind and the adaptation of the single nucleon case to the nuclear case will be discussed in the next section. The non-resonant contributions to the pion production amplitude e.g. diagrams (a)-(d) of figure 2.4 are described using standard Born terms with a mixed pseudovector-pseudoscalar πNN coupling. The resonant contributions are assumed to have Breit-Wigner forms and are included while taking into account unitarity.

2.3.3 Nuclear π^0 photoproduction

The process of adapting the single nucleon pion photoproduction operator of section 2.3.2 to the nuclear case is complicated by several factors, namely:

- The Fermi momentum of the nucleons.
- Pion-nucleus final state interactions.
- The modification in the medium of the $\Delta(1232)$ resonance.

The Dreschel model [8] gives predictions for nuclear pion photoproduction with different levels of complexity in the theoretical description. The plane wave impulse approximation accounts for effect (1). The distorted wave impulse approximation accounts for both (1) and (2). The full calculation accounts for (1), (2) and (3), supplementing the optical potential (used to account for (2)) with a term to account for medium modifications of the Δ resonance. Each of these calculations are discussed in more detail in the following sections.

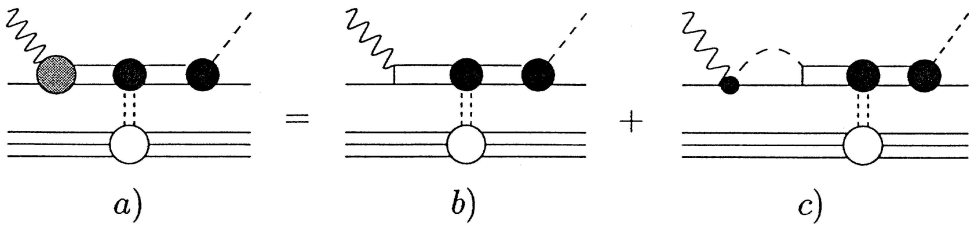

Figure 2.7: Diagram (a) is the sum of (b) and (c), the two main mechanisms contributing to the excitation of the Δ and the corresponding medium effects. (b) direct excitation of the isobar, (c) the Δ is excited via pion rescattering. Diagram from [8].

2.3.4 Plane Wave Impulse Approximation

The simplest model of nuclear pion photoproduction is the plane wave impulse approximation (PWIA). The impulse approximation treats the interaction between the photon and the nucleus as a sum of two body interactions i.e. the photon couples to one nucleon and the interactions with the other constituent nucleons are ignored. For the weakly coupled electromagnetic interaction, this is a good approximation. The nuclear transition operator is then calculated as a linear sum of the elementary transition operator over all constituent nucleons i.e.

$$T = \sum^{N} t_{(\gamma,\pi^0)} \tag{2.16}$$

No attempt is made to account for the pion FSI or any in-medium effects and the pion leaves the nucleus as a plane wave. The resulting differential cross section for coherent production can be expressed as [8]:

$$\frac{d\sigma_{PWIA}}{d\Omega}(E_\gamma, \theta_\pi) = \frac{s}{m_N^2} A^2 \frac{d\sigma_E}{d\Omega^*}(E_\gamma^*, \theta_\pi^*) F^2(q), \tag{2.17}$$

where, $q(E_\gamma,\theta_\pi)$ = momentum transfer to the nucleus
- A = atomic mass number
- s = invariant mass of the photon nucleon pair
- E_γ = incident photon energy
- θ_π = pion polar angle in the photon-nucleus cm frame
- m_N = average nucleon mass
- E_γ^* = incident photon energy in the photon-nucleon cm system
- θ_π^* = pion polar angle in the photon-nucleon cm system
- F(q) = matter form factor
- q = the momentum transfer to the nucleus

In the case of spin-zero nuclei the spin-dependent terms in the cross section cancel and the elementary cross section is equivalent to the spin independent cross section, given as equation 2.18. It uses the standard CGLN amplitude F_2 (appendix B).

$$\frac{d\sigma_E}{d\Omega^*} = \frac{d\sigma_{NS}}{d\Omega^*}(E_\gamma^*, \theta_\pi^*) = \frac{1}{2}\frac{q_\pi^*}{k^*}|F_2(E_\gamma^*, \theta_\pi^*)|^2 \sin^2(\theta_\pi^*), \tag{2.18}$$

where, k^* = photon momentum in the photon-nucleon cm frame
- q_π^* = pion momentum in the photon-nucleon cm frame

The factorisation approximation (equation 2.19) is used to account for the Fermi momentum of the nucleon i.e. the dependence of the elementary amplitude on the nucleon's initial momentum. $\mathbf{p}_N$ is the average momentum of the nucleon and follows from the momentum transferred to the nucleus:

$$\mathbf{p}_N = -\mathbf{q}\left(\frac{(A-1)}{2A}\right), \tag{2.19}$$

Krusche [14] showed that the PWIA calculation gives an approximate description of the coherent π^0 process at low photon energies close to pion production threshold. As expected, at higher photon energies when the produced pion becomes more energetic the role of pion FSI increases and the PWIA approach breaks down.

2.3.5 Distorted Wave Impulse Approximation

The distorted wave impulse approximation (DWIA) goes beyond the PWIA calculations by attempting to model the pion-nucleus FSI. Like the PWIA calculations, the model takes the elementary pion production operator and adapts it to the nuclear case via the impulse approximation. The pion FSI is included as a distortion of the outgoing pion plane wave by a complex pion-nucleus optical potential. In physical terms this has the effect of changing the wavelength and reducing the amplitude of the pion plane wave. The earliest calculations accessed the distorted pion wave in coordinate space by solving the Klein-Gordon equation with an optical potential for each of the contributing partial waves. More recent calculations have been performed in momentum space making it easier to include the Fermi motion of the nucleons and simplifying transformations between π-nucleon and π-nucleus centre of mass systems [7]. Momentum-space formulations also allow easier cross referencing between pion photoproduction and pion scattering. The parameters for the optical potential are fixed from fits to pion scattering data.

For the calculations presented here, the distortions of the outgoing pion waves are introduced via a second order pion-nucleus optical potential formulated in momentum space [7]. The first order potential is constructed microscopically and is parameter free. Physically, this corresponds to the interaction of the pion with a single nucleon. This is supplemented with a second order phenomenological term with energy dependent free parameters which are fitted to pion scattering data on ^{12}C, ^{6}Li, ^{16}O, ^{28}Si, and ^{40}Ca and were found to be consistent for all nuclei. This takes account of the interaction of the pion with a pair of nucleons [15].

2.3.6 Delta Resonance Energy Model of Dreschel et. al.

In the DWIA model, the pion-nucleus FSI are introduced by a pion-nucleus optical potential. The assumption is that the pion is created by the interaction of a photon with a single nucleon and once produced, the pion moves in a mean field due to the presence of the other constituent nucleons. However, as the pion momentum increases and the role of intermediate Δ excitation increases, the pion-nucleus optical potential is no longer enough to account for the pion-FSI effects. The effect of the creation and propagation of the Δ resonance in the nuclear medium must also be explicitly included (figure 2.7). The full Dreschel calculation [8] which will be referred to as the Delta Resonance Energy Model (DREN) attempts to do just that.

The elementary pion photoproduction amplitude is incorporated into the nuclear environment as described for the PWIA and DWIA calculations. However, a phenomenological Δ self energy is also introduced which modifies the effective mass and width of the Δ. The Δ self energy parameters are fitted to pion photoproduction data on ^{4}He and ^{12}C [8]. The similarity of the self energy for the two cases was taken as evidence that the Δ self energy saturates quickly with increasing nuclear mass, and the parameters fitted to low mass nuclei should suffice for heavier nuclei [8].

2.3.7 Coherent π^0 Photoproduction in the DREN model

Presented in this section are the predicted total and differential cross sections for coherent π^0 photoproduction in the framework of the PWIA, DWIA and DREN models. Comparisons of the predictions give an indication of the role of π-nucleus FSI to the coherent production process. The PWIA, DWIA and DREN calculations require the input of the matter form factor (e.g. see equation 2.17) which is the Fourier transform of the matter density distribution, ρ(r). The calculations assume that the matter distribution matches that of the charge distribution which is parametrised as a symmetrised Fermi function:

$$\rho(r) = \rho_0 \frac{sinh(c/b)}{cosh(c/b) + cosh(r/b)} \tag{2.20}$$

$$\rho_0 = \frac{3}{4\pi c^3}\left[1 + \left[\frac{\pi b}{c}\right]^2\right]^{-1} \tag{2.21}$$

where c is the half height radius and b controls the diffuseness of the edge of the distribution. The r.m.s. radius of this distribution is calculated as:

$$r_{r.m.s} = \frac{3}{5}c^2\left[1 + \frac{7}{3}\left(\frac{\pi b}{c}\right)^2\right] \tag{2.22}$$

The matter distributions used in the calculations are shown in figure 2.8. On the same figure, the charge density distributions taken from elastic electron scattering are shown.

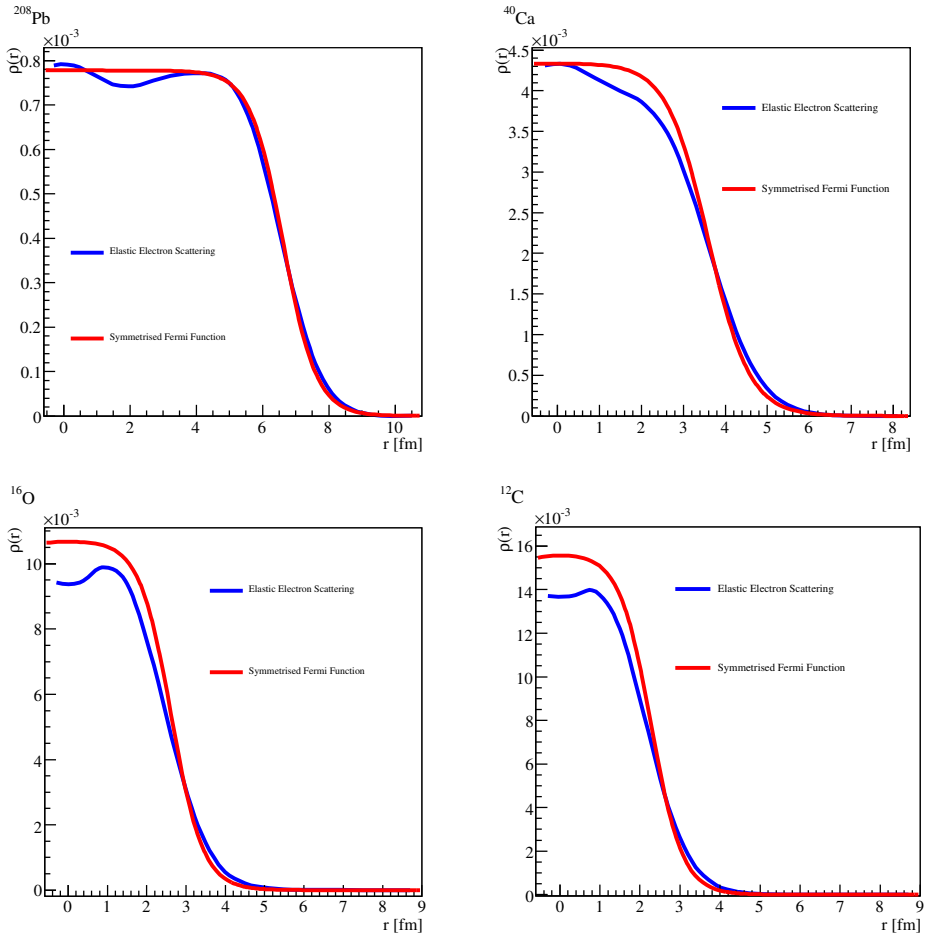

Figure 2.8: Blue line: charge distribution from elastic electron scattering [2]. Red line: symmetrised Fermi function used in Kamalov's DREN calculations.

The calculations were made using the theoretical code made available to us by S. Kamalov [17] which was run for discrete values of the incident photon energy, E_γ, in 0.5 MeV steps and then averaged to correspond to the experimental photon energy bins. Figure 2.9 shows the total cross sections for all four nuclei under investiagtion in this thesis. Figures 2.10(a) to 2.11(b) show the differential cross sections as a function of outgoing pion angle for two incident photon energies, $E_\gamma = 150$ MeV and $E_\gamma = 200$ MeV.

For the total cross sections, below $E_\gamma = 180$ MeV, the difference in the PWIA, DWIA and DREN calculations is small. However, at higher incident photon energies as the outgoing pion energy approaches those near the peak of the Δ resonance, the importance of including the pion FSI and medium modifications is very apparent.

The effect on the differential cross sections of the pion FSI is complex. The pion distortion modifies the interference between the competing partial waves which alters the angular dependence of the differential cross sections. The gross shape of the cross section however is still controlled by the form factor. For the PWIA calculations, the cross sections are simply proportional to the square of the form factor which is the Fourier transform of the density distribution. While the diffraction pattern is still present in the DWIA and DREN calcualtions, in general, the minima are moved to smaller angles as a result of the attractive pion-nucleus potential. For a heavy nucleus like ^{208}Pb, the movement in the first minimum is however relatively modest. The pion distortions also have the effect of 'filling in' the minima due to the smearing effect on the pion angle caused by the pion-nucleus interaction as the pion leaves the nucleus.

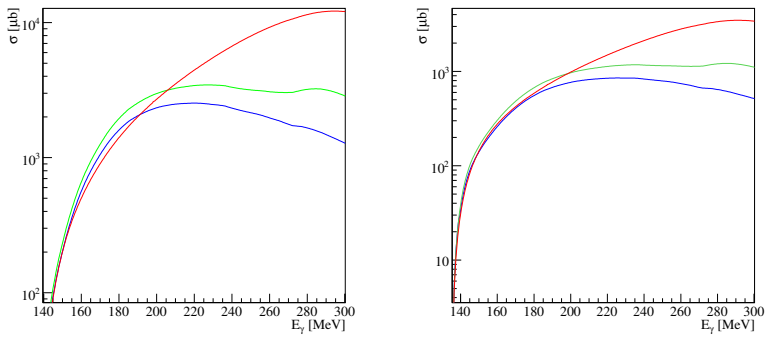

(a) ^{208}Pb (b) ^{40}Ca

(c) ^{16}O (d) ^{12}C

Figure 2.9: Comparison of PWIA, DWIA and DREN calculations of total cross sections. Red line: PWIA. Green line: DWIA. Blue line: DREN.

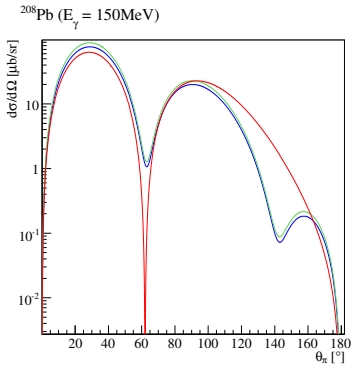

(a) ^{208}Pb

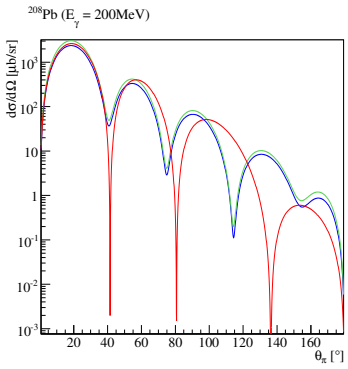

(b) ^{208}Pb

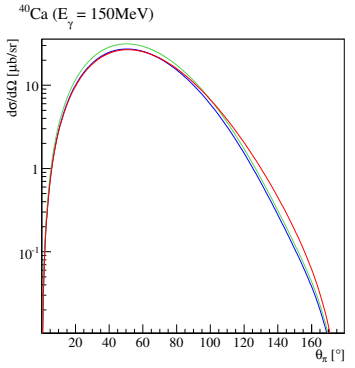

(c) ^{40}Ca

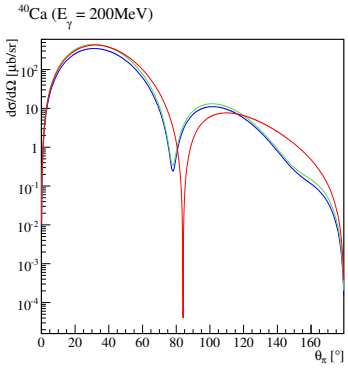

(d) ^{40}Ca

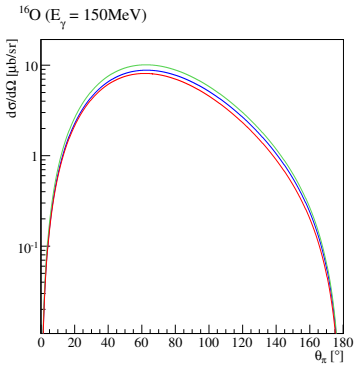

(e) ^{16}O

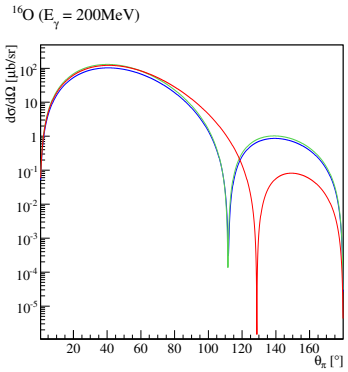

(f) ^{16}O

Figure 2.10: Comparison of PWIA, DWIA and DREN calculations of differential cross sections. Red line: PWIA. Green line: DWIA. Blue line: DREN.

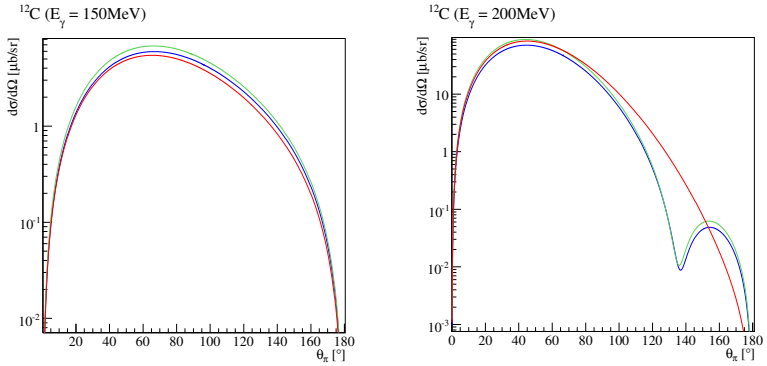

(a) ^{12}C (b) ^{12}C

Figure 2.11: Comparison of PWIA, DWIA and DREN calculations of differential cross sections. Red line: PWIA. Green line: DWIA. Blue line: DREN.

2.4 Previous Measurements

It was recognised as early as 1958 that coherent π^0 photoproduction could be a useful tool in determining the nuclear matter distribution [18]. However, the difficulty in detecting π^0 mesons with sufficient accuracy and producing a suitable monochromatic photon beam meant experimental progress was slow. The inherently small photonuclear cross sections demand high beam intensities, however, with high intensities comes an increased rate of random coincidences. The ratio of real to random events can be minimised by increasing the duty factor of the beam (section 4.2). Only in the past 10-15 years have suitably high duty factor accelerators become available.

The detection of neutral π mesons is more complicated than for charged π mesons which deposit energy readily in electromagnetic calorimeters or can be momentum analysed in a magnetic spectrometer. The detection of neutral π mesons is more complicated. The π^0 decays predominantly to two photons in 10^{-18}s which, for a stationary π^0 are almost back to back in the lab frame.

The photoproduction of pions from a nuclear target can proceed via a range of processes. The coherent channel of interest occurs with a background of incoherent processes which must be separated out. The separation of coherent and incoherent π^0 events can be done two ways:

- A missing energy analysis which, for a known incident photon energy, E_γ, compares the detected pion energy with the calculated energy for a coherent reaction (section 5.7.1).

- By exploiting the kinematics of the π^0 decay (appendix A) i.e. that each pion energy has a corresponding minimum opening angle Ψ_{min} between its decay photons. For a given incident photon energy, the energy of an incoherent π^0 will always be less than that of a coherent one. Therefore: $\Psi_{min}^{incoh} > \Psi_{min}^{coh}$.

Both techniques require accurate determination of the incident photon 4-momentum and accurate reconstruction of the pion 4-momentum. Experimentally this translates to excellent energy and angular resolution in the photon detectors.

Thus for accurate reconstruction of the π^0 4-momentum and isolation of coherent events, large acceptance photon spectrometers with excellent energy and angle resolution are preferred. These are technically challenging and expensive and even today only a few detector systems meeting these specifications are in operation.

For these reasons the first detailed measurement of the differential cross section for coherent π^0 photoproduction were not made before the 1990s. These experiments are discussed in section 2.4.1. Earlier measurements dating back to the 1950s had much lower quality, although they did identify the main qualitative features of the coherent π^0 reaction, confirming the forward bias of the π^0 angular distribution as well as the diffraction structure in the cross sections. Schrack et. al. went as far as to extract an r.m.s. matter radius for ^{12}C, however both the pion energy and angular resolution was poor and at best the uncertainty in the radius was ∼20% [19]. For a complete review of these early measurements the reader is directed to reference [20] and references therein.

2.4.1 TAPS Measurements

The most recent coherent π^0 photoproduction measurements have been made using the TAPS spectrometer. TAPS (section 4.7) is comprised of several hundred BaF_2 crystals which together form a highly segmented photon spectrometer (figure 2.12). The design is deliberately flexible, allowing for multiple different configurations. In 1998, Krusche et. al. [21,14] made measurements on ^{12}C, ^{40}Ca, ^{93}Nb and ^{nat}Pb at MAMI with 320 of the TAPS crystals arranged as shown in figure 2.12 and with incident photons in the energy range E_γ = 200-400 MeV.

In 1999, a group from Glasgow University used an improved TAPS setup of 512 BaF_2 crystals in a similar configuration to figure 2.12, to make measurements on ^{12}C, ^{16}O, ^{40}Ca and ^{208}Pb [20]. Using a lower beam energy, they were able to sample the reaction from E_γ = 135-380 MeV i.e. from threshold right the way through the Δ region.

Unfortunately, the improved statistical accuracy and more detailed analysis of the latter TAPS measurements uncovered a significant failing in the detector's response to

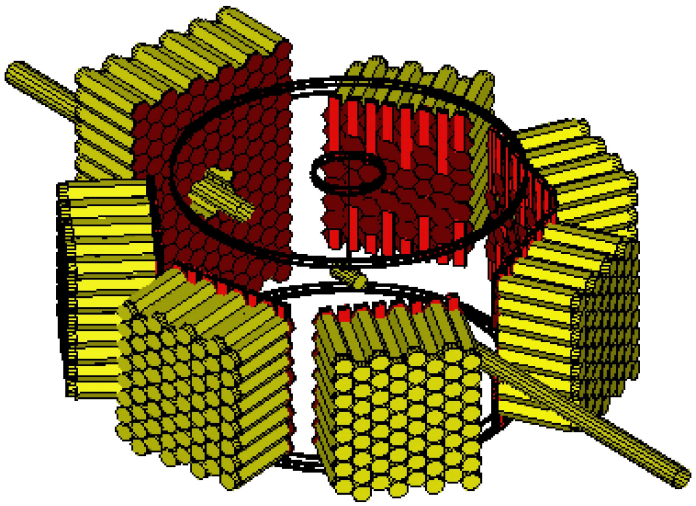

Figure 2.12: TAPS configuration for Krusche measurement. Extracted from [21].

photons. Photons deposit their energy in TAPS via an electromagnetic shower in a cluster of crystals and their energy and angle are inferred from a weighted sum of the individual crystal energies. After anomolies were observed in the data, Monte-Carlo simulations highlighted systematic effects in the TAPS reconstruction of the photon momenta. When aimed directly at the centre of a TAPS block the photon momentum was found to be reconstructed accurately. As photons were aimed towards the edge of a block, parts of the electromagnetic shower were lost out the sides and back of the crystals. The flat surface of the TAPS blocks also presents a problem as away from the centre of the blocks, the photons are no longer incident perpendicular to the crystal faces and the distribution of energy to the crystals in the shower is no longer symmetric.

As a result, the reconstruction of the pion 4 momentum suffered large unsystematic and unpredictable variations with angle ($\sim$5 MeV variations in the pion energy) introducing significant ambiguities into the separation of coherent and incoherent processes via the missing energy method. This was a significant effect given the typically small energy gaps ($<$5 MeV) between the ground and excited states of a nucleus. The effect of this on the differential cross sections was difficult to quantify. Furthermore, the π^0 detection efficiency was in the range 2% to 5% and was strongly dependent on the pion angle and incident photon energy (figure 2.13) necessetating a very accurate determination of the efficiency by the monte carlo simulation software. While these data are certainly the most complete study of coherent π^0 production to date, it remains unpublished. These issues can be avoided by using a large acceptance symmetric detector such as the Crystal Ball (section 4.6). A comparison of the present Crystal Ball data

to both TAPS experiments and some further discussion will be presented in Chapter 7.

Although the Krusche TAPS data cover the incident photon energy range where FSI effects are relatively large (for example see figure 2.9(a)) and is therefore not ideal for probing the matter distribution, it has been used to extract a matter radius of ^{208}Pb. The value obtained results in a negative neutron skin thickness i.e. the r.m.s. neutron radius is smaller than the r.m.s. proton radius. This is very surprising and contradicts all predicted values of the ^{208}Pb neutron skin from theory and supports the need for new, more accurate measurements with reduced systematic uncertainties.

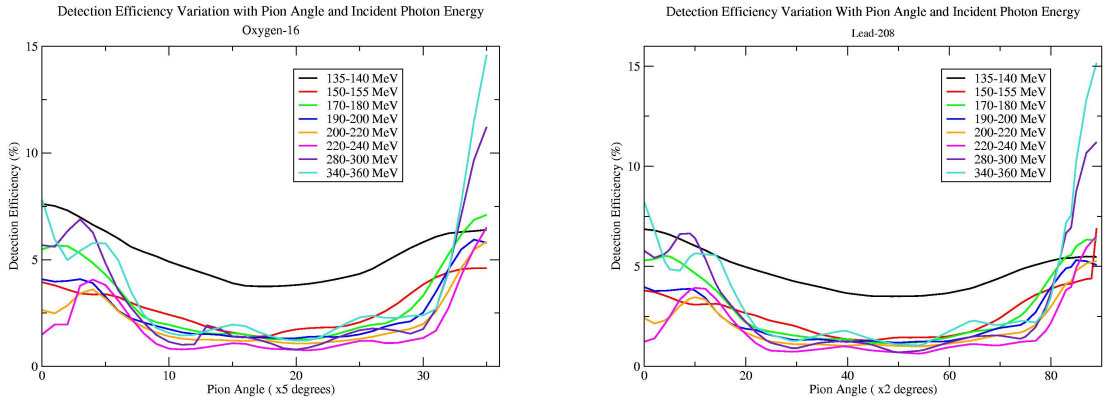

Figure 2.13: π^0 detection efficiency for ^{16}O (left) and ^{208}Pb for Glasgow TAPS data. Extracted from [20].

2.5 Incoherent π^0 photoproduction

In the same way that coherent π^0 photoproduction is analagous to elastic electron scattering, an analogy can be made between incoherent π^0 photoproduction (where the nucleus is left in an excited state) and inelastic electron scattering. In particular, the differential cross section of incoherent π^0 photoproduction where the final state of the nucleus is known gives access to the matter transition form factor between the ground state and that excited state. Investigations of matter transition form factors via incoherent π^0 photoproduction from complex nuclei would make an interesting complimentary study to that of charge transition form factors in inelastic electron scattering.

No measurements of incoherent π^0 production from complex nuclei have been made to date where the final excited state of the nucleus was cleanly isolated. The Krusche TAPS experiment (section 2.4.1) published an incoherent differential cross section from

^{12}C [21], however, the cross section was taken for all combined incoherent processes and no final excited nuclear state was isolated. No information on the matter transition form factor can be extracted without isolating a specific incoherent process. This will be possible in the future with the new Crystal Ball data described in this thesis. The coincident detection of π^0 s and low energy photons from the deexcitation of an excited nucleus will allow certain specific final state to be cleanly identified.

While coherent π^0 production has been the subject of a variety of theoretical investigations in the past 40 years, the incoherent process has not benefitted from the same scrutiny. The theoretical treatment is more complicated than for the coherent channel where only the nuclear ground state is needed for the initial and final state. The most recent models of the incoherent process within complex nuclei are transport models or mean free path monte carlo models [22,23].

2.6 Current Work

The data presented in Chapter 6 was taken over 6 weeks in March and April 2005 at the MAMI facility in Mainz, Germany. The experiment is one of the first to exploit the Crystal Ball detector's new home in the A2 hall at MAMI, combining it for the first time with the Glasgow Tagged photon beam. Data has been taken on four spin-0 targets: ^{208}Pb, ^{40}Ca, ^{16}O and ^{12}C over the energy range 135 MeV $< E_\gamma <$ 300 MeV. The ultimate goal of this research program is to make an accurate measurement of the neutron skin on ^{208}Pb, the importance of which is discussed in the next chapter. Both differential and total cross sections have been obtained and compared to the previous TAPS data of both Krusche and the Glasgow group. A comparison has also been made with the DREN model of Dreschel et. al. A preliminary evaluation of the nature of the neutron skin on ^{208}Pb has been made via comparison with the DREN calculations.

Chapter 3

The Nuclear Matter Distribution

3.1 Overview

The nuclear matter radius is a fundamental nuclear observable and yet there is a wide gap between the exceptional accuracy with which the nuclear charge radius is known and the present knowledge of the matter radius. This is justification enough for new investigations of the nuclear matter distribution, however, a new matter radius measurement of ^{208}Pb has further implications. Since the ultimate goal of the detailed coherent π^0 measurements presented in this thesis is a precise measurement of the nuclear matter distribution, it is important to stress the wide ranging implications the measurement will have. In particular, recent publications have shown the link between the neutron skin thickness of ^{208}Pb and the structure of neutron stars, the properties of heavy ion collisions and atomic parity non-conservation.

3.2 Nuclear Theories

In principle, the modelling of a nucleus should be straight forward: solve the many body Schrödinger equation with a suitable nucleon-nucleon potential. In practice however this is almost impossible for anything but the lightest nuclei as we cannot solve the many body problem analytically. In recent years there has been much success using Green's function and variational monte carlo techniques which uses a stochastic refinement of a wave function to predict the energy level structure of nuclei based on the basic interactions of the nucleons [24]. This is computationally very intensive and is presently limited to nuclei of A $<$ 12. Instead, for heavier nuclei, models which simplify the many body problem to nucleons moving in mean field potentials are employed. These models can be broadly split into two categories:

- Models based on the Skyrme interaction.

- Relativistic mean field theories.

The first category employs a non-relativistic framework with the effective Nucleon-nucleon interaction potential constructed to fit experimental nucleon-nucleon scattering data. Relativistic mean field theory (RMF) calculations model the nucleon-nucleon interaction as an exchange of ω, ρ and σ mesons. The RMF models are fully relativistic and the parameters of the meson exchange are fitted to observable saturation properties of nuclei. Both methods use Hartree-Fock iterative procedures to obtain a solution for the nuclear wavefunction.

There now exists a wealth of models that fall into these two categories which reproduce bulk nuclear observables such as charge radii, binding energies, spin-orbit splitting, etc. consistently. The same models, however, offer widely varying r.m.s. neutron radius values [25,26]. Figure 3.1 demonstrates the power a measurement of ΔR_{Pb} could have in discriminating between different models. The filled markers represent typical relativistic mean field theory calculations (RMF) and the open markers signify calculations based on a Skyrme type interaction. The sole circular data point shows how a 1% measurement of the neutron skin on ^{208}Pb can be used as a calibration point for nuclear models.

Moreover, the uncertainty in the neutron radius of stable nuclei produce large uncertainties in the extrapolation of the model predictions to the neutron and proton drip line. These extrapolations are important for nuclear astrophysics applications[27].

3.3 The Nuclear Equation of State

The equation of state (EOS) of nuclear matter is defined as the energy per nucleon in infinite nuclear matter as a function of both density (ρ) and isospin asymmetry (α):

$$\frac{E}{A}(\rho, \alpha) \tag{3.1}$$

where the isospin asymmetry is defined as:

$$\alpha = \frac{N - Z}{A} \tag{3.2}$$

with N,Z and A the neutron number, proton number and the atomic mass number respectively. From this all infinite nuclear medium parameters can be calculated. One of the first and most successful equations of state was the semi-empirical mass formula (SEMF) [28] arising from the liquid drop model of the nucleus:

$$\frac{E}{A} = a_{vol} - a_{surf}A^{-1/3} - a_{sym}\frac{(N-Z)^2}{A^2} - ... \tag{3.3}$$

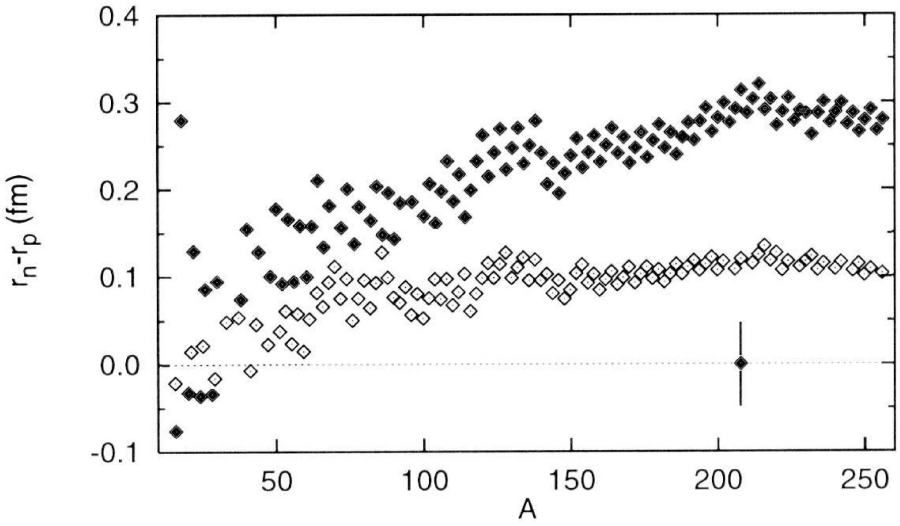

Figure 3.1: Figure taken from reference [25]. Filled markers correspond to relativistic mean field theory calculations, while open markers correspond to calculations based on a Skyrme interaction. Further details of the models can be found in reference [25].

If one considers the above equation when multiplied by A, then the first term is proportional to A ($\propto R^3$) and is therefore called the volume term. The second term is proportional to $A^{2/3}$ ($\propto R^2$) and is therefore the surface term. The third term is referred to as the symmetry energy and will be discussed in more detail in the next section. By design the SEMF provides a good description of symmetric nuclear matter at nuclear densities, however at higher densities or for more asymmetric matter the model breaks down. One of the most active current areas of research in nuclear physics is concerned with developing a microscopic theory allowing the EOS to be extended into uncharted regions of density and asymmetry e.g. the neutron star regime.

3.3.1 The Nuclear Symmetry Energy

Without the electromagnetic interaction, stable nuclei would have an equal number of protons and neutrons and the valley of stability on the familiar N-Z plot of isotopes could be fitted with a straight line of gradient 1. The presence of the long range repulsive electromagnetic force in the nucleus and the short range nature of the nucleon-nucleon force however make this situation energetically unfavourable. As more protons are added to the nucleus an excess of neutrons is found to give the most stable configuration. Although the additional strong force extended by the extra neutrons helps to overcome the Coulomb repulsion, this move away from symmetric matter where N=Z

incurs an energy penalty i.e the binding energy per nucleon increases. Figure 3.2(b) shows this as a function of nucleon density for several different models. This extra energy is referred to as the symmetry energy or more accurately, the isospin asymmetry energy and reflects the isospin dependence of the nucleon-nucleon interaction - that the nn and pp interactions are less attractive than the np interaction. Its presence is evidenced in nature by the fact that symmetric matter is bound whereas pure neutron matter is unbound e.g. the deuteron is bound and the dineutron is not. The symmetry energy is an important feature underlying a wide range of physics from nuclei to neutron stars as discussed by Steiner et al. in their review of the subject [29] and summarised in Figure 3.3. A measure of the symmetry energy (around the nuclear saturation density) has been made from data on binding energies of nuclei and giant dipole resonances. However, the symmetry energy has only been restricted to (27-36) MeV [30] (Atomic Data and Nuclear Data Tables give this value as (30±4) MeV [31]). Given its far reaching influence, it is perhaps surprising that the symmetry energy and its density dependence are so poorly known, however, Furnstahl [32] using a variety of mean field models, has shown that a measurement of the neutron skin thickness in ^{208}Pb could be used to calibrate these quantities at nuclear densities.

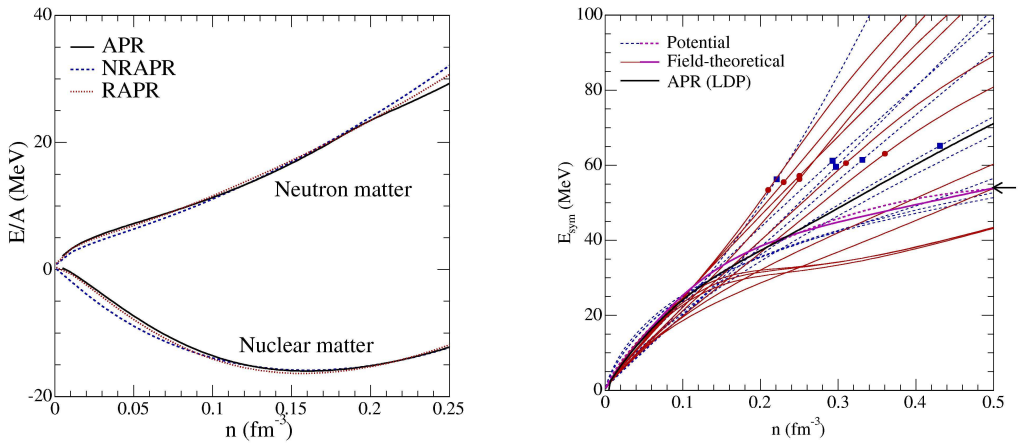

(a) (b)

Figure 3.2: Figure is taken from reference [29]. (a), the energy per particle for nuclear matter and pure neutron matter as a function of density for 3 different models. (b), the symmetry energy as a function of density i.e. the energy per particle for nuclear matter minus the energy per particle for pure neutron matter.

The energy per particle of nuclear matter can be expanded in a Taylor Series about the nuclear saturation density, ρ_0 and α=0 i.e. the case of symmetric matter at nuclear

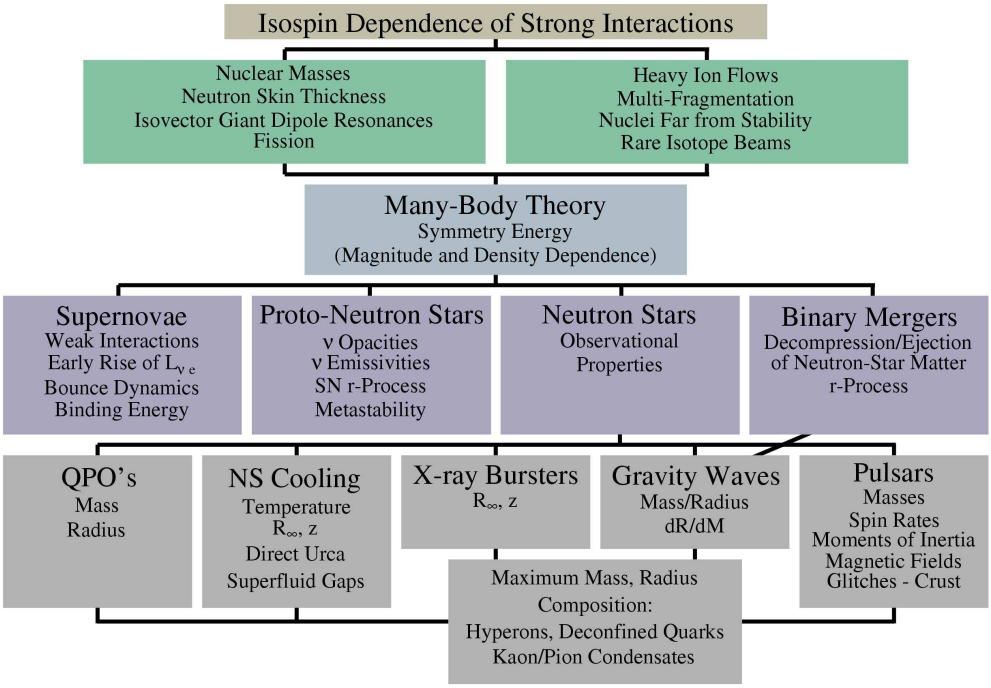

Figure 3.3: The extensive influence of the nuclear symmetry energy. Figure from reference [29].

densities [32]:

$$E(\rho,\alpha) = E(\rho,0) + S_2(\rho)\alpha^2 + S_4(\rho)\alpha^4 + ..., \tag{3.4}$$

$$E(\rho,0) = -a_v + \frac{K_0}{18\rho_0^2}(\rho-\rho_0)^2 + ..., \tag{3.5}$$

$$S_2(\rho) = a_4 + \frac{p_0}{\rho_0^2}(\rho-\rho_0) + \frac{\Delta K_0}{18\rho_0^2}(\rho-\rho_0)^2 + ..., \tag{3.6}$$

$$\tag{3.7}$$

where ρ is the density, α is defined in equation 3.2, K_0 is the compression modulus of nuclear matter and ΔK_0 the correction to the incompressibility. S_2 is the symmetry energy and p_0 is its first derivative with respect to density evaluated at the nuclear saturation density:

$$p_0 = \frac{\partial S_2(\rho)}{\partial\rho}|_{\rho=\rho_0} \equiv S_2'(\rho_0) \tag{3.8}$$

The Taylor series expansion of equation 3.5 can be truncated after just one term for the cases of ^{208}Pb and neutron star matter as further terms become negligible [30].

$$E(\rho,\alpha) = E(\rho,0) + S_2(\rho)\alpha^2, \tag{3.9}$$

This approximation is widely used in neutron star calculations [33,34,35] and has been shown to be a good approximation of nuclear matter. Thus S_2, the symmetry energy can be expressed as:

$$S_2(\rho) \quad = \quad \left(\frac{1}{2}\frac{d^2(E)}{d\alpha^2}\right)|_{\rho,\alpha=0} \tag{3.10}$$

Furthermore, the pressure of cold, beta stable nucleonic matter, P, can be expressed as:

$$P(\rho,\alpha) \quad = \quad \rho^2[E'(\rho,0) + S_2'(\rho)\alpha'], \tag{3.11}$$

where primes indicate first order derivatives with respect to density. As a result the EOS is often expressed as P(ρ,α) as opposed to E(ρ,α) particularly for neutron star applications.

Neither a_v, K_0 or ρ_0 show any correlation with the neutron skin thickness. However, as can be seen in Figure 3.4, the symmetry energy at saturation density, $S(\rho_0) = a_4$, is tightly correlated with the neutron skin thickness and this correlation shows little dependency on the type of nuclear model employed. This is also the case for p_0, the linear density dependence of the symmetry energy. Thus an accurate determination of the neutron skin thickness will constrain the symmetry energy and its first derivative at saturation densities, $S_2'(\rho_0)$.

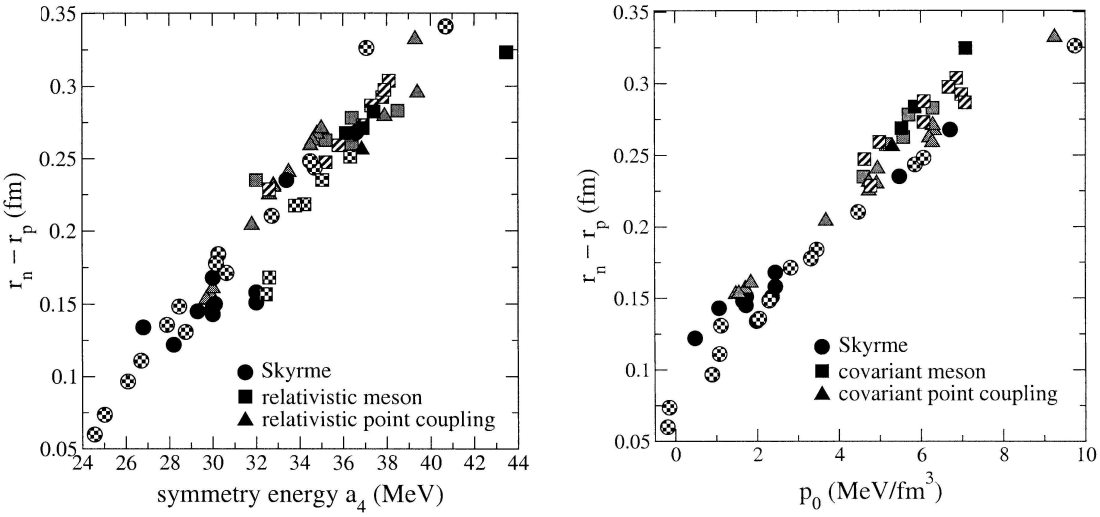

Figure 3.4: Both figures from reference [32]. Left: the neutron skin in ^{208}Pb against symmetry energy for a variety of models. Right: Correlation between neutron skin in ^{208}Pb and the linear density dependence of the symmetry energy. Notation as in equations 3.5-3.11.

3.3.2 ^{208}Pb and Neutron Stars

The connection between a heavy nucleus such as ^{208}Pb and a neutron star is not immediately obvious. The difference in size is a massive 18 orders of magnitude and the central density of a neutron star is around 5 times greater than the central density of the lead nucleus. However, recent studies have shown surprising correlations between the two reflecting their shared dependence on the equation of state and particularly the symmetry energy.

Neutron stars are some of the most dense objects in our universe. Formed when a massive star ($> 8M_{\odot}$) undergoes a type II supernova explosion and the core collapses under gravity, neutron stars were first theorised in the 1930s and observed for the first time in the 1960s. A typical star resulting from the core collapse is ∼12km in radius and has a mass on the order of $1.5M_{\odot}$. A simple calculation of mass over volume shows the high average density of the body (about twice the nuclear saturation density, $\rho_0 = 0.16\text{fm}^{-3}$) however, the central density of the star, ρ_c is thought to be even greater - about 5-10 times that of ρ_0 [36]. Conservation of angular momentum during the core collapse leads to extremely fast rotation speeds, the maximum detected frequency of rotation is 700 Hz. They are also characterised by their large magnetic fields ($B_{max} \sim 10^{18}$gauss).

During and after the supernova explosion, large numbers of neutrinos are emitted. The loss of neutrinos forces electrons and protons to combine, ultimately resulting in very neutron rich matter. A schematic of the possible composition of a neutron star is shown in figure 3.5. 'Normal' neutron stars are thought to have a solid crust of non-uniform neutron rich matter sitting on a liquid core. Within this extemely dense core it is possible that another phase transition takes place to an exotic state such as hyperon matter, strange quark matter or kaon or pion condensates. Some models predict the existence of strange quark stars composed entirely of deconfined strange quark matter (SQM stars) with a bare quark surface [37]. These models reflect predictions that normal hadronic matter composed of up and down quarks may not be the absolute ground state of matter and that when exposed to sufficiently high densities matter undergoes a phase trasnsition to deconfined quark matter. If this quark matter was degenerate enough it may then try to use another degree of freedom, strangeness, to lower its overall energy. This strange quark matter would then be the ground state of hadronic matter. Thus neutron stars offer a unique opportunity to study matter under extreme conditions and to probe the QCD phase diagram in the low temperature, high density regime (figure 3.6). This study gives complimentary information to the high temperature search for a quark-gluon plasma using relativistic heavy ion collisions at RHIC facility at Brookhaven National Laboratory.

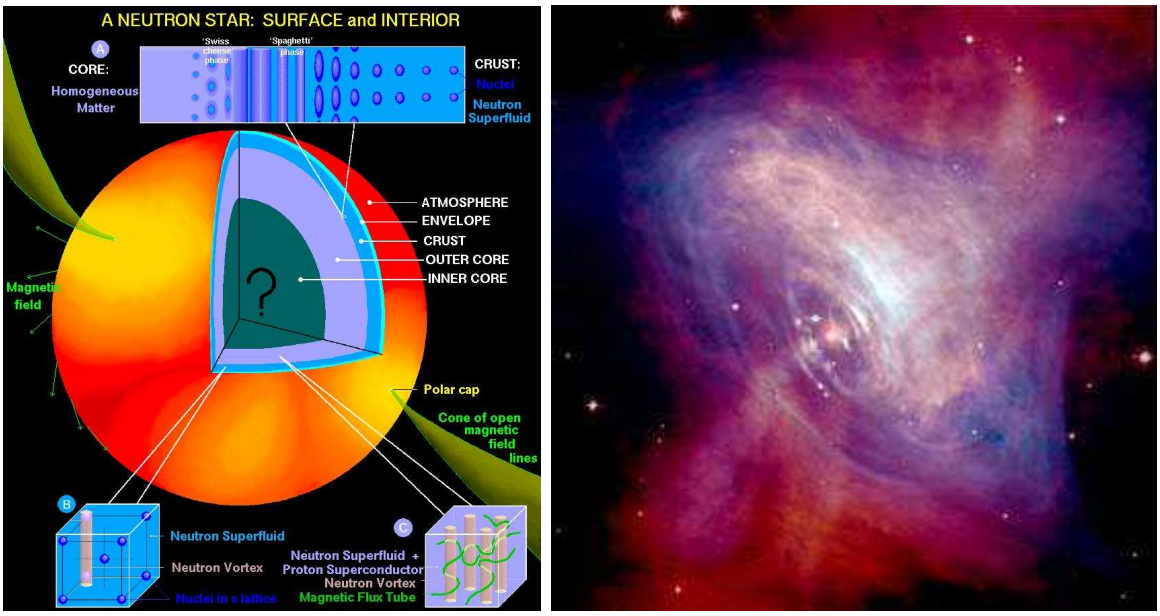

Figure 3.5: Left: Schematic showing possible composition of a normal matter neutron star. Figure from reference [36]. Right: The pulsar at the centre of the Crab Nebula.

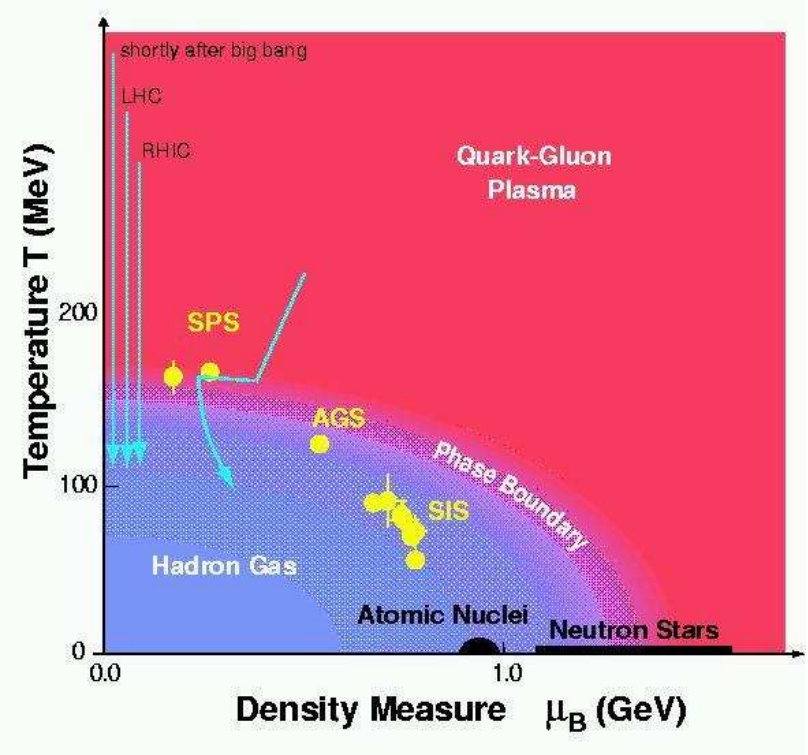

Figure 3.6: Figure from reference [41]. The QCD phase diagram.

3.3.3 Neutron Star Structure

The relationship between observable properties of neutron stars, their mass and radius, and properties resulting from the interactions between the constituent nucleons can be expressed in the Tolman-Oppenheimer-Volkov (TOV) equations (equations 3.12, 3.13), for a spherical object in hydrostatic equilibrium.

$$\frac{dP}{dr} = \frac{G(m(r) + 4\pi r^3 P/c^2)(\rho + P/c^2)}{r(r - 2Gm(r)/c^2)}, \tag{3.12}$$

$$\frac{dm(r)}{dr} = 4\pi\rho r^2 \tag{3.13}$$

where G is the gravitational constant, P is the outward pressure resulting from the internucleon forces, m is the mass of the neutron star and r is the radius. Specifically, the TOV equations show the correspondence between the mass-radius relationship and the equation of state of a neutron star i.e. between m(r) and P(ρ). Equations of state based on different neutron star models thus lead to different M-R relations and it follows that accurate mass and radius observations provide information on the underlying interactions between neutron star matter. This can be seen in figure 3.7 where the M-R relationships calculated for models of neutron stars containing only normal matter are shown as black curves and those including some exotic matter are shown as green curves.

The variation in the normal star M-R curves can in part be attributed to the uncertainty in the symmetry energy (equation 3.11) [29,36]. As discussed in section 3.3.1, a sufficiently accurate measurement of the neutron skin of ^{208}Pb will further constrain the symmetry energy and its density dependence.

Recent studies by Brown [38] and Horowitz [39,40] have also shown empirical relationships between the skin thickness of ^{208}Pb and neutron star properties. Brown's results are based on a wide range of calculations encompassing both non-relativistic Skyrme interactions and relativistic mean field calculations and show a tight correlation between the neutron skin thickness in ^{208}Pb and the derivative of the equation of state with respect to density at ρ=0.1fm^{-3} (Figure 3.8). In particular, the neutron skin thickness constrains the pressure of neutron star matter i.e. the equation of state at a density of $\sim$0.1fm^{-3} (equation 3.11). With the same models Brown investigated the neutron skin thickness of other heavy nuclei as a function of the skin thickness in ^{208}Pb and shows a linear relationship. Thus a measurement of a single nucleus should be sufficient to constrain the pressure of nuclear matter just below saturation density.

Investigations by Horowitz et al. have shown the linear dependence of the neutron skin thickness and the density at which the solid to liquid phase transition between neutron star crust and interior take place (Figure 3.9). A general trend is also presented

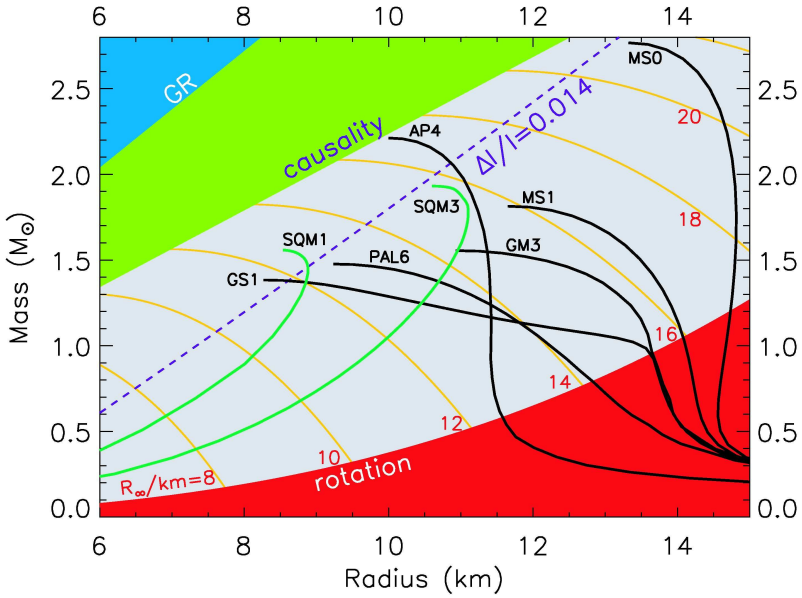

Figure 3.7: MR curves representing different equations of state. Black curves are for normal matter neutron stars, green curves represent strange quark matter stars. The red, blue and green shaded areas show the regions eliminated by rotation, general relativity and causality considerations respectively. Figure from reference [30].

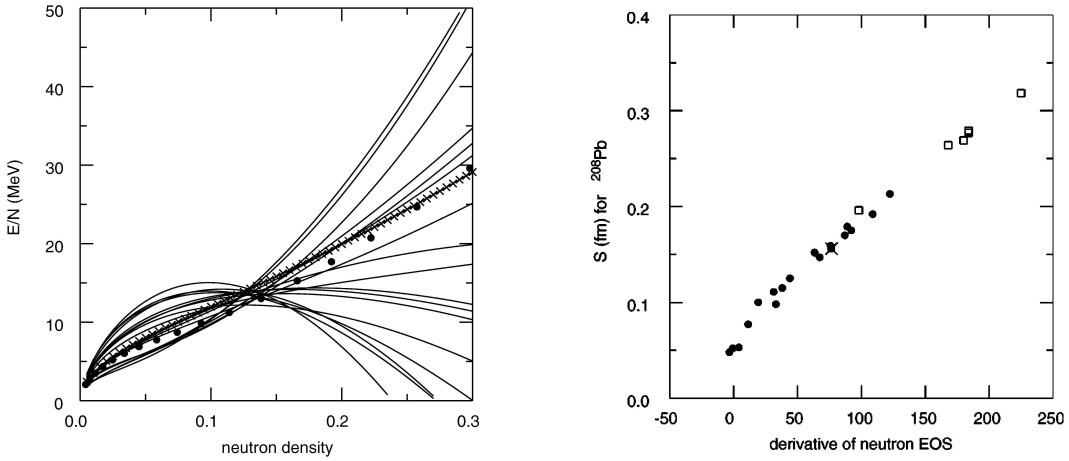

Figure 3.8: Left: The neutron equation of state for 18 different Skyrme parameter sets, taken from reference [38]. Right: The derivative of the neutron equation of state at $\rho = 0.10$neutrons/fm^3 vs the skin value in ^{208}Pb for 18 Skyrme parameter sets (filled cirlces) and for six relativistic models (squares). Figure taken from [42].

showing models that produce a large neutron skin thickness, produce large neutron star radii. Furthermore, for stars of $\sim 0.5 M_{\odot}$ the relationship between the neutron star radius and the neutron skin thickness has been shown to be relatively model independent (Figure 3.10). This could prove particularly useful in discriminating between different equations of state. As shown in figure 3.7 observations of both high and low mass neutron stars are required to pin down the equation of state. $0.5 M_{\odot}$ neutron stars may not exist in nature and if they do, they would be very difficult to observe because of their small luminosity. A measurement of the neutron skin in ^{208}Pb could act as a substitute for a radius measurement of a low mass neutron star.

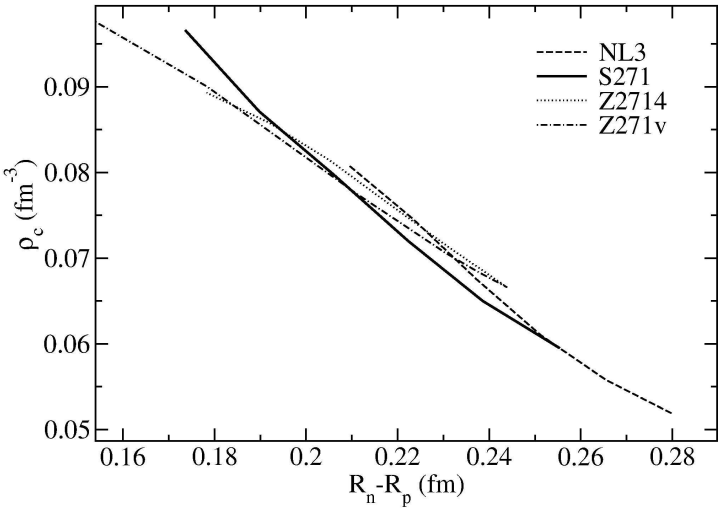

Figure 3.9: Figure from reference [39]. The transition density in a neutron star (taken to be the density at which the phase transition from crust to liquid interior takes place) vs the neutron skin thickness of ^{208}Pb.

3.3.4 Neutron Star Cooling

Once formed, neutron stars begin to cool rapidly by the emission of neutrinos. The process driving this neutrino loss was until recently thought to be the modified URCA process:

$$n + n \rightarrow n + p + e^{-} + \overline{\nu}_e \tag{3.14}$$

Some recent observations however have uncovered neutron stars that appear to cool faster than expected by matter undergoing the relatively slow modified URCA process [36]. This could be an indication that there is some exotic matter present within the star and that energy is being taken away by neutrinos from the weak decay of

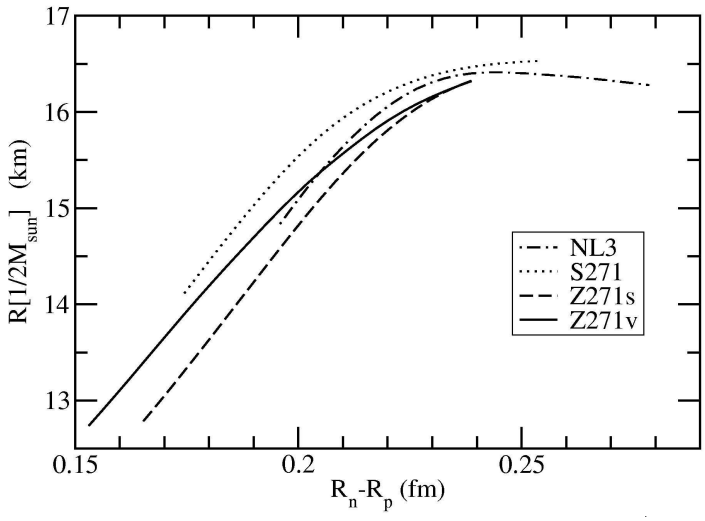

Figure 3.10: Figure from reference [40]. Predicted radius of a $0.5M_{\odot}$ neutron star vs the neutron skin thickness in ^{208}Pb.

pion or kaon condensates. Another possibility is that the star is cooling via the direct URCA process:

$$n \rightarrow p + e^{-} + \overline{\nu}_e \tag{3.15}$$

$$e^{-} + p \rightarrow n + \nu_e \tag{3.16}$$

Energy and momentum conservation require that for this process to dominate the proton fraction (x = Z/A) within the star must be relatively high [43]. It has been shown that the proton fraction is dependent on the nuclear symmetry energy [36], specifically:

$$x \cong 0.048 \left[\frac{S_2(\rho)}{S_2(\rho_0)}\right]^3 \left(\frac{\rho_0}{\rho}\right) (\alpha)^3 \tag{3.17}$$

Horowitz et al. [43] have investigated the relationship between x and density, again using a wide variety of relativistic mean field theories. Their results are presented in figure 3.12 which shows the threshold density of nuclear matter for the direct URCA process as a function of the neutron skin thickness of ^{208}Pb. They conclude that a measurement of $\Delta R_{Pb} < 0.2$ fm would not lead to a high enough proton fraction for the direct URCA process to be a viable means of neutron star cooling. However, a measurement > 0.25 fm would imply the direct URCA process is possible. If the direct URCA process is ruled out, this could provide additional evidence for the presence of exotic matter at the centre of neutron stars.

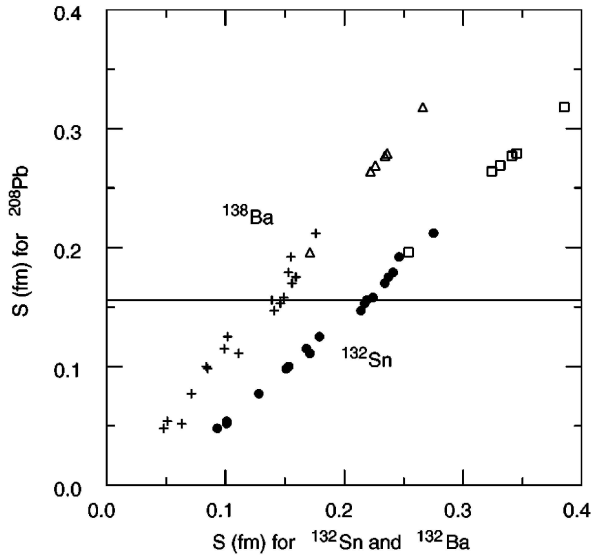

Figure 3.11: The skin thickness value for ^{208}Pb versus skin thickness for ^{132}Sn (filled cirlces and squares) and ^{138}Ba(crosses and triangles) for 18 Skyrme parameter sets (filled cirlcles and crosses) and six relativistic models (squares and triangles). Taken from [38].

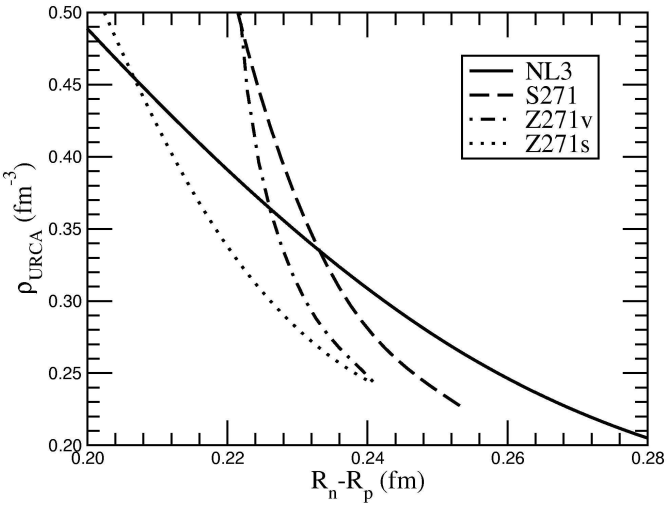

Figure 3.12: Figure from reference [43]. Critical density for direct URCA process to be viable vs the neutron skin thickness in ^{208}Pb.

3.3.5 Heavy Ion Collisions

Theoretical investigations have also recently uncovered relationships between the experimental results of intermediate energy heavy ion collisions and the neutron skin thickness of ^{208}Pb. In particular, the skin thickness is related to the isospin diffuseness in a heavy ion collision, reflecting their shared dependence on the symmetry energy. In a heavy ion collision, isospin diffusion is the net exchange of isospin (the exchange of neutrons and protons) between the target and the projectile (figure 3.13(a)).

To quantify the isospin diffusion of a reaction A+B, two further reactions must be measured, A+A and B+B. The diffusion is then measured via the isospin diffusion parameter, R_i [44]:

$$R_i = \frac{2X^{A+B} - X^{A+A} - X^{B+B}}{X^{A+A} - X^{B+B}} \tag{3.18}$$

where X is an isospin sensitive observable. Given a particular equation of state, R_i can be calculated for a reaction using transport models. Using the same underlying equation of state, Steiner and Li [44] have made calculations of the diffusion parameter for the reaction (^{112}Sn + ^{124}Sn) as well as the neutron skin thickness of ^{208}Pb. The results are shown in figure 3.13(b). The different data points result from variations in the transport model used to calculate R_i. Thus a measurement of the neutron skin of lead can be used as a constraint for the theories behind heavy ion collisions and vice versa.

3.4 Atomic Parity Non-Conservation

Atomic electrons undergo transitions between energy levels primarily through the electromagnetic exchange of photons with the nucleus. Transitions can also proceed via the exchange of Z^0 bosons and the weak interaction, which unlike the electromagnetic process does not conserve parity. Parity violation by the weak force manifests itself as a change in an experimental result under reflection of all three spatial co-ordinates. For example, within the atom, these effects can be seen by observing the 6s→7s electron transition in ^{133}Cs. Without the presence of the weak neutral current (i.e. the Z^0 boson) the 6s→7s transition is highly forbidden. By placing the atoms under electromagnetic fields however, the optical signature from this transition can be seen and if the handedness of the fields are switched, a modulation in the signal is observed [45]. Data from these experiments observing atomic parity non-conservation are signicant since they can be used to extract the weak nuclear charge, Q_w, which is used as a fundamental low energy test of the standard model. Specifically, the observable parity

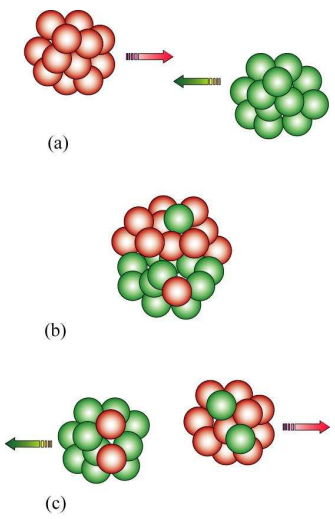

(a) Diagram of a heavy ion collision. (a) Projectile and target before collision. (c) Recoiling projectile and target with some isospin diffusion.

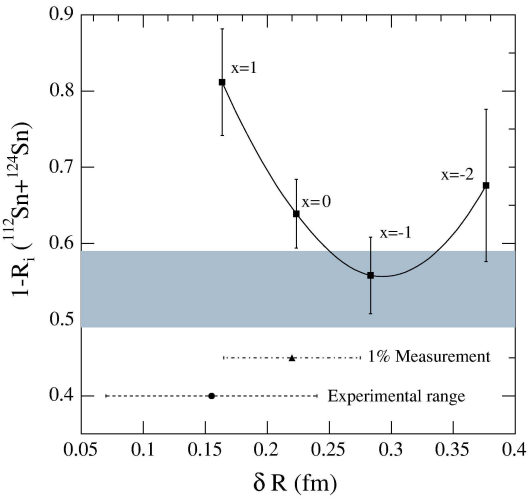

(b) Taken from reference 44. The relationship between the skin thickness of lead and the isospin diffuseness parameter R_i.

Figure 3.13: Isospin diffusion in heavy ion collisions.

non conserving effects are related to the matrix element between the two atomic states, i and j:

$$\langle i|H_{PNC,1}|j\rangle = \frac{G_F}{2\sqrt{2}}C_{ij}(Z)\mathcal{N}[Q_w + \Delta Q_w^{n-p}], \tag{3.19}$$

where:

$$Q_w = (1 - 4sin^2\theta_w)Z - N, \tag{3.20}$$

$$\Delta Q_w^{n-p} = N(1 - q_n/q_p), \tag{3.21}$$

$$q_n = \int \rho_n(r)f(r)d^3r \tag{3.22}$$

C_{ij} contains all atomic structure effects, G_F is the weak coupling constant, α is the fine structure constant, $\mathcal{N}$ is a normalisation factor, $\rho_{n(p)}$ is the nuclear neutron(proton) distribution, f(r) is a folding function determined from the radial dependence of the electron transition matrix element and θ_w is the weak mixing angle. ΔQ_w contains a correction because the proton and neutron distributions are not the same. If they were, ΔQ_w would be zero.

The observed quantity is therefore $\langle i|H_{PNC,1}|j\rangle$ and from this a value for Q_w is to be extracted. At present the uncertainty in the extraction of Q_w is dominated by uncertainties in atomic theory contained within C_{ij} (uncertain to ~1% compared with experimental errors of 0.3%) and to a lesser extent the poor knowledge of the nuclear matter distribution, ΔQ_w [46]. Advances in atomic structure calculations are dramatically reducing their uncertainties and the lack of information on the nuclear matter distribution is expected to soon become the limiting factor through ΔQ_w [47]. Calculations by Pollock et al. [47] have shown how a measurement of the r.m.s neutron radius of ^{208}Pb can help constrain these errors and this is shown in figure 3.14.

3.5 Previous Matter Distribution Measurements

The most comprehensive investigations of matter distributions to date have been carried out using elastic proton scattering, notably at TRIUMF and Saclay. The analysis of proton scattering data is far from simple and suffers from large theoretical uncertainties in the description of the strongly interacting probe. The strength of the interaction is such that the contribution from processes where the proton scatters more than once cannot be neglected and leads to complications in the analysis. Ray and Hoffman [48] performed a detailed analysis of elastic proton scattering data to extract values for the r.m.s. neutron radius of ^{48}Ca and ^{208}Pb in the framework of the relativistic impulse approximation (RIA) and the non-relativistic multiple scattering approach of Kerman,

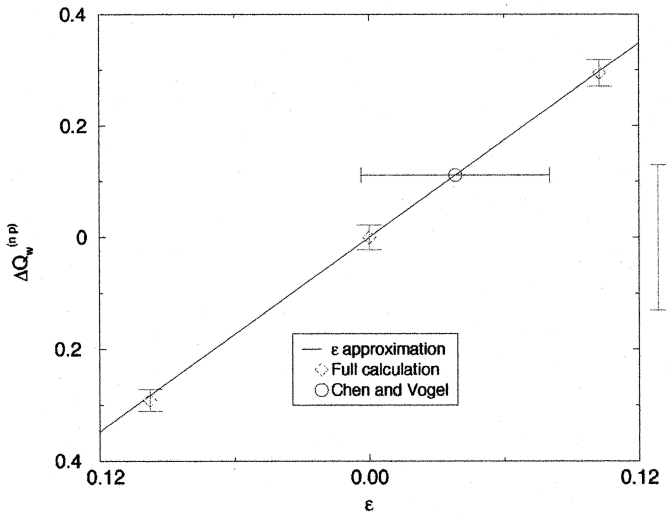

Figure 3.14: Correction to the weak charge of Cs due to differences between neutron and proton spatial distributions as a function of $\epsilon = R_n^2/R_p^2$ - 1. The line and different data points represent calculations using different types of neutron density distributions. The vertical error bar to the side of the plot shows just the uncertainty in the standard model prediction of Q_w. Figure taken from [47].

McManus and Thaler (KMT). Their results for ^{208}Pb are shown interpreted as neutron skin thickness measurements in figure 3.15. Despite their thorough analysis, the results still show an unphysical dependence on the proton beam energy with a systematic variation of ∼0.5fm. The variation is much larger than the skin thicknesses predicted from the various nuclear theories. New analyses of these data have recently been carried out, prompted by renewed interest in neutron distribution measurements from the fields detailed in sections 3.2 - 3.4. Using different theoretical models values of ΔR_{Pb} were calculated of 0.097±0.014 fm for the 0.5-1.04 GeV data [49] and 0.17 fm for the 40 MeV, 65 MeV and 200 Mev data. The energy dependence of the results was not addressed. Furthermore, a recent recent detailed study of the field by Piekerawicz [50] has concluded that the proton-nucleus scattering cross section is in fact insensitive to the neutron radius of ^{208}Pb. A series of calculations for different neutron densities were performed using the impulse approximation with a KMT multiple scattering optical potential. The resulting calculations all showed excellent agreement with the proton-nucleus scattering data.

While elastic proton scattering has been the main tool for investigating the matter distribution, there have been parallel research programmes utilising pion scattering [51], α scattering as well as neutron and proton pick up reactions. Pion- and α-scattering largely suffer from the same theoretical uncertainties in descibing the strongly inter-

acting probes as proton scattering [52]. The latest result from neutron and proton pick up reactions is a value for the neutron skin of ^{208}Pb of 0.51 fm, which is larger than almost all theoretical predictions of the value.

At best, the overall uncertainty in the present knowledge of the neutron skin of ^{208}Pb could be placed at ∼0.2fm , however, others are not so optimistic. Fortson et al. [46] in their review of the current accuracy of the radial neutron distribution give a value of ∼10% or ∼0.5fm.

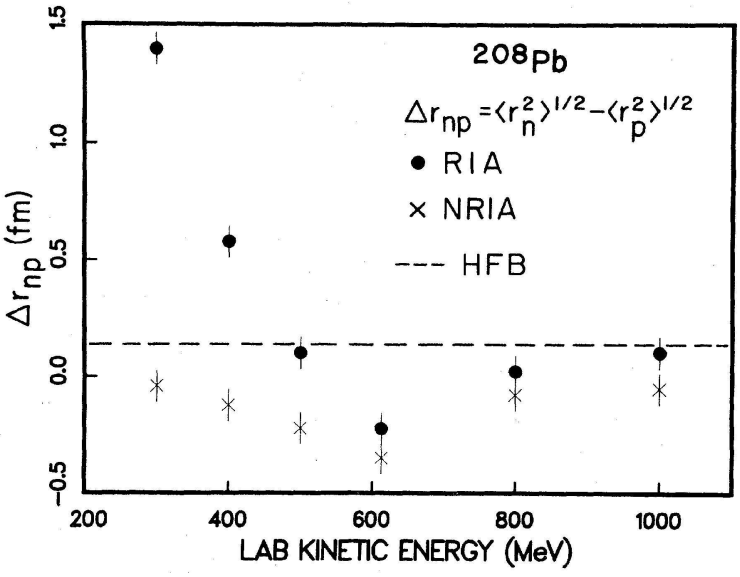

Figure 3.15: Taken from [53].

3.6 Summary

To summarise, the r.m.s matter radius is a fundamental nuclear quantity which at present can not be accurately calculated from experimental data or theory. New, accurate matter radius measurements, particularly of a heavy nucleus such as ^{208}Pb will have an impact on a wide range of physics including nuclear structure theory, atomic parity violation, heavy ion collisions and the predictions of the properties of neutron stars.

Chapter 4

Experimental Details

4.1 Introduction

The neutral pion is the lightest bound state of quarks and as such cannot decay via the strong force to another hadron. Instead it decays (with a branching ratio of ∼99%[5]) via the electromagnetic interaction to two photons i.e. $\pi^0 \rightarrow \gamma\gamma$. Since this decay takes place in 10^{-18}s the π^0 is too shortlived to detect directly. Instead, the presence of a neutral pion can be inferred by measuring the 4-momenta of the decay photons which combine to give the 4 momentum and rest mass (within experimental resolutions) of the π^0 . In the pion's centre of mass frame, the decay photons are produced back to back and to ensure a high detection efficiency, a large acceptance photon spectrometer is required. One of the few π^0 detectors of this sort in the world currently resides in the A2 hall at MAMI in the shape of the newly installed Crystal Ball and TAPS detector system. The experiment described in this thesis made use of this apparatus over 6 weeks in March and April 2005.

Briefly, a beam of electrons from the high duty factor Mainz Microtron [54,55] was directed onto a thin metal foil generating (via a bremsstrahlung process) a beam of high energy photons. The corresponding bremsstrahlung electrons were momentum analysed in the Glasgow Photon Tagging Spectrometer [56,57] and the photon beam was directed towards one of four nuclear targets at the centre of the Crystal Ball. The neutral pions created in these reactions were detected by measuring their decay photons in two highly segmented photon spectrometers - Crystal Ball and TAPS. Charged particles were identified and tracked using multi wire proportional chambers (MWPCs) and plastic scintillators, and their total kinetic energy was measured in the two large calorimeters. The following sections describe each component of the experiment in more detail.

4.2 The Mainz Microtron

Housed in the Insitüt fur Kernphysik at Johannes Gutenberg Universität, the Mainz Microtron is an intense, stable, continuous wave electron accelerator. The accelerator in its current configuration was constructed in 3 stages - MAMI-AI, MAMI-AII and the present facility, MAMI-B. Comprised of a linear accelerator and one race track microtron, MAMI-AI came into operation in 1979, producing electrons of up to 14 MeV at a maximum intensity of 25μA. That machine was upgraded in 1983 with the addition of a second microtron accelerating the electrons from 14 MeV up to 183 MeV and above production threshold for the first time. A third microtron was added in 1990, taking the maximum electron energy up to 855 MeV. At these energies the photon has a spatial resolution of $\sim$0.23fm, and sufficient energy to produce both π and η mesons. A fourth, double-sided microtron (MAMI-C) has just been completed and now delivers beam energies up to 1.5GeV, crossing the reaction threshold for the production of particles containing strange quarks.

4.2.1 Race Track Microtrons

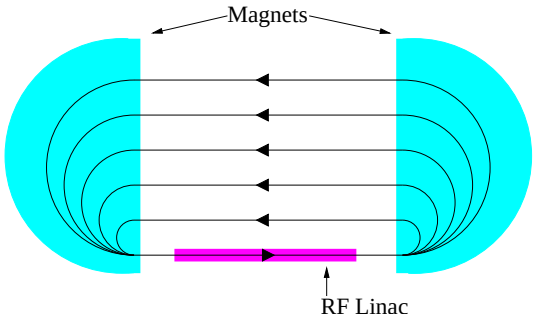

Figure 4.1: Typical microtron schematic.

Electron scattering has been the work horse of nuclear and particle physics for over 50 years now. The discoveries made using this technique are remarkable, ranging from some of the first measurements of nuclear shapes and sizes to the discovery of partonic degrees of freedom within the nucleon [58,59]. Almost all electron scattering experiments done until the early 1980's were of the inclusive variety where only the scattered electron was detected and the physics of the reaction inferred from that one measurement. While the results from these inclusive reactions were impressive it was realised that exclusive measurements, where a specific final state can be isolated, would give new information. For these to be possible, coincidence measurements of the scattered electron and other reaction products are necessary. However, coincident

measurements placed new constraints on the necessary beam quality, introducing the need for continuous beams. The finite time resolution of any detector system means that while trying to detect two or more particles in timing coincidence, it is always possible that one of these particles is uncorrelated, having originated from a reaction on a different nucleus. This is particularly a problem for 'bunched' beams where the event rate in the bunch is very high. It is possible to reduce the probability of random events by making the time window within which they can occur as large as possible relative to the time resolution of the detector i.e. by utilising a continuous wave beam. One possible way of achieving this high duty factor beam is by using race track microtrons.

The basic design of a microtron is shown in figure 4.1. A relatively short linear accelerator (LINAC) with a small accelerating gradient is placed between two 180° bending magnets. A beam of electrons is passed through the LINAC where it is accelerated through a series of standing wave cavities powered by radio frequency klystrons. Its path is then deflected through 360° by the large magnets, returning the electrons to their starting position. This race track formation means the field in the two dipole magnets can be kept constant - there is no need to 'ramp' them up as in a storage ring. The electrons pass through the radio frequency LINAC section many times, each time returning to their starting position via orbits of steadily increasing diameter. As the beam is passed repeatedly through the LINAC, high energies can be achieved with a relatively modest accelerating gradient. Crucially, as the accelerating gradient is small, the LINACS can be operated in continuous wave mode, giving a 100% duty electron beam. This design also naturally ensures excellent energy resolution as electrons whose energy is too high will have a slightly larger orbital radius and be out of phase with the RF accelerating field therefore undergoing smaller accelerations until the phase is restored.

4.2.2 MAMI-B

A floorplan of the MAMI facility is included as figure 4.2. Electrons are boiled off a 100keV electron gun via thermionic emission and passed into 3 successive LINAC sections where they are accelerated to 3.46 MeV. They then enter race track microtron 1 (RTM1) where they undergo 18 recirculations gaining 10.93 MeV in kinetic energy. Upon entering race track microtron 2 (RTM2) they make 51 passes through a linac and are extracted with an energy of 179.8 MeV. The final microtron (RTM3) has the potential to accelerate the electrons up to 883 MeV in steps of 15 MeV depending on how many recirculations are chosen through its 5 RF cavities. As has been noted the energy resolution of the microtron design is inherently good and the small variation in the MAMI-B energy (∼50keV at 855 MeV) is mainly due to synchrotron radiation

effects. A maximum beam intensity of 100μA can be achieved. After extraction from the final microtron the beam is passed through a series of dipoles and quadrupoles directing it into one of 4 experimental halls labelled A1, A2, A4 and X1 in figure 4.2.

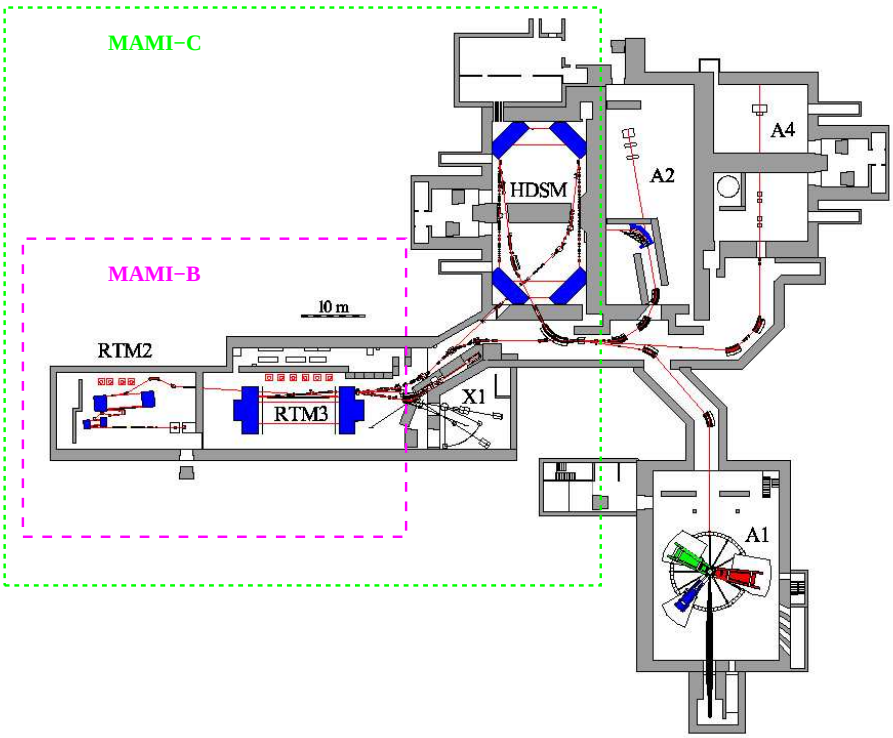

Figure 4.2: Floorplan of the MAMI facility.

4.3 Glasgow Photon Tagging Spectrometer

This experiment was performed in the A2 hall of MAMI where the high quality electron beam was directed on to a 10μm thick nickel radiator. A fraction of the electrons in the beam were accelerated in the Coulomb field of the heavy Ni nuclei and radiated photons via the bremsstrahlung process: $e^- + N \rightarrow e^- + N + \gamma$. The energy spectrum of bremsstrahlung radiation is approximately E_γ^{-1} and is produced in a forward directed cone of half angle $\frac{m_e}{E_e}$ where m_e and E_e are the mass and initial energy of the electron respectively.

The bremsstrahlung electrons were momentum analysed in a large momentum acceptance magnetic spectrometer - the Glasgow Photon Tagging Spectrometer (figure 4.3) [56]. By detecting an electron in timing coincidence with particles from a photonuclear reaction in the experimental detectors, the energy of the photon inducing the reaction was dedcuced or 'tagged'. Before traversing the radiator, the mixed

beam of electrons and photons emitted from the radiator passed through a quadrupole magnet, focussing the electron beam in the vertical direction. The electrons were then momentum dispersed via the ∼1T field of the tagger dipole magnet and directed on to a detector residing in the focal plane of the spectrometer. Electrons that did not radiate and therefore still had maximum energy were bent at shallower angles onto a beam dump. The bremsstrahlung photons of course passed unhindered through the magnetic field and continued on to impinge on the experimental target. Using energy and momentum conservation, and neglecting the relatively small kinetic energy of the recoiling nucleus (a few keV), the photon energy is simply:

$$E_\gamma = E_0 - E_e \tag{4.1}$$

where E_0 is the electron beam energy and E_e is the bremsstrahlung electron energy.

The focal plane electron detector (FP) [57] was constructed from 353 overlapping, 2mm thick, plastic scintillators (type NE 111) oriented at ∼90° to the electron trajectories. Each scintillator was viewed by a Hamamatsu R1635 phototube, the signal from which was sent to timing and coincidence electronics. The complete spectrometer is capable of tagging photons in the range 40-800 MeV with an energy resolution of ∼2 MeV at the highest electron beam energies. The maximum flux of photons was constrained by the rate limitations of the Hamamatsu PMTs and results in a maximum rate of 1MHz per channel. For this experiment, in order to maximise the flux of photons on the target, the channels corresponding to the lowest photon energies, where the count rates were largest, were switched off and only photons in the range (120-800) MeV were tagged.

If the amorphous nickel radiator is replaced with a diamond radiator, it is possible to produce a polarised beam by correctly orienting the planes of the crystals with respect to the electron beam. A high degree of linear photon polarisation (75%) or, when a polarised electron beam is used, cirular photon polarisation (85%) can be achieved [60].

4.4 Photon Beam Collimation and Tagging Efficiency

To ensure the beam spot size on the target and the resulting uncertainty in the reaction vertex position was small, the photon beam was collimated after passing through the tagger. The collimator consisted of 4 lead cylinders each 20mm long and with a 4mm diameter hole bored through the centre, aligned on the beam axis. To normalise the measured cross sections, an estimate of the absolute beam luminosity was made. Without collimation, this would relate directly to the rate of electrons detected in the

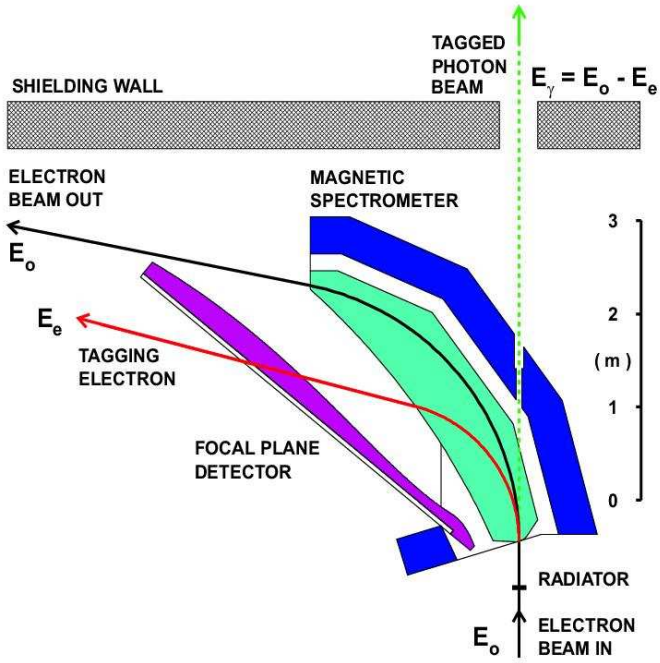

Figure 4.3: Tagger schematic

tagger focal plane. With collimation, however, the number of photons lost in the collimater must be taken into account. This was done by measuring the 'tagging efficiency' which for each focal plane detector element is defined as:

$$\epsilon_{tagg} = \frac{N_\gamma}{N_e} \tag{4.2}$$

where N_γ is the number of photons after collimation and N_e is the number of electrons detected in the tagger focal plane element. The tagging efficiency was obtained in separate experimental runs using an almost 100% efficient Pb-Glass detector placed downstream of the collimator in the beam line to measure N_γ. N_e was taken as the number of tagged electrons measured in coincidence with the Pb-Glass. A reduced beam current was used firstly to protect the Pb-Glass detector and secondly to ensure the contribution from random coincidences was negligible.

4.5 Targets

Details of the 4 targets used are given in Table 4.1. The thickness of each of the targets was chosen as a compromise between having a surface density large enough to give a sufficient π^0 yield and having sufficiently little material so that photon conversion in the target was not above 0.1 radiation lengths. ^{nat}C and ^{nat}Ca are both sufficiently

close to isotopic purity (98.90% ^{12}C and 96.94% ^{40}Ca respectively [61]) that they make suitable targets. ^{nat}Pb on the other hand is only composed of 52.4% ^{208}Pb and an isotopically pure target from ISOFLEX (Moscow) was employed in the measurement. The oxygen content of water is composed of 99.75% ^{16}O which makes water an ideal ^{16}O target. To hold the water, a simple target cell made of perspex, aluminium and two thin Melinex windows was designed and constructed (Figure 4.4).

Table 4.1: Experimental Targets

Target	Thickness (mm)	Atomic Mass $\frac{m_a}{u}$	Surface Density (gcm^{-2})
^{12}C	15 ±0.5	12.01	2.55
^{16}O	31.4 ±0.5	15.9994	3.52
^{40}Ca	10 ±0.5	40.07	1.55
^{208}Pb	0.52 ±0.01	207.977	0.8369

The targets were placed in an evacuated, carbon fibre tube at the centre of the particle detectors. The Pb, Ca and C targets were held in place in the tube by thin rohacell holders and the water target was designed to fit in the target pipe without fixings. The carbon fibre pipe stopped 14.5cm downstream from the geometric centre of the particle detectors and a thin (100μm) kapton window sealed the downstream end of the pipe.

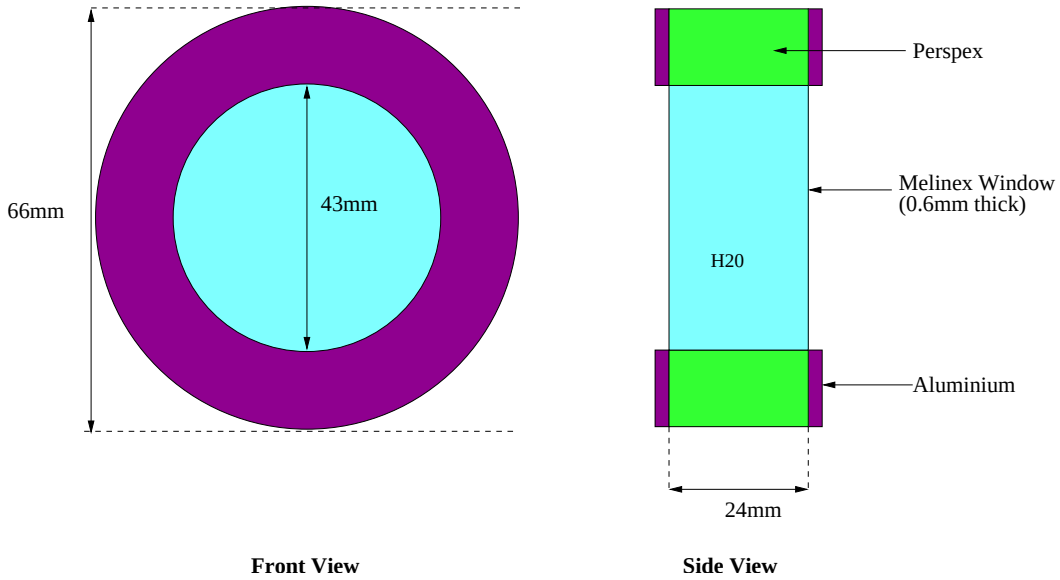

Figure 4.4: Water Target Schematic.

In the vacuum within the target pipe the melinex windows of the water cell expanded outwards, effectively increasing the surface density of the target. To accurately measure the increase in target thickness, the target was subjected to an overpressure of ^{3}He gas equivalent to the difference in pressure during the experiment. The expansion of the window was then measured with a pair of digital calipers. This expansion was found to be ∼10%.

4.6 Crystal Ball

The Crystal Ball was designed in the 1970's as a means of detecting high energy photons from the decays of hadrons produced in e^+e^- collisions at the Stanford Linear Accelerator (SLAC). For this, a large acceptance photon spectrometer with excellent energy and angular resolution across the range E_γ= (1-1000) MeV was required. In fact the detector was proposed only a few months before the discovery of the J/ψ particle in 1974 (jointly at SLAC and Brookhaven National Laboratory) and was perfectly timed to make some of the first and most accurate measurements of the J/ψ and its excited states. The design and construction of the ball was a joint project between the High Energy Physics Laboratory (HEFL, Stanford), Caltech and the Universities of Harvard and Princeton and was completed in 1978 when it began taking data at the Stanford Positron Electron Accelerator Ring (SPEAR) at SLAC. The Crystal Ball remained in place there for 3 years continuing spectroscopy of the J/ψ [62] and its excited states. From 1982 to 1987, the ball was used at the Deutsches Elektronen-Synchrotron (DESY) and during that time it was again involved in a program of meson spectroscopy, specifically investigations of b-quark physics [63]. After a period in storage at SLAC, the detector was moved in 1995 to the Alternating Gradient Synchrotron (AGS) at Brookhaven National Laboratory. Its use with secondary pion and kaon beams from AGS facilitated studies of strange and non-strange baryon resonances [64], and these studies continued until 2002. In November of that year the ball returned to Germany, this time to Mainz and the MAMI facility. A major upgrade of the detector's electronics was completed before an experimental program covering a wide range of physics topics was embarked upon in May 2004. This first round of experiments using MAMI-B was completed in April 2005, however a new program of experiments with MAMI-C is already underway after an accelerator and tagger upgrade were completed at the end of 2006.

4.6.1 Crystal Ball Design

The geometry of the crystal ball is based on the structure of a 20 sided polyhedron - an icosahedron. Each triangular face of the icosahedron is divided in to 4 smaller triangles which in turn contain 9 modules (figure 4.5). The smallest triangular surface represent the base of a NaI(Tl) crystal shaped into a truncated pyramid. When stacked together in this way, a near spherical shell of 720 elements is formed. By removing 24 crystals from opposite poles of the sphere a tunnel is created through the centre allowing space for the beam and target holding structures.

Each of the remaining 672 crystals (figure 4.6) are 40.6cm in length (or 15.7 radiation lengths). The side of the inner face is 5.1cm in length and the side of the outer face is 12.7cm. The ball has an outer radius of 66.0cm and an inner radius of 25.3cm. The crystals are individually wrapped in reflecting paper and aluminized mylar to ensure optical isolation and viewed, via a glass window and a 5cm air gap, by their own ZXRC L50 B01 photomultiplier tube. NaI(Tl) is hygroscopic and will therefore deteriorate when it comes into contact with moisture in the atmosphere. For this reason, the crystals were hermetically sealed in 2 separate hemispheres made of 1.5mm thick stainless steel which were studded with glass windows as part of the optical coupling between the scintillator and phototubes. This mechanical separation of the ball into two parts also allows for easy mounting and maintenance of the targets and detectors in the tunnel region. The pressure within the steel casing as well as the environment in the A2 hall in general must be closely monitored.

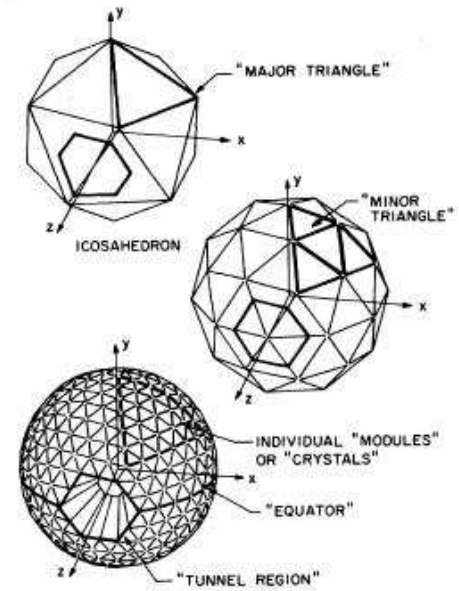

Figure 4.5: Crystal Ball Geometry.

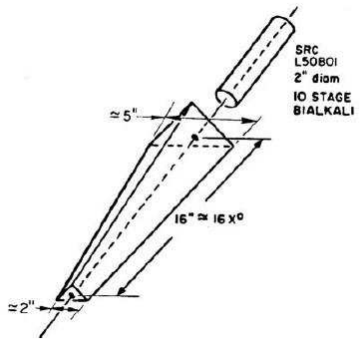

Figure 4.6: NaI(Tl) Crystal

During the experiment, photons deposited energy in the NaI(Tl) via the development of electromagnetic showers originating from the initial interaction of the incident photon. The size of the electromagnetic shower was dependent on the energy and type of particle, for example a photon below 10 MeV will typically only deposit energy in one or two crystals. However for photons up to ∼400MeV, 98% of the deposited energy is contained in a cluster of 13 crystals. Energy deposits in the crystals from hadrons tend to involve fewer crystals. For example, protons generally only deposit energy in one or two crystals.

The energy and direction of particle events in the Crystal Ball were then reconstructed by analysing the cluster of NaI crystals in the resulting shower. The choice of a scintillator with high light output (NaI(Tl)) ensured good energy resolution for photons over a wide range. The thickness of the crystals was enough to stop 245 MeV pions, 340 MeV kaons and 425 MeV protons and the high granularity provided excellent angular resolution. Some of the detection properties of the Crystal Ball are summarised in Table 4.2 [65].

Table 4.2: Principle Characteristics of Crystal Ball

Angular Acceptance	
Azimuthal coverage	$0\,^\circ < \phi < 360\,^\circ$
Polar coverage	$20\,^\circ < \theta < 160\,^\circ$
Angular Resolution	
Azimuthal resolution	$\sim \frac{2^\circ}{sin\theta}$
Polar resolution	∼2-3 °
Photon Energy Resolution	
$\frac{\sigma}{E_\gamma}$	$\sim \frac{1.7\%}{E_\gamma}$ $(\mathrm{GeV})^{0.4}$

As a large acceptance, high granularity photon spectrometer, the Crystal Ball is first and foremost ideally suited to the detection and measurement of neutral mesons (π^0, η) which decay to photons. However, by utilising the free space in the beam tunnel around the target and including detectors for charged particle identification and tracking, the Crystal Ball has become an excellent detector for multiple charged and uncharged particles in the final state.

4.6.2 Particle Identification Detector

The Crystal Ball's particle identification detector (PID) is a dE/dx detector and used in conjunction with the ball provided particle identification of protons and charged pions via the ΔE-E technique. Located in the tunnel region of the ball, the PID was comprised of 24 (2 x 300 x 12)mm EJ204 plastic scintillators forming a cylinder around the beam axis centred on the target (figure 4.7). The cross section of each detector element is right-angled trapezium, ensuring that the gaps between the detector elements when forming the barrel were minimised. Each scintillator was individually wrapped in foil to ensure optical isolation and the entire detector was lightproofed via a covering of black Tedlar (PVF). The scintillators were viewed via perspex light guides by 24 Hamatsu R1365 photomultiplier tubes. The barrel design of the PID allowed for full 360° coverage of the azimuthal angle and the length of the scintillators provided coverage between (20 to 160)° of the polar angle matching the coverage of the Crystal Ball.

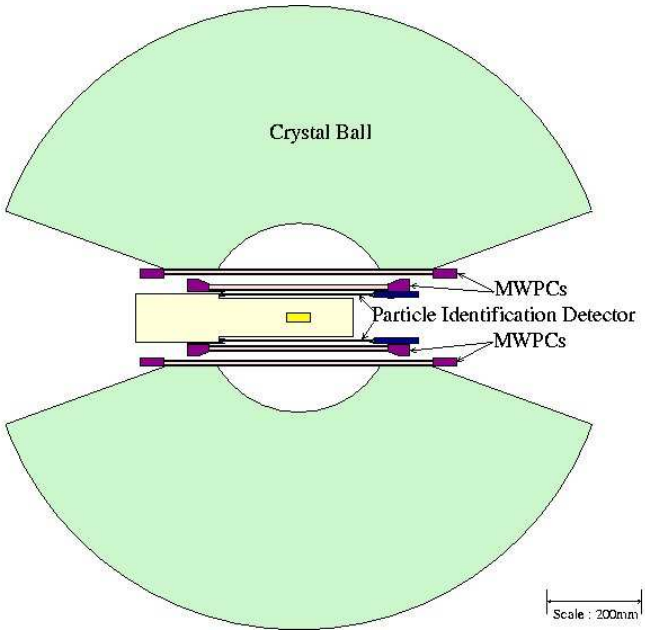

Figure 4.7: Crystal Ball and sub detectors schematic [66].

4.6.3 Multi Wire Proportional Chambers

Surrounding the PID within the tunnel region of the ball was a high resolution tracking detector comprised of two multi wire proportional chambers (MWPCs - figure 4.7). This sub-detector system was originally part of the DAPHNE [67] detector system and has been used in that setup for a number of years with great success. Both chambers were constructed from three layers - the inner and outer layers acted as cathodes for the proportional counter and were formed from 1mm thick rohacell, laminated with 0.1μm thick, 4mm wide aluminium strips. The anodes were sandwiched between these two cathode layers and consisted of 20μm diameter Tungsten wires running parallel to the beam axis. A separation of 2mm was allowed between each of the wires and 4mm between the aluminium strips which were wound helically in opposite directions at an angle of $\pm 45^\circ$ with respect to the wires (figure 4.8). The ionising gas used to fill the chambers is a mixture of 74.5% Argon, 25% ethane and 0.5% freon. Once again the barrel design ensured coverage of the full 360° of ϕ and the total length provided coverage in θ between 21° and 159°.

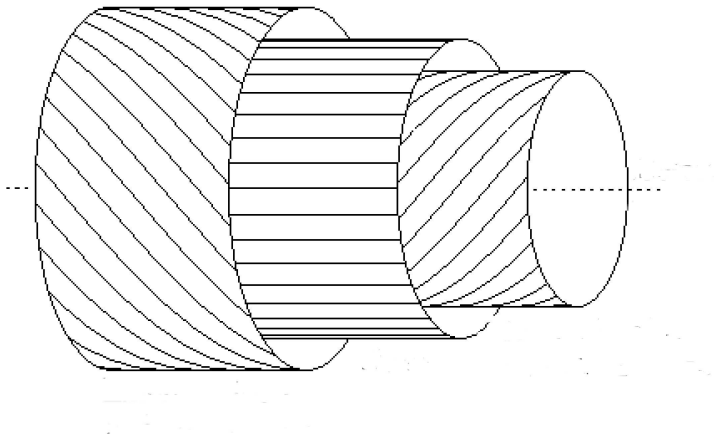

Figure 4.8: Diagram showing relative positions of strips and wires in one of the two MWPCs.[68]

By combining information from all 6 layers, the tracks of charged particles through the detector were reconstructed. First and foremost this provided an improved angular resolution on charged particles than that provided by the Crystal Ball alone. An important application for the coherent π^0 experiment is the ability to reconstruct from the wire chamber the vertex position of multiple charged particle events. In this way, it was possible to very accurately pin down the target position within the Crystal Ball. Some of the detector properties are summarised in Table 4.3.

Table 4.3: Principle Characteristics of MWPCs

Angular Acceptance	$0 < \phi < 360°$
	$21 < \theta < 159°$
Angular Resolution	
Azimuthal resolution	1.8°
Polar resolution	2°

4.7 TAPS Forward Wall

As has been noted, the Crystal Ball was designed for colliding beam experiments at SLAC. For experiments involving colliders, the lab frame is essentially the centre of mass frame and the reaction products are produced isotropically about the reaction vertex. However, for fixed target experiments like those carried out at MAMI, the reaction products are Lorentz boosted forward in the lab frame. To improve detection efficiencies at forward angles and compensate for the forward gap in the Crystal Ball coverage necessitated by the beam exit tunnel, a forward wall detector was introduced - TAPS.

TAPS[69] is a highly segmented photon spectrometer comprised of 522 BaF_2 crystals that can be configured into a variety of different geometries. Like the Crystal Ball, TAPS was proposed as a means of detecting primarily neutral mesons via their photon decays. The acronym TAPS was originally assigned to stand for Two/Three Arm Photon Spectrometer reflecting the geometric setup used in its first experimental run in 1990. Since that time, the detector system has been used all over Europe and the acronym is now more commonly taken to stand for the Travelling Around Photon Spectrometer. For this experiment all 522 crystals were located in a single plane, 1.5m downstream from the reaction vertex (Figures 4.10 and 4.11) covering the angular range $0° < \theta < 20°$. This combined setup of Crystal Ball and TAPS covered 93% of the 4π sr of solid angle.

4.7.1 TAPS Design

BaF_2 has a significantly lower scintillation light output than NaI(Tl) (about 29% of that produced by NaI [69]), however, its high density($4.89 g/cm^3$) and high atomic number (^{56}Ba) ensure that it maintains a high detection efficiency. Its scintillation light is made up of two different components - one with a very fast decay time ($\sim$ 0.6ns) and another slower one ($\sim$ 620ns) both in the UV range (220nm and 310nm respectively). The fast component provides very accurate timing information on detected signals. The energy

resolution for photons is also similar to that of the Crystal Ball: $\frac{\sigma}{E_\gamma} \sim \frac{0.59\%}{E_\gamma}\ (\mathrm{GeV})^{-1/2}$ + 1.9%.

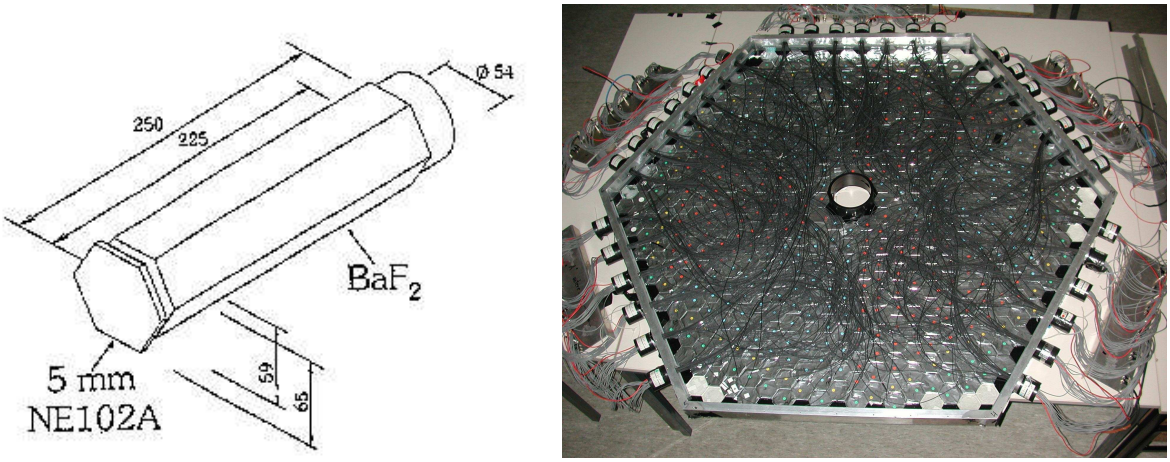

(a) (b)

Figure 4.9: Left: Technical drawing of one BaF_2 crystal. Right: Photograph of the dismounted TAPS veto wall showing the veto detectors and light guide fibres.

Each BaF_2 crystal is hexagonally shaped with a cylindrical end part, the dimensions of which are shown in Figure 4.9. They were individually wrapped in 8 layers of 38μm thick UV reflecting PTFE and one layer of 15μm thick aluminium foil. The crystals were viewed via a coating of silcone grease by their own Hamamatsu R2059 photo tube. The phototubes and cylindrical part of the crystals were surrounded by a magnetic shield to protect the tubes from stray electromagnetic fields in the close packed detector.

Mounted in front of the crystals were an equal number of 5mm thick NE102A plastic scintillators of the exact same granularity. Their scintillation light was collected in Valvo XP2972 phototubes by way of an optical fibre light which can be seen in Figure 4.9. Particle identification in TAPS can be done by several different methods. Firstly the plastic scintillators are used as veto detectors separating out charged and uncharged particles. The excellent timing resolution provided by the fast decay component of the BaF_2 also allows separation of the slower protons and neutrons from the relativistic photons, electrons and pions via time of flight. Finally, the fraction of light deposited in the slow component of the BaF_2 light output is mainly dependent on the energy loss of the detected particle. By placing both a short and long gate on the BaF_2 QDC, it is possible to separate particles via an analysis of the ratio of energy deposited in the fast and slow components i.e. a pulse shape analysis.

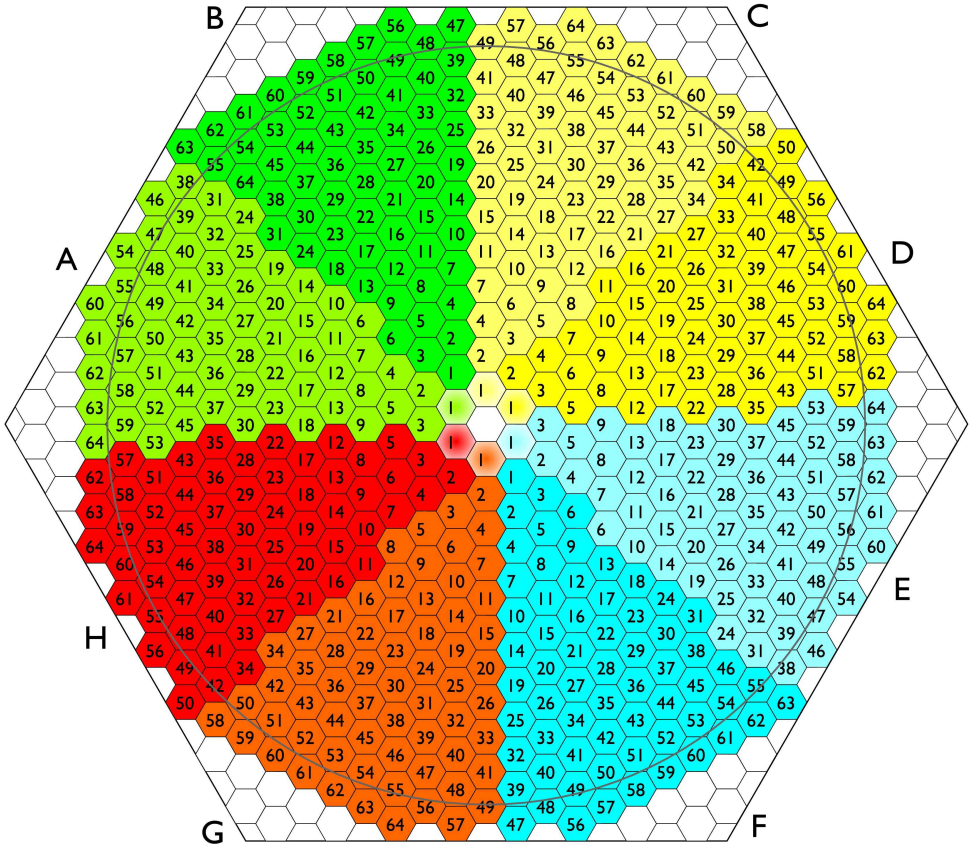

Figure 4.10: Diagram of TAPS forward wall looking downstream from the target.

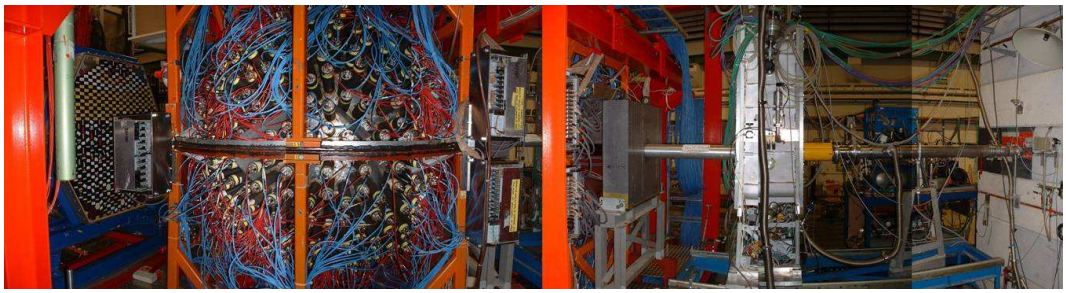

Figure 4.11: Photograph of A2 hall from tagger wall (far right) to TAPS (far left) [70].

4.8 Data Acquisition

The analogue signals from all detectors were digitised and read by the data acquisition system (DAQ). In most cases, the signals were fed to both a charge to digital converter (QDC) and, via a discriminator, to a time to digital converter (TDC). The QDC returned a value which was proportional to the amount of energy deposited in the detector by integrating over a sample of the pulse. The TDCs required both a start and a stop signal above the discriminator threshold. The start signal was provided by the experimental trigger while the stop came from the relevant detector signal. The timing of a signal in a particular detector is then relative to the other detectors. The QDCs were gated by triggering electronics which determined whether or not that 'event' was read out and stored.

4.8.1 Tagger Electronics

The energy of the detected bremsstrahlung electrons in the Tagger was determined by its hit position on the focal plane. When a signal from a focal plane detector element passed the discriminator threshold, a logic pulse was sent to the relevant TDC which started counting, it was stopped by a logic pulse from the triggering electronics. The logic pulses from the discriminators were also fed to FASTBUS scalers which are not gated by the trigger, and were used to obtain a measurement of the electron event rate in the detectors which is eventually used to calculate the photon flux in the experiment.

4.8.2 TAPS Electronics

The signals from the BaF_2 PMTs were passed through a splitter producing 3 outputs (Figure 4.12) [72]. The first was sent to a leading edge discriminator (LED) and used for triggering information. The second output went, via a delay to two QDC's with different integration times: a long gate (200ps) and short one (40ps). This facilitated pulse shape analysis. The third output was sent to a constant fraction discriminator (CFD) and a TDC providing accurate timing information on the pulse.

The signals from the TAPS veto counters were sent to an LED, with a threshold calibrated to lie between the background signal noise and the energy of a minimum ionising particle incident on the detector. Any signal which passed this threshold was considered an indication of a 'hit' in that veto detector and the selection of detectors that had fired within that event gate was recorded by a pattern unit and recorded in the data stream for every event.

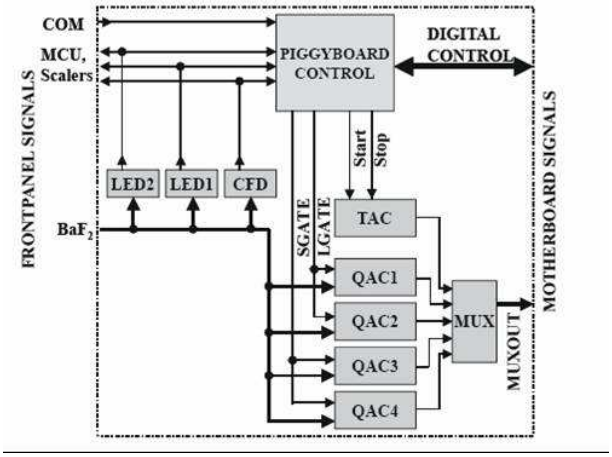

Figure 4.12: Diagram of TAPS read out electronics.

4.8.3 Crystal Ball and sub-detector Electronics

With its arrival in Mainz the Crystal Ball electronics underwent a total upgrade [71, 72]. Central to this upgrade were new discriminators, an active splitter and new multi sampling Flash ADCs (FADCs) and CATCH TDCs. The signals from the NaI PMTs were thus sent to the active 1:1 splitter, producing 3 matched outputs (Figure 4.13). One branch was sent via a delay to a Flash ADC (section 4.8.4), the second, via discriminators to a CATCH TDC (Compass Accumulation, Transfer and Control Hardware, section 4.8.5) and the final branch was used for triggering electronics (section 4.8.6).

4.8.4 Flash ADC modules

The FADCs used here were designed for the WASA detector at CELSIUS in Upsala and sampled the shape of the signal with a sampling frequency of 40MHz. They are also capable of returning multiple integrated values. In principle the sampled shape of each pulse could be recorded but to reduce readout time for this experiment only integrated pulse amplitudes were recorded. Three samples of the signal were taken - over the pedestal, signal and tail region of the pulse. In this way a measure of the residual charge in the ADC and remnant light in the crystals (the pedestal) was made for every event and was dynamically subtracted from the signal. This improves the attainable energy resolution of the crystals.

4.8.5 CATCH TDC modules

The new CATCH TDC modules used here were developed at Freiburg University for the Compass experiment at CERN. Standard TDCs like those used in the Tagger

are started/stopped by a hit in the corresonding detector and stopped/started by a logic pulse from triggering electronics. The CATCH TDCs used here work quite differently. They each have a ∼10GHz oscillator which essentially acts as a free running clock and results in a standard channel to time conversion of 117ps/channel. The synchronicity of the TDCs is ensured by a CERN-standard trigger control system (TCS). One TDC is set aside as a reference TDC and is attached to the trigger. When an event passes each level of the triggering electronics a logic pulse is sent to the reference TDC which stores the oscillator value. When a hit is recorded in any of the TDCs, they simply store the oscillator value. To convert this to a time the value in stored in the reference TDC simply has to be subtracted and the standard 117ps/channel conversion used. They are capable of storing multiple hits as well as running at a higher time resolution, ∼75ps/channel, although this higher resolution was not exploited during the experiment described here.

4.8.6 Triggering Electronics

While the DAQ is reading out an event the electronics are blind to any further hits in the detectors - this is known as dead time. To minimise this dead time, the triggering electronics were made as selective as possible.

In the current CB-TAPS setup, the trigger was determined by two LeCroy LRS 4805 logic units (Figure C.2) i.e. for an event to be read out and stored, it must satisfy two sets of conditions. For each experiment the trigger must be optimised and the two programmable logic units can be programmed in a variety of ways to reflect this. For the experiment described in this thesis, the first level trigger was satisfied if a sum of the energy deposited in all 672 elements of the CB was more than 50 MeV. If so, the second level trigger was initialised, otherwise the triggering electronics were reset. For the second level trigger, the energy in the individual NaI crystals were summed together in groups of sixteen elements. If 2 or more of these trigger sections contained a crystal with more than 13 MeV deposited in it and a hit had been recorded in the Tagger, the second level trigger was satisfied. The QDCs and TDCs were then gated, the event read out and the triggering electronics reset.

4.8.7 Analysis Software

Online data monitoring and offline data analysis are done using a new object oriented analysis package written specifically for the new Crystal Ball experiments at MAMI - AcquRoot [73]. Written in C++, it is based heavily on the ROOT analysis package from CERN [74] and provides a framework of classes that can be extended and inherited

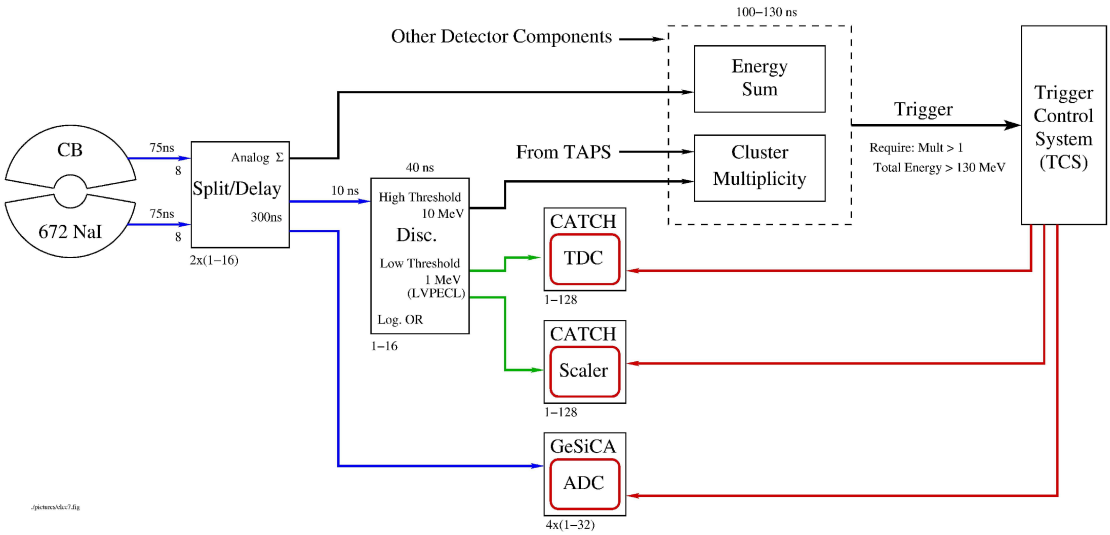

Figure 4.13: Simplified view of the Crystal Ball front end electronics [76].

from to meet the needs of the individual user. The experiment described in this thesis was one of the first to be performed with the Crystal Ball at MAMI and as such there was no developed analysis code in place. As a result the code for the analysis presented in the next chapter was largely written from scratch.

Chapter 5

Data Analysis

5.1 Overview

The process of translating the raw data stored by the experimental data acquisition into an experimental cross section is summarised in the sequence below. Each of the steps will be discussed in more detail later in this section.

- The first step in the analysis is the conversion of the raw QDC and TDC values for each detector element to real physical quantities by way of a calibration. The values recorded by the QDCs were thus converted to energies in MeV and those recorded by the TDCs were converted to times in ns.
- Cluster finding algorithms were applied to data from the Crystal Ball and TAPS to group together detector hits originating from the same incident particle.
- The 'tracks' of charged particles incident on the Crystal Ball were extracted from the MWPC data.
- The information from the PID, MWPC, CB and TAPS was combined to carry out particle identification for each event. This procedure comprised ΔE-E tehniques in the Crystal Ball and Pulse Shape Analysis (PSA) in TAPS. Knowledge of the particle type (i.e. its mass) and the energy deposited by the particle in the detector apparatus allows the 4-momentum to be obtained for each particle.
- π^0 meson candidates were then identified by reconstructing the invariant mass of photon pairs detected in the calorimeters.
- Coherent and incoherent π^0 photoproduction events were separated by combining the π^0 and photon tagger information in a missing energy analysis. The coherent π^0 yield was then determined from a fitting procedure to the missing energy spectra.

- Detection efficiencies and photon beam properties were assessed to allow the detected yield to be normalised into differential and total cross sections.

The Crystal Ball, TAPS and Photon Tagger comprise a large scale detector system with almost 3000 individual elements requiring calibration. As a result, the calibrations were shared between a number of students within the A2 collaboration. A description of each calibration stage follows. Any calibrations performed by colleagues are explicitly referenced below.

5.2 Tagger Calibration

5.2.1 Photon Beam Energy Calibration

Unlike the closely monoenergetic electron beam produced by MAMI-B, the energy of the resulting photon beam has a flux curve over a range of energies with an intensity which closely follows the E_γ^{-1} (figure 5.2(a)). The tagged photon energy was inferred from the incident electron beam energy and the measured energy of the recoiling bremsstrahlung electron in the tagger focal plane detector (equation 4.1). Accurate determination of the photon beam energy therefore requires accurate knowledge of the incident electron beam energy which is set by the number of recirculations of the beam around the microtron. Accurate energy measurements were performed by the MAMI operators at intervals of a few days, however the electron energy was not constantly monitored. Instead, the magnetic field of the final microtron dipole (which is proportional to the electron energy) was tracked. Figure 5.1 shows the dipole strength in RTM3 over a period of $\sim 2\frac{1}{2}$ weeks during the course of the experiment. The two spikes are a result of the MAMI procedure for optimising the beam. Away from these events during normal running conditions the variation in the field strength corresponds to a variation in beam energy of <0.05 MeV. A beam energy measurement of $E_e^- = 883.24$ MeV was made just prior to the start of the graph.

The energy of the bremsstrahlung electron was determined from its hit position in the tagger focal plane detector. The relationship between hit position, beam energy and tagger dipole field strength is parametrised by the tagcalv6_cern computer program [75]. The magnetic field strength of the tagger was determined and monitored using an NMR probe. The calculated relationship between electron energy and focal plane detector delement for an NMR value of 1.049T is shown in figure 5.2(b).

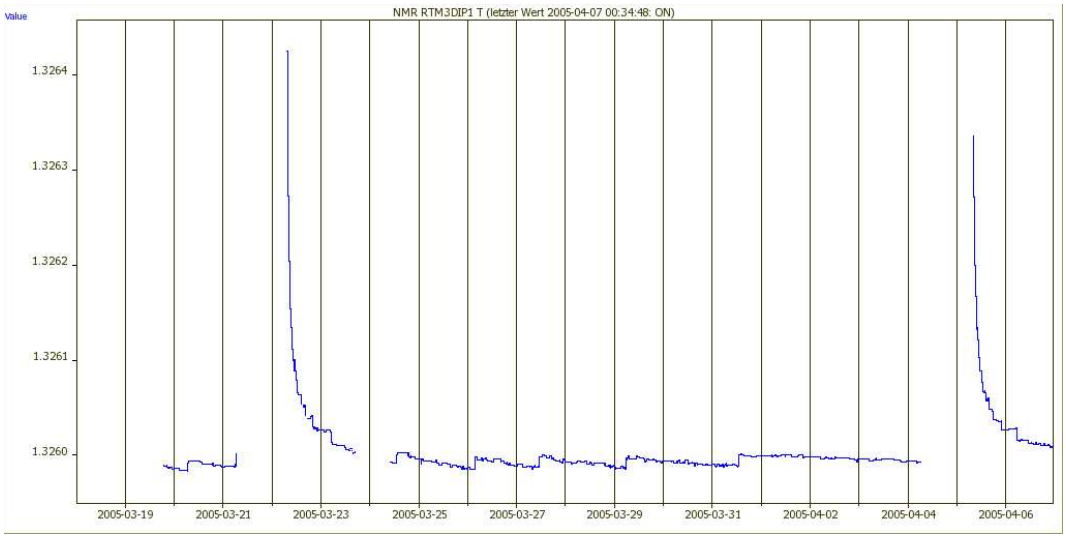

Figure 5.1: Field strength in the third MAMI microtron as a function of time [77].

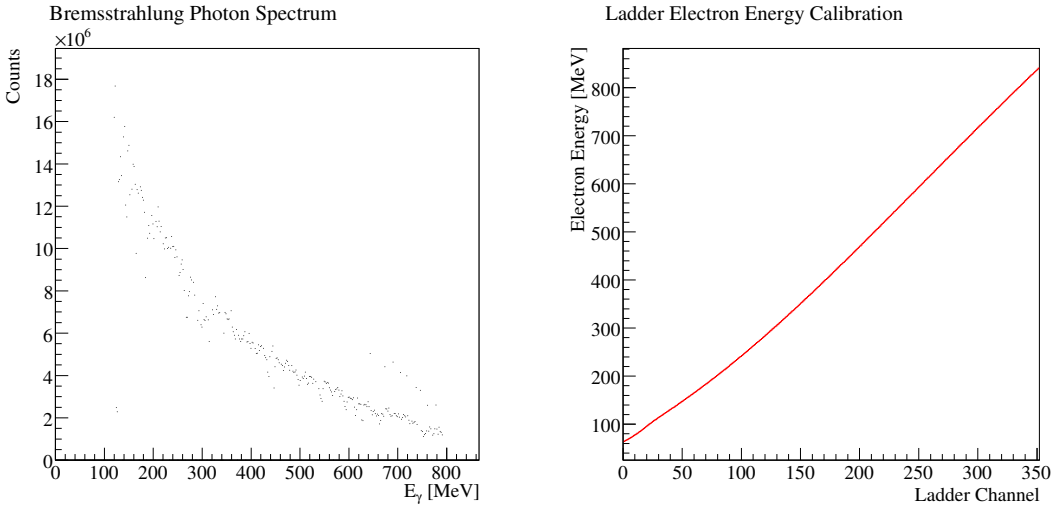

(a) Calibrated Photon Energy Flux Spectrum.

(b) Tagger Calibration.

Figure 5.2: Tagger energy calibration.

5.2.2 Tagger Timing Alignment and Tagger Random Subtractions

Along with the recoiling bremsstrahlung electron corresponding to the photon producing the reaction in the target, there is always additional background of electron hits in the tagger focal plane. These are associated with photons that pass straight through the target without an interaction, non-radiative processes in the radiator (Möller Scattering), photons that were stopped in the collimator system or background as a result of the beam hitting the beam pipe structure or beam dump. As a result, for each 'event' in the Crystal Ball and TAPS, there may be several associated electron hits in the tagger focal plane introducing an ambiguity as to which electron corresponds to the photon which interacted.

The background events in the tagger are accounted for by studying their relative timing with respect to the experimental trigger. The time recorded by the TDC for each element of the focal plane corresponds to the time difference between the hit in the tagger element and the experimental trigger (section 4.8.1). Events which are associated with the photon causing the trigger will have a constant time difference which is simply related to the time of propagation of the photon to the target and the time taken for the produced particles to make the experimental trigger. This results in a 'prompt' peak in each of the tagger TDC spectra. Electrons which were not associated with the photon producing the experimental trigger form a flat 'random' background (figure 5.3). It is not possible to determine which electron (and therefore which photon energy) is the correct one on an event by event basis since even when selecting the prompt region (blue on figure 5.3) there is clearly still some random background underneath the prompt peak. To account for this a sample of both prompt and random events must be taken when looking at any observables which require knowledge of the photon energy. Then an appropriately weighted sample of the random events (pink in figure 5.3) can be subtracted from the prompt events.

To facilitate uniform cuts on the combined timing spectrum from the complete focal plane array, the individual tagger TDCs were aligned such that the prompt peaks of all elements were coincident (figure 5.4). This procedure was carried out using experimental data from separate runs where the Crystal Ball and TAPS were left out of the DAQ and the experimental trigger was made by an ∼100% efficient Pb-Glass detector placed in the photon beam downstream of the target (section 4.4). Because of the low intensity electron beam, the number of random coincidences in the tagger focal plane was small and the timing spectrum was dominated by the prompt peak. The lack of background greatly simplified the alignment process. The channel to time

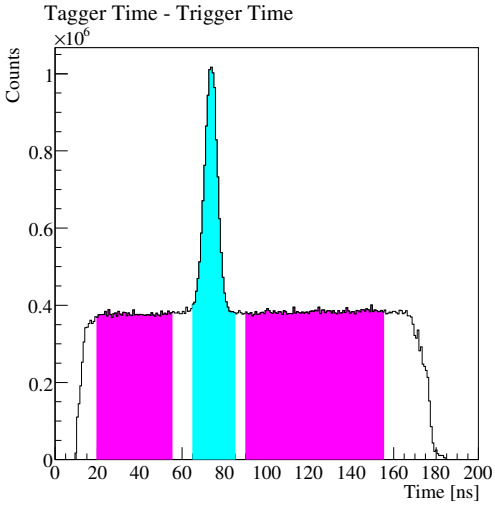

Figure 5.3: Tagger timing spectrum for all tagger focal plane elements. The light blue region (67-85)ns indicates events taken as prompt events. The pink regions were used to sample the random background.

conversion for the tagger TDCs is set by the TDC modules and has been established as 0.18ns/channel [57].

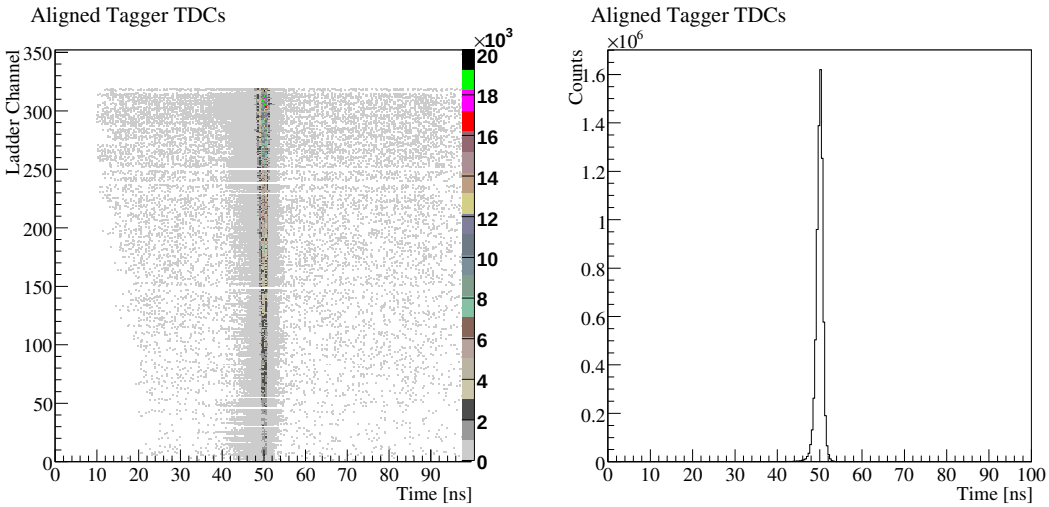

(a) Aligned tagger TDCs.

(b) Projection of (a).

Figure 5.4: Tagger timing alignment.

5.3 Crystal Ball Calibration

5.3.1 Photon Cluster Algorithm

Accurate determination of the π^0 4-momentum from the $\pi^0 \rightarrow \gamma\gamma$ decay requires accurate knowledge of the photon direction and energy. As has been noted (section 4.6) , photons deposit energy in the Crystal Ball via the development of an electromagnetic shower. In ∼98% of events the energy deposited is contained within a cluster of 13 NaI crystals. The cluster algorithm attempts to identify groups of crystals with energy deposited originating from the same incident photon. In analysing a shower the cluster algorithm first finds the crystal with the largest energy deposit then considers additionally its 12 neighbouring crystals (figure 5.5). The deposited energy in any cluster is then taken as the sum of the energies in each of the 12 crystals. If the energy sum did not exceed 25 MeV then the cluster was rejected. The position of the 'hit' was calculated as a weighted sum of each of the cluster elements. For example, the reconstructed hit position, X_{rec} was calculated as:

$$X_{rec} = \frac{\sum_i \sqrt{E_i} x_i}{\sum_i \sqrt{E_i}} \tag{5.1}$$

where x_i is the x-coordinate and E_i the energy deposited in the i-th crystal.

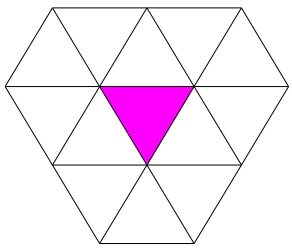

Figure 5.5: A NaI cluster. Each triangle represents the triangular face of a NaI crystal. The cluster finding algorithm searches for the highest energy crystals and sums that crystal with its 12 nearest neighbours.

5.3.2 Crystal Ball Energy Calibration

The energy calibration procedure converts the QDC values from each CB element into an energy. This was taken to be a linear relationship as possible energy dependent corrections such as scintillation light collection efficiency and shower loss effects were

found to have small effects for the photon energies used in this experiment. In general for a linear energy calibration, two known parameters are needed:

$$Energy\ (MeV) \quad = \quad offset + gain \ \times \ QDC(channels) \tag{5.2}$$

As the Flash ADCs used with the Crystal Ball NaI detectors employ dynamic pedestal subtraction (section 4.8.4) the 'offset' can be taken to be zero.

5.3.3 Crystal Ball Low Energy Photon Calibration

An initial calibration of the NaI crystals was performed by colleagues from the University of Mainz and UCLA [78,79] using the 4.4MeV gamma decay from an AmBe source as the sole energy point.

The analysis of the present experimental data has been used to improve this low energy photon calibration of the Crystal Ball using a new nuclear decay photons technique. The gains were aligned using the 4.4 MeV photon decay from the reaction $^{12}C(\gamma,\pi^0)^{12}C^*$, where the nucleus is left in its first excited state. Figure 5.6 shows the 4.4 MeV peaks in the energy deposition spectra of a selection of NaI crystals. These peaks were fitted with an exponential and a Gaussian function. The centroid of the gaussian was then used to extract the magnitude of the gain as defined in equation 5.2.

5.3.4 Crystal Ball High Energy Calibration

The low energy photons described in section 5.3.3 are not typical of the photons produced in a meson decay which generally have energies above 40 MeV. Therefore a calibration of higher energy photons is required and for this purpose, the $\pi^0 \rightarrow \gamma\gamma$ decay proves an excellent source of high energy photons.

Three cuts were applied to the data to better select $\pi^0 \rightarrow \gamma\gamma$ events suited to the calibration procedure:

1. Events were rejected if the energy deposited in the central detector of the cluster was less than 80% of the total cluster energy.

2. The energy difference between the two decay photons was required to be small such that $|E_1 - E_2| < \frac{1}{4}(E_1 + E_2)$.

3. The tagged photon energies were restricted to $E_\gamma < 180$ MeV, resulting in π^0 decay photons with energies between 40 - 125 MeV.

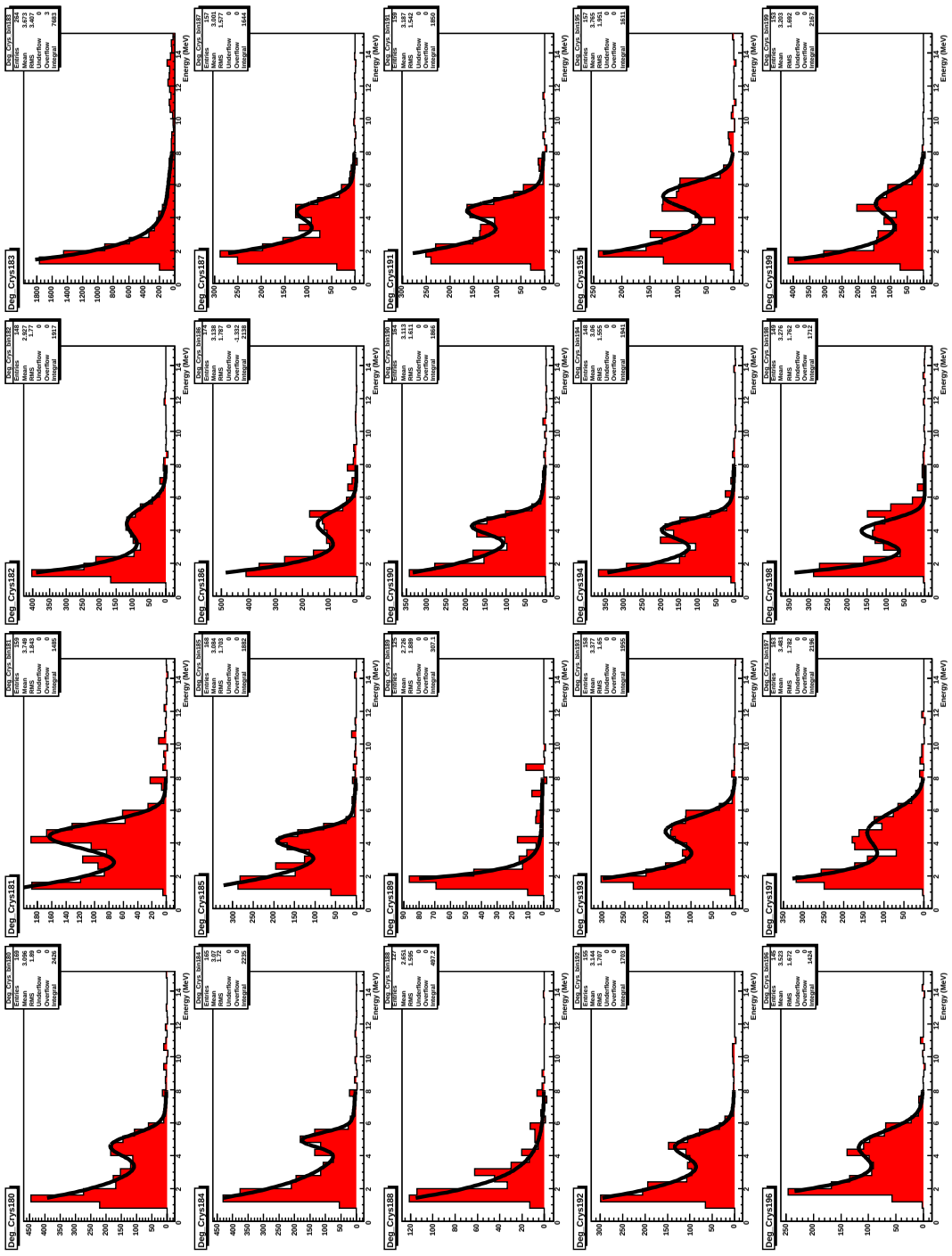

Figure 5.6: Fits to low energy photon spectra for a selection of NaI crystals.

The first cut was employed to ensure the cluster energy was dominated by an energy deposit in a single central cluster element. This is desirable as we need to obtain a calibration on a crystal by crystal basis. The second cut limited the energy difference between the two decay photons so that for any single event the photons used in the calibration had a similar energy. The third cut ensured that the π^0s were low energy. This gives a larger contribution of π^0 events where the opening angle between the decay photons is large and therefore the photons are produced almost back-to-back. The restriction to lower incident photon momenta results in a more isotropic angular distribution for the π^0 decay photons in the lab than observed at higher energies and the crystals were therefore sampled more evenly. Additionally, the application of cut (3) ensured the range of π^0 decay photon energies was limited. This was employed to minimise any energy dependent variations in shower loss effects or losses of scintillation light due to collection effects in the crystals. Restricting the range of photon energies effectively places a restriction on the position of the shower within the crystals which is desirable for the gain matching process.

The procedure can be summarised as follows.

- Decay photon pairs from the reaction ^{12}C(γ,π^0) were selected with the applicataion of cuts (1) to (3) and their invariant masses reconstructed.
- The invariant masses were then histogrammed, using information only from the central (or largest energy) crystal of the two photon clusters (figure 5.7(a)).
- The 2D histogram was projected into 672 individual invariant mass spectra (one per crystal). Each histogram represented the sum of all photon pair combinations where that crystal was one of the central cluster elements.
- The invariant mass peaks were fitted with an asymmetric Gaussian and the fitted peak values, $m_{\gamma\gamma}$, used to calculate new MeV/channel gains i.e.

$$\frac{MeV}{channel}(new) = \left(\frac{m_{\gamma\gamma}}{m_{\pi^0}}\right)\frac{MeV}{channel}(old) \tag{5.3}$$

This process was repeated 3 times with a new set of gains for each iteration.

5.3.5 NaI(Tl) Timing

The design of the CATCH TDCs used with the Crystal Ball is such that the channel to time conversion is fixed at 117ps/channel (section 4.8.5). The timing of each of the NaI TDCs was aligned to a reference crystal (figure 5.8) by a colleague from the University of Mainz [76].

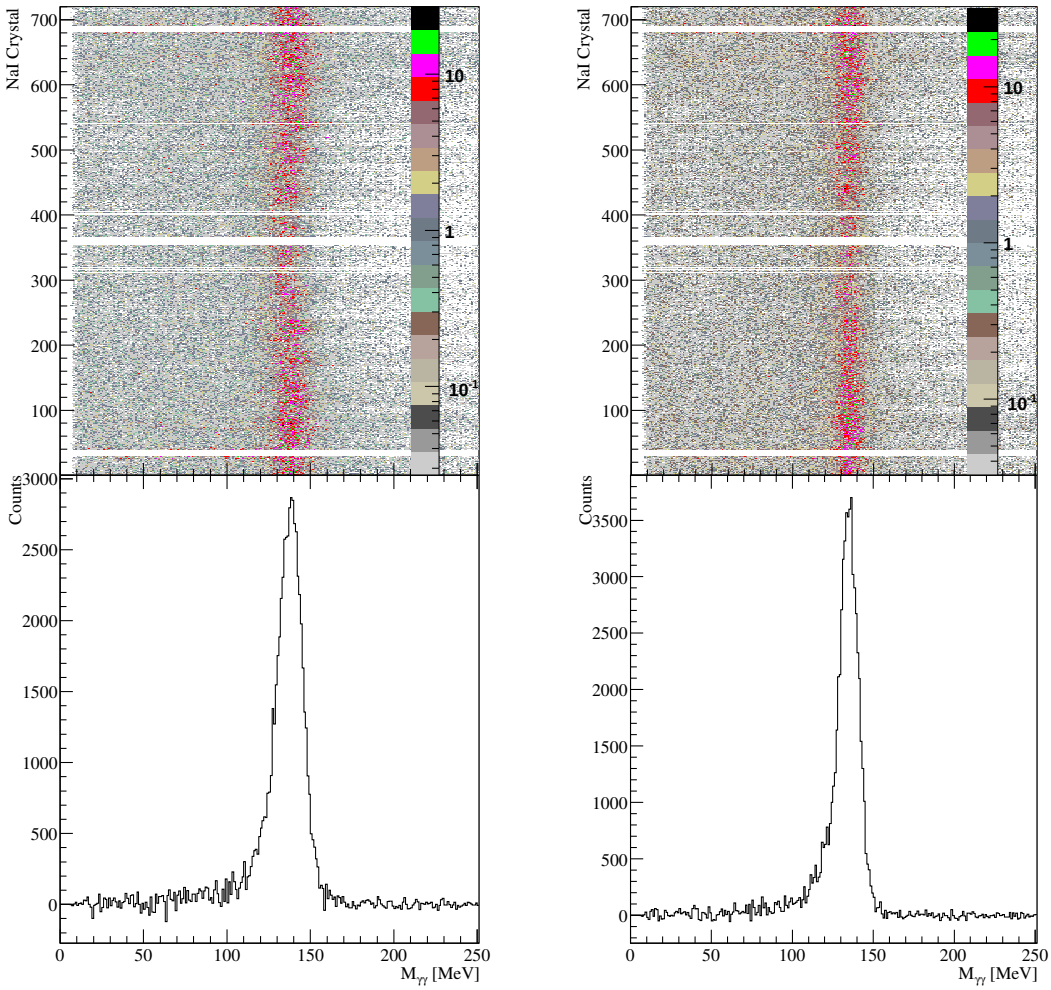

(a) Initial π^0 mass with low energy γ calibration.

(b) π^0 mass after 3 iterations of the high energy γ calibration.

Figure 5.7: NaI high energy calibration.

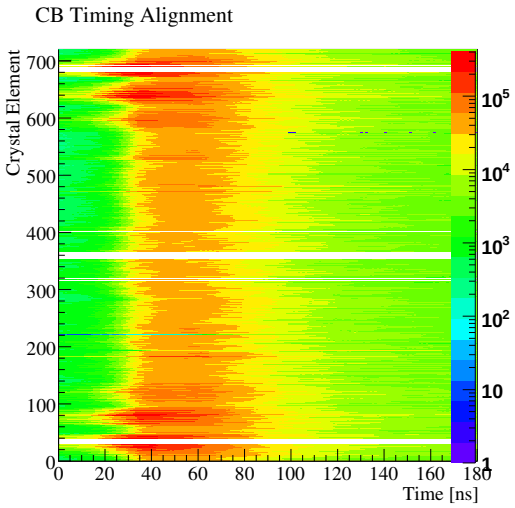

Figure 5.8: Aligned CB TDCs.

The slow timing response of NaI is well known [80] (NaI signals have a typical rise time of 250ns) and as a result the times recorded by the TDCs must be corrected for time walk effects. Time walk is introduced by leading edge discriminators whereby a signal with a small amplitude will take longer to reach the discriminator threshold than a signal with a large amplitude (figure 5.9). Low energy pulses therefore appear to have a later timing than high energy pulses. With the assumption that the pulse shape can be approximated as a parabola, the following parameterisation can be used to correct for the walk effect:

$$T' = T - r\sqrt{\frac{a_0}{a}} \tag{5.4}$$

where T$'$ is the corrected time, T is the uncorrected time, a is the pulse height, r is the rise time and a_0 is the discriminator threshold. The product of rise time and

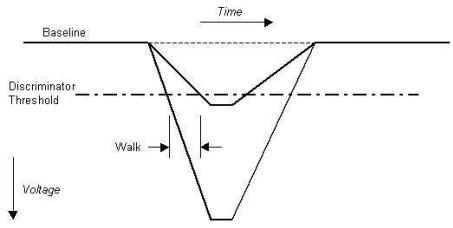

Figure 5.9: Time walk.

discriminator thresholds (ra_0) were obtained from fits to time vs energy plots using functon 5.4. Figures 5.10(a) and 5.10(b) show the effect of the resulting walk correction on the NaI timing versus energy.

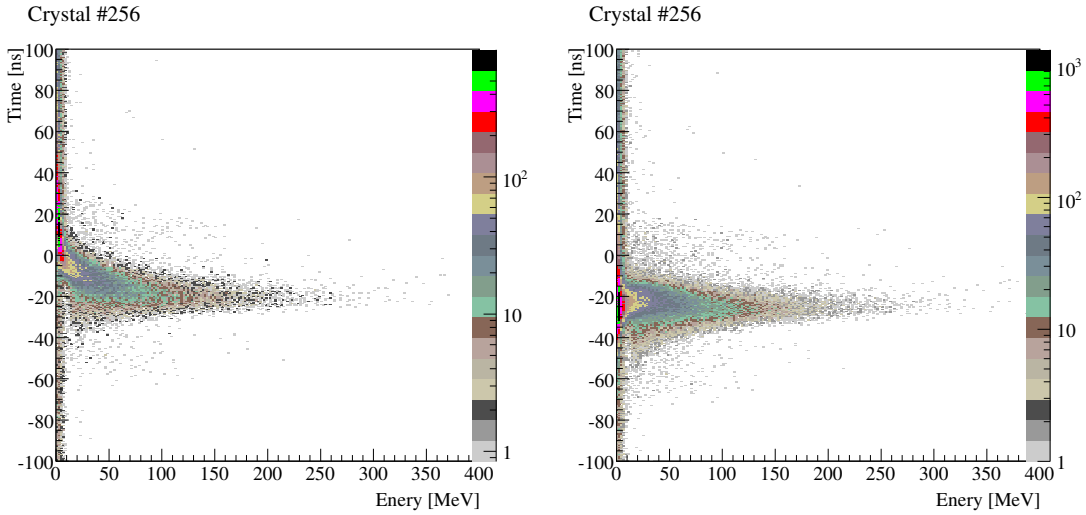

(a) Without walk correction.

(b) With walk correction.

Figure 5.10: NaI timing as a function of energy.

5.3.6 Crystal Ball Particle Identification Detector Calibrations

The CB particle identification detector (PID) was equipped with the same CATCH TDCs as the Crystal Ball. As such the time/channel conversion was also fixed at 117ps/channel. The timing alignment of each of the 24 PID elements was performed by R.Codling at the University of Glasgow [81]. Colleagues at Glasgow University also performed an energy calibration of the PID via a comparison of the experimental data with data from a Geant3 Monte Carlo simulation (for more details of the simulation see section 5.8). Briefly, a simulation was performed to test the response of the Crystal Ball and PID detectors to protons, charged pions and electrons. The energy deposited in the PID (ΔE) was plotted against the energy deposited by the particle in the Crystal Ball (E). The resulting spectra showed the characteristic curves associated with particles of differing masses (figure 5.11(a)). Figure 5.11(b) shows the PID energy depostion spectrum corresponding to an energy in the Crystal Ball between 38 and 42MeV. There are two distinct peaks: the lower one corresponding to charged pions and the higher one corresponding to protons. Gaussians were fitted to the two and a similar procedure was followed for the experimental data. The PID QDC gains for each element were adjusted so that the pion and proton peak positions lay at the same energy in MeV as those of the simulated data.

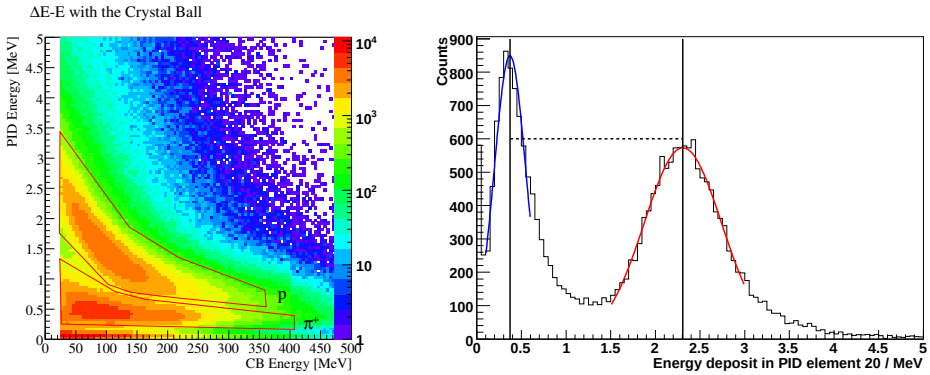

(a) PID ΔE-E. The projection to the y-axis between x values of 38MeV and 42 MeV was used for the calibration procedure.

(b) Projection of (a) for CB energies between 38 and 42 MeV

Figure 5.11: CB particle identification

5.3.7 Crystal Ball MWPCs

The two multi wire proportional chambers used in the present experiment were inherited from the DAPHNE [67] experiment, along with the analysis code developed to extract information on the track of charged particles from the anode and cathode signals. The MWPC fortran code was translated to C++ for use with the new AcquRoot analysis package by S.Schumman at the University of Mainz [82]. The same colleague has also produced a calibration of the relative position of the two proportional chambers via the analysis of cosmic ray events in the chamber.

5.3.8 CB Particle Identification

The Crystal Ball is ideally suited to detecting photons but is also capable of stopping up to 245 MeV pions, 340 MeV kaons and 425 MeV protons. The correlation of energy deposited in the PID and the Crystal Ball for each charged particle was used to distinguish between different particle species via a ΔE-E analysis.

The particle identification procedure starts by initially assuming all particles detected in the ball are photons. If there was a hit in the PID correlated in ϕ (azimuthal angle) with the Crystal Ball hit, the particle was identified as charged. The azimuthal correlation has to be within $\pm 15^\circ$ of the centre of a PID element. A comparison of the energy deposited in the PID with that in the ball results in the characteristic curves on the ΔE-E plots corresponding to different particle types (figure 5.11(a)). Particles were identified as protons or pions if they fell within the regions shown on the figure.

5.4 TAPS Calibration

5.4.1 BaF_2 Energy Calibration

The energy response of the BaF_2 detectors over the energy range used in the experiment described here is closely linear [69] and can be described by an offset and a gradient. The offset corresponds to the pedestal position which is the amount of background charge recorded by the QDC under the real pulse. The pedestal shows up in the energy deposition spectra as a single channel peak with a height several orders of magnitude larger than the genuine signals, and can be seen at the most left hand point of figure 5.12(a). The second point for the calibration was taken from the minimum ionising muon peak at 37.7 MeV (figure 5.12) from cosmic rays passing vertically through the TAPS detector. The cosmic ray data were accumulated during separate calibration runs before and after the experiment. The TAPS energy calibrations used in this work were performed by B. Boillat of the University of Basel [83].

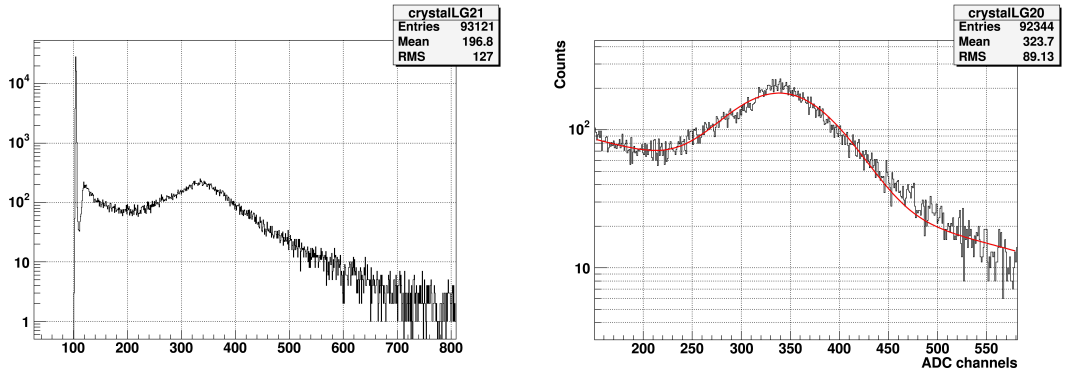

(a) Cosmics energy spectrum in TAPS including the pedestal.

(b) Example of a fit to the minimum ionising muon peak (cosmic rays) in TAPS.

Figure 5.12: TAPS Energy Calibrations [83].

5.4.2 BaF_2 Timing Calibration

The timing alignment of the BaF_2 TDCs was performed by F. Zehr from the University of Basel [84] and was done relative to the trigger arising from signals in the Crystal Ball. Signals from the BaF_2 crystals were fed to TDCs via constant fraction discriminators (CFD - section 4.8.2). Unlike leading edge discriminators, CFDs do not suffer from large walk effects as they only produce an output logic pulse after the leading edge of the signal has reached a constant fraction of the signal's peak height. This time is virtually independent of the amplitude of the signal.

5.4.3 TAPS Particle Identification

The procedure for identifying particles in TAPS initially also assumes all particles are photons. The TAPS veto detectors served to distinguish between charged and uncharged particles. If a pulse from one of the detectors passed the relevant discriminator threshold a logic pulse was passed to the DAQ. The selection of vetoes that fired for any event was then recorded by a pattern unit. The threshold for the TAPs vetoes was set to be between the noise and minimum ionising peak of the energy deposition spectrum.

The BaF_2 scintillation output contains both a fast component with a decay time of 0.6ns and a slow scintillation component with a decay time of 620ns. The presence of the two components make possible pulse shape discrimination techniques to identify different particle types. The signals from the BaF_2 were read out by two QDCs: one with a short integration gate and one with a long integration gate (section 4.7.1). The gates were timed such that most of the energy from the fast component was deposited within the timing of the short gate, while the energy from the slow component was deposited within both gates. For hadronic particles which have high rates of energy loss (protons, pions) the relative contribution of the fast component to the slow is lower than for relativistic particles (electrons, photons). Thus in a plot of the energy deposited in the fast component vs the energy deposited in the slow component (figure 5.13(a)) one sees a narrow band at an angle of 45° corresponding to relativistic particles and a band at smaller angles corresponding to heavier particles. In order to apply more conventient particle selection cuts to the data the BaF_2 energies were re-plotted as a function of r and angle as defined in equation 5.5 and 5.6 (figure 5.13(b)).

$$r = \sqrt{E_{short}^2 + E_{long}^2} \tag{5.5}$$

$$angle = arctan\left(\frac{E_{short}}{E_{long}}\right) \tag{5.6}$$

where E_{short} and E_{long} are the energies integrated over the short and long gate. This 2D histogram was then projected along the x-axis into separate histograms of the angle variable for different values of r. Each individual angle histogram was fitted with two Gaussians (one corresonding to relativistic particles and one to hadronic particles). The fitted parameters were used to define data cuts separating photons and electrons from pions and protons. These data cuts were supplied by R. Gregor and S. Lugert from the University of Giessen [85,86].

The excellent timing resolution of the BaF_2 also facilitates particle identification by time of flight. However this analysis method was not exploited for the current analysis where only photon events will be analysed.

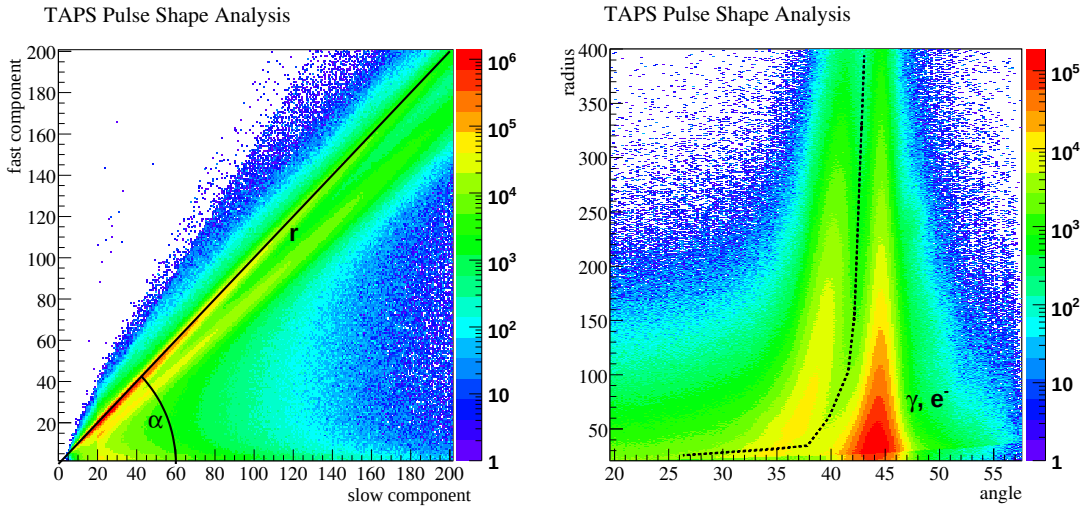

(a) (b)

Figure 5.13: TAPS pulse shape analysis.

5.5 Target Position Correction

Precise knowledge of the reaction vertex position along the z-axis (parallel to the photon beamline) is vital to reconstruct the photon (and therefore the π^0) polar angle accurately. The MWPCs were used to accurately determine the target position (relative to the wire chambers) by analysing events in which two charged tracks were produced from the target, such as A(γ,pp)A-2. The reaction vertex position with respect to the centre of the wire chambers were reconstructed from the intersection point of the tracks. The reconstructed z vertex positions from double charged tracks are presented in figure 5.14(b). These spectra were used to extract the position of the four targets relative to the wire chambers. The small peak at ∼100mm downstream from the centre of the MWPCs corresponds to events produced on the kapton exit window of the target vacuum pipe.

To extract the position of the target with respect to the Crystal Ball the further step of determining the relative position of the wire chambers and the Crystal Ball is necessary. Every care was taken during the installation of the MWPCs within the Crystal Ball to place them as close to the geometric centre as possible. A further check of the wire chamber position was done by looking at charged particle events in the Crystal Ball and plotting the corresponding z intersection point on the outer wire chamber (figure 5.14(a)). Any offset of the wire chambers from the centre of the CB would see this spectrum shifted along the z axis. The distribution is symmetric about the zero position of the wire chamber to an accuracy of ∼0.5mm. The data shown in

figure 5.14(a) were taken with the ^{208}Pb target and the dip in the spectrum at z=0mm can be attributed to a loss of flux for charged particles when travelling along the target. It can be seen from figure 5.14 that the water target has the largest offset from the

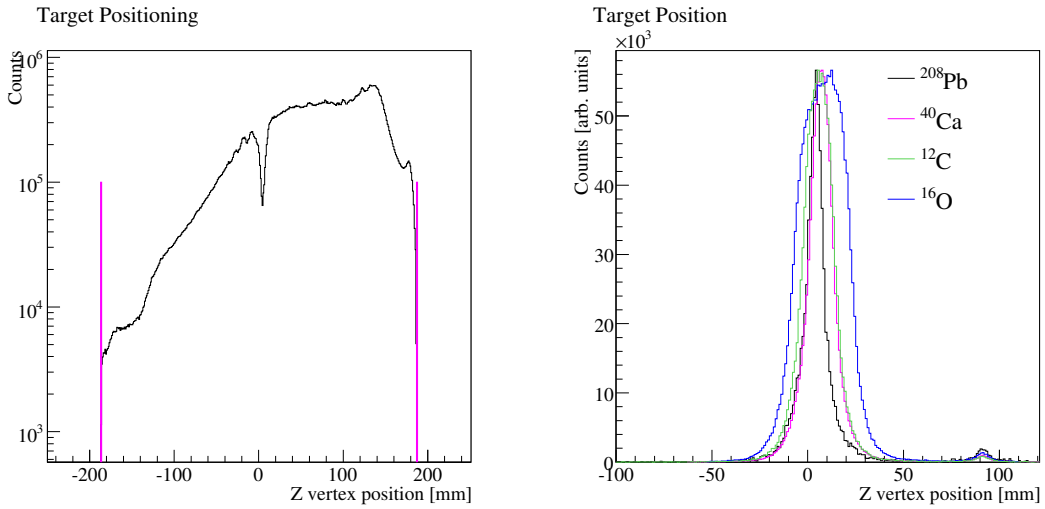

(a) MWPC intersection point for charged particles detected in the CB.

(b) Charged particle reaction vertices.

Figure 5.14: target positioning

centre of the crystal ball and is positioned ∼9mm downstream. The target offsets were accounted for by correcting the 3-momenta of the detected particles. For targets centered in the CB the momentum of a photon detected in the Crystal Ball was set as:

$$\mathbf{p} = \frac{E_{det}}{\sqrt{x^2+y^2+z^2}}(x,y,z) \tag{5.7}$$

where x, y, and z were the reconstructed x, y and z positions of the centre of mass of the cluster (section 5.3.1) and E_{det} was the energy deposited in the cluster. For non-central targets the corrected momentum is:

$$\mathbf{p} = \frac{E_{det}}{\sqrt{x^2+y^2+(z-z_{offset})^2}}(x,y,z-z_{offset}) \tag{5.8}$$

where z_{offset} was taken from the difference between the reconstructed target position and the centre of the CB.

5.6 Selection of π^0s

As has been noted, the π^0 cannot be detected directly and its presence and properties must be inferred by measuring the 4-momenta of its decay photons. Once the calibration and charged particle identification process had been completed events where fewer

than two photons had been detected were rejected from the analysis. The invariant mass of all detected photon pairs was reconstructed via the relation (Appendix A):

$$m_{\gamma\gamma} = \sqrt{2E_1E_2(1-cos\psi)} \tag{5.9}$$

where, ψ = The opening angle between the two photons.
E_1= The energy of photon 1.
E_2= The energy of photon 2.

A photon pair resulting from a π^0 decay should have an invariant mass of 134.98 MeV within the experimental resolutions (figure 5.16). Photon pairs were identified as resulting from a π^0 decay if their invariant mass was between $m_{\gamma\gamma}$ = (117-150)MeV.

Photons from the same π^0 decay should also show a strong timing correlation. The timing of each photon cluster was taken as the time returned by the TDC of the central cluster element. A cut was placed on the relative timing between the two photon clusters (figure 5.15). For candidates passing the $m_{\gamma\gamma}$ and timing constraints, the π^0 4-momentum in the lab frame was set as:

$$p^{\mu}_{\pi} = p^{\mu}_1 + p^{\mu}_2 \tag{5.10}$$

where, p^{μ}_1 and p^{μ}_2 are the 4-momenta of the decay photons:

$$p^{\mu}_1 = (E_1, \mathbf{p}_1) \tag{5.11}$$

$\mathbf{p}_1$ is the 3-momentum of one of the decay photons and is fixed as in equation 5.8.

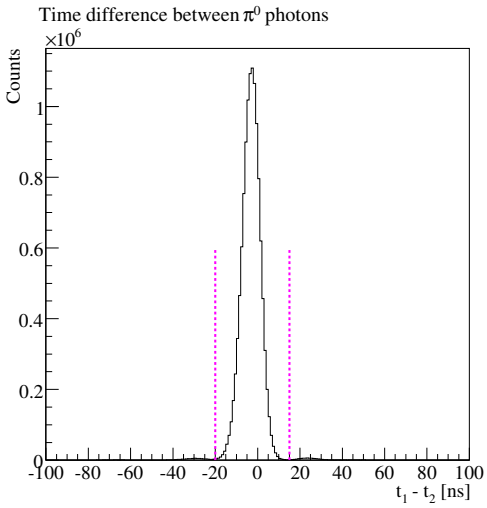

Figure 5.15: Time difference between two π^0 photon clusters detected in the crystal ball. Lines indicate the data cut applied to select π^0s.

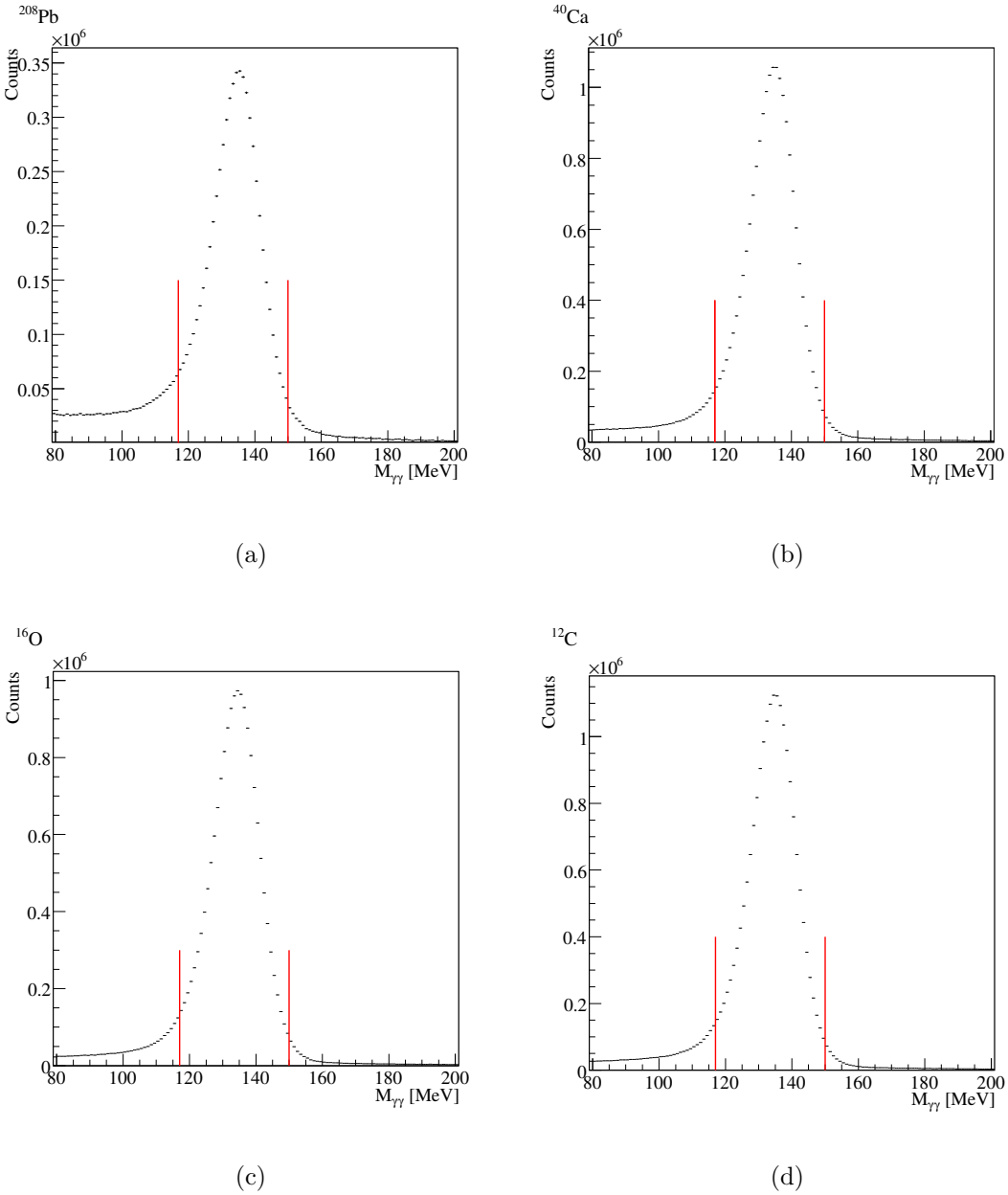

(a) (b)

(c) (d)

Figure 5.16: Invariant masses all energies E_γ=(135-400) MeV.

5.6.1 Empty Target Subtraction

The four targets were supported in the Crystal Ball within an evacuated carbon fibre pipe (section 4.5) which was sealed at the downstream end by a 100μm thick kapton window (figure 4.7). π^0s can of course be photoproduced on this extra material in the beam line as well as from the target of interest. To sample this background 3 hours of data were taken with just the rohacell target holder in the vacuum pipe. As the water target contained additional 60μm melinex windows, 2 hours of data with just the empty water target were obtained . Figure 5.17 shows the reaction vertex positions of charged particles reconstructed by the MWPCs for the two empty target data sets and illustrates the presence of background contributions from the kapton and melinex windows. In accounting for the target out contribution to the π^0 yield, the target-out

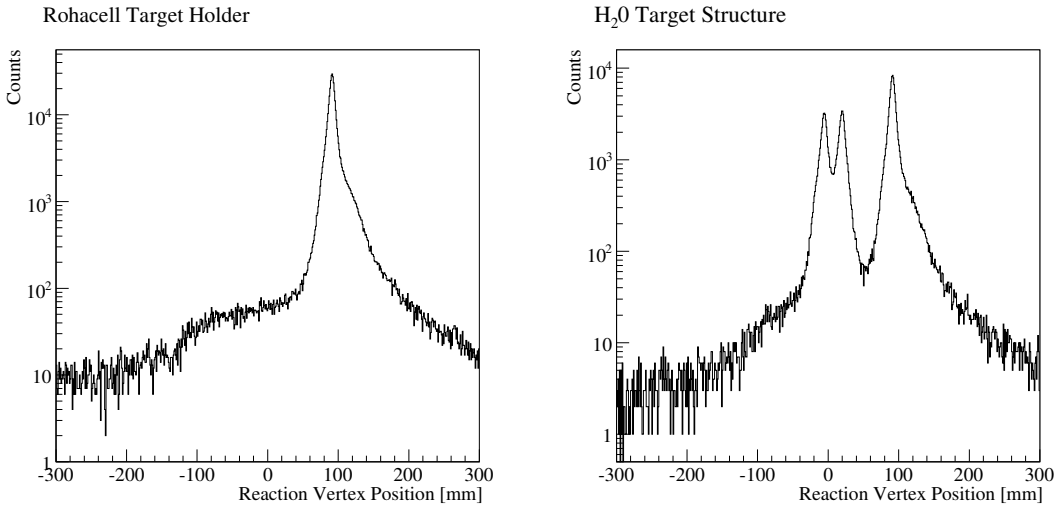

(a) Reaction vertex position for empty target data where only the rohacell target holder was in the beam pipe.

(b) Reaction vertex position for empty target data where only the H_20 target structure was in the beam pipe.

Figure 5.17: Empty target data.

data were subjected to the exact same analysis procedure as the target-in data and then subtracted off. The number of π^0s relative to the target of interest can be seen in figure 5.18.

5.6.2 TAPS data

Once the detector calibrations were completed and a preliminary analysis of the π^0 yield had been performed a problem with the TAPS data was identified. Initially the number of π^0s detected in TAPS appeared lower than had been simulated prior to the

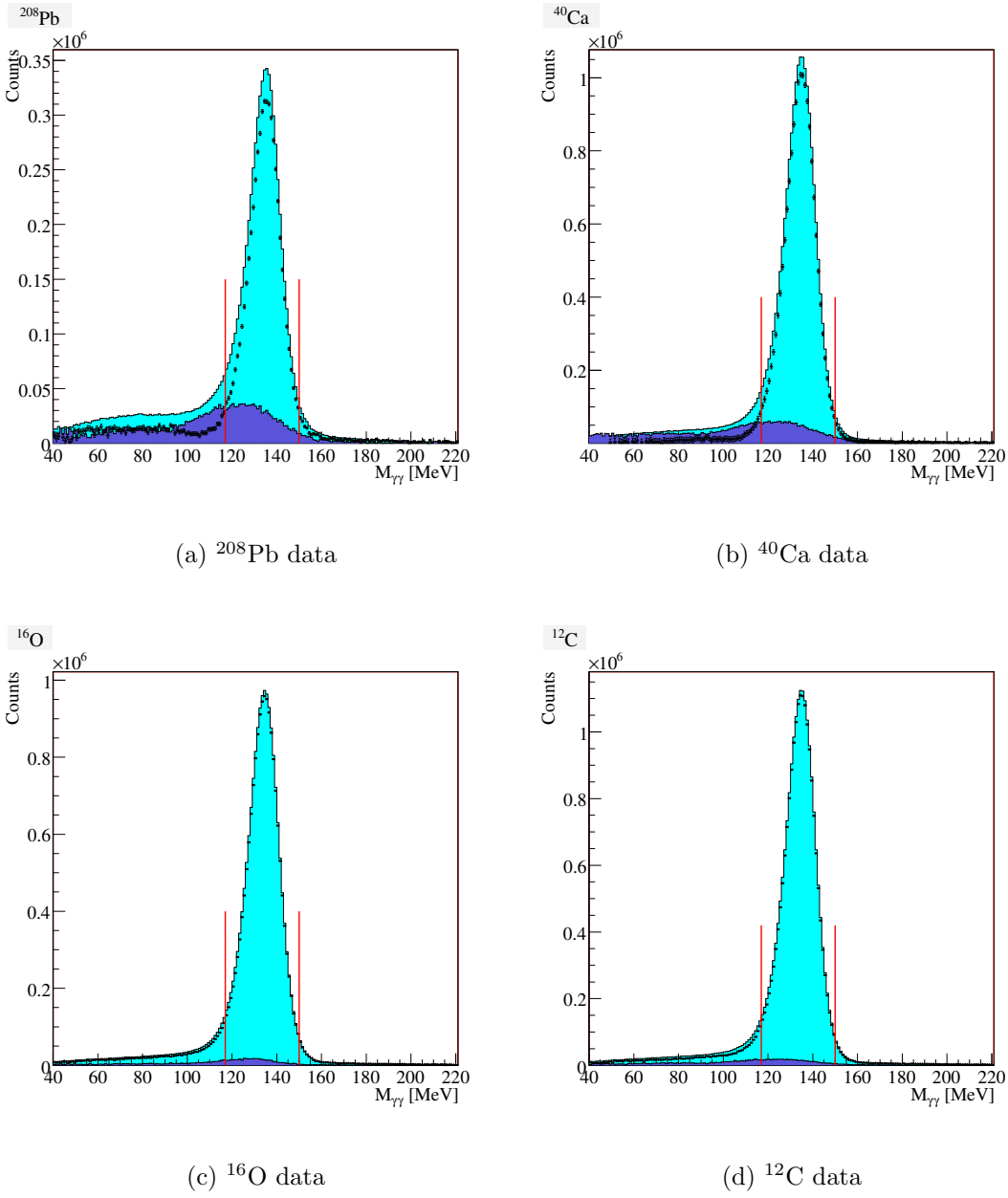

(a) ^{208}Pb data

(b) ^{40}Ca data

(c) ^{16}O data

(d) ^{12}C data

Figure 5.18: Effect of empty target. Light blue filled histogram: invariant mass spectrum (2 photons) for all events. Purple filled histogram: invariant mass spectrum resulting from empty target. Black markers: with empty target data subtracted. The red lines indicate cuts applied to the data.

experiment running. After some further analysis it has been shown that the photon detection rate in TAPS was much lower than anticipated. Figure 5.19 shows the angular distribution of all π^0 decay photons in Crystal Ball and TAPS. This distribution should be forward biased reflecting the isotropic π^0 decay in the centre of mass frame. (The regular structure arises from the cluster finding algorithm and the segmentation of the Crystal Ball and is reproduced by GEANT3 simulations). However, the sharp drop off observed in the region of phase space covered by TAPS (θ <22°) is not expected. At 10° this drop in photon yield could be conservatively estimated to be ∼70%. A similar effect has also been seen for proton events detected in TAPS. There is as yet no satisfactory explanation for this reduced rate from the groups who setup TAPS and the TAPS data acquisition system. A possible cause unfortunately is the development of electronic deadtime in the TAPS electronics at high event rates. Because of this presently unsolved problem with the TAPS data, TAPS has been removed from the analysis to avoid any ambiguities in the results. As TAPS only covers a small part of the phase space this will not have a large effect on the quality of the data set in the photon energy region of interest for extracting the matter distribution.

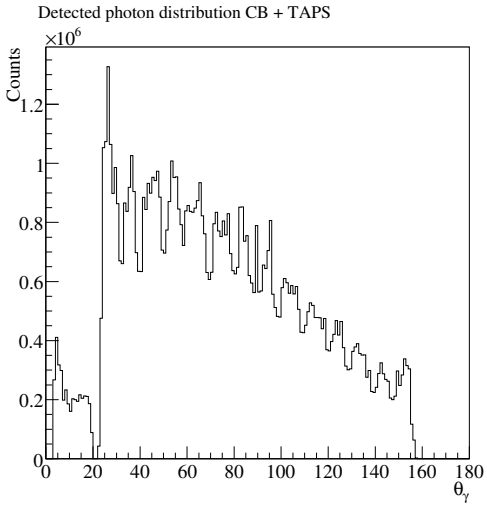

Figure 5.19: Angular distribution of π^0 decay photons in both the Crystal Ball and TAPS.

5.7 Selection of Coherent Events

The photoproduction of π^0 mesons from nuclei can proceed by a variety of channels. The coherent π^0 yield of interest occurs with a background of incoherent proceses (where the nucleus is left in a discrete excited state), quasifree processes (where a neutron or proton is knocked out of the nucleus) and double π^0 production. Two

methods have been attempted to separate out coherent π^0 events from these background processes:

- Missing energy analysis.
- Coincident detection of the decay gammas from a nuclear excitation.

The first technique exploits the different threshold energies for each background channel (table 5.1) and makes explicit use of the π^0 4-vector and the incident photon energy determined by the tagger. The second technique was used to study incoherent events where the nucleus was left in a specific excited state which subsequently gamma decayed. Only the first technique was used to extract the cross sections presented in this thesis. However, preliminary studies of the suitability of coincident π^0 and nuclear decay photon detection in the CB are presented in Appendix D and will be the topic of future additional work.

Table 5.1: Extra energy required (in MeV) for non-coherent processes.

Nucleus	Nuclear Excitation	Proton Knockout	Neutron Knockout	Double π^0 Production
^{12}C	4.4, 15.0...	16.0	12.5	134.98
^{16}O	6.05, 6.13...	12.1	15.7	134.98
^{40}Ca	3.7, 4.5...	12.5	9.9	134.98
^{208}Pb	2.61,3.20...	8.0	7.4	134.98

5.7.1 Pion Missing Energy

The pion missing energy, ΔE_π is defined as:

$$\Delta E_\pi = E_\pi^{cm}(E_\gamma) - E_\pi^{cm}(\gamma_1\gamma_2) \tag{5.12}$$

where $E_\pi^{cm}(E_\gamma)$ is the pion energy in the pion-nucleus centre of mass frame calculated using the incident photon energy and assuming a coherent event:

$$E_\pi^{cm}(E_\gamma) = \frac{s + m_\pi^2 - M^2}{2\sqrt{s}} \tag{5.13}$$

and $E_\pi^{cm}(\gamma_1,\gamma_2)$ is the detected pion energy Lorentz transformed to the pion-nucleus centre of mass frame. The terms in the above equations are defined as:

E_γ = the incident photon energy.
s = the invariant mass of the photon-nucleus pair.
m_π = the pion mass.
M = the mass of the relevant nucleus.

The detected energy of the π^0 (in the lab frame), E_π, can most simply be taken as:

$$E_\pi = E_1 + E_2 \tag{5.14}$$

where E_1 and E_2 are the detected energies of the two photons. However, this method does not use all the information from the detector system. Better energy resolution can be obtained if angular information is used as well. The pion energy in the lab frame was therefore calculated as [16]:

$$E_\pi = \sqrt{\frac{2m_\pi^2}{(1-X^2)(1-cos\psi)}} \tag{5.15}$$

where,

$$X = \frac{E_1 - E_2}{E_1 + E_2} \tag{5.16}$$

and ψ is the opening angle between the two π^0 photons. The Lorentz transformation of the lab pion energy to the centre of mass is given by:

$$E_\pi^{cm} = \gamma\left(E_\pi - \beta\left(E_1 cos\theta_2 + E_2 cos\theta_2\right)\right) \tag{5.17}$$

where θ_1 and θ_2 are the polar angles of the two pion decay photons, E_π is the pion energy in the lab frame and β is known from the incident photon energy and recoil mass:

$$\beta = \frac{E_\gamma}{E_\gamma + M} \tag{5.18}$$

A more detailed derivation of formulae 5.13 to 5.18 is included in appendix A.

For the coherent process the calculated pion energy, $E_\pi^{cm}(E_\gamma)$ should match the detected pion energy, $E_\pi^{cm}(\gamma_1,\gamma_2)$. For incoherent and quasifree events however, less energy is available for the pion since energy can be taken away by other particles or left as excitation energy in the recoiling nucleus. Incoherent events should therefore have pion missing energies at negative values. Figures 5.20(a)- 5.20(d) show the pion missing energy averaged over all pion angles and for the incident photon energy range E_γ = (135-300) MeV. The peak arising from coherent π^0 production is clearly visible near to $\Delta E_\pi = 0$ for all nuclei. To extract the coherent π^0 yield, these spectra were

split into 18 incident photon energy bins ranging from (135-300) MeV and up to 180 pion angular bins (θ_π) ranging from (0-180)°. Each of the resulting ∼2000 pion missing energy spectra were then fitted with one or more functions to represent the coherent and background contributions so that the coherent π^0 strength for each chosen E_γ, θ_π bin could be extracted.

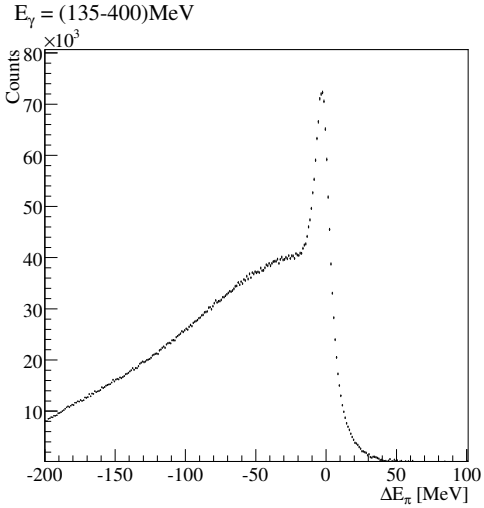

(a) Pion missing energy for ^{208}Pb data

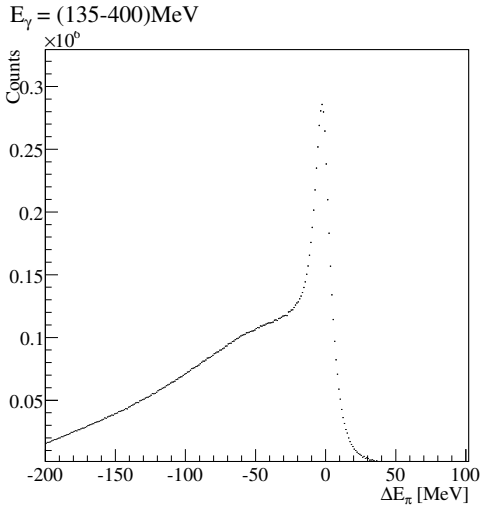

(b) Pion missing energy for ^{40}Ca data

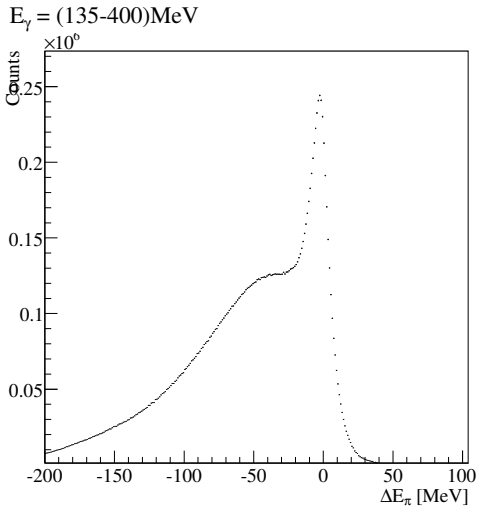

(c) Pion missing energy for ^{16}O data

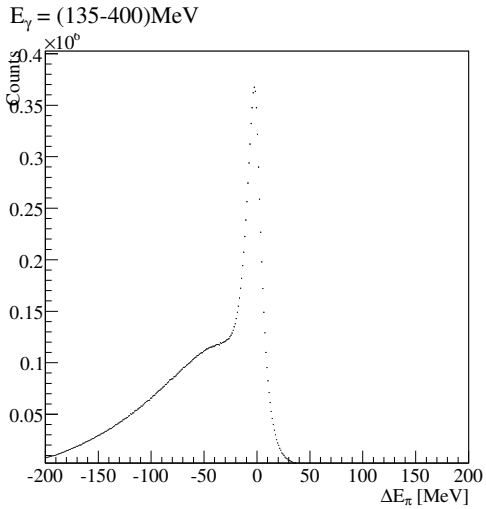

(d) Pion missing energy for ^{12}C data

Figure 5.20:

Our existing knowledge of the general features of the coherent and incoherent cross sections can be used to guide the fitting procedure. For example, it is known that the coherent cross section is forward peaked due to its scaling with the square of the matter

form factor. This is in contrast to the combined incoherent processes which vary much more slowly with pion emission angle [23]. As a result, for coherent θ_π regions, the pion missing energy spectrum can be completely dominated by the coherent peak and it is therefore possible to exclusively determine the width and position of the missing energy distribution for the coherent process. This information can then be used for the fits in regions where there is a larger incoherent contribution to the pion missing energy.

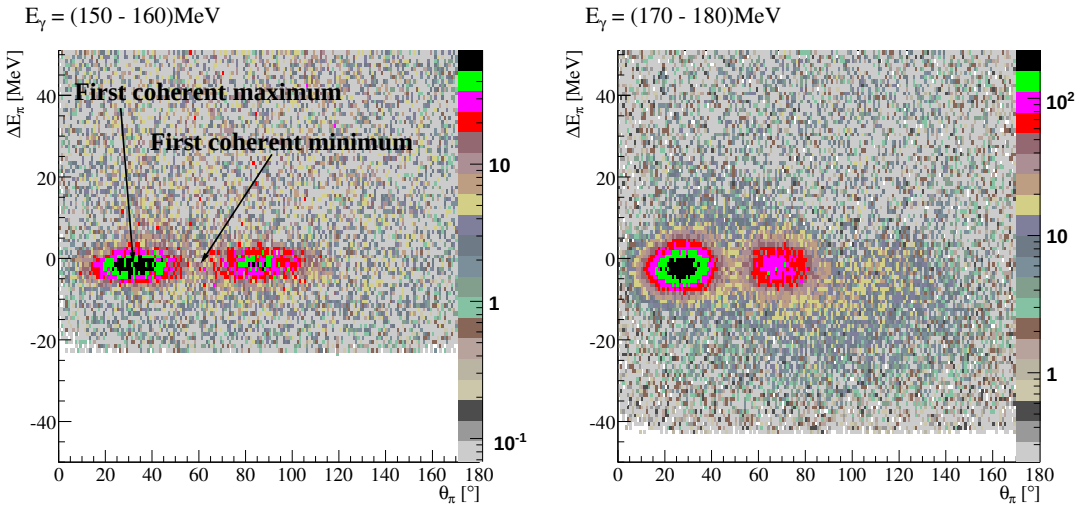

(a) (b)

Figure 5.21: ^{208}Pb data. Pion missing energy vs pion polar angle. The diffraction structure in the differential cross section is evident in the angular distribution.

The fitting procedure employed to extract the yield of the coherent process from the data is outlined below:

1. 2D spectra of pion missing energy versus pion angle were accumulated for E$_\gamma$=(135-300) MeV (examples are given in figure 5.21).

2. These 2D spectra were then projected along the y axis into individual 1D pion missing energy spectra in as small angular bins as permitted by the statistical accuracy of the data. The θ_π bin size ranged from 1° to 5°.

3. To sample the shape of the coherent peak (its width and position), either a single Gaussian or the upper half of a Gaussian was fitted to the 1D pion missing energy spectra for θ_π regions corresponding to the coherent maximum. For example between θ_π = (24-36)° in figure 5.21(b).

4. With the width and position of the coherent Gaussians constrained from the process described in (3), a second iteration of fits was performed for all pion missing energy spectra including additional functions to fit the non-coherent background.

During the second iteration of fits each 1D spectrum was fitted with one of three functions corresponding to coherent alone (5.19), coherent plus a Fermi function (5.20) and coherent plus incoherent plus a Fermi function (5.21):

$$f(x) = \frac{A_1}{\sqrt{2\pi}\sigma} e^{-\frac{(x-x_c)^2}{2\sigma^2}} \tag{5.19}$$

$$f(x) = \frac{A_1}{\sqrt{2\pi}\sigma} e^{-\frac{(x-x_c)^2}{2\sigma^2}} + \frac{H\sigma\sqrt{2\pi}}{1+e^{\frac{2.4(x-x_c+E_{av})}{\sqrt{2}\sigma}}} \tag{5.20}$$

$$f(x) = \frac{A_1}{\sqrt{2\pi}\sigma} e^{-\frac{(x-x_c)^2}{2\sigma^2}} + \frac{A_2}{\sqrt{2\pi}\sigma} e^{-\frac{(x-x_c+E_{ex})^2}{2\sigma^2}} + \frac{H\sigma\sqrt{2\pi}}{1+e^{\frac{2.4(x-x_c+E_{av})}{\sqrt{2}\sigma}}} \tag{5.21}$$

where A_1 = area of the first Gaussian.
A_2 = area of the second Gaussian.
σ = width of Gaussians.
x_c = coherent peak offset from zero.
E_{ex}= energy of first excited state of nucleus e.g. 4.4MeV for ^{12}C.
E_{av}= average q-value required for neutron/proton knockout.
H = height of the Fermi function.

In all three functions, the coherent contribution is accounted for by a Gaussian function. The Gaussian shape of the coherent contribution was confirmed by fits in the regions of θ_π and E_γ where the coherent process dominates.

In equation 5.20 the quasi-free background is fitted with a Fermi function and in equation 5.21 the quasi-free plus incoherent background is approximated by a Fermi function plus a Gaussian respectively. The Fermi function represents the fall off of the distribution from the quasi-free process below its average threshold energy, E_{av} due to the experimental resolution (table 5.1). The second Gaussian fit in function 5.21 contains an offset, E_{ex}, at the energy of the first excited state of the nucleus under study. The analysis of the coincident nuclear decay photons (Appendix D) suggest dominant populations of only the lower lying excited states for the reactions on the light targets and tend to indicate less relative incoherent strength for the heavier targets.

The widths and positions of the coherent Gaussians were constrained according to the first iteration of fits where no attempt was made to fit the background. The fitted widths from the data (σ) give good agreement with the widths extracted from

the Geant3 simulated data which included the experimental resolution of the incident and detected photons. These comparisons are shown in figure 5.22 and give improved confidence in the validity of the fitting procedure. For more details of the simulation see section 5.8.

The coherent π^0 yield for each E_γ, θ_π bin was then taken as the fitted area of the Gaussian associated with the coherent peak (A_1). The error in A_1 is given by the results of the fit. Table 5.2 lists the functions used to fit the data for each incident photon energy bin. Given the small energy gaps between the first excited state of a nucleus and its ground state, it is clearly a difficult task to cleanly separate coherent and incoherent events from fits to the missing energy spectra, especially at higher energies as the absolute energy resolution of the detector worsens and for heavier targets where the first excited state is very close to the ground state. Because of this, fit function 5.21 was only applied to the lighter targets.

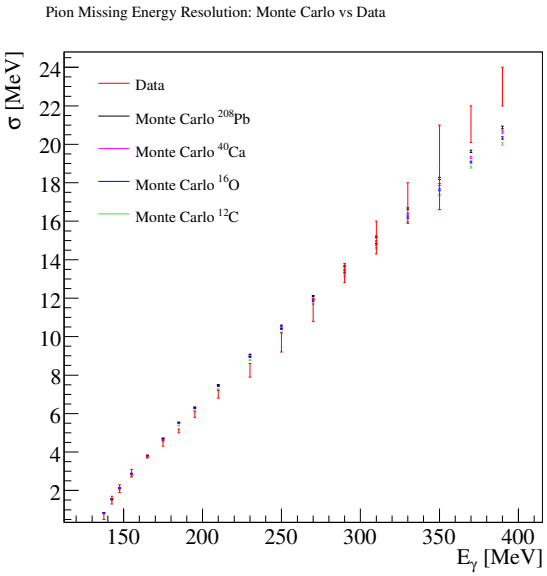

Figure 5.22: The simulated pion missing energy peaks were fitted with a Gaussian to extract the width which was averaged over all pion angles. The red markers correspond to the width of the Gaussian fitted to the pion missing energies (from the experimental data) in the coherent maxima. The widths are averaged over all pion angles and the error bars give the spread between targets.

5.7.2 ^{208}Pb

The ^{208}Pb data would be expected to be the simplest case of the 4 targets to extract the coherent strength as the A^2 factor in the cross section gives an expectation of the largest relative contribution from coherent events. It was found that attempting to

Table 5.2: Pion Missing Energy Fitting Methods

E_γ (MeV)	^{208}Pb	^{40}Ca	^{16}O	^{12}C
140-145	5.19	5.19	5.19	5.19
145-150	5.19	5.19	5.19	5.19
150-160	5.19	5.19	5.19	5.19
160-160	5.20	5.21	5.21	5.21
170-160	5.20	5.21	5.21	5.21
180-160	5.20	5.21	5.21	5.21
190-200	5.20	5.21	5.21	5.21
200-220	5.20	5.21	5.21	5.21
220-240	5.20	5.21	5.21	5.21
240-260	5.20	5.21	5.21	
260-280	5.20		5.21	
280-300	5.20			
300-320	5.20			

fit the incoherent contribution from low lying excited states made little difference to the extracted cross section (an example is shown in figure 5.25). For the final analysis this was therefore neglected. Fitting the quasi-free background is however necessary as can be seen in figure 5.24(b). Below E_γ=160 MeV the contribution from background processes was small and the data were well described by function 5.19.

At photon energies greater than 160 MeV an increased background was observed in the pion missing energy spectra and it was appropriate to account for this in the fitted function. The entire data set above E_γ=160 MeV was therefore fitted with function 5.20 i.e. a Gaussian fitted to the coherent peak and a Fermi function to approximate the slowly increasing quasifree processes. Examples of the ^{208}Pb fits are shown in figures 5.23 and 5.24.

5.7.3 ^{40}Ca, ^{16}O and ^{12}C

For the lighter targets the A^2 dependence of the coherent cross section gives expectation that the relative contribution of incoherent to coherent events may be increased compared to ^{208}Pb. Clear evidence of this can be seen in the pion missing energy spectra for ^{40}Ca, ^{16}O and ^{12}C shown in figures 5.28 to 5.30 where function 5.20 can be seen to no longer provide a good description of the shape of the data. For these nuclei function 5.21 was used to fit the data. This function includes a second Gaussian to account for the pion missing energy contribution where the nucleus is left in its

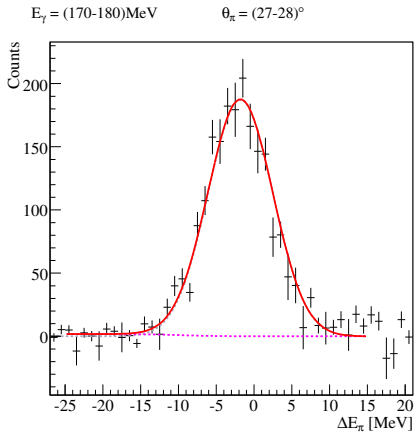

(a) Example of pion missing energy spectrum in the coherent maximum.

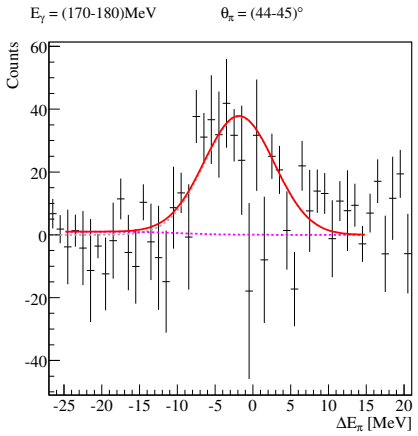

(b) Example of pion missing energy spectrum in the coherent minimum.

Figure 5.23: ^{208}Pb data

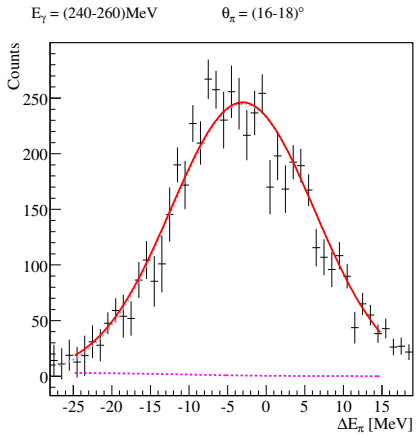

(a) Example of pion missing energy spectrum in the coherent maximum.

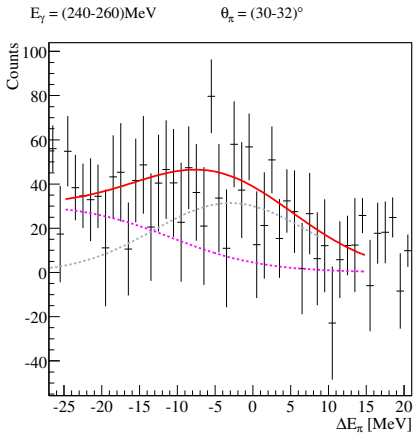

(b) Example of pion missing energy spectrum in the coherent minimum.

Figure 5.24: ^{208}Pb data

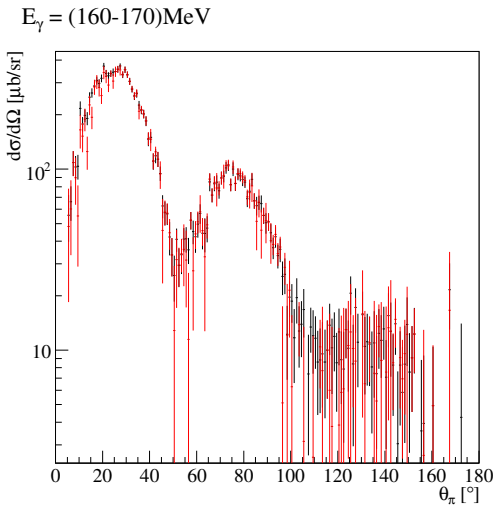

Figure 5.25: ^{208}Pb data. Black markers: cross section where equation 5.20 was fitted to the pion missing energy. Red markers: cross sections where equation 5.21 was fitted.

first excited state. The stronger role of incoherent events is also suggested from the preliminary nuclear decay gamma analysis (appendix D) where the first excited states for all three lighter nuclei appears to be the most strongly excited and appears more prominentley than in ^{208}Pb.

While for ^{208}Pb the cross sections suffer only small variations depending on what function is fitted (figure 5.25), for the lighter nuclei the choice of function is more important. Figures 5.26 and 5.27 show the effect of changing the fitted function on the calcium and oxygen cross sections. In this case, fitting function 5.21 to account for incoherent strength to the lowest states brings out features of the diffraction pattern not present in the simpler fits. The fitted function also looks to have a better agreement with the pion missing energy spectra (figures 5.28 and 5.29). For certain spectra, the more complicated fits were not well constrained by the low statistics in the diffraction minima and because of this satisfactory fits were not possible. These cases are illustrated in the results presented in the next chapter.

The ^{16}O data have an added complication in that for certain combinations of photon energy and pion angle a peak was observed at negative missing energy values, attributable to π^0 production from the hydrogen in the H_2O target (figure 5.31). Since the coherent cross section scales approximately with A^2, it is clear that the pion yield will be dominated by those produced on oxygen. However, it is also possible to exploit the reaction kinematics to enhance the contributions from events originating on ^{16}O. For example, a neutral pion produced coherently on oxgen and detected at a particular angle will have a different energy than one produced by the same photon on hydrogen and detected at the same angle. This is demonstrated in figure 5.32. The energy dif-

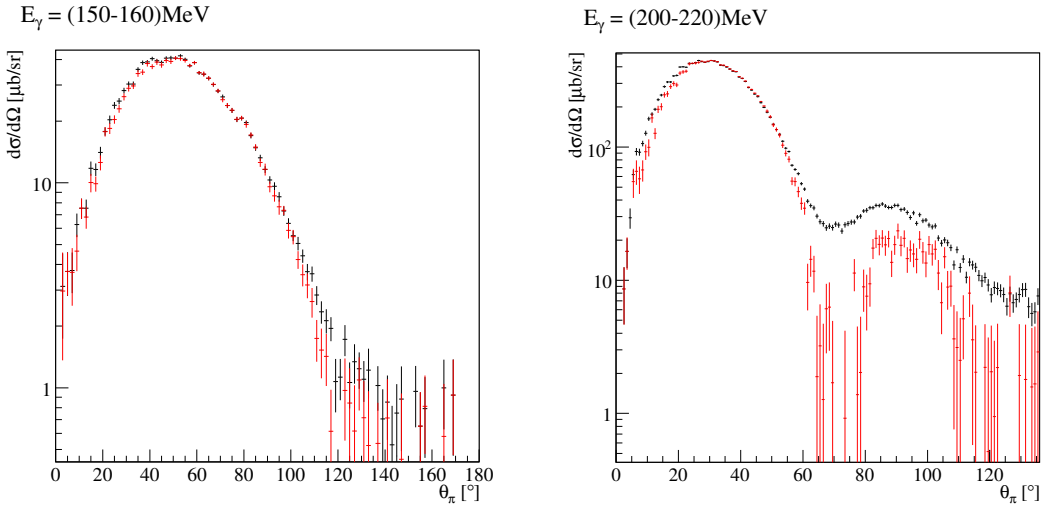

(a) (b)

Figure 5.26: ^{40}Ca data. Black markers: cross section where equation 5.20 was fitted to the pion missing energy. Red markers: cross sections where equation 5.21 was fitted.

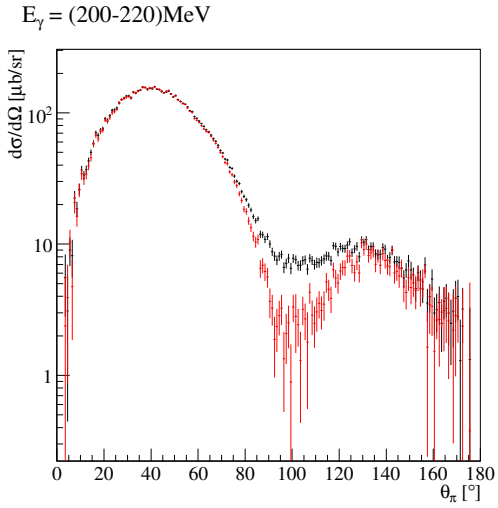

Figure 5.27: ^{16}O data. Black markers: cross section where equation 5.20 was fitted to the pion missing energy. Red markers: cross sections where equation 5.21 was fitted.

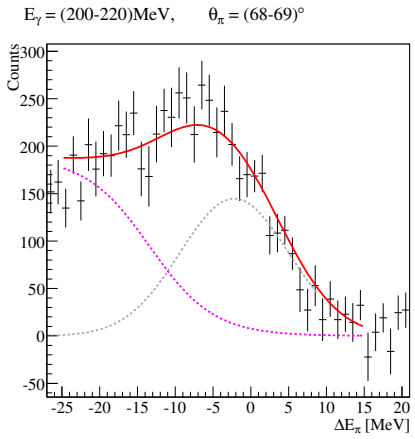

(a) Example of pion missing energy in the coherent minimum where a single Gaussian plus a Fermi function were fitted (i.e. equation 5.20)

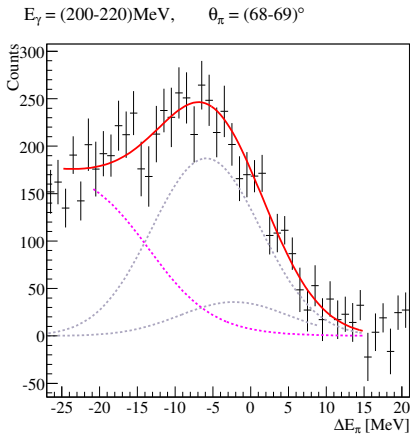

(b) Example of pion missing energy in the coherent minimum where 2 Gaussians plus a Fermi function were fitted (i.e. equation 5.21)

Figure 5.28: ^{40}Ca data.

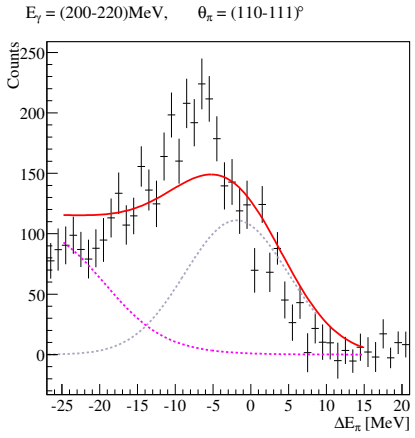

(a) Example of pion missing energy in the coherent minimum where a single Gaussian plus a Fermi function were fitted (i.e. equation 5.20)

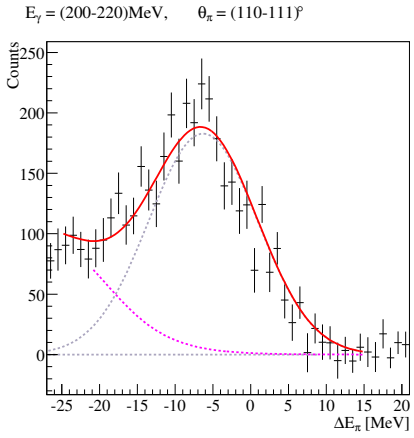

(b) Example of pion missing energy in the coherent minimum where 2 Gaussians plus a Fermi function were fitted (i.e. equation 5.21)

Figure 5.29: ^{12}C data.

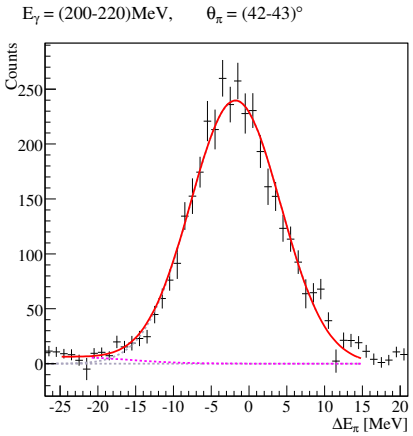

(a) Example of pion missing energy in the coherent maximum.

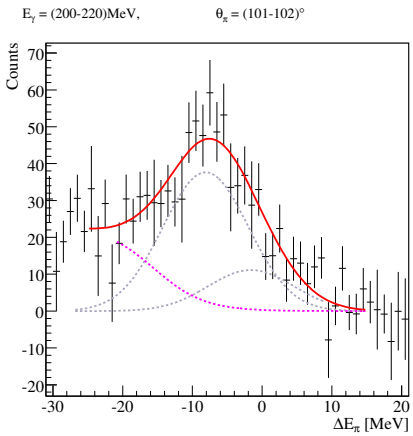

(b) Example of pion missing energy in the coherent minimum.

Figure 5.30: ^{16}O data.

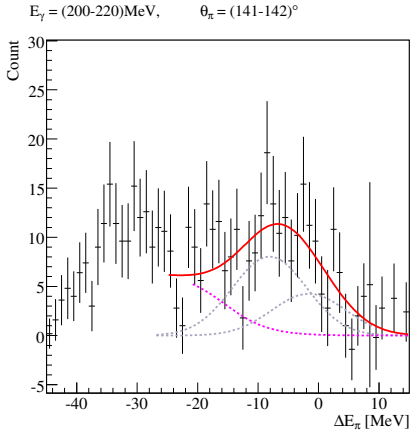

Figure 5.31: ^{16}O data. Hydrogen peak at ΔE_π = -35 MeV

ference is small at forward angles and is generally larger than the energy resolution of the detector. At the higher photon energies and at forward angles the hydrogen contribution is likely to be difficult to separate. However, away from these regions good separation is expected. When the Hydrogen peak fell within the range of the fit, it was fitted with the same background function as the rest of the data i.e. function 5.21.

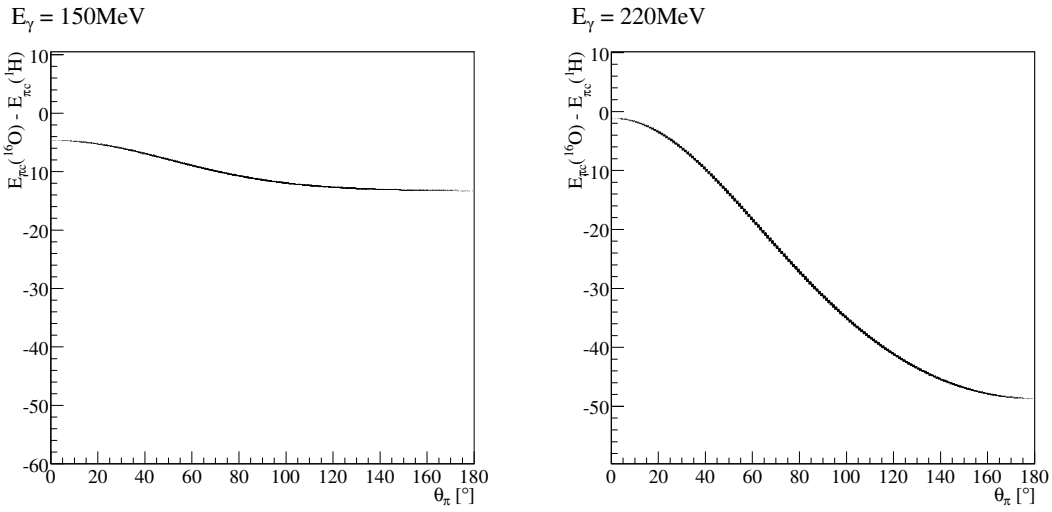

(a) (b)

Figure 5.32: Calculations of the difference betweeen the centre of mass pion energy of a pion produced coherently on oxygen and one produced on hydrogen from the same energy photon and detected at the same pion angle.

5.8 π^0 Detection Efficiency

Monte Carlo simulations are vital in the analysis and understanding of data from complex nuclear and particle physics experiments. Geant3 [87] is a Monte Carlo package that provides Fortran routines for tracking particles through detectors in order to simulate the detector response. For this analysis, a Geant3 Monte Carlo simulation [88] was used to calculate the efficiency of the experimental setup as a whole for detecting neutral pions. Figure 5.33 shows the geometry of the Crystal Ball and TAPS system as programmed in the simulation.

26 million A(γ,π^0)A events with a phase space distribution of energy and momenta between the π^0 and the recoiling nucleus were simulated for each target covering the energy range E$_\gamma$ = (135-400) MeV. The simulated data were then run through the same analysis code as the real data. Figure 5.34 shows the good agreement between

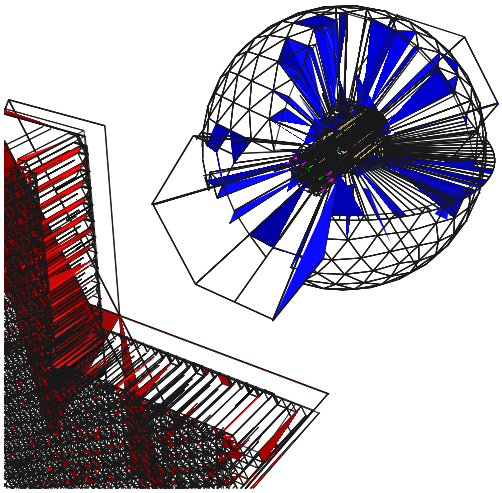

Figure 5.33: Crystal Ball and TAPS geometry in the Geant3 Monte Carlo simulation.

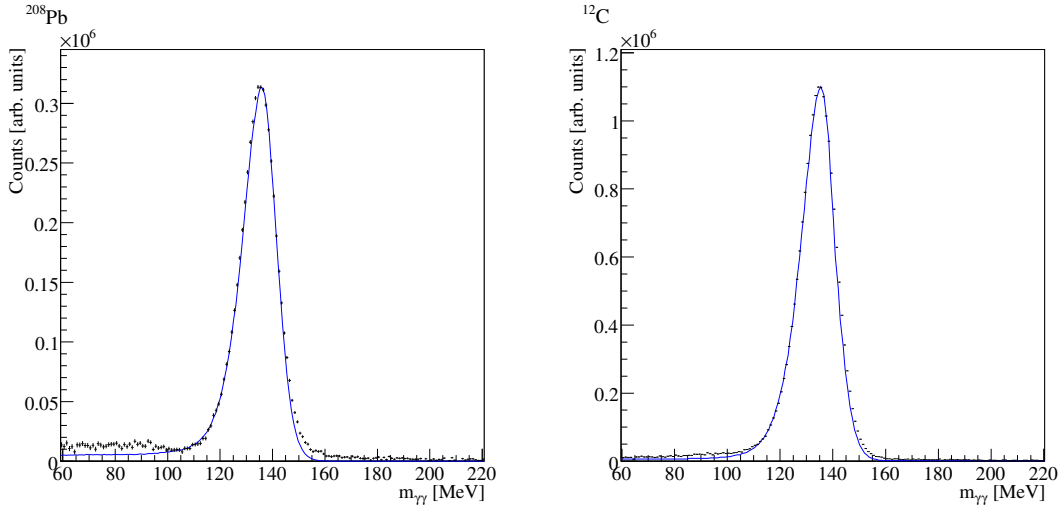

(a) ^{208}Pb (b) ^{40}Ca

Figure 5.34: Data compared with the monte carlo simulation.

the simulated and real data for the π^0 invariant mass peaks. For each E_γ, θ_π bin, the π^0 detection efficiency was calculated as:

$$\epsilon_{det}(E_\gamma, \theta_\pi) = \frac{No\ \pi^0 s\ detected\ in\ that\ E_\gamma, \theta_\pi\ bin}{No\ \pi^0 s\ thrown\ in\ that\ E_\gamma, \theta_\pi\ bin} \tag{5.22}$$

A selection of the pion detection efficiencies as a function of E_γ and θ_π for each of the targets is shown in figure 5.35. At higher energies as the opening angle between the π^0 decay photons decreases, it becomes increasingly likely that both π^0 photons will go into TAPS. With TAPS removed from the analysis because of the presently unresolved issues with the readout electronics (section 5.6.2) it is not surprising that the detection efficiencies drop to zero at the most forward angles. The detection efficiencies for ^{208}Pb are at most 20% lower than the highest efficiencies (for ^{12}C) and this can be explained by the significant rise of photon interactions in the target because of the high density and atomic number of lead. The effect is exacerbated for $\theta_\pi = 90°$ as this presents the largest path length for the decay photons in the target material.

5.9 Tagging Efficiency

An accurate deterimination of the photon flux incident on the target is needed to normalise the π^0 yield into a cross section. This incident flux is inferred from the number of electrons detected in the photon tagger. For each tagger channel the number of electron hits is recorded by the tagger scalers. This number must be adjusted, to account for the photons subsequently removed from the beam by the collimator. This correction is known as the tagging efficiency.

As has been noted the photon beam tagging efficiency was measured in separate data runs with a lower beam intensity (section 4.4). A separate tagging efficiency was measured for each target. This is presented as a function of tagger channel (effectively photon energy) in figure 5.36. At most the spread in tagging efficiency over the entire beam period was ∼2%. Theses small variations are likely due to slight variations in electron beam divergences or alignment.

5.10 Cross Section Calculations

At its most basic, the cross section of a reaction A(a,b)B is given by:

$$\sigma = \frac{N_b}{N_a N_A} \tag{5.23}$$

where N_b is the number of particles emitted, N_a the number of particles incident per unit area and N_A the number of target nuclei visible to the beam. The differential cross

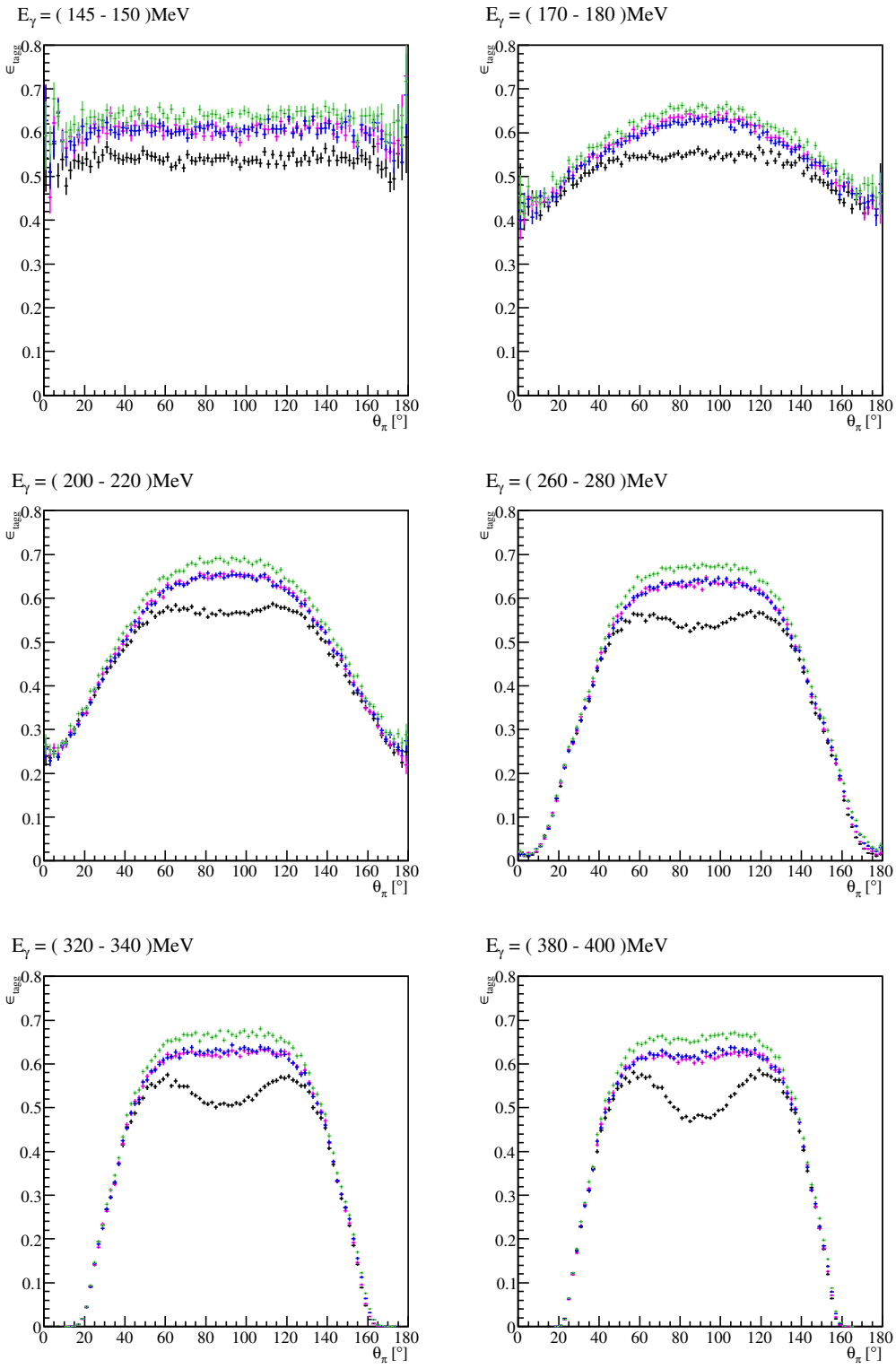

Figure 5.35: Dependece of π^0 detection efficiencies on incident photon energy and π^0 emission angle. Detection Efficiencies: black markers are ^{208}Pb, pink markers are ^{40}Ca, blue markers are ^{16}O, green markers are ^{12}C.

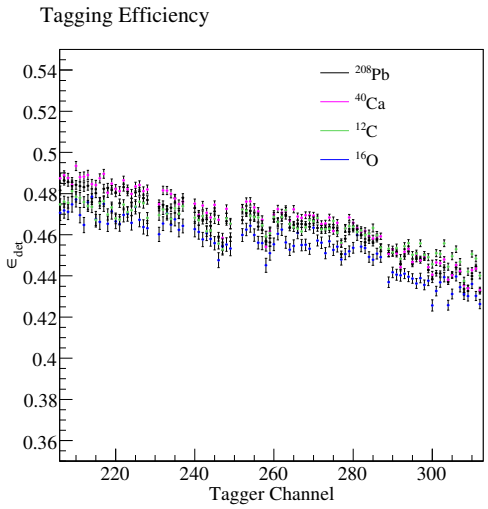

Figure 5.36: Tagging Efficiencies as a function of tagger channel. Channel 206 corresponds to a photon energy of 400 MeV, channel 312 corresponds to a photon energy of 135 MeV.

section is then the derivative of σ with respect to solid angle. For this experiment, N_a corresponds to the π^0 yield and N_b the incident photon flux. N_a is thus the π^0 yield as calculated in section 5.7 corrected with the π^0 detection efficiency from section 5.8. N_b is the number of hits in the tagger scalers corrected with the tagging efficiency from section 5.9.

So the differential cross section for a given photon energy and pion angle in terms of measured quantities becomes:

$$\frac{d\sigma}{d\Omega} = \frac{N_{\pi^0}}{\epsilon_{tagg}\epsilon_{det}N_s\rho\Omega\Gamma_{\gamma\gamma}} \tag{5.24}$$

where N_{π^0} = number of π^0 s detected in that E_γ, θ_{π^0} bin.
ϵ_{tagg} = tagging efficiency for that E_γ bin.
ϵ_{det} = pion detection efficiency for that E_γ, θ_{π^0} bin.
ρ = target density [nuclei/cm^2].
N_s = number of tagger scalers in that E_γ bin.
Ω = $\int_{\phi_1}^{\phi_2}\int_{\theta_1}^{\theta_2} d\phi sin\theta d\theta$ [sr].
$\Gamma_{\gamma\gamma}$ = branching ratio of the decay.

5.11 Error Evaluation

This section will outline the sources of statistical and systematic errors in the measured cross sections and include estimates of the total magnitude where appropriate.

5.11.1 Statistical Uncertainties

There are 3 sources of statistical error in the cross section calculations described in the previous section:

- The statistical error associated with determining the number of π^0 events in each E_γ, θ_π bin.
- The statistical error arising from the attainable event sample simulation of the detection efficiency.
- The error associcated with the tagging efficiency measurements.

For all three of these cases, the statistical error simply reflects the fact that the experiment is measuring a probability. As such, as the number of measurements increases, the statistical error decreases following Poisson statistics. The first error has the largest contribution. The number of coherent π^0s for any E_γ, θ_π bin was taken from a fit to the pion missing energy spectra in which each data point has a statistical error arising from the number of π^0 events detected and also the statistical accuracy of the tagger random subtraction (section 5.2.2) used in the photon energy selection. The π^0 detection efficiency was calculated from a Monte Carlo simulation. The number of events simulated was chosen to keep the statistical error for ϵ_{det} at $\sim$1%. The statistical uncertainty in the tagging efficiency for each individual tagger channel is also $\sim$1% for all targets.

5.11.2 Systematic Uncertainties

The largest systematic uncertainties in the current measurements arise from:

- The uncertainty in the target surface density.
- Systematics arising from the ΔE_π fitting procedure.

The first of these is simple to calculate from the uncertainty in the measurement of the target thickness. This is $\sim$5% for both ^{40}Ca and ^{12}C, $\sim$1% for ^{16}O and $\sim$2% for ^{208}Pb.

It is more difficult to quantify the systematic error arising from the pion missing energy fitting procedure. A simple method to test the stability of the fits is to vary the fitting constraints within reasonable limits and observe the effect on the extracted cross sections. For the fitting procedure described in section 5.7.1, the widths of the Gaussians and Fermi functions fitted were allowed to vary within the limits shown as red error bars in figure 5.22. These widths were shown to be in good agreement with the simulated data. The largest difference between the widths fitted for the

experimental data and the simulated data was ∼10%. As a conservative estimate of the systematic error associated with constraining the fitted resolutions, the fitted widths were increased by 20% then decreased by 20% and the effect on the cross sections quantified.

Investigations of the effect of varying the centroid of the coherent gaussian were also carried out. For the data analysis the centroids of the coherent Gaussians were fixed at a position determined by the first iteration of fits described in section 5.7.1. A conservative estimate of the error in the determination of this position is ∼0.5 MeV indicated by the error in the centroids extracted from the fit in the coherent maxima. As such, the coherent offsets were set at 0.5 MeV higher and 0.5 MeV lower and the effect on the cross section observed. To summarise:

1. The resolutions (widths) were increased by 20% (red markers on subsequent plots).

2. The resolutions (widths) were decreased by 20% (green markers on subsequent plots).

3. The coherent peak was fixed at a pion missing energy 0.5 MeV higher than the best peak position (blue markers on subsequent plots).

4. The coherent peak was fixed at a pion missing energy 0.5 MeV lower than the best peak position (pink markers on subsequent plots).

The variation with fitting technique is small for ^{208}Pb, as illustrated by the sample figure 5.37. The height of the first maximum varies by at most ∼(3-6)% over the energy range shown. For ^{40}Ca, ^{16}O and ^{12}C the variation in height of the first maximum is slightly larger at ∼10%.

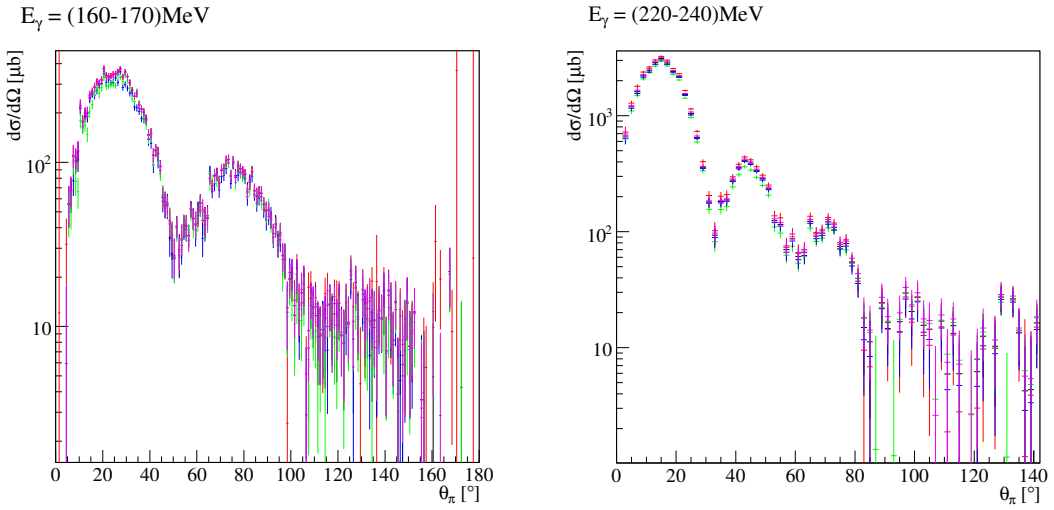

(a) (b)

Figure 5.37: ^{208}Pb data. Black markers: final cross section. Red makers: widths increased by 20%. Green markers: widths decreased by 20%. Blue markers: coherent peaks offset by +0.5MeV. Pink markers: coherent peaks offset by -0.5MeV.

Chapter 6

Results and Discussion

Presented in this chapter are the differential and total cross sections for the A(γ,π^0)A reaction on ^{208}Pb, ^{40}Ca, ^{16}O and ^{12}C. Comparisons are made between the current data and measurements by the Glasgow group using TAPS (section 2.4.1)and those by Krusche using TAPS (section 2.4.1). The data are compared with the DREN theoretical calculations by Kamalov (section 2.3.6). Some preliminary conclusions about the nature of the neutron skin on ^{208}Pb are made before an outline is presented of the future work planned to use this comprehensive new data set for a full extraction of the matter distribution.

6.1 Comparison to Previous Data and Theory

The new data are compared to the previous data taken with TAPS which is described in section 2.4.1. As already discussed the data are unpublished and the analysis was affected by strong angle dependent variations in the π^0 detection properties of the apparatus which led to systematic effects in the extracted coherent strength which were difficult to predict. However, the Glasgow TAPS data remain the best available previous measurement of the coherent process. The symmetric composition of the Crystal Ball crystals means the problems suffered by TAPS are negligible in the present data. Furthermore, the π^0 detection efficiency of the CB detector setup is increased by a factor of $\sim$25 compared to TAPS (for example compare figure 5.35 to figure 2.13).

The data will be compared to the DREN calculations of the coherent π^0 photoproduction process (described in section 2.3.6). The calculations are not yet available folded with the experimental resolutions but presently these effects are being included in the theoretical predictions and will be available for use in the later final extraction of the ^{208}Pb matter radius based on the data set presented in this thesis. It is expected that the main effect of this smearing will be a filling in of the predicted minima in

the theoretical predictions, particularly the steep minima in the cross section at higher energies.

The differential and total cross sections for the 4 targets are presented in figures 6.1 - 6.28. The data have been split into a range of incident photon energy (E_γ) bins ranging in width from 5 MeV to 20 MeV and the cross sections are presented on both a linear (upper) and log (lower) scale. The present data are overlayed with the appropriate Glasgow TAPS results when available (red markers) as well as the appropriate DREN calculation (blue line). The Krusche TAPS data covers a higher incident photon energy range and as such there is only one overlapping energy bin at E_γ = 200 MeV and this comparison is presented in section 6.2.2.

6.1.1 ^{208}Pb

Total Cross Section

The total cross section (figure 6.1) rises rapidly from the reaction threshold and reaches a maximum near E_γ=220 MeV. The shape of the new data is similar to the Glasgow TAPS data, although the new data show cross sections ∼10-15% higher than the previous measurement. At incident photon energies greater than 180 MeV there is some discrepency in the total cross section with the Glasgow TAPS data which are ∼25% lower than the current data.

The present data are described well by the DREN calculation over the entire E_γ range - at most the discrepency between theory and experiment is ∼10% at E_γ = (220-240) MeV. This suggests that the treatment of the pion photoproduction process and the pion FSI are well under control in the theory. At E_γ = 300 MeV there is a difference of almost an order of magnitude between the PWIA calculation (i.e. where there are no FSI effects included in the calculation) and the DREN calculation (the full model). This highlights the strong FSI effects as the outgoing π energy increases, but illustrates the smaller role of distortions in the E_γ <200 MeV range. The difference between the DREN and the DWIA indicates the importance of a detailed treatment of effects arising from the production and propagation of the Δ in the nucleus particularly at the higher incident photon energies. It is also clear that there is better agreement between the present data set and the theory than between the TAPS data and the model.

Differential Cross Sections

The differential cross sections (figures 6.2 - 6.8) have a diffraction pattern structure of maxima and minima due to the presence of the matter form factor in the cross section. In the lowest energy bins a single minimum is seen, however at higher incident photon energies (E_γ >160 MeV), the accessible momentum transfers to the nucleus

become sufficient to see higher order minima in the form factor. For a derivation of the relationship between E_γ, θ_π, and the momentum transfer to the nucleus, see Appendix A. Above $E_\gamma > 240$ MeV the minima at larger pion angles become less well resolved although the first maximum and minimum are still clear and a drop of over two orders of magnitude in the cross section between $\theta_\pi = 0°$ and $\theta_\pi = 180°$ is still evident.

The Glasgow TAPS data are shown in the same figures. The new data show a significant improvement in statistics which makes possible the use of finer angular bins and expands the angular range of the data. The reduced binning will allow a more accurate determination of the diffraction minima positions. Below $E_\gamma = 180$ MeV the cross section of the Glasgow TAPS data in the first maximum is consistently higher than the new data by ∼20-28%. Also for most of the E_γ bins the apparent position of the first maximum is different in the two data sets, with the Glasgow data showing a clear tendency to have first maxima positions at lower θ_π. Similar tendencies are observed for the higher maxima. It would also appear that the first minimum of the Glasgow TAPS data is consistently shifted to smaller angles than in the present data although the larger angular bins make the determination of the minimum position more difficult.

Figure 6.9 overlays the ^{208}Pb data at $E_\gamma = 200$ MeV with the only matching Krusche TAPS cross section. The first maximum position of the Krusche data occurs ∼1.5° to the right of the current data, a shift in the opposite direction to the Glasgow TAPS data. Similar shifts appear in the first minimum. The origin of the systematic shifts in the θ_π spectrum are difficult to pin down and could arise from systematic effects in the fitting procedure, in determining the angular dependence of the π^0 detection efficiency or in the target positioning. The systematic effects in fitting the TAPS data have already been highlighted. During the TAPS experiment, the target was placed in an evacuated pipe at the centre of the particle detectors and the target position had to be measured with a ruler over a distance of around one metre. With the direct measurement and monitoring of the target position with the new data using the MWPCs (section 5.5), it is expected that the current data have smaller systematic uncertainties than the TAPS data. The new CB data also have π^0 detection efficiencies ∼25 times larger than the previous measurements.

The theoretical calculations from the DREN model are also presented in figures 6.2 - 6.8. In general, the new experimental data are well reproduced by the DREN calculations. In particular in the incident photon energy range E_γ = (160-300) MeV there is good agreement and the height of the first maximum agrees to within ∼7%. Below 160 MeV there is some discrepency in the magnitude of the cross section in first maximum which at most is ∼30% for E_γ = (145-150) MeV. The minima in the

theory tend to be deeper than observed in the data. This can at least partly be accounted for by the fact that the calculations have not yet been folded with the experimental resolutions, but could also arise due to some incoherent or quasi-free background remaining in the data.

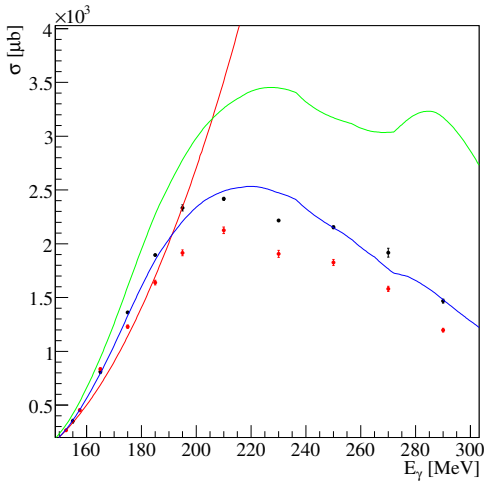

Figure 6.1: ^{208}Pb. Total cross section. Black markers: CB data. Red markers: Glasgow TAPS data. Blue Line: DREN calculation. Green line: DWIA calculation. Red line: PWIA calculation.

6.1.2 ^{40}Ca

Total Cross Section

The total coherent cross section for ^{40}Ca (figure 6.10) shares a similar overall shape as observed for ^{208}Pb. There is a fast rise in the cross section above threshold with a maximum around E_γ = 210 MeV. The new data are in good general agreement with the previous Glasgow TAPS data albeit with a cross section typically ∼10% lower.

The DREN calculation reproduces the total cross section quite well indicating the model gives a good description of the pion photoproduction process and the FSI of the outgoing pion. The largest difference between data and theory occurs at E_γ = (240-260) MeV where the DREN model overpredicts the present data by ∼10%. As with the ^{208}Pb data, the PWIA and DWIA calculations give a poor description of the data, grossly overestimating the cross sections above E_γ = 200 MeV where the effects of the pion FSI become large.

Differential Cross Sections

The differential cross sections for ^{40}Ca (figures 6.11 - 6.15) contain clear diffraction

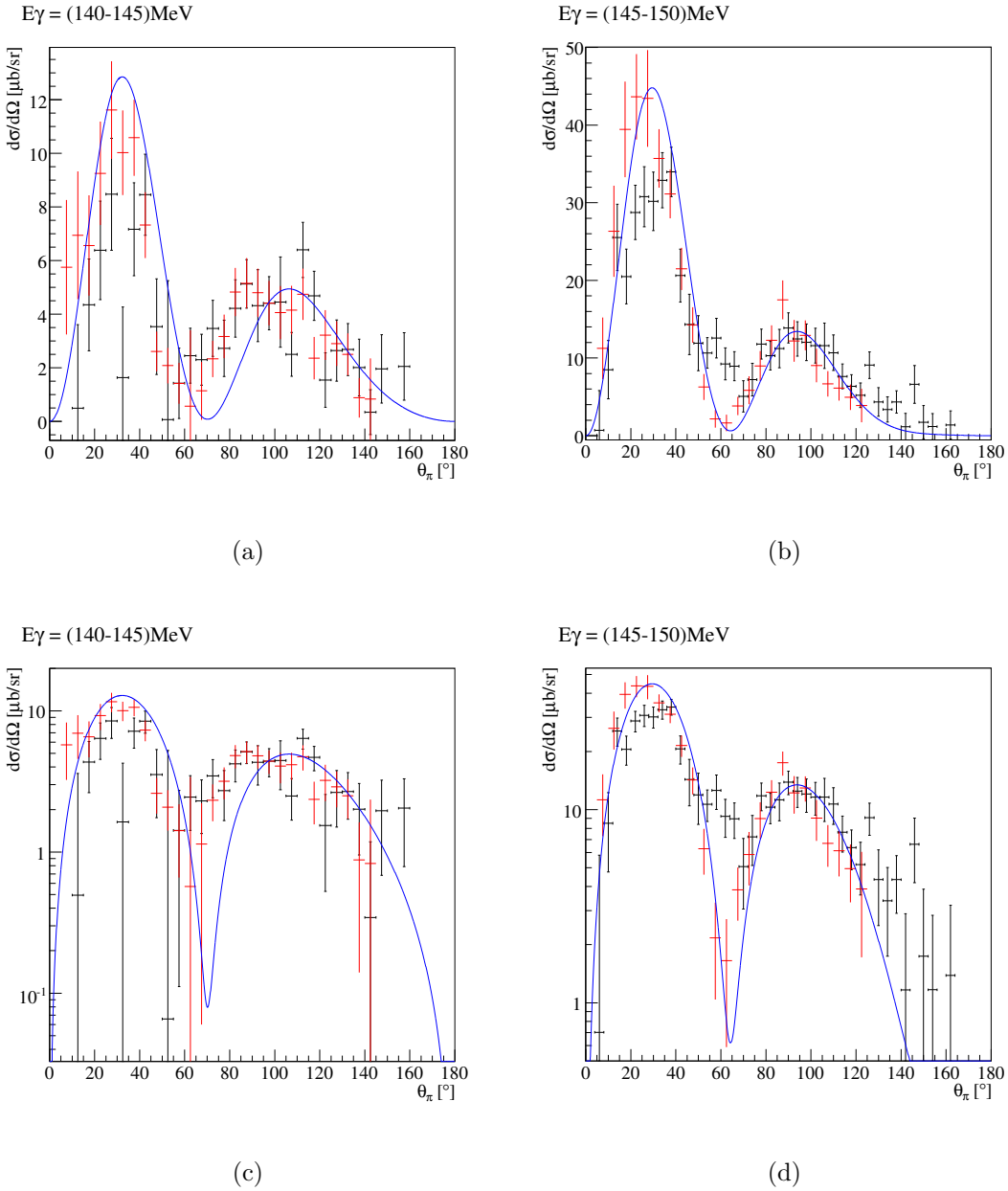

Figure 6.2: ^{208}Pb differential cross sections both on linear (a and b) and log (c and d) scales. Black markers: CB data. Red markers: Glasgow TAPS data. Blue Line: DREN calculation.

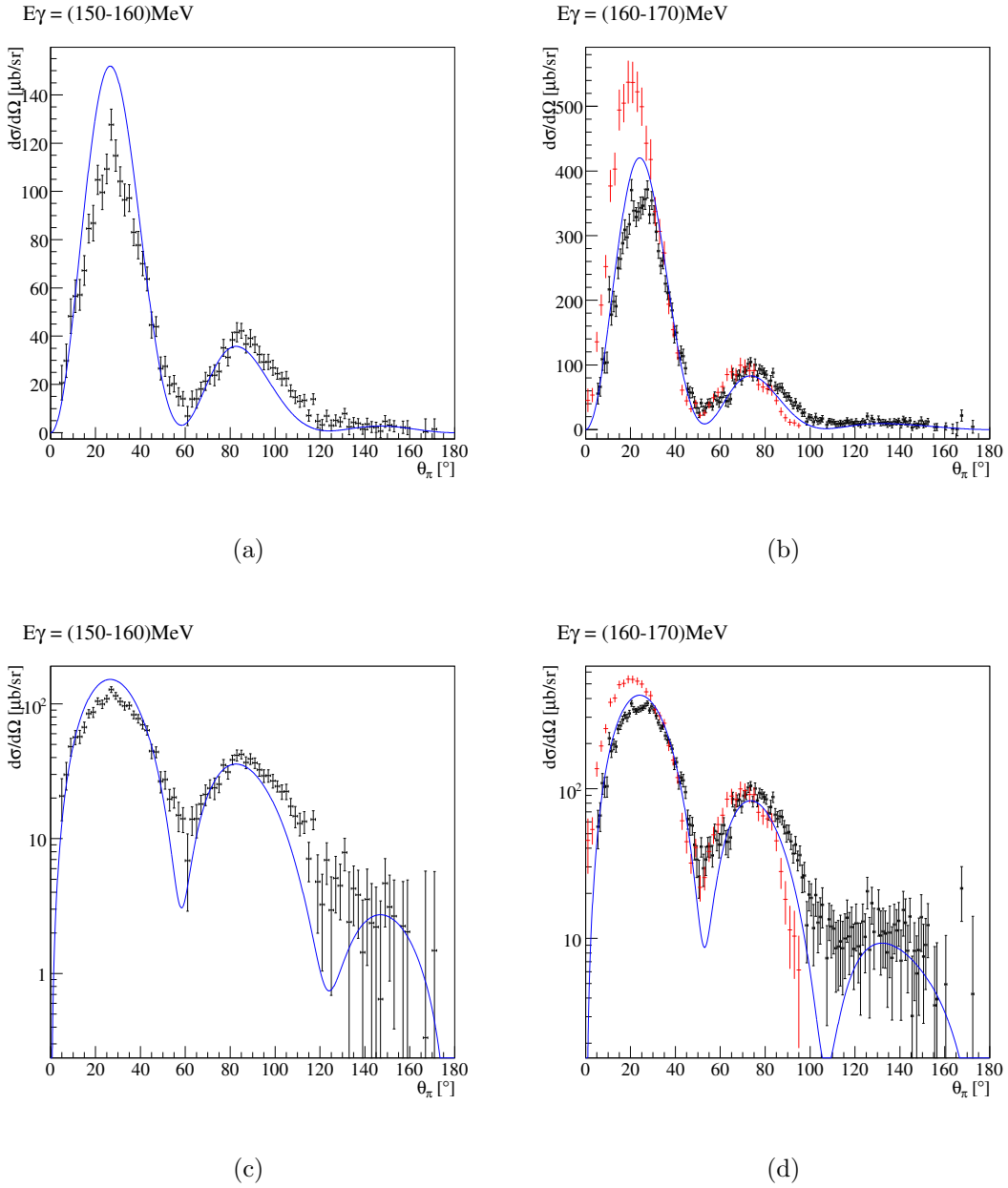

Figure 6.3: ^{208}Pb differential cross sections. Black markers: CB data. Red markers: Glasgow TAPS data. Blue Line: DREN calculation.

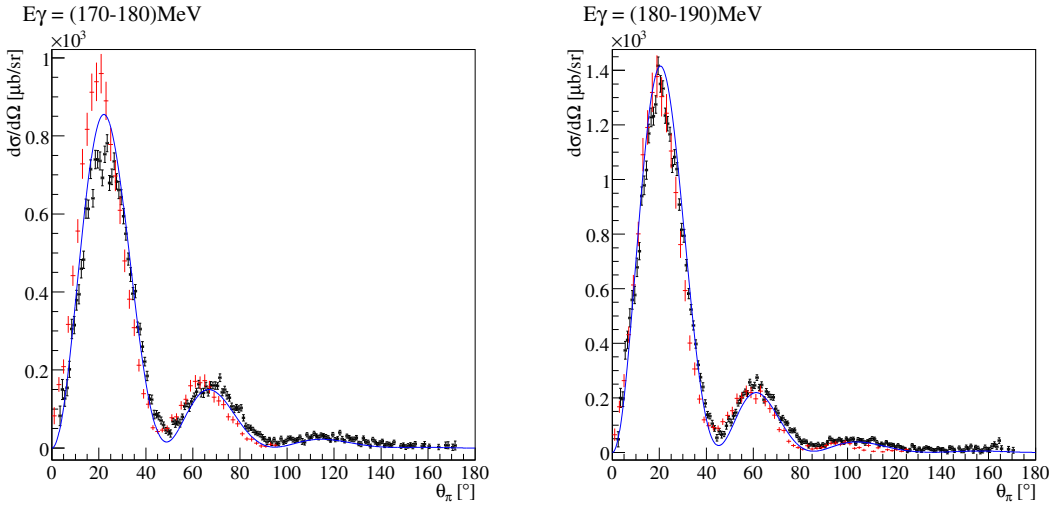

(a) (b)

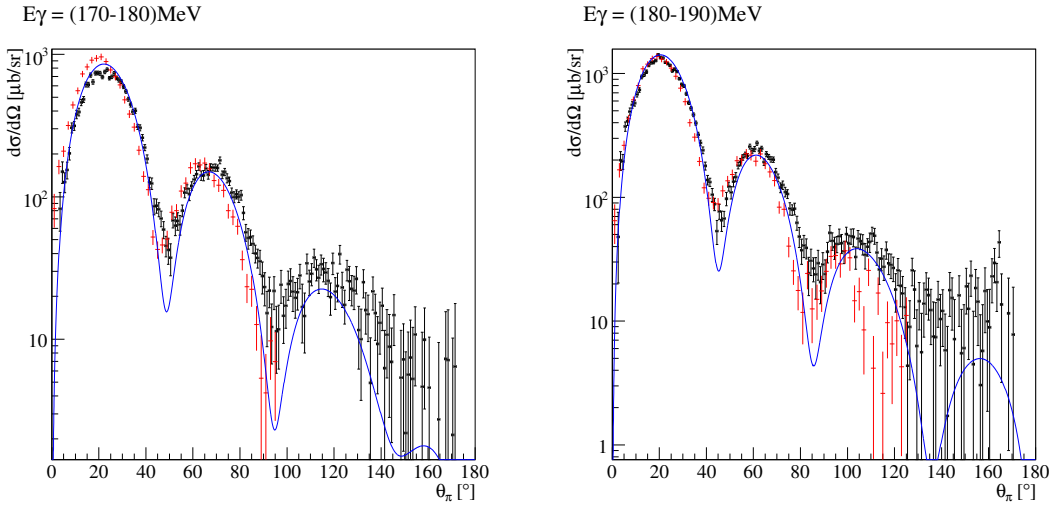

(c) (d)

Figure 6.4: ^{208}Pb differential cross sections both on linear (a and b) and log (c and d) scales . Black markers: CB data. Red markers: Glasgow TAPS data. Blue Line: DREN calculation.

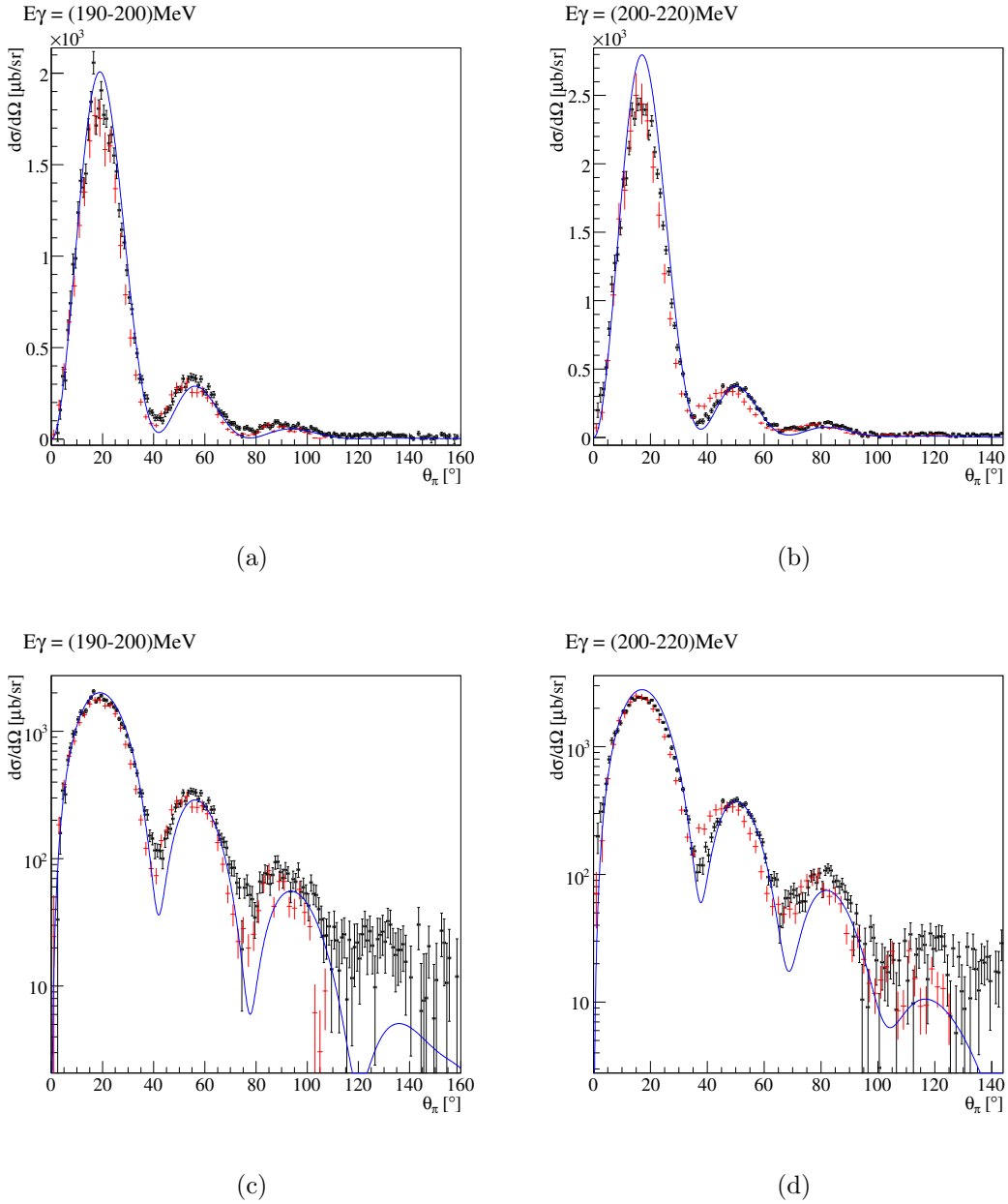

Figure 6.5: ^{208}Pb differential cross sections both on linear (a and b) and log (c and d) scales. Black markers: CB data. Red markers: Glasgow TAPS data. Blue Line: DREN calculation.

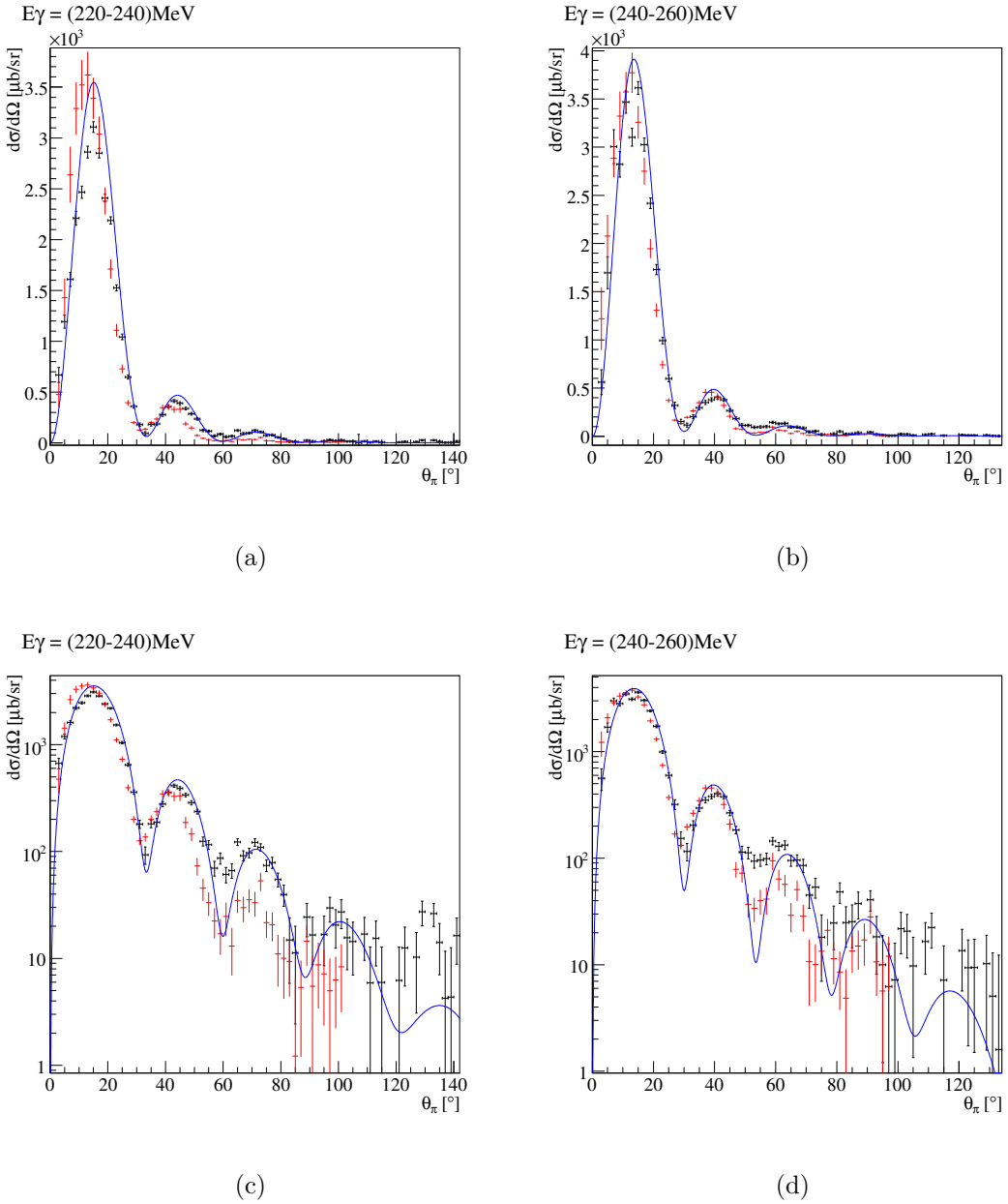

Figure 6.6: ^{208}Pb differential cross sections both on linear (a and b) and log (c and d) scales. Black markers: CB data. Red markers: Glasgow TAPS data. Blue Line: DREN calculation.

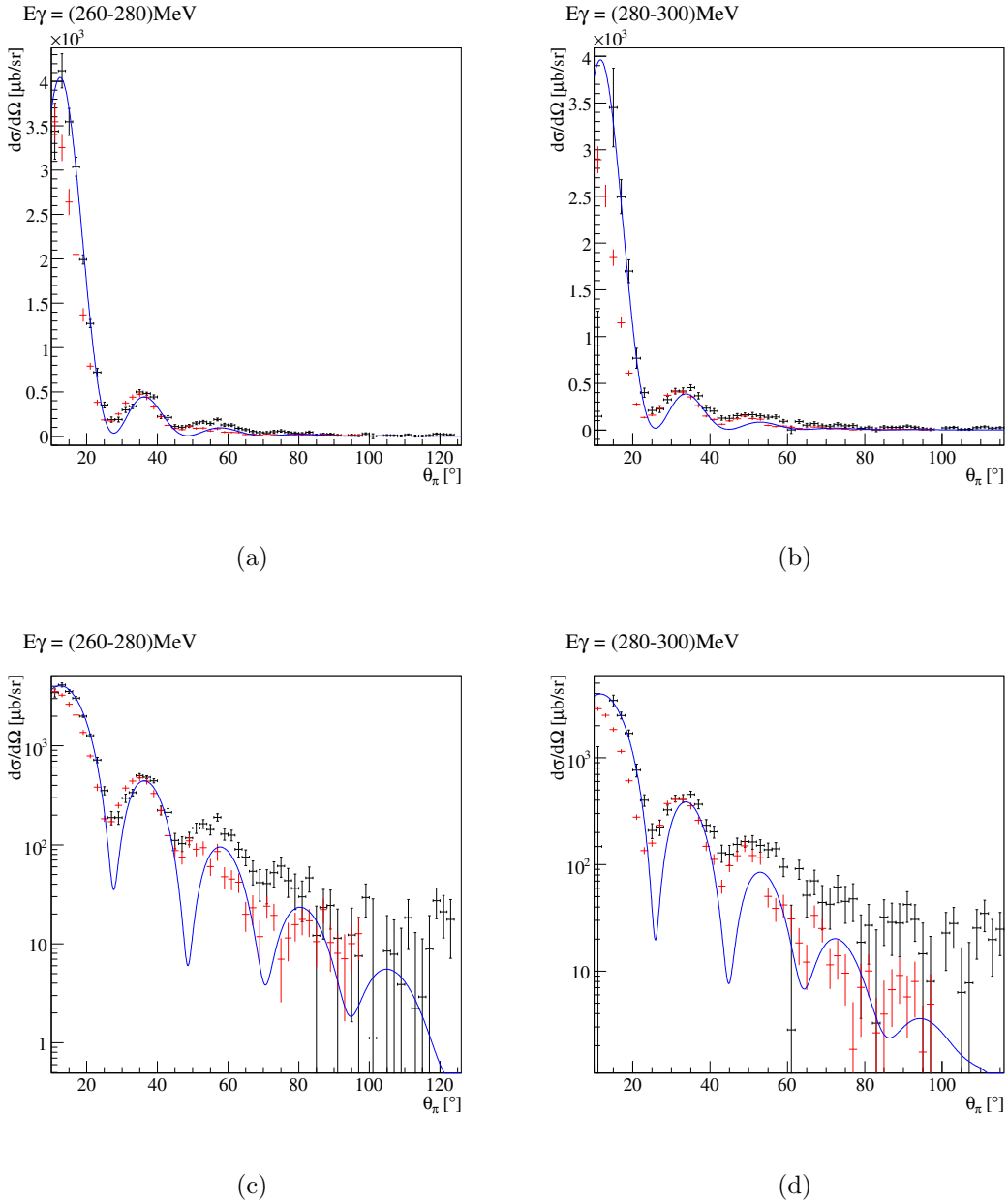

Figure 6.7: ^{208}Pb differential cross sections. Black markers: CB data. Red markers: Glasgow TAPS data. Blue Line: DREN calculation.

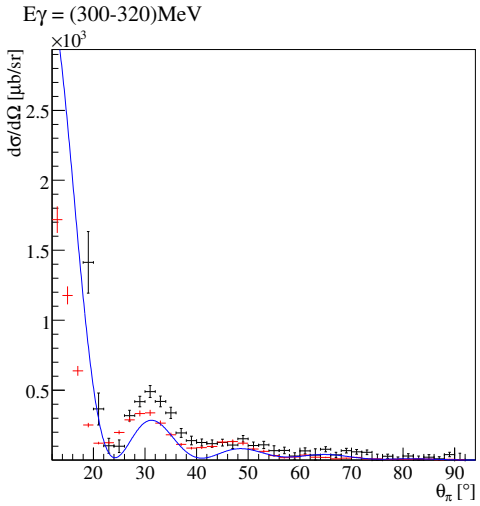

(a)

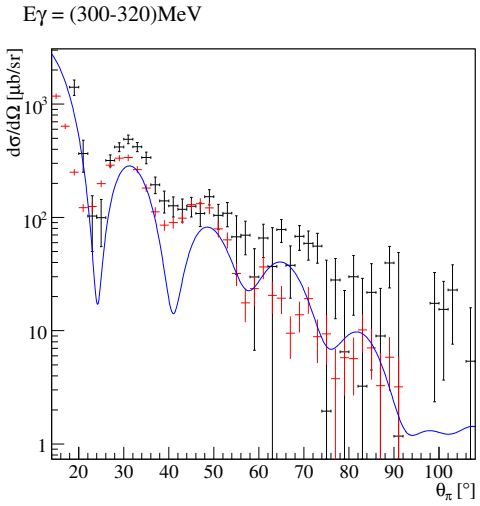

(b)

Figure 6.8: ^{208}Pb differential cross sections both on linear (a) and log (b) scales. Black markers: CB data. Red markers: Glasgow TAPS data. Blue Line: DREN calculation.

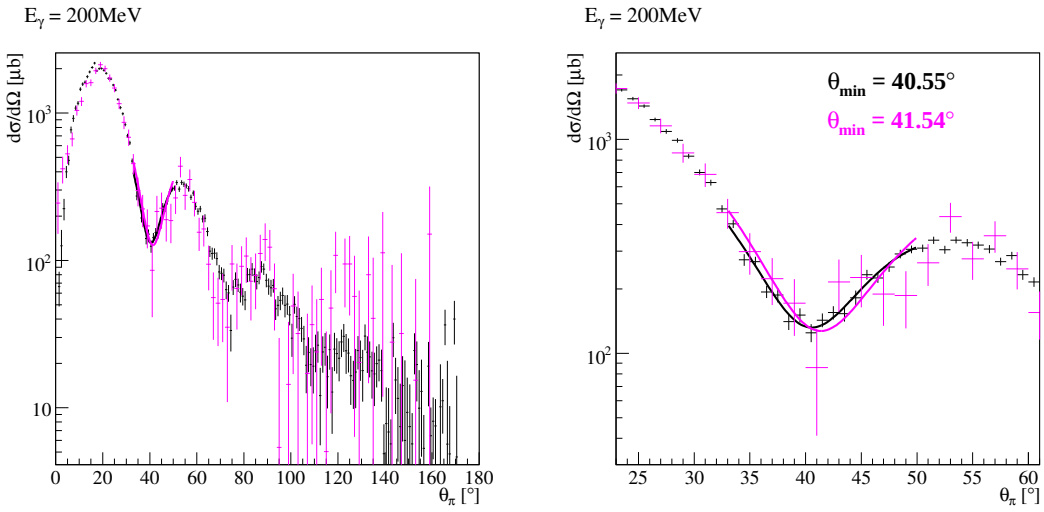

(a) (b)

Figure 6.9: Comparison of ^{208}Pb data to Krusche TAPS measurement. Black markers: present data, weighted average of cross sections for E_γ = (190-200)MeV and E_γ = (200-220)MeV. Pink markers: Krusche TAPS data.

patterns reflecting the effect of the matter form factor in the cross section. Because of the smaller radius of ^{40}Ca (compared with ^{208}Pb), the first minimum occurs at a larger momentum transfer, resulting in the absence of a minimum below 160 MeV until suitably large momentum transfers can be reached.

The general agreement between the angular distribution of the present data and the Glasgow TAPS data is quite good. However, there are differences in the height of the first maxima (up to$\sim$30%) and the position of the first maxima (and higher order maxima) appear shifted to the left compared with the new measurements. These effects were also seen in ^{208}Pb. Between 180 MeV and 260 MeV the coherent contribution extracted from the fit tends to be ill defined at the very bottom of the minima. The statistical accuracy appears to be insufficient to accurately constrain the fits in this region. However, the overall shape of the minima are more clearly visible in the new data set compared with the Glasgow TAPS data.

The ^{40}Ca cross sections are generally well reproduced by the DREN theory and over the entire energy range, the largest difference in the height of the first maximum is $\sim$10%. At backwards angles between 160 MeV and 200 MeV the data are underpredicted by the theory calculations. The next step in exploring these possible discrepencies is to include a more realistic shape for the matter distribution in the calculations as discussed in secion 2.3.7.

It can be seen that the predicted shape of the maxima tend to follow more closely the new CB data. In particular, the Glasgow data show a less symmetrical shape than predicted by the theory for the first maximum.

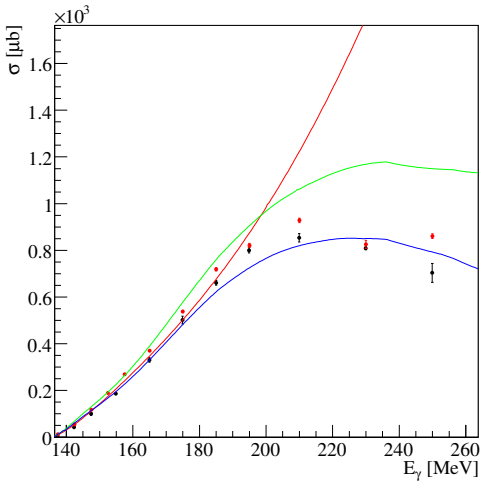

Figure 6.10: ^{40}Ca. Total cross section. Black markers: CB data. Red markers: Glasgow TAPS data. Blue Line: DREN calculation. Green line: DWIA calculation. Red line: PWIA calculation.

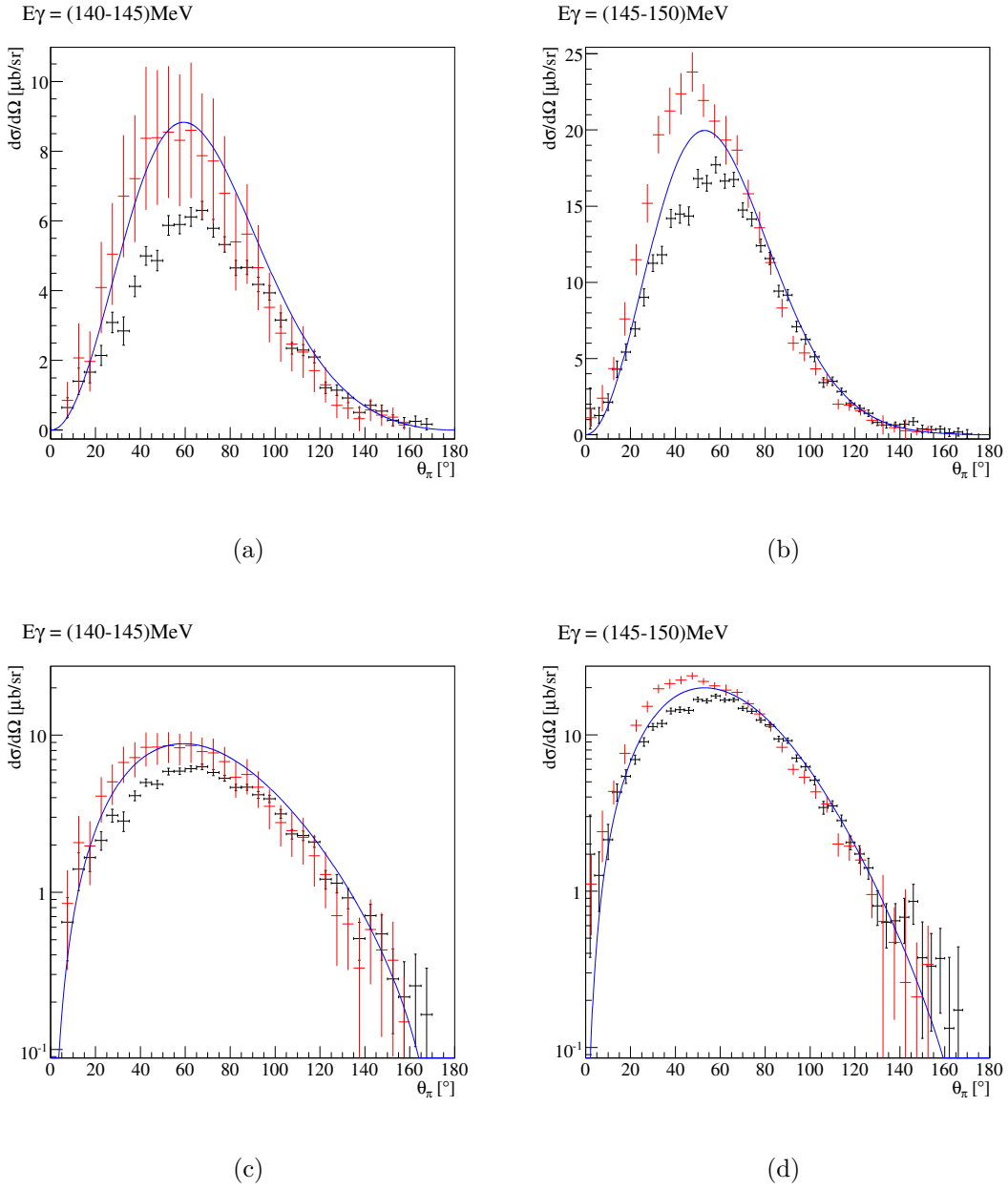

Figure 6.11: ^{40}Ca differential cross sections both on linear (a and b) and log (c and d) scales. Black markers: CB data. Red markers: Glasgow TAPS data. Blue Line: DREN calculation.

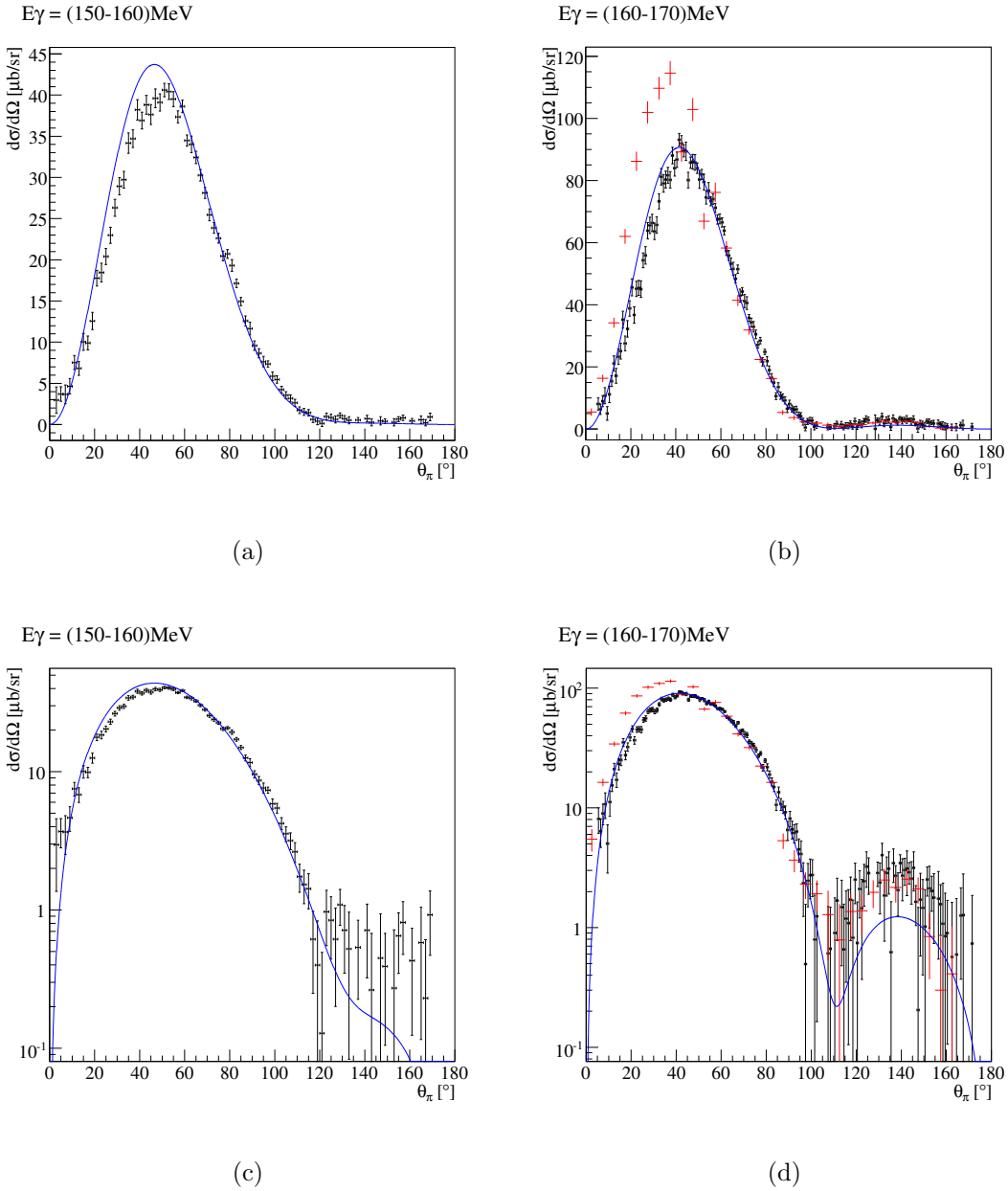

Figure 6.12: ^{40}Ca differential cross sections both on linear (a and b) and log (c and d) scales. Black markers: CB data. Red markers: Glasgow TAPS data. Blue Line: DREN calculation.

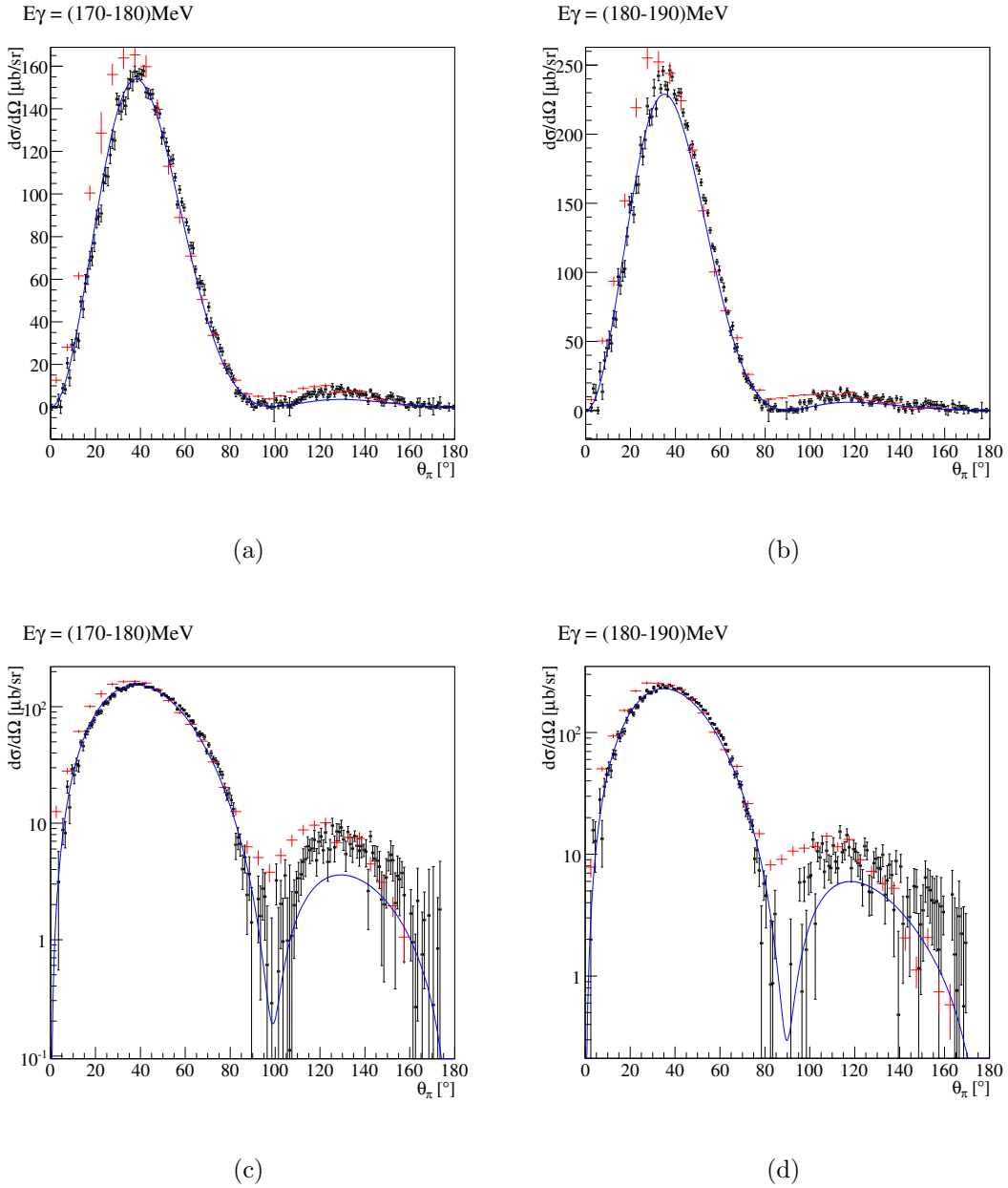

Figure 6.13: ^{40}Ca differential cross sections both on linear (a and b) and log (c and d) scales. Black markers: CB data. Red markers: Glasgow TAPS data. Blue Line: DREN calculation.

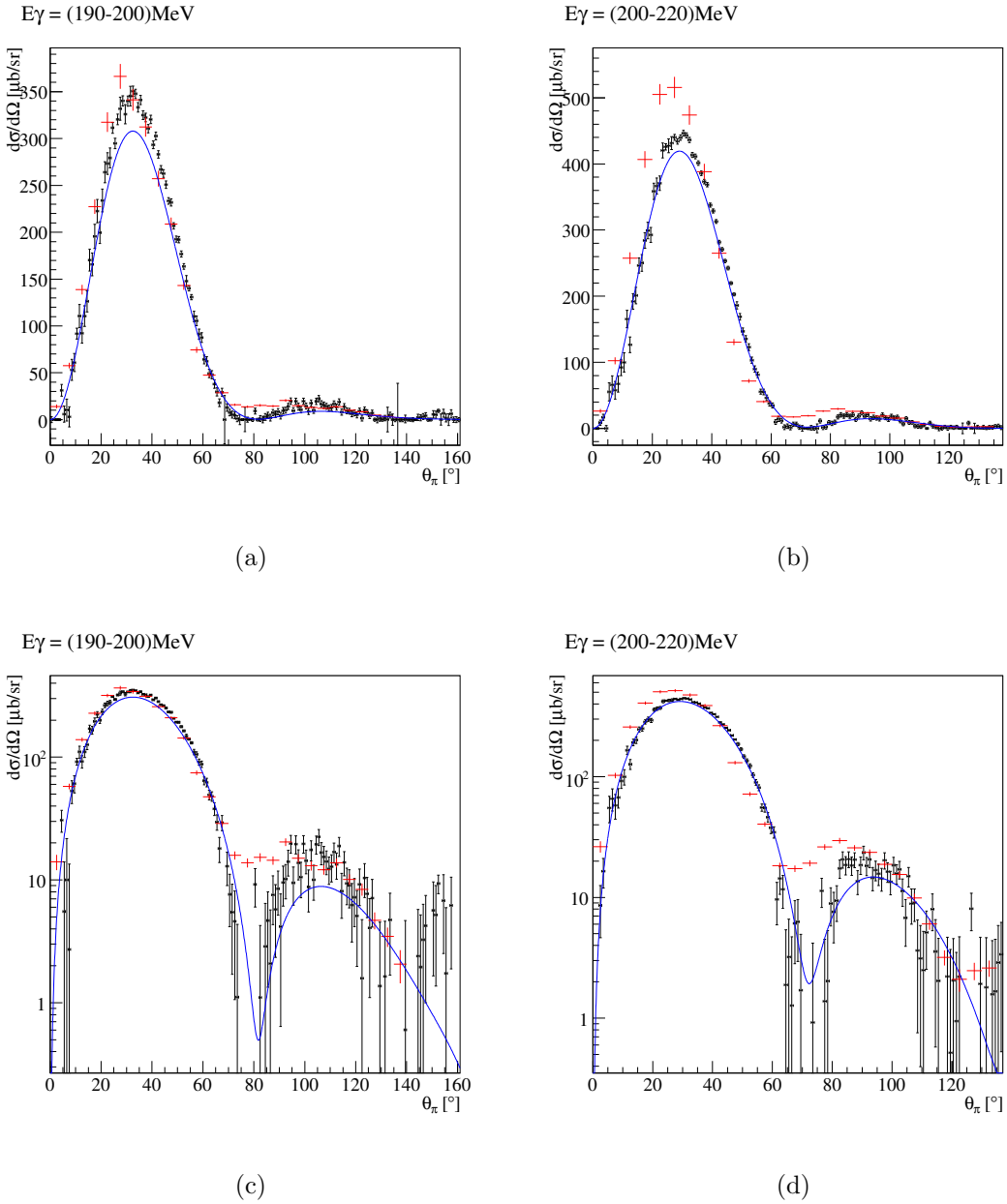

Figure 6.14: ^{40}Ca differential cross sections both on linear (a and b) and log (c and d) scales. Black markers: CB data. Red markers: Glasgow TAPS data. Blue Line: DREN calculation.

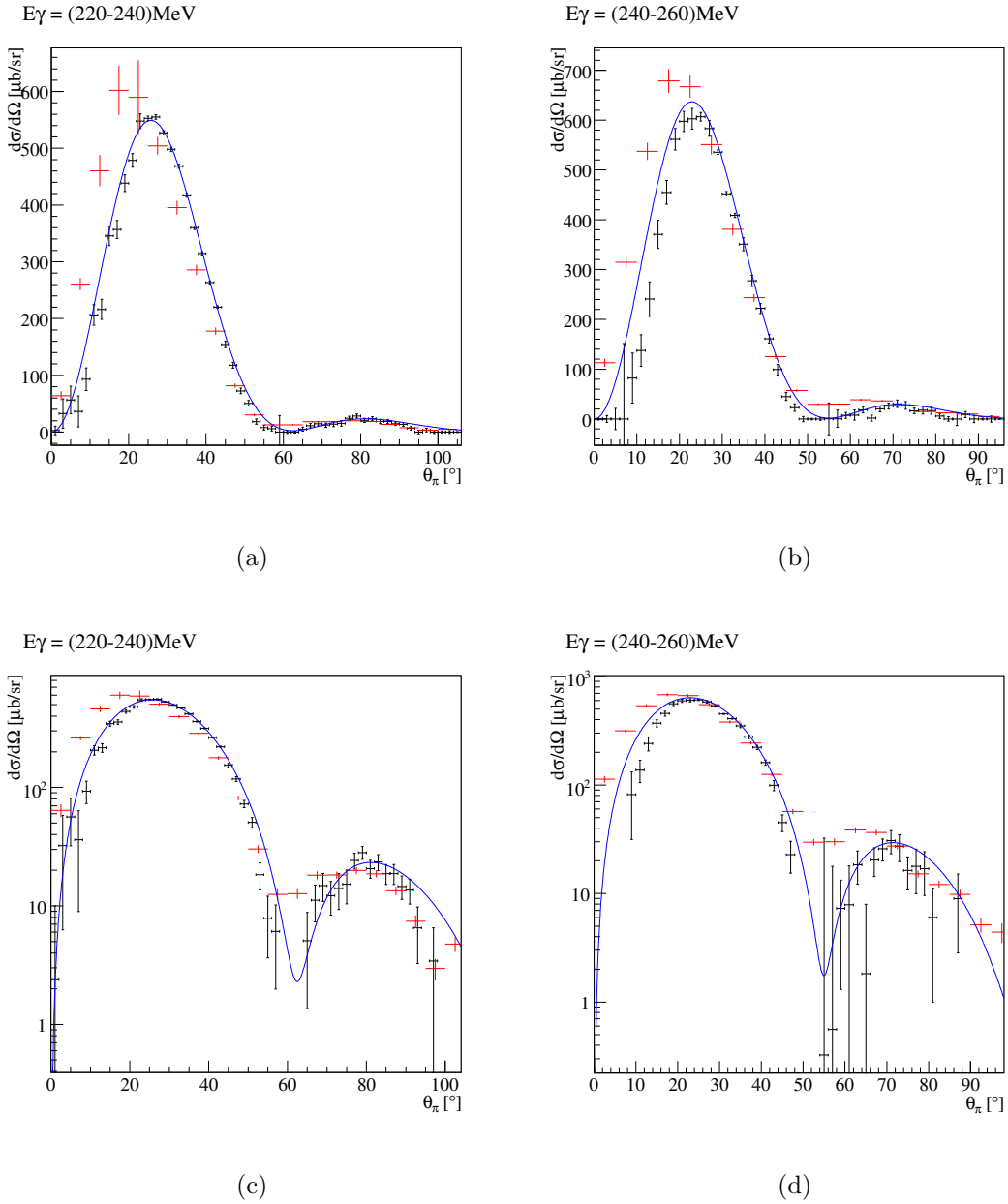

Figure 6.15: ^{40}Ca differential cross sections both on linear (a and b) and log (c and d) scales. Black markers: CB data. Red markers: Glasgow TAPS data. Blue Line: DREN calculation.

6.1.3 ^{16}O

Total Cross Section

The total cross section for ^{16}O (figure 6.16) shares the same general shape as for the other targets, but has a maximum at a higher photon energy of E_γ = 250MeV. The new data are in agreement with the Glasgow TAPS measurement up to E_γ = 190 MeV however, for higher E_γ there is a clear discrepency between the current data set and the Glasgow TAPS data of up to 25%. The full calculation (DREN) does not describe the magnitude of the present data well although it gives a good description of the shape. The DWIA calculation is seen to give a better description of the magnitude but disagrees with the shape since it does not reproduce the fall off in the cross section above E_γ ∼240 MeV. The DREN model gives closer agreement in magnitude with the previous Glasgow TAPS data.

Differential Cross Sections

The differential cross sections for ^{16}O are shown in figures 6.17 - 6.22. Due to the small size of ^{16}O the first minimum in the form factor does not come on scale until $E_\gamma \sim$ 200 MeV.

In terms of the magnitude and shape of the cross sections the CB and TAPS data sets are in relatively good agreement below E_γ = 200 MeV. The position of the first maxima still tends to appear at smaller angles in the Glasgow TAPS data than the present data, as observed for the other targets. Above these photon energies, there is a divergence between the data sets which is most obvious in the heights of the first and second maxima. The TAPS data are consistently lower, and the difference increases with increasing photon energy up to a maximum of ∼25% in the height of the first maximum.

The present ^{16}O data are not as well described by the DREN model as the ^{208}Pb and ^{40}Ca data. Above E_γ = 200 MeV there is a divergence between the data and the model and in fact the model is in close agreement with the magnitude of the TAPS cross sections in this energy region at least in terms of the height of the first maximum. However, the predicted position and shape of the first and second maxima show much better agreement with the new CB data. The predicted heights of the higher order maxima may well be modified with the planned inclusion of more realistic matter distributions in the model (at present a symmetrised Fermi function is used in the model - figure 2.8). However, the discrepency could also point to the contribution of incoherent background to the cross sections at high E_γ.

It is expected that the nuclear decay gamma analysis currently being developed (Appendix D) would help in establishing the angular shape and strength of the inco-

herent contribution from low lying nuclear states. This additional information could help to improve or confirm the coherent cross sections presented here.

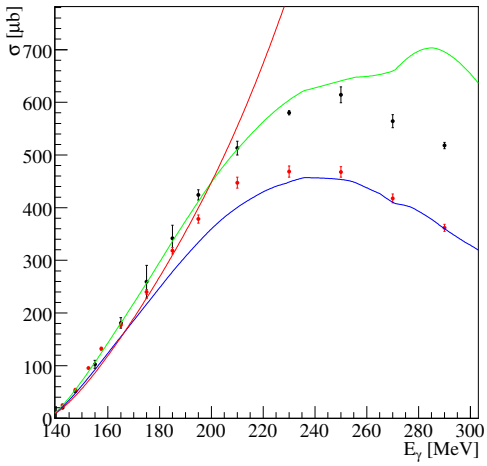

Figure 6.16: ^{16}O. Total cross section. Black markers: CB data. Red markers: Glasgow TAPS data. Blue Line: DREN calculation. Green line: DWIA calculation. Red line: PWIA calculation.

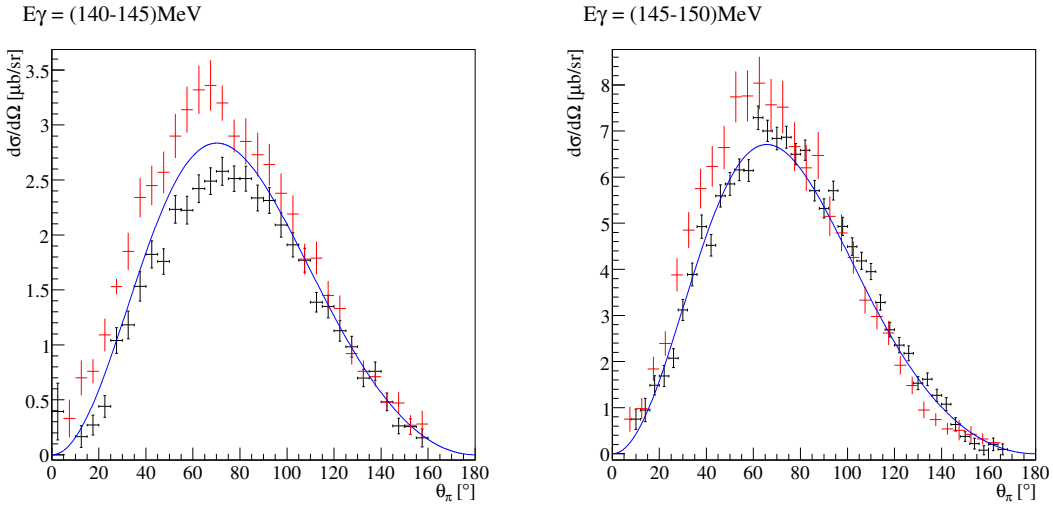

(a) (b)

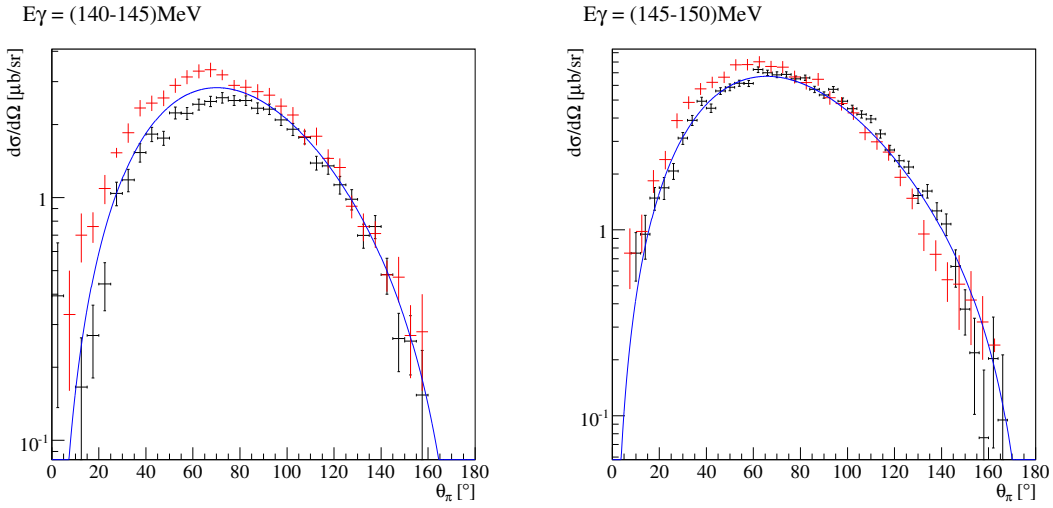

(c) (d)

Figure 6.17: ^{16}O differential cross sections both on linear (a and b) and log (c and d) scales. Black markers: CB data. Red markers: Glasgow TAPS data. Blue Line: DREN calculation.

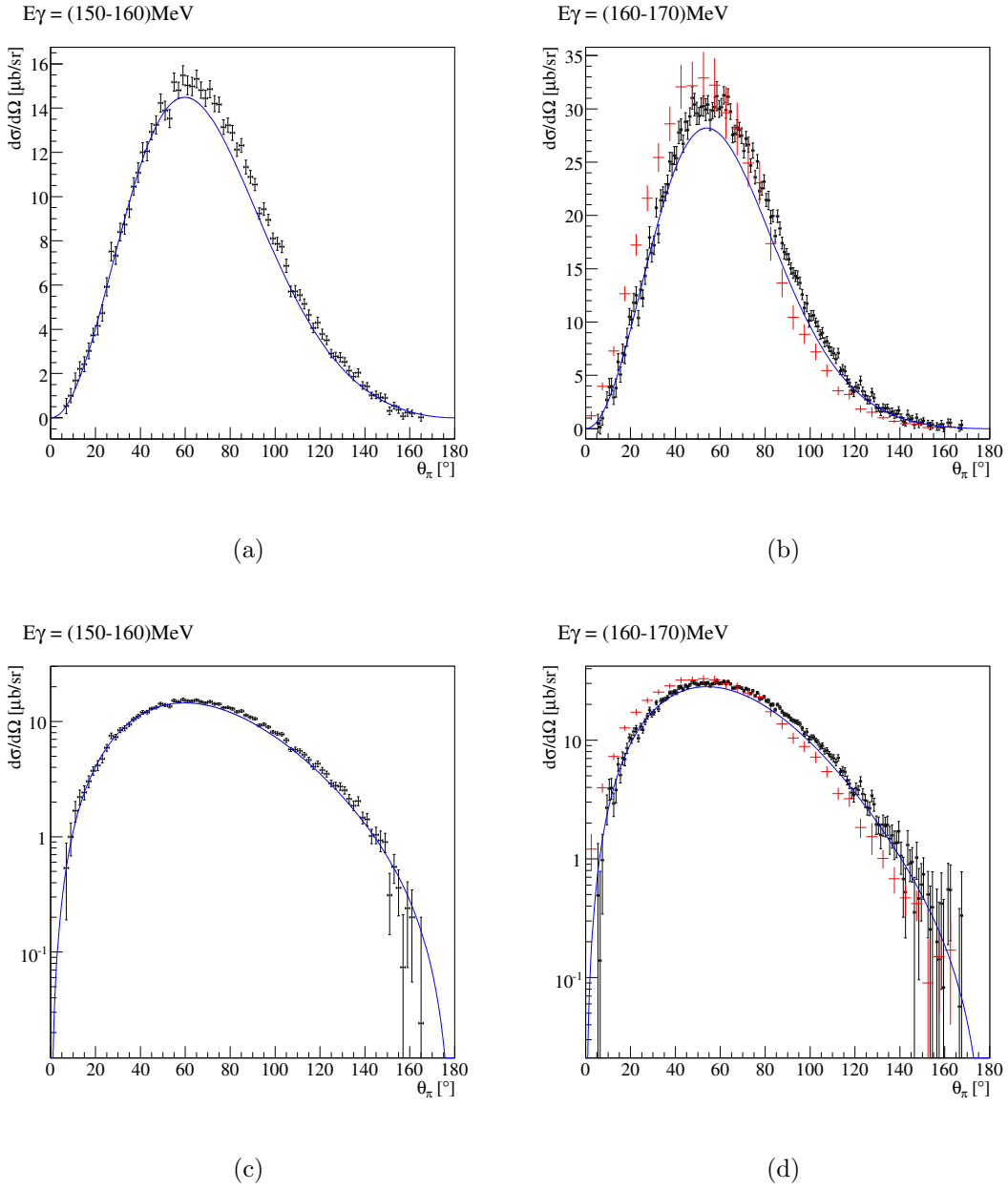

Figure 6.18: ^{16}O differential cross sections both on linear (a and b) and log (c and d) scales. Black markers: CB data. Red markers: Glasgow TAPS data. Blue Line: DREN calculation.

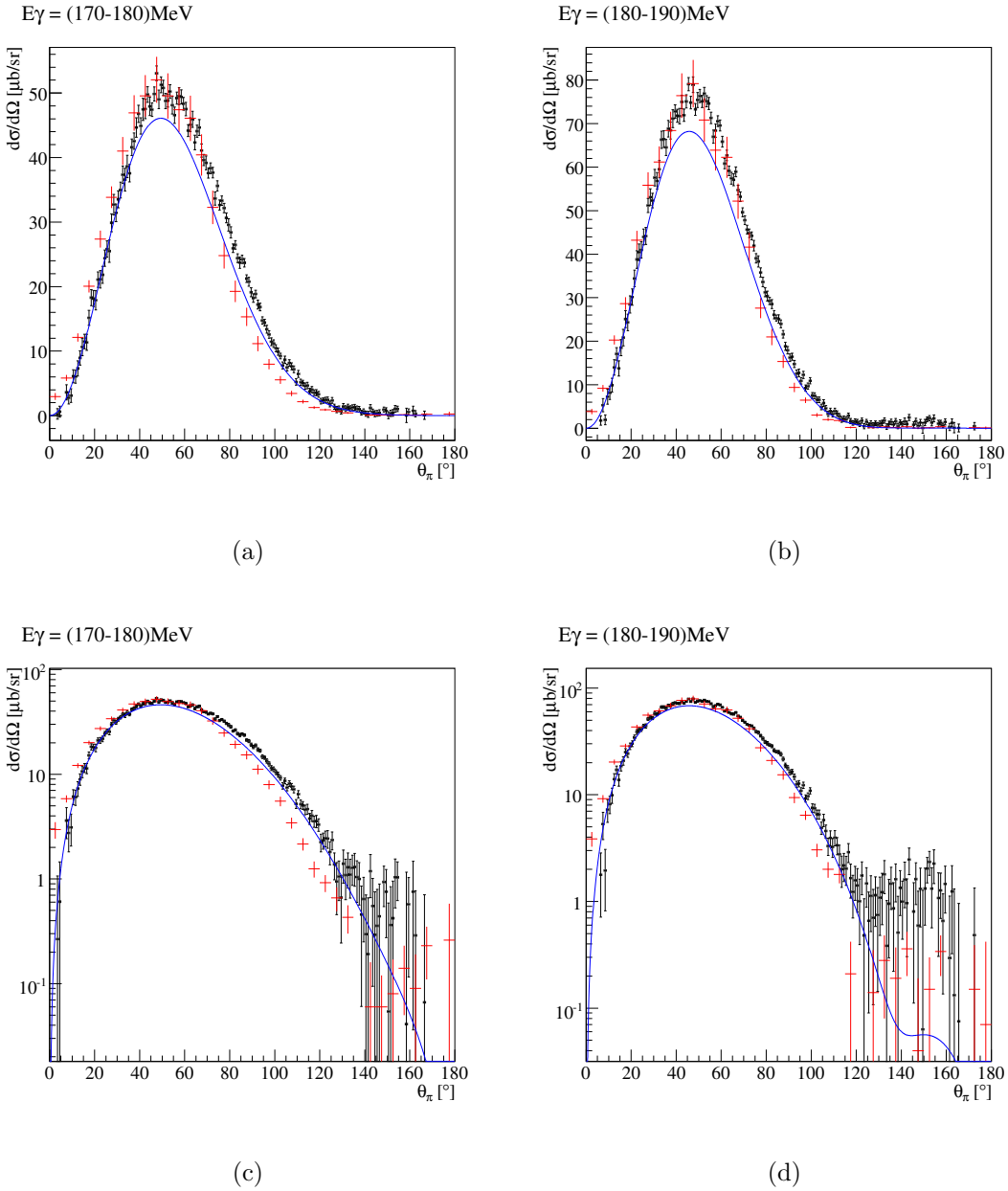

Figure 6.19: ^{16}O differential cross sections both on linear (a and b) and log (c and d) scales. Black markers: CB data. Red markers: Glasgow TAPS data. Blue Line: DREN calculation.

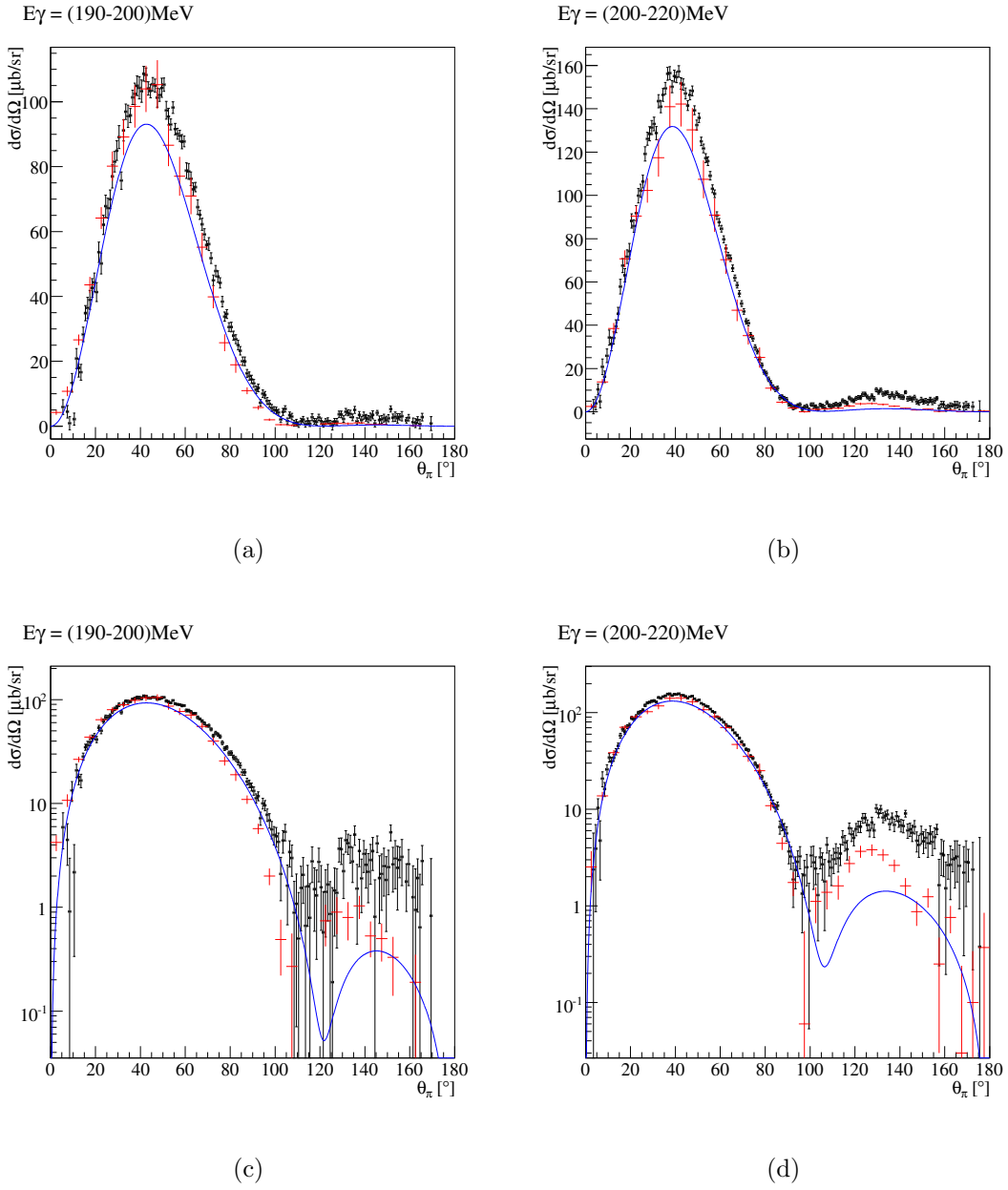

Figure 6.20: ^{16}O differential cross sections both on linear (a and b) and log (c and d) scales. Black markers: CB data. Red markers: Glasgow TAPS data. Blue Line: DREN calculation.

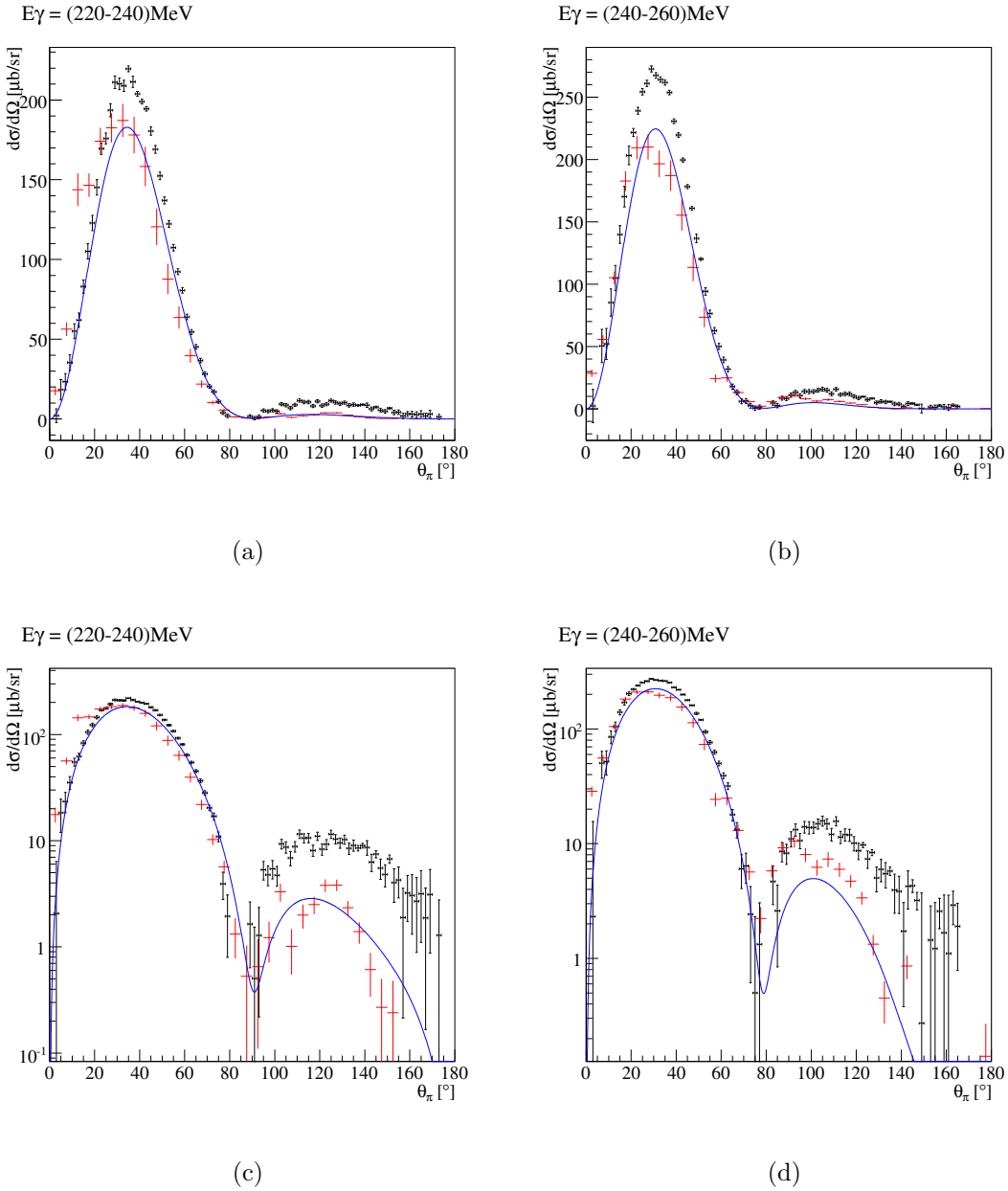

Figure 6.21: ^{16}O differential cross sections both on linear (a and b) and log (c and d) scales. Black markers: CB data. Red markers: Glasgow TAPS data. Blue Line: DREN calculation.

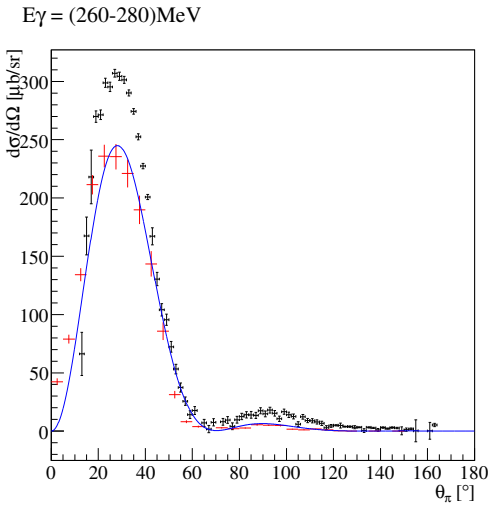

(a)

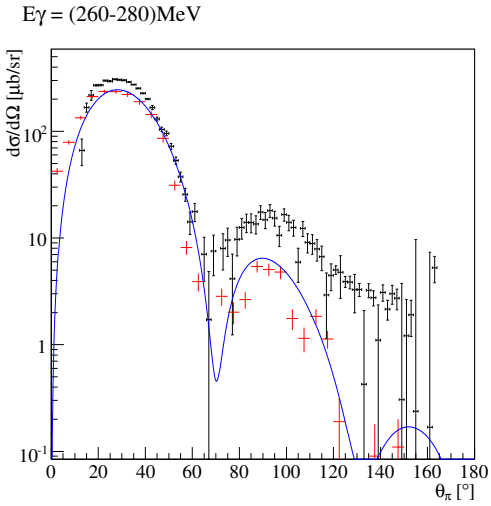

(b)

Figure 6.22: ^{16}O differential cross sections both on linear (a) and log (b) scales. Black markers: CB data. Red markers: Glasgow TAPS data. Blue Line: DREN calculation.

6.1.4 ^{12}C

Total Cross Section

The total cross section for ^{12}C (figure 6.23) shows a similar shape and magnitude to the ^{16}O data. The new ^{12}C measurement has a lower cross section than the Glasgow TAPS data (up to ∼25%). While the Glasgow TAPS data are not closely reproduced by the DREN theory curve, there is a much better agreement between the current data and the DREN calculation.

Differential Cross Sections

The differential cross sections for ^{12}C are presented in figures 6.24 - 6.28. As already noted for the total cross section, the present data have a smaller cross section than the previous Glasgow TAPS data. Below E_γ = 200 MeV, and for θ_π greater than 90° the two data sets show similar cross sections . For smaller θ_π and at higher energies the Glasgow TAPS data are consitently higher than the new data. There are indications of unphysically sharp changes in the cross sections around this point in the Glasgow TAPS data (e.g. figure 6.27(b)) which may point to some systematic effects in the fitting procedure in the older data.

Above E_γ = 200 MeV as the first coherent minimum comes on scale the cross sections extracted from the new data drop to being consistent with zero in the minima. This effect was already seen in ^{40}Ca and suggests that the coherent strength and background is not being well constrained by the fitting procedure when the statistical accuracy of the data worsens and the coherent contribution becomes small compared to the incoherent.

The magnitude of the differential cross sections is not as well described by the DREN model as the ^{208}Pb and ^{40}Ca data. The magnitude of the data and model are in good agreement below E_γ = 200 MeV however, above that energy there is a divergence between the data and model. At those energies the predicted heights of the first and second maxima are consistently below the data. It is clear that the DREN code provides a much better description of the present data than the Glasgow TAPS data. As discussed for ^{16}O, the DREN calculations could be improved with the inclusion of realistic matter distributions and from figure 2.8 it is clear that the charge density distribution is not well approximated by a symmetrised Fermi function. This is currently in progress. Future analysis of the nuclear decay gammas may help to establish the background incoherent contribution, which will help to improve or confirm the coherent cross sections presented here.

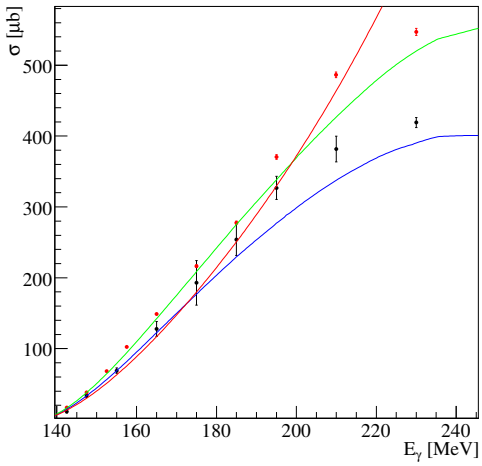

Figure 6.23: ^{12}C. Total cross section.Black markers: CB data. Red markers: Glasgow TAPS data. Blue Line: DREN calculation. Green line: DWIA calculation. Red line: PWIA calculation.

6.1.5 Summary of Results

To summarise, the present ^{208}Pb and ^{40}Ca data are in good overall agreement with the magnitude of both the previous data sets and the DREN theoretical calculations. There is an improvement of around a factor 4 in the statistics from previous measurements. The DREN code reproduces the ^{208}Pb cross sections to within 10% implying that the model gives a good description of the coherent pion production process, and importantly that the pion FSI are under control. The cross sections for the lighter nuclei show larger discrepencies with the theory code, although the gross features of the cross sections are reproduced. The theoretical model is presently being improved to include more detailed matter distributions for light nuclei. However, the discrepency may also arise due to remaining incoherent π^0 production that has not been adequately supressed by the pion missing energy fitting procedure. It is suggested that the ^{16}O and ^{12}C data sets would benefit from exploiting the observed nuclear decay photons from incoherent events to evaluate and subtract the incoherent contribution further. This will involve a detailed study of low energy photon interactions in the Crystal Ball and is beyond the scope of this thesis.

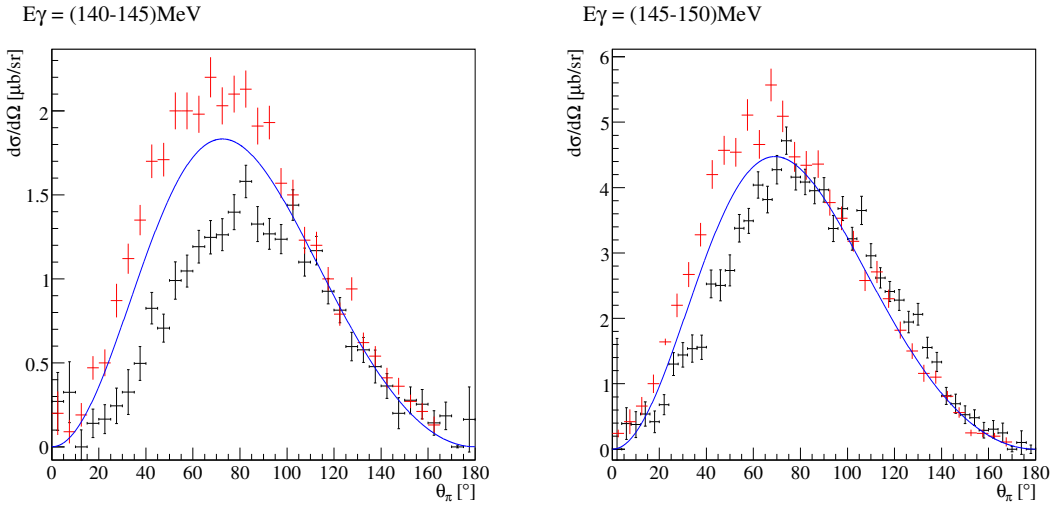

(a) (b)

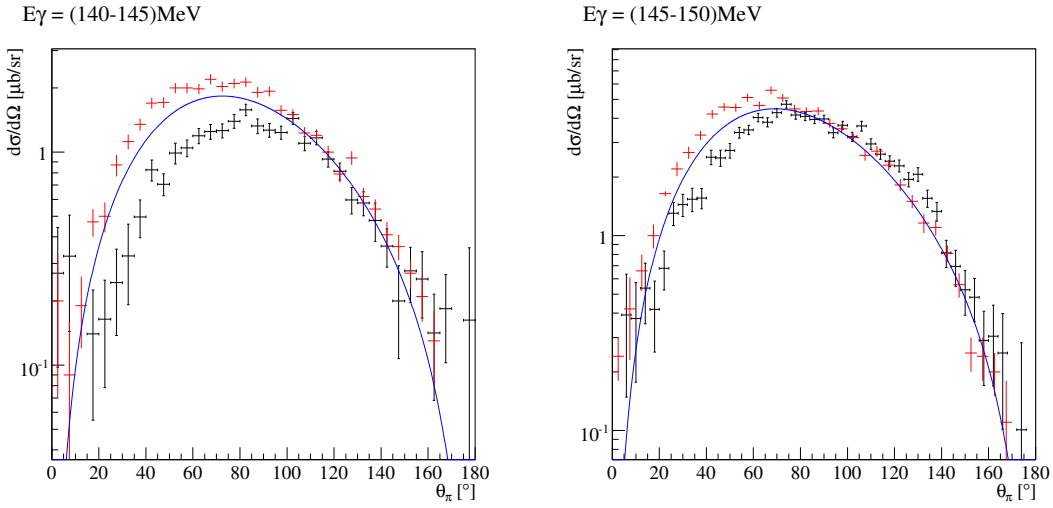

(c) (d)

Figure 6.24: ^{12}C differential cross sections both on linear (a and b) and log (c and d) scales. Black markers: CB data. Red markers: Glasgow TAPS data. Blue Line: DREN calculation.

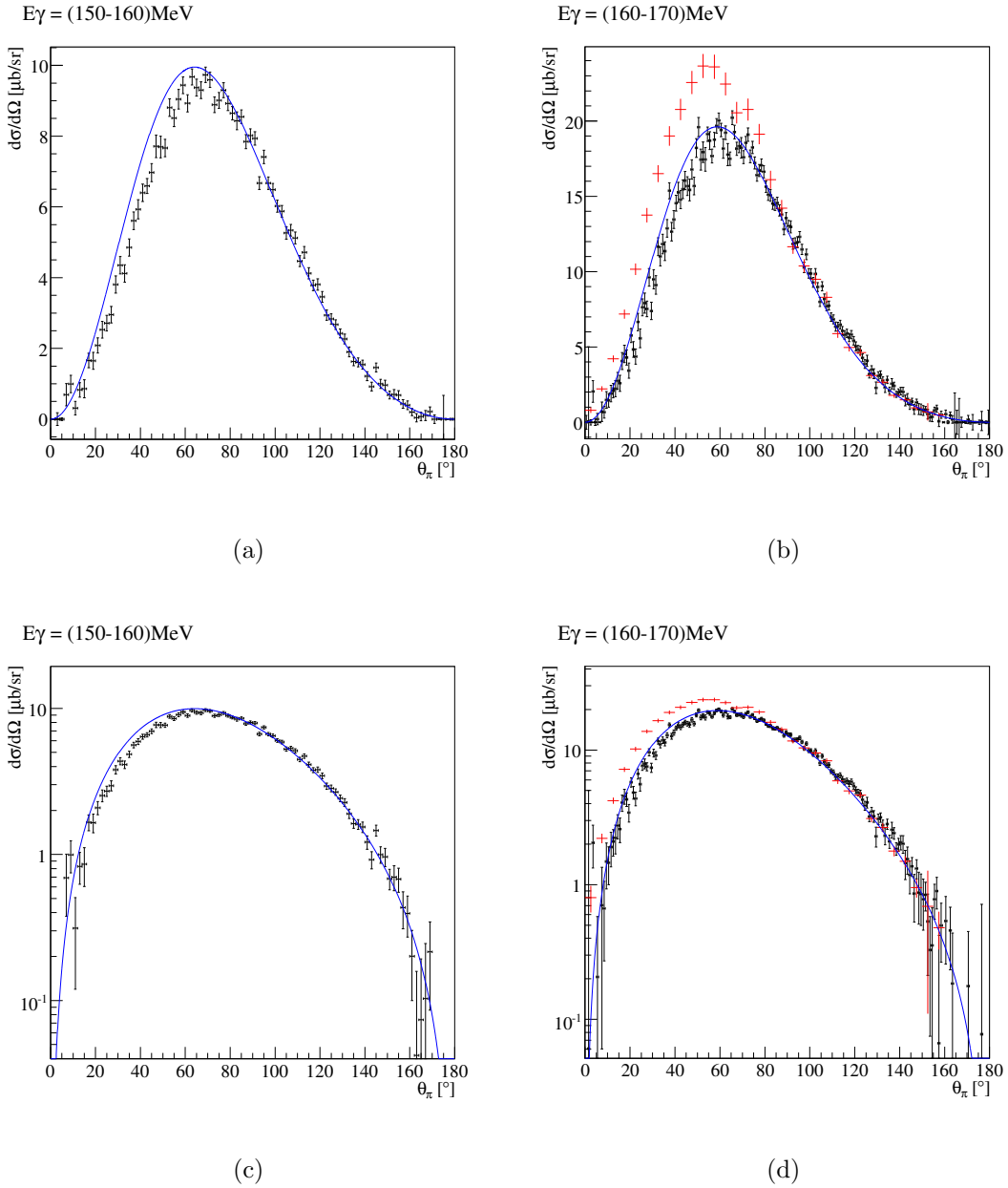

Figure 6.25: ^{12}C differential cross sections both on linear (a and b) and log (c and d) scales. Black markers: CB data. Red markers: Glasgow TAPS data. Blue Line: DREN calculation.

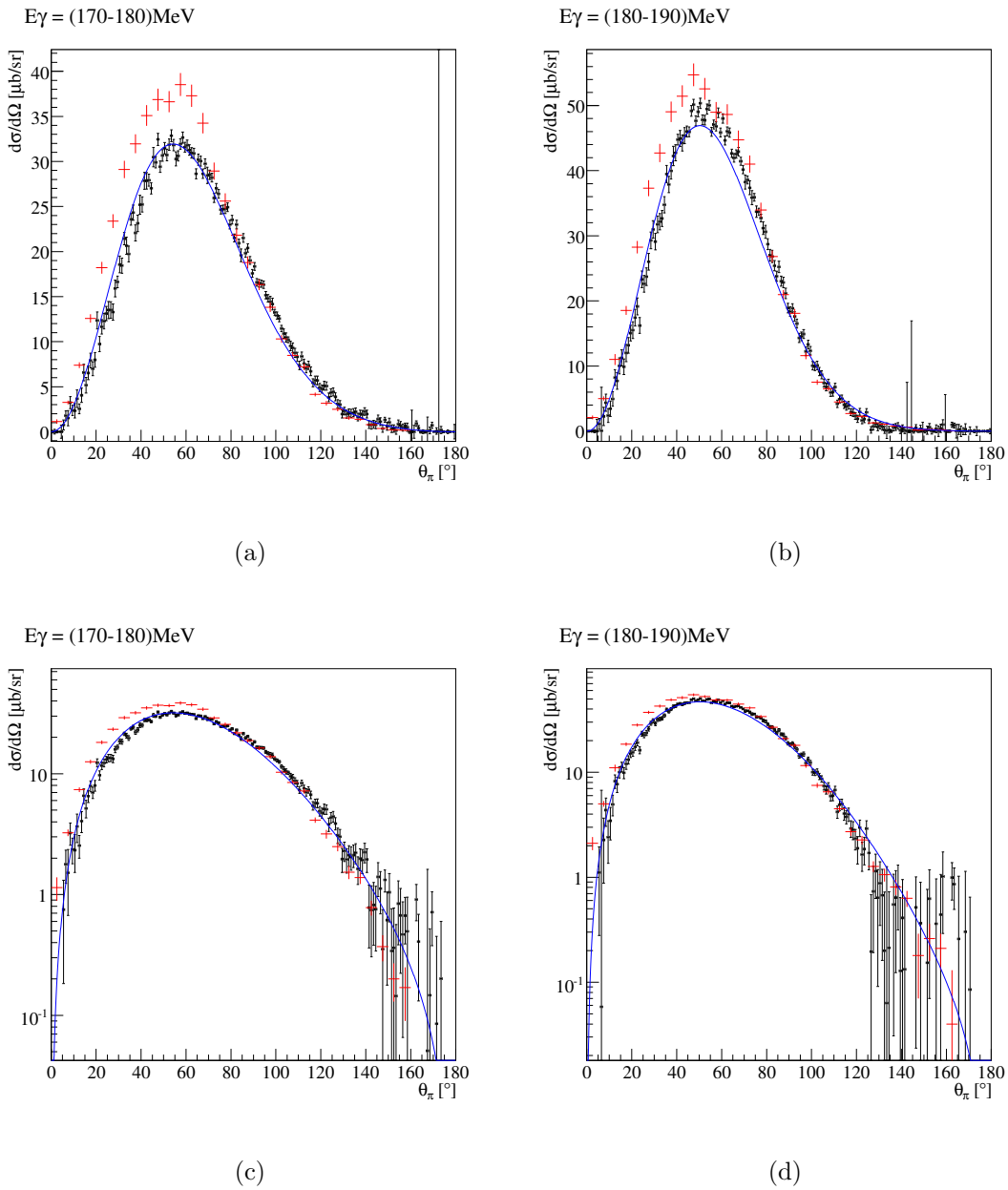

Figure 6.26: ^{12}C differential cross sections both on linear (a and b) and log (c and d) scales. Black markers: CB data. Red markers: Glasgow TAPS data. Blue Line: DREN calculation.

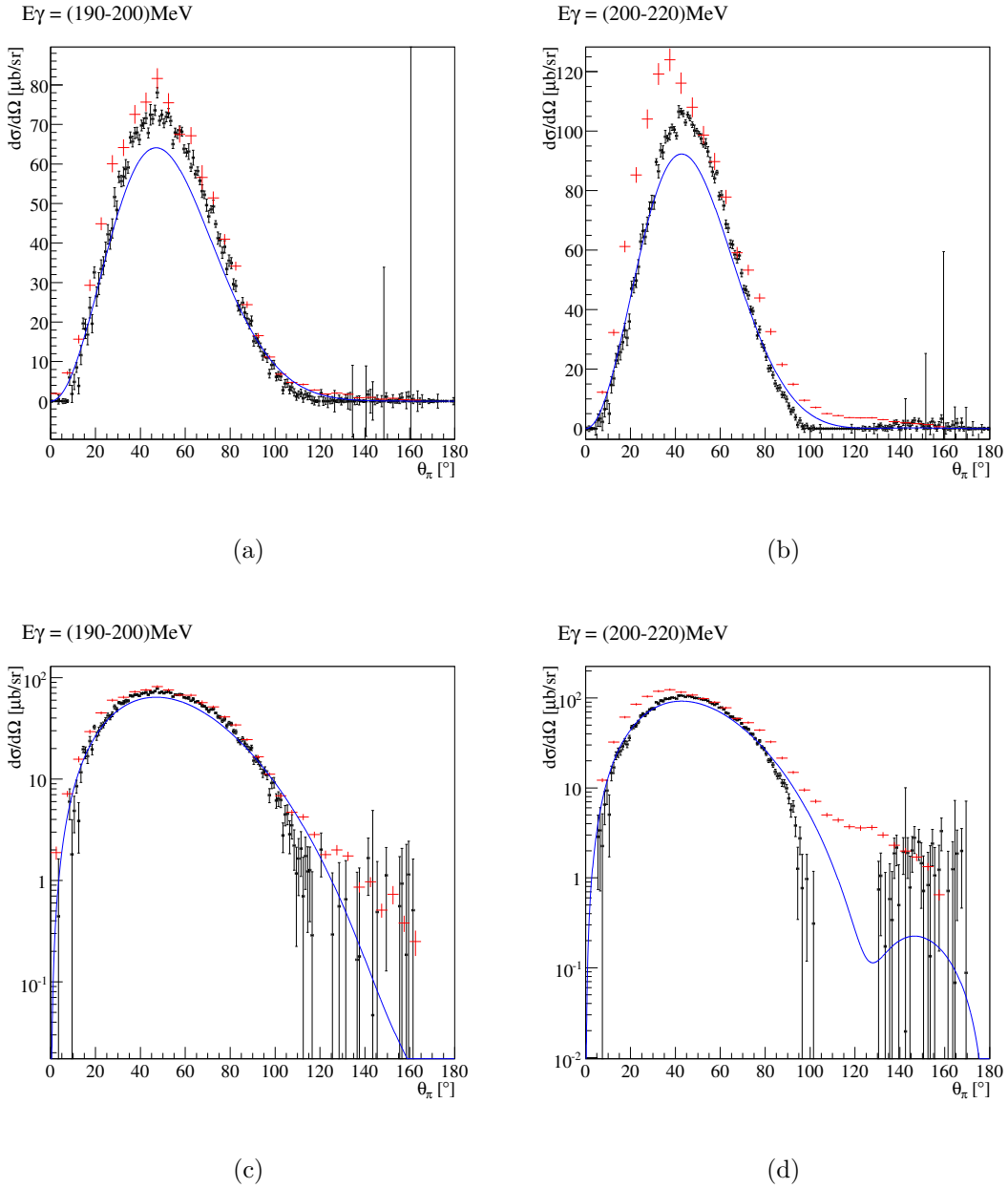

Figure 6.27: ^{12}C differential cross sections both on linear (a and b) and log (c and d) scales. Black markers: CB data. Red markers: Glasgow TAPS data. Blue Line: DREN calculation.

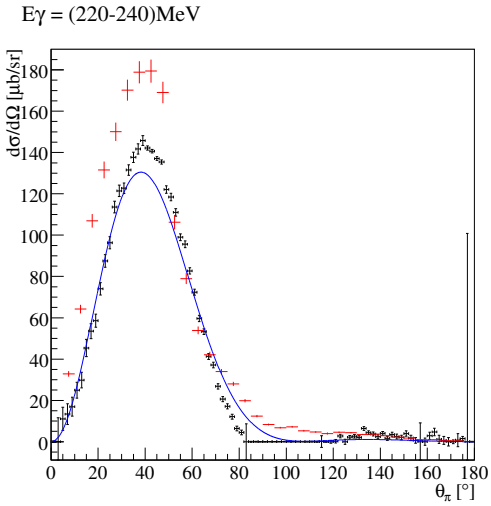

(a)

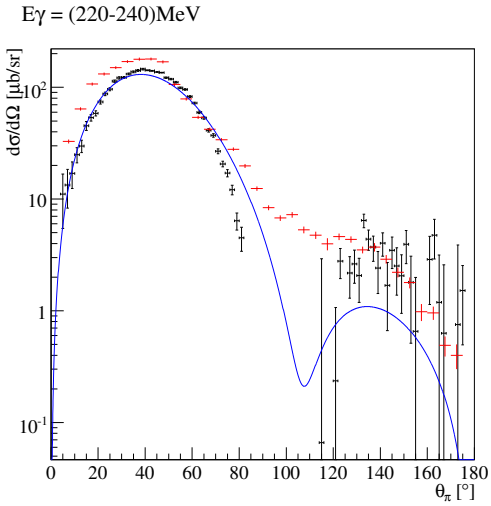

(b)

Figure 6.28: ^{12}C differential cross sections both on linear (a) and log (b) scales. Black markers: CB data. Red markers: Glasgow TAPS data. Blue Line: DREN calculation.

6.2 Preliminary Evaluation of the Neutron Skin of ^{208}Pb

In this section an attempt is made to draw some preliminary conclusions regarding the nature of the neutron skin on ^{208}Pb via a comparison with the DREN calculations for the low energy cross sections where the FSI effects are not as strong. The comparisons made in sections 6.2.1 and 6.2.3 are not intended as a rigorous examination of the matter distribution of ^{208}Pb. This will be done in a future analysis using the data set described in this thesis. An outline of the possible procedures for this next step are given in section 6.3.

6.2.1 Comparison with DREN Calculations

The first evaluation of the ^{208}Pb matter distribution was made via a comparison with the DREN calculations. In order to produce a differential cross section, the DREN code reads in the matter form factor of the nucleus. The form factors used are fourier transforms of the matter density distributions as approximated by symmetrised Fermi functions (equation 2.20). In the previous section, the DREN calculations used matter distributions where the distribution of neutrons matched that of the protons i.e. with no neutron skin. For the comparison shown in figure 6.29, the DREN calculations were run several times using different density distributions which include different neutron skin thicknesses.

The neutron skin is defined as the difference between the r.m.s. proton and neutron radii:

$$\Delta R \;=\; r_n - r_p$$

The incorporation of different skin thicknesses into the model required the construction of a new matter distribution from the weighted addition of the charge distribution (ρ_c), and a neutron distribution (ρ_n):

$$\rho_m(r) \;=\; \frac{Z}{A}\rho_p(r) + \frac{N}{A}\rho_n(r) \tag{6.1}$$

where $\rho_m(r)$ is the matter distribution. The half height and diffuseness parameters (b and c in equation 2.20) for the charge distribution were fitted to elastic electron scattering data. The neutron distribution was given the same diffuseness (i.e. shape) and only the half height radius was increased to increase the r.m.s. radius.

The ^{208}Pb cross sections for two incident photon energy bins are shown in figure 6.29 overlayed with the DREN calculations with no neutron skin, a 0.1 fm neutron skin, a

0.2 fm neutron skin and a 0.3 fm neutron skin. Only the first minimum position of the calculations and the data were compared. To pin down the first minimum position, the data were fitted with a Bessel function in the first minimum region:

$$f(x) \quad = \quad a + \frac{bsin(cx-d)}{cx-d} \tag{6.2}$$

where a, b, c and d are fitted parameters. The first minimum position was taken as the minimum of the fitted function. An estimate of the error in this value was made by varying the range of the fit within reasonable limits. The error in the minimum of the present data is placed at $\pm 0.2°$. The dotted lines in figure 6.29 marks the fitted minima positions. From this simple comparison, the neutron skin thickness that gives the best match to the data is $\sim$0.15 fm. While this is clearly a very basic preliminary analysis it is a worthwhile comparison to make. At the very least it shows that the first minimum position in the matter form factor appears shifted to a higher momentum transfer than the first minimum in the charge form factor. This implies that the r.m.s radius of the matter distribution is larger than the r.m.s. charge distribution i.e. there appears to be a non-zero neutron skin on ^{208}Pb.

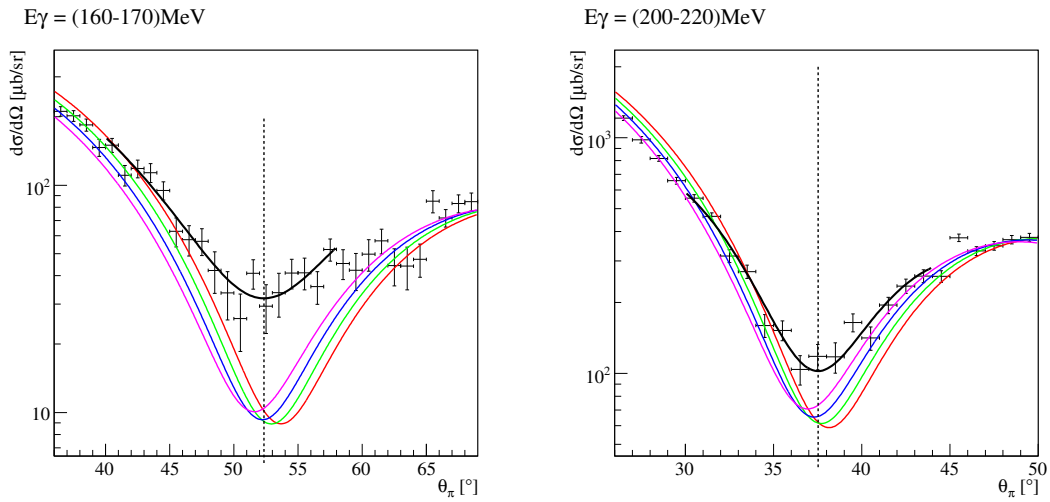

(a) (b)

Figure 6.29: Comparison of ^{208}Pb data to DREN calculations. Solid black line: fitted Bessel function to minimum of cross section. Dotted black line: minimum of fitted function. Red line: no neutron skin. Green line: 0.1fm neutron skin. Blue line: 0.2fm. Pink line: 0.3fm.

6.2.2 Krusche TAPS data

The Krusche TAPS results (section 2.4.1) sample the coherent reaction in the Δ resonance region where the pion FSI effects are significant. At these energies the energy resolution of TAPS is also significantly reduced compared with the resolution near to the pion production threshold, making the separation of coherent and incoherent processes via the missing energy method increasingly difficult. The Krusche experiment also used a similar TAPS setup as the Glasgow experiment and as such it is prone to the same inconsistencies in the reconstruction of the detected pion 4-momentum (section 2.4.1).

Nevertheless, this data set has been analysed to extract a value for the r.m.s. matter radius of ^{208}Pb [89] and was found to be smaller than that of the charge distribution known from electron scattering leading to a neutron skin of $\sim$-0.1 fm. This negative neutron skin is in disagreement with all Skyrme and RMF predictions of the ^{208}Pb neutron skin. Given the previous result from the Krusche TAPS data it is informative to compare the new and old data sets. This is outlined below.

6.2.3 Comparison to Krusche TAPS data

The Krusche data has been separated into three energy bins and only the lowest one, centred at E_γ=200 MeV, overlaps with the current data set. To compare the consistency of the data sets in the minima, the first minima were again fitted with equation 6.2 (figure 6.9). An estimate of the error in this value was made by varying the range of the fit within reasonable limits. The error in the minimum of the present data is placed at $\pm 0.2^\circ$ compared with $(+0.8, -0.3)^\circ$ for the Krusche TAPS data. There is a discrepency in the minima position of $\sim 1^\circ$. From the DREN predictions shown in figure 6.29, for this E_γ bin a 1° shift in the minimum to smaller θ_π corresponds to a difference in skin thickness of $\sim$0.2 fm. With the assumptions of this simple analysis the new data therefore are not expected to confirm the negative neutron skin thickness of the old TAPS data.

6.3 The Way Forward to the Matter Distribution of ^{208}Pb

The various techniques that will be used in the near future to obtain the matter distribution from the new data set will be outlined in this section.

The next step will be to plot the data as a function of momentum transfer, q, instead of θ_π. The small statistical errors achieved in the new measurement will allow

the photon energy bins to be reduced to the smallest binning allowed by the resolution of the tagger (2MeV). For each of the 90 photon energy bins, the form factor will be extracted in the plane wave impulse approximation (equation 2.17) such that:

$$F^2(q) = \frac{\frac{d\sigma_{exp}}{d\Omega}}{\frac{s}{m_N^2} A^2 \frac{d\sigma_E}{d\Omega^*}(E^*_\gamma, \theta^*_\pi)} \tag{6.3}$$

The PWIA is not a good approximation of the data and some correction is required for in medium effects (section 2.3.3). This correction will be applied by multiplying the extracted PWIA form factor from the experiment by the ratio of Kamalov's DREN and PWIA calculations for that bin. The corrected form factor is in principle then the Fourier transform of the matter distribution:

$$F(q) = \int \rho(r) e^{iq\cdot r} d^3r \tag{6.4}$$

Once the form factors have been corrected for FSI, all 90 will be combined into the same plot to improve statistical accuracy. The accuracy of the correction for pion distortion can be guided by looking at the consistency of the form factors extracted for the different incident E_γ bins.

In principle, the measured form factor is the fourier transform of the matter density distribution, although the transformation is not straight forward. Firstly, the form factor extracted from the experimental data is a series of data points and not a continuous function. Furthermore, the form factor is measured over a finite range of q. This introduces ambiguities in the density distribution for small values of r corresponding to the undetermined form factor at large q. It is of course possible to make an assumption about the shape of the matter distribution e.g. approximate it as a Fermi function, and calculate the corresonding form factor via a direct Fourier transform. The calculated form factor can then be compared to the data. Krusche employed a similar technique in determing a value of the ^{208}Pb r.m.s. radius and compared his measured form factors to form factors calculated in the Helm model [90]. This parametrised the density distribution as the convolution between a hard sphere density distribution and a Gaussian. The resulting radial distribution is similar to a Fermi function with a flat central part and a diffuse edge. The minima positions of the extracted form factor were compared with the minima positions of the Helm model form factors to find the best r.m.s. radius. However, this is far from ideal since it makes an assumption about the shape of the density distribution.

This is in fact the same problem that arose in the 1970s in the interpretation of elastic electron scattering data. Several techniques were developed to extract the charge distribution in a model independent way from measured charge form factors and these

same techniques can be applied to the present data. In particular, it is anticipated that the Fourier-Bessel analysis of Dreher et. al. [91] will be used. Dreher's method approximates the density distribution as a sum of Bessel functions:

$$\rho(r) = \sum_{\nu=1}^{\infty} a_\nu j_0(q_\nu r) \quad \text{for r}\leq\text{R} \tag{6.5}$$

$$= 0 \qquad \text{for r}>\text{R} \tag{6.6}$$

$j_0(q_\nu r)$ is a Bessel function of the zeroth order. If F(q) is measured up to the momentum transfer q_{max}, the first N coefficients a_ν can be calculated directly from the measured form factor values such that:

$$a_\nu = \frac{1}{\sqrt{\pi R^3}} \frac{1}{j_1^2(q_\nu R)} F_(q_\nu) \tag{6.7}$$

where $F(q_\nu)$ is the form factor at the momentum transfer q_ν. With these N values of a_ν, the series expansion of ρ_ν can be calculated.

Chapter 7

Conclusion

One of the most interesting and active areas of research in nuclear physics at present is the investigation of the equation of state of nuclear matter. In particular investigations of how the equation of state can be extended to highly dense and highly isospin asymmetric regimes, where the equation of state is not well known. Recent publications have shown that experiments on nuclei in the lab can be used to constrain the equation of state at supra-nuclear densities. Specifically, it has been shown that an accurate measurement of the size of the neutron skin of ^{208}Pb would constrain the equation of state and its density dependence at nuclear densities. Furthermore, a precise measurement could be used to constrain nuclear models, will be important for the interpretation of experiments measuring parity non-conserving electron transitions in atoms, and for a deeper understanding of heavy ion collisions.

The coherent π^0 photoproduction differential cross section contains information on the matter distribution within the nucleus since in the plane wave impulse approximation the cross section contains the matter form factor. As the first step in making an accurate measurement of the nuclear matter distribution of ^{208}Pb, a measurement of coherent π^0 photoproduction on ^{208}Pb was made using the newly installed $\sim 4\pi$ Crystal Ball and TAPS detector system at the MAMI electron accelerator facility. This experiment was one of the first to exploit the Crystal Ball's new home in the A2 hall of MAMI utilising the Glasgow tagged photon beam. Although the main physics goal of the experiment lies in the ^{208}Pb cross sections, data were taken on 3 lighter nuclear targets as a test of the experimental techniques and the theoretical model.

Differential and total cross sections for coherent π^0 photoproduction on ^{208}Pb, ^{40}Ca, ^{16}O and ^{12}C have been obtained in the energy region E_γ = (140-300) MeV. The cross sections have smaller statistical and systematic uncertainties than previous measurements and have been extended to larger angles in smaller angular bins. As such the cross sections presented in this thesis set a new standard for coherent π^0 photoproduction measurements.

In the reaction A(γ,π^0)A, the pion is strongly interacting in the final state and this can lead to pion-nucleus final state interactions. These pion FSI must be modelled before the matter form factor can be extracted from the differential cross section. As such the cross sections for all nuclei were compared to the latest theoretical calculations of Dreschel et. al. which describe the pion photoproduction process in the unitary isobar model and which use detailed pion optical potentials to describe the pion-nucleus FSI.

The theoretical calculations reproduce the ^{208}Pb and ^{40}Ca cross sections very well suggesting that the pion-nucleus FSI is well described by the model. An initial comparison of the ^{208}Pb differential cross secttions to the calculations of Dreschel et. al. as well as to the previous Krusche TAPS data have shown the first hints of a neutron skin on ^{208}Pb via the shift of the coherent minima to smaller angles. Given the good agreement between the DREN model and the ^{208}Pb data it appears to be realistic to use the DREN calculations in the detailed analysis of the nuclear matter distribution using this new data. There is some discrepency between the theoretical calculations and the data from the lighter nuclei at higher E_γ where the experimental energy resolution worsens. There are improvements that can be made to the theoretical calculations. Specifically, the inclusion of realistic form factors based on realistic density distributions is necessary. For better comparison with the data, the calculations must also be folded with the experimental angular resolutions. Additionally it may be possible to improve or confirm the coherent sample by studying incoherent events which are tagged by the observation of a nuclear decay gamma. This work gives the first indications of the possibility for coincident detection of a nuclear decay photon in the same detector as the high energy products of photoproduction. Future study of the nuclear decay γs from ^{12}C and ^{16}O will facilitate one of the first studies of exclusive incoherent π^0 photoproduction where the excited state of the residual nucleus is identified.

Appendix A

Kinematics

A.1 Pion Decay

For the $\pi^0 \rightarrow \gamma\gamma$ decay, the invariant mass of the two photons should equal the rest mass of the π^0 . The invariant mass can be calculated via:

$$\begin{aligned} m^2 &= E^2 - \mathbf{p}^2 \qquad \text{(A.1)} \\ m^2_{\gamma\gamma} &= (E_1 + E_2)^2 - (\mathbf{p}_1 + \mathbf{p}_2)^2 \\ &= E_1^2 + E_2^2 + 2E_1E_2 - (p_1^2 + p_2^2 + 2p_1p_2cos\psi) \\ &= 2E_1E_2(1 - cos\psi) \qquad \text{(A.2)} \end{aligned}$$

where the notation matches that of figure A.1. In the case of photon pairs resulting from a pion decay, $m_{\gamma\gamma} = m_\pi$, the mass of the neutral pion, and equation A.2 can be rewritten as:

$$cos\psi = 1 - \frac{m_\pi^2}{2E_1E_2} \qquad \text{(A.3)}$$

or alternatively:

$$sin\psi = \frac{m_\pi}{2\sqrt{E_1E_2}} \qquad \text{(A.4)}$$

It is clear that there is a maximum value that $\sqrt{E_1E_2}$ can take when $E_1 = E_2 = (E_\pi/2)$. At this value $\sin\psi$ is also at a minimum and has a magnitude given by:

$$sin\frac{\psi_{min}}{2} = \frac{m_\pi}{E_\pi} \qquad \text{(A.5)}$$

The opening angle between the two photons is plotted versus photon energy in figure A.2 for the ^{208}Pb experimental data. As the pion energy increases with E_γ the

plot gives indication of how the range of pion opening angle varies. In particular, the predominantly back to back photon emission for low pion energies is apparent as well as the small range of opening angles for high energy pions caused by the Lorentz boost.

A.2 Pion Energy

Consider figure A.3 which shows the coherent photoproduction of a π^0 from a nucleus (i.e. the target and recoiling nucleus are both in the ground state). If the incident photon energy is known, and the mass of the target nucleus is known, then the energy of the created pion can be calculated. The total energy in the CM frame of the incoming photon and target nucleus ($\sqrt{s}$) can be calculated as:

$$\begin{aligned} s &= (E_\gamma + E_A)^2 - (\mathbf{p}_\gamma + \mathbf{p}_A)^2 && \text{(A.6)} \\ &= (E_\gamma + M)^2 - (E_\gamma + 0)^2 && \text{(A.7)} \\ &= E_\gamma^2 + 2E_\gamma M + M^2 - E_\gamma^2 && \text{(A.8)} \\ &= 2E_\gamma M + M^2 && \text{(A.9)} \end{aligned}$$

Similarly, the total energy available in the CM fame of the produced pion and target recoil pair can be calculated as:

$$\begin{aligned} s &= (E_\pi^{cm} + E_A^{cm})^2 - 0^2 && \text{(A.10)} \\ &= (E_\pi^{cm} + E_A^{cm})^2 && \text{(A.11)} \\ \sqrt{s} &= E_\pi^{cm} + E_A^{cm} && \text{(A.12)} \end{aligned}$$

The difference in the invariant masses of the recoil nucleus and pion is:

$$\begin{aligned} M^2 - m_\pi^2 &= (E_A^{cm^2} - \mathbf{p}^{cm^2}) - (E_\pi^{cm^2} - \mathbf{p}^{cm^2}) && \text{(A.13)} \\ &= E_A^{cm^2} - E_\pi^{cm^2} && \text{(A.14)} \\ &= (E_A^{cm^2} + E_\pi^{cm})(E_A^{cm} - E_\pi^{cm}) && \text{(A.15)} \\ &= \sqrt{s}(E_A^{cm} - E_\pi^{cm}) && \text{(A.16)} \end{aligned}$$

Rearranging A.16 the difference between the recoil energy and the pion energy is:

$$E_A^{cm} - E_\pi^{cm} = \frac{M^2 - m_\pi^2}{\sqrt{s}} \qquad \text{(A.17)}$$

Subtracting A.12 from A.17 is then:

$$\begin{aligned} 2E_\pi^{cm} &= \sqrt{s} - \frac{M^2 - m_\pi^2}{\sqrt{s}} && \text{(A.18)} \\ E_\pi^{cm} &= \frac{s - M^2 + m_\pi^2}{2\sqrt{s}} && \text{(A.19)} \end{aligned}$$

Substituting A.9 into A.19 the energy of a coherently produced pion in the pion-nucleus centre of mass frame in terms of the incident photon energy and the pion and recoil masses is thus:

$$E_\pi^{cm} = \frac{2E_\gamma M + m_\pi^2}{2\sqrt{E_\gamma M + M^2}} \tag{A.20}$$

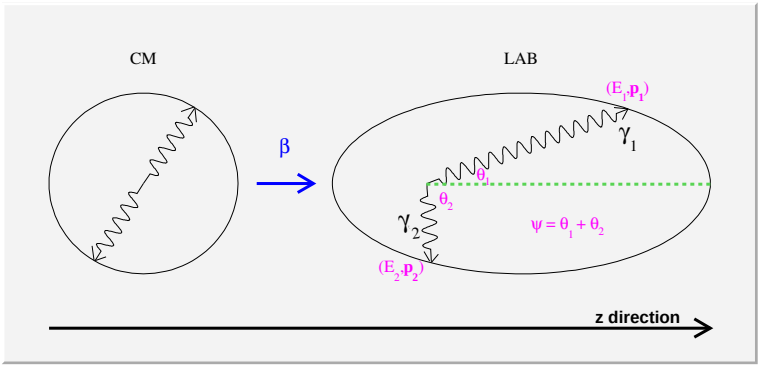

Figure A.1: The π^0 two photon decay in the pion centre of mass frame and in the lab frame.

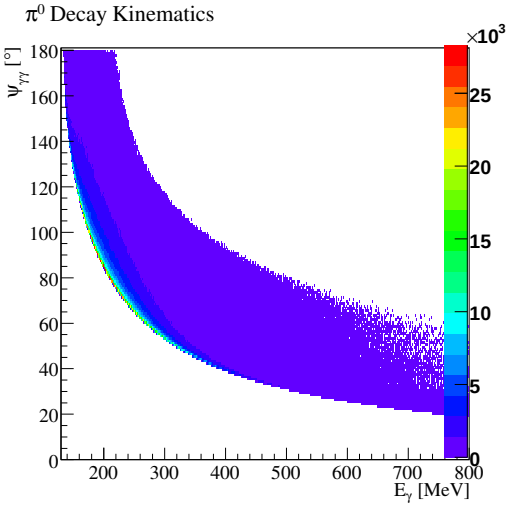

Figure A.2: π^0 photon opening angle as a function of incident photon energy (effectively a measure of the π^0 energy).

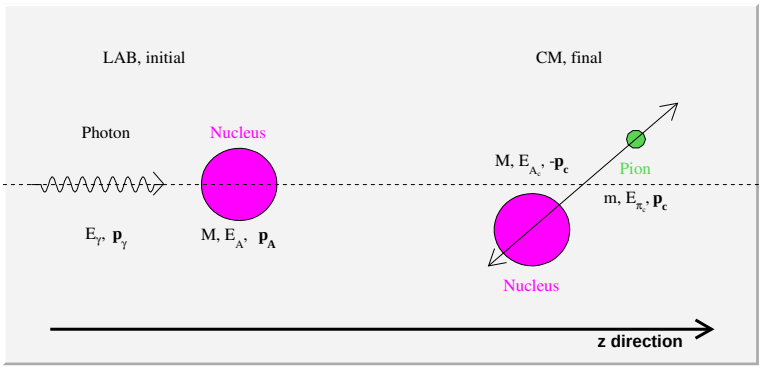

Figure A.3: Pion photoproduction on the nucleus.

A.3 Pion Missing Energy

The pion missing energy used to separate coherent and incoherent events in chapter 5 is defined as:

$$\Delta E_\pi = E_\pi^{cm}(E_\gamma) - E_\pi^{cm}(\gamma_1\gamma_2) \tag{A.21}$$

$E_\pi^{cm}(E_\gamma)$ is defined as in equation A.20. $E_\pi^{cm}(\gamma_1,\gamma_2)$ is the detected pion energy transformed to the pion-nucleus centre of mass frame i.e.

$$E_\pi^{cm} = \gamma(E_\pi - \beta p_{z\pi}) \tag{A.22}$$

where E_π is the detected pion energy and $p_{z\pi}$ is the component of the pion momentum along the beam direction.

$$\beta = \frac{E_\gamma}{E_\gamma + M} \tag{A.23}$$

$$\gamma = \frac{1}{\sqrt{1-\beta^2}} \tag{A.24}$$

Via momentum conservation, $p_{z\pi}$ is just the sum of the z components of the two decay photon momenta:

$$p_{z\pi} = p_{z1} + p_{z2} \tag{A.25}$$

$$= E_1 cos\theta_1 + E_2 cos\theta_2 \tag{A.26}$$

The detected pion energy in the lab frame is simply:

$$E_\pi = E_1 + E_2 \tag{A.27}$$

However, this does not use any of the angular information recorded by the particle detectors. If we define the energy sharing parameter, X, as:

$$X = \frac{E_1 - E_2}{E_1 + E_2} \tag{A.28}$$

$$= \frac{E_1 - E_2}{E_\pi} \tag{A.29}$$

From this, E_1 and E_2 are:

$$\begin{aligned} E_1 &= E_2 + E_\pi X && \text{(A.30)} \\ &= (E_\pi - E_1) + E_\pi X && \text{(A.31)} \\ 2E_1 &= E_\pi(1+X) && \text{(A.32)} \\ E_1 &= \frac{E_\pi}{2}(1+X) && \text{(A.33)} \\ E_2 &= \frac{E_\pi}{2}(1-X) && \text{(A.34)} \end{aligned}$$

The product of A.33 and A.34 is then:

$$\begin{aligned} E_1E_2 &= \left(\frac{E_\pi}{2}\right)^2 (1+X)(1-X) && \text{(A.35)} \\ &= \frac{E_\pi^2}{4}(1-X^2) && \text{(A.36)} \end{aligned}$$

Rearranging A.36 gives:

$$E_\pi^2 = \frac{4E_1E_2}{1-X^2} \qquad \text{(A.37)}$$

Combining this with A.2 gives:

$$\begin{aligned} E_\pi^2 &= \frac{4}{1-X^2}\frac{m_\pi^2}{2(1-cos\psi)} && \text{(A.38)} \\ &= \sqrt{\frac{2m^2}{(1-X^2)(1-cos\psi)}} && \text{(A.39)} \end{aligned}$$

The detected pion energy transformed to the pion-nucleus centre of mass frame now becomes:

$$E_\pi^{cm}(\gamma_1,\gamma_2) = \gamma\left(\sqrt{\frac{2m^2}{(1-X^2)(1-cos\psi)}} - \beta(E_1cos\theta_1 + E_2cos\theta_2)\right) \qquad \text{(A.40)}$$

A.4 Momentum Transfer to the Nucleus

N.B. in this section, the pion and photon 4-momenta are represented by P_γ and P_π respectivley. The corresponding 3-momenta will be lower case and in bold i.e. $\mathbf{p}_\gamma$ and $\mathbf{p}_\pi$.

The 3-momentum transfered to the nucleus, $\mathbf{q}$, in the reaction A(γ,π^0)A in terms of experimental observables is a function of E_γ, θ_π, M and m_π. The Lorentz invariant

4-momentum, Q, is defined as:

$$\begin{aligned} Q^2 &= (P_\gamma - P_\pi)^2 = (P_\gamma^{cm} - P_\pi^{cm})^2 && \text{(A.41)} \\ &= P_\gamma P_\gamma - P_\pi P_\pi - 2P_\gamma P_\pi && \text{(A.42)} \\ &= E_\gamma^2 - \mathbf{p}_\gamma^2 - (E_\pi^2 - \mathbf{p}_\pi^2) - 2(E_\gamma E_\pi - \mathbf{p}_\gamma \mathbf{p}_\pi) && \text{(A.43)} \\ &= (E_\gamma - E_\pi)^2 - (\mathbf{p}_\gamma - \mathbf{p}_\pi)^2 && \text{(A.44)} \\ &= (E_\gamma^{cm} - E_\pi^{cm})^2 - (\mathbf{p}_\gamma^{cm} - \mathbf{p}_\pi^{cm})^2 && \text{(A.45)} \end{aligned}$$

The 3-momentum transferred to the nucleus in the pion-nucleus centre of mass frame is defined as:

$$q^{cm^2} = (\mathbf{p}_\gamma^{cm} - \mathbf{p}_\pi^{cm})^2 \quad \text{(A.46)}$$

From equation A.45 this is then:

$$\begin{aligned} q^{cm^2} &= (E_\gamma^{cm} - E_\pi^{cm})^2 - (E_\gamma - E_\pi)^2 + (\mathbf{p}_\gamma - \mathbf{p}_\pi)^2 && \text{(A.47)} \\ &= (E_\gamma^{cm} - E_\pi^{cm})^2 - E_\gamma^2 - E_\pi^2 + 2E_\gamma E_\pi + p_\gamma^2 + p_\pi^2 - 2p_\gamma p_\pi cos\theta && \text{(A.48)} \\ &= (E_\gamma^{cm} - E_\pi^{cm})^2 - m_\pi^2 + 2E_\gamma E_\pi - 2E_\gamma p_\pi cos\theta && \text{(A.49)} \\ &= (E_\gamma^{cm} - E_\pi^{cm})^2 - m_\pi^2 + 2E_\gamma (E_\pi - p_\pi cos\theta) && \text{(A.50)} \\ &= (E_\gamma^{cm} - E_\pi^{cm})^2 - m_\pi^2 + 2E_\gamma (E_\pi - \sqrt{E_\pi^2 - m_\pi^2} cos\theta) && \text{(A.51)} \end{aligned}$$

E_γ^{cm} is the incident photon energy in the centre of mass frame. This is simple to calculate via:

$$E_\gamma^{cm} = \gamma(E_\gamma - \beta p_{z\gamma}) \quad \text{(A.52)}$$

$p_{z\gamma}$ the photon's momentum component in the beam direction of course is equal to E_γ. β and γ are the same as in equations A.23 and A.24. The pion energy in the centre of mass frame, E_π^{cm} is given by equation A.19. The pion energy in the lab frame can be calculated via the Lorentz transform of E_π^{cm}:

$$E_\pi^{cm} = \gamma(E_\pi - \beta p_\pi cos\theta_\pi) \quad \text{(A.53)}$$

where $p_\pi cos\theta_\pi$ is the z component of the pion momentum in the lab frame. This becomes:

$$(E_\pi^{cm} - \gamma E_\pi)^2 = \gamma^2 \beta^2 (E_\pi^2 - m_\pi^2) cos^2\theta_\pi \quad \text{(A.54)}$$

Therefore,

$$E_\pi^{cm^2} + \gamma^2 E_\pi^2 - 2E_\pi^{cm} E_\pi \gamma - \gamma^2 \beta^2 (E_\pi^2 - m_{\pi^2}) cos^2\theta_\pi = 0 \quad \text{(A.55)}$$

Which leads to the quadratic in E_π:

$$\gamma^2(1-\beta^2 cos^2\theta_\pi)E_\pi^2 - 2E_\pi^{cm}E_\pi\gamma + \gamma^2\beta^2 m_\pi^2 cos^2\theta_\pi + E_\pi^{cm^2} = 0 \tag{A.56}$$

Solving this quadratic for E_π gives:

$$E_\pi = \frac{E_\pi^{cm} \pm \sqrt{E_\pi^{cm^2} - (1-\beta^2 cos^2\theta_\pi)(\gamma^2\beta^2 m_\pi^2 cos^2\theta_\pi + E_\pi^{cm^2})}}{\gamma(1-\beta^2 cos^2\theta_\pi)} \tag{A.57}$$

which relates the pion energy in the CM frame to measurable quantities. There is an ambiguity in the solution of equation A.57 i.e. for each possible pion angle there are two possible pion energies. This can be resolved by considering pion production at threshold where only the positive solution to equation A.57 is physically meaningful.

The momentum transfer to the nucleus in the pion-nucleus centre of mass frame as derived here has been plotted in figures A.4(a) and A.4(b) as an illustration of its behaviour as a function of E_γ and θ_π.

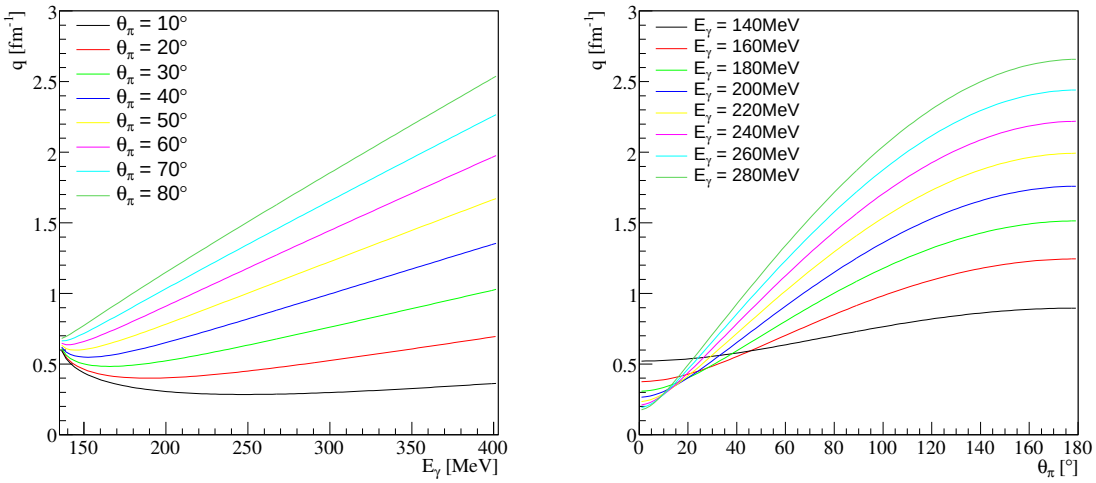

(a) (b)

Figure A.4: The momentum transfer to the nucleus in the pion-nucleus centre of mass frame for the reaction ^{208}Pb(γ,π^0)^{208}Pb.

Appendix B

Pion Photoproduction

B.1 Properties of the Pion

Table B.1: Properties of the π meson [5].

	π^0	π^+	π^-
J^π(spin,parity)	0^-	0^-	0^-
I^G(isospin,G-parity)	1^-	1^-	1^-
I_z	0	+1	-1
Mass [MeV/c^2]	134.97	139.57	139.57
Decay modes	$\gamma\gamma$ (98.78%) $e^+e^-\gamma$ (1.98%)	$\mu\nu$ ($\sim$100%)	$\mu\nu$ ($\sim$100%)

B.2 Pion Photoproduction Amplitudes

The Lorentz invariants for pion photoproduction are an expression of the momentum and energy conservation of the process [10]:

$$M_1 = i\gamma_5 \epsilon k \tag{B.1}$$

$$M_2 = 2i\gamma_5 (P \cdot \epsilon \not{q} \, q \cdot k - P \cdot k q \cdot \epsilon) \tag{B.2}$$

$$M_3 = \gamma_5 (\epsilon q \cdot k - k \cdot q \cdot \epsilon) \tag{B.3}$$

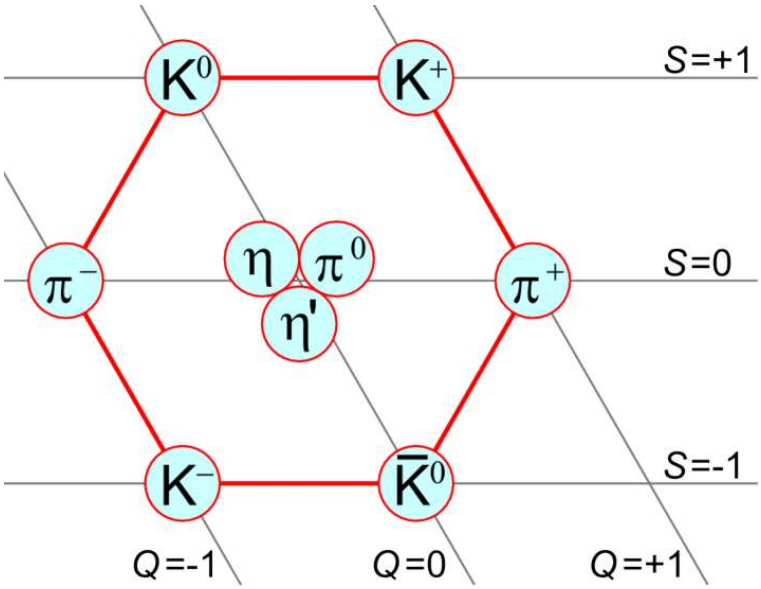

Figure B.1: Meson nonet

$$M_4 = 2\gamma_5(\epsilon P \cdot k - kP \cdot \epsilon - iM\epsilon k) \tag{B.4}$$

where P = $(p_i + p_2)/2$ and the notation matches that of section 2.3.1. $\not{\epsilon}$ is the scalar product $\gamma \cdot \epsilon$ etc.

The differential cross section for a transition from an initial state, i, to a final state, f can be expressed as:

$$\frac{d\sigma}{d\Omega} = \frac{q}{k}|\langle\chi_f|F|\chi_i\rangle|^2 \tag{B.5}$$

where χ_i is the two component Pauli spinor. These Pauli amplitudes takes the general form [6]:

$$F = iF_1\vec{\sigma}\cdot\vec{\epsilon} + F_2(\vec{\sigma}\cdot\vec{q})(\vec{\sigma}\cdot(\vec{k}\times\vec{\epsilon})) + iF_3(\vec{\sigma}\cdot\vec{k})(\vec{q}\cdot\vec{\epsilon}) + iF_4(\vec{\sigma}\cdot\vec{q})(\vec{q}\cdot\vec{\epsilon}) \tag{B.6}$$

$\vec{\sigma}$ are the nucleon spin matrices. The Pauli amplitudes can be further expanded into electric (E) and magnetic multipoles (M) and in terms of channels with orbital angular momentum l and total angular momentum J. These are the CGLN amplitudes [10]:

$$F_1(\theta) = \sum_{l=0}^{\infty}(E_{l+} + lM_{l+}P'_{l+1})(cos\theta) + (E_{l-} + (l+1)M_{l-})P'_{l-1}(cos\theta) \tag{B.7}$$

$$F_2(\theta) = \sum_{l=1}^{\infty}(l+1)M_{l+} + lM_{l-}P'_{l-1}(cos\theta) \tag{B.8}$$

$$F_3(\theta) = \sum_{l=1}^{\infty}(E_{l+}) - M_{l+}P''_{l+1}(cos\theta) + (E_{l-} + M_{l-})P''_{l-1}(cos\theta) \tag{B.9}$$

$$F_4(\theta) = \sum_{l=2}^{\infty}(M_{l+}) - E_{l+} - M_{l-} - E_{l-}P_l^{''}(cos\theta) \tag{B.10}$$

P_l are Legendre polynomials, $P_l^{'}$ and $P_l^{''}$ their first and second derivatives. l is the orbital angular momentum of the emitted pion, the $\pm$ subscript when considered with l gives the total angular momentum of the intermediate state. For example, E_{1+} describes the electric absorption of a photon with the emission of a p-wave pion and the intermediate state would have a total angular momentum of $\frac{3}{2}$. Similarly, M_{1-} refers to the magnetic absorption of a photon, the emission of a p-wave pion and an intermediate state of total angular momentum $\frac{1}{2}$.

For s- and p-wave pions the CGLN amplitudes reduce to:

$$F_1(\theta) = E_{0+}3(M_{1-} + E_{1+})cos\theta \tag{B.11}$$
$$F_2(\theta) = 2M_{1+}M_{1-} \tag{B.12}$$
$$F_3(\theta) = E_{1+}M_{1+} \tag{B.13}$$
$$F_4(\theta) = 0 \tag{B.14}$$

The second term in equation B.6 can be rewritten as [92]:

$$F_2(\vec{\sigma}\cdot\vec{q})(\vec{\sigma}\cdot(\vec{k}\times\vec{\epsilon})) = (\vec{q}(\vec{k}\times\vec{\epsilon}) + i\vec{\sigma}(\vec{q}\times(\vec{k}\times\vec{\epsilon}))) \tag{B.15}$$

This allows the Pauli amplitudes (equation B.6) to be split into a spin-dependent and a spin-independent term such that:

$$F = L + i\vec{\sigma}\vec{K} \tag{B.16}$$
$$L = \vec{q}(\vec{k}\times\vec{\epsilon})F_2 \tag{B.17}$$
$$K = \vec{\epsilon}F_1 + (\vec{q}\times(\vec{k}\times\vec{\epsilon}))F_2 + \vec{k}(\vec{q}\vec{\epsilon})F_3 + \vec{q}(\vec{q}\vec{\epsilon})F_4 \tag{B.18}$$

If only s- and p-wave terms are considered, it follows that the spin-independent cross section becomes:

$$\frac{d\sigma}{d\Omega} = \frac{1}{2}\frac{q}{k}|2M_{1+} + M_{1-}|^2 sin^2\theta \tag{B.19}$$

Appendix C

Triggering Electronics

Detailed diagrams of the experimental trigger are included overleaf.

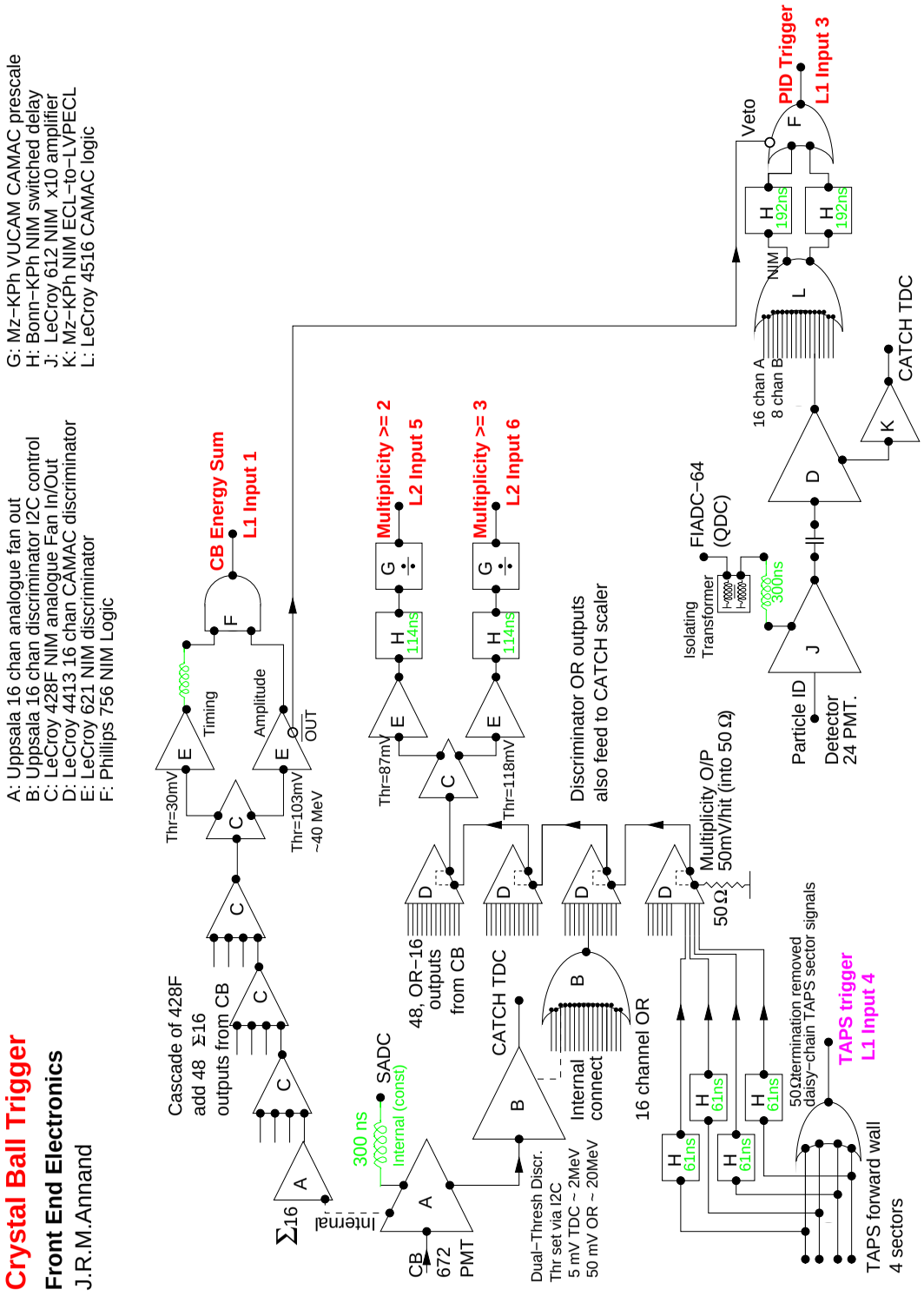

Figure C.1: Crystal Ball front end electronics [93].

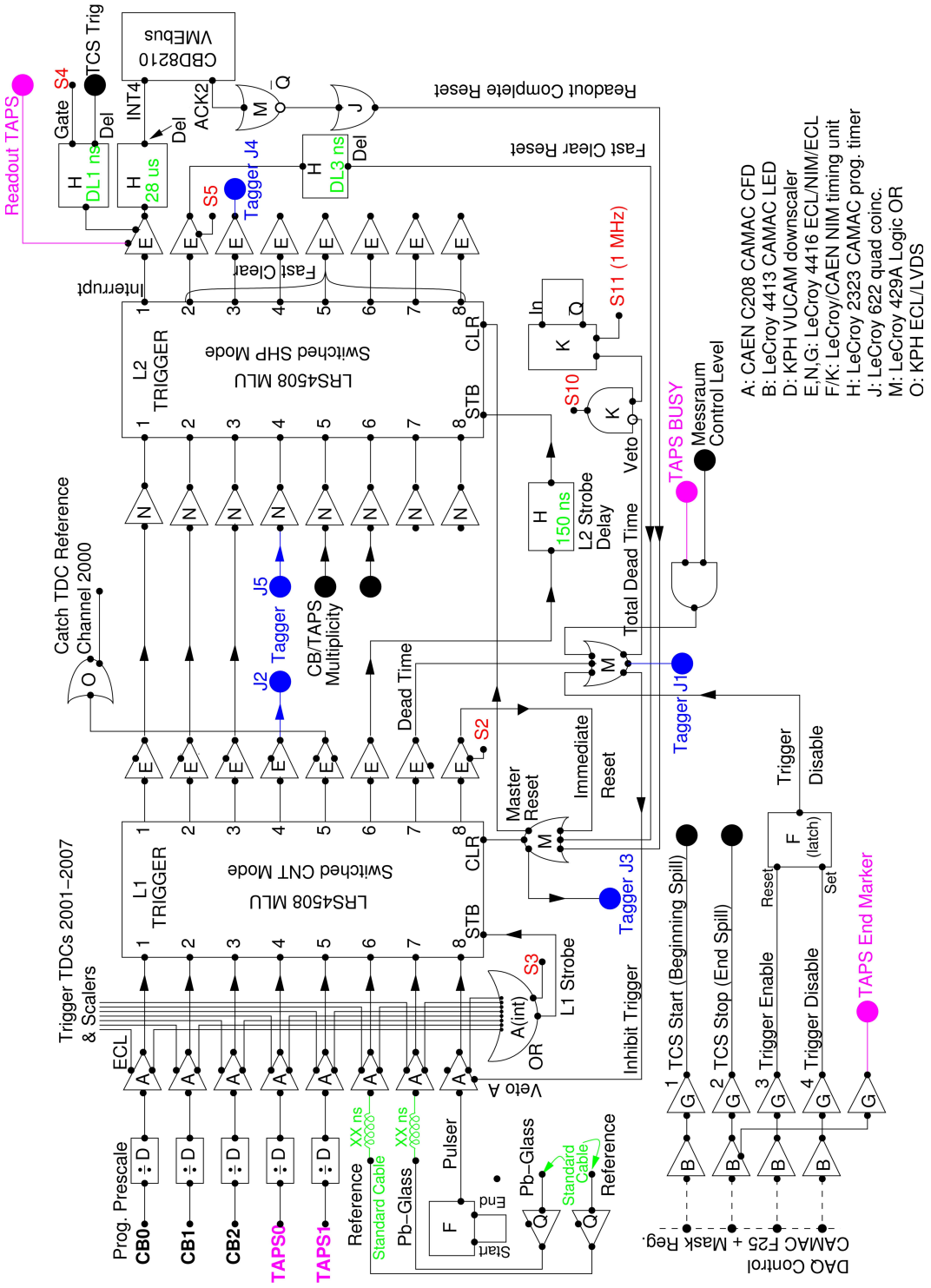

Figure C.2: Trigger diagram [93].

Appendix D

Nuclear Decay γs from ^{12}C and ^{16}O

D.0.1 Nuclear Decay γs

Incoherent π^0 photoproduction is an interesting reaction in its own right (section 2.5). An incoherent π^0 event can leave the target nucleus in an excited state which can subsequently gamma decay. If these low energy photons are detected in coincidence with a π^0 they can be used to identify incoherent events where the nucleus was left in a specific excited state. In a first attempt to identify these nuclear decay photons, a second iteration of the cluster finding algorithm was performed for events where a π^0 was detected. The second iteration employed a lower cluster threshold (0.8 MeV) and used the low energy photon calibration of the Crystal Ball (section 5.3.3). The same particle identification procedure for the high energy clusters employed.

A significant source of low energy background in the ball arises from split-off clusters. These occur when the energy from a high energy photon is not completely contained within the 12 surrounding crystals that are grouped together by the cluster finding algorithm. The resulting split-off clusters appear as low energy clusters which in a large fraction of cases maintain an angular correlation with the initial high energy photon. To suppress split-offs, a cut was placed on the angle between the π^0 decay photons and any low energy clusters. The distribution of these angles for the CB data is shown in figure D.3(a). Low energy clusters were only accepted if the event had an angle greater than 35°. A further cut was placed on the timing between the π^0 and the low energy clusters (figure D.3(b)) to select prompt events.

The resulting spectra of low energy photons for each of the 4 targets is shown in figure D.4. The spectra from the light nuclei show clear peaks on top of a decreasing background. As a first attempt to interpret the spectra, they have been fitted with a Gaussian and an exponential background. For the ^{12}C data a clear peak can be seen at

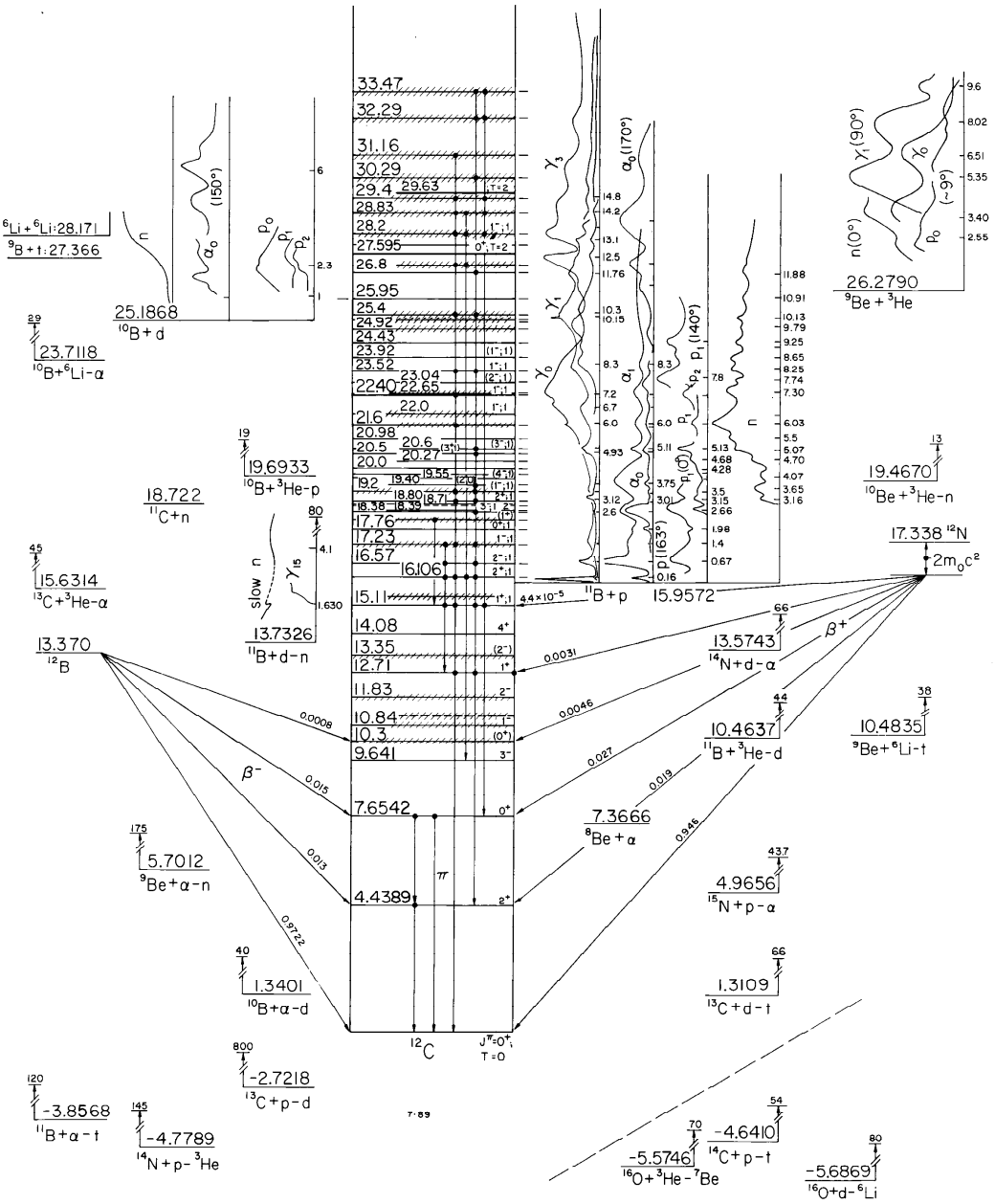

Figure D.1: Decay scheme for ^{12}C [94]

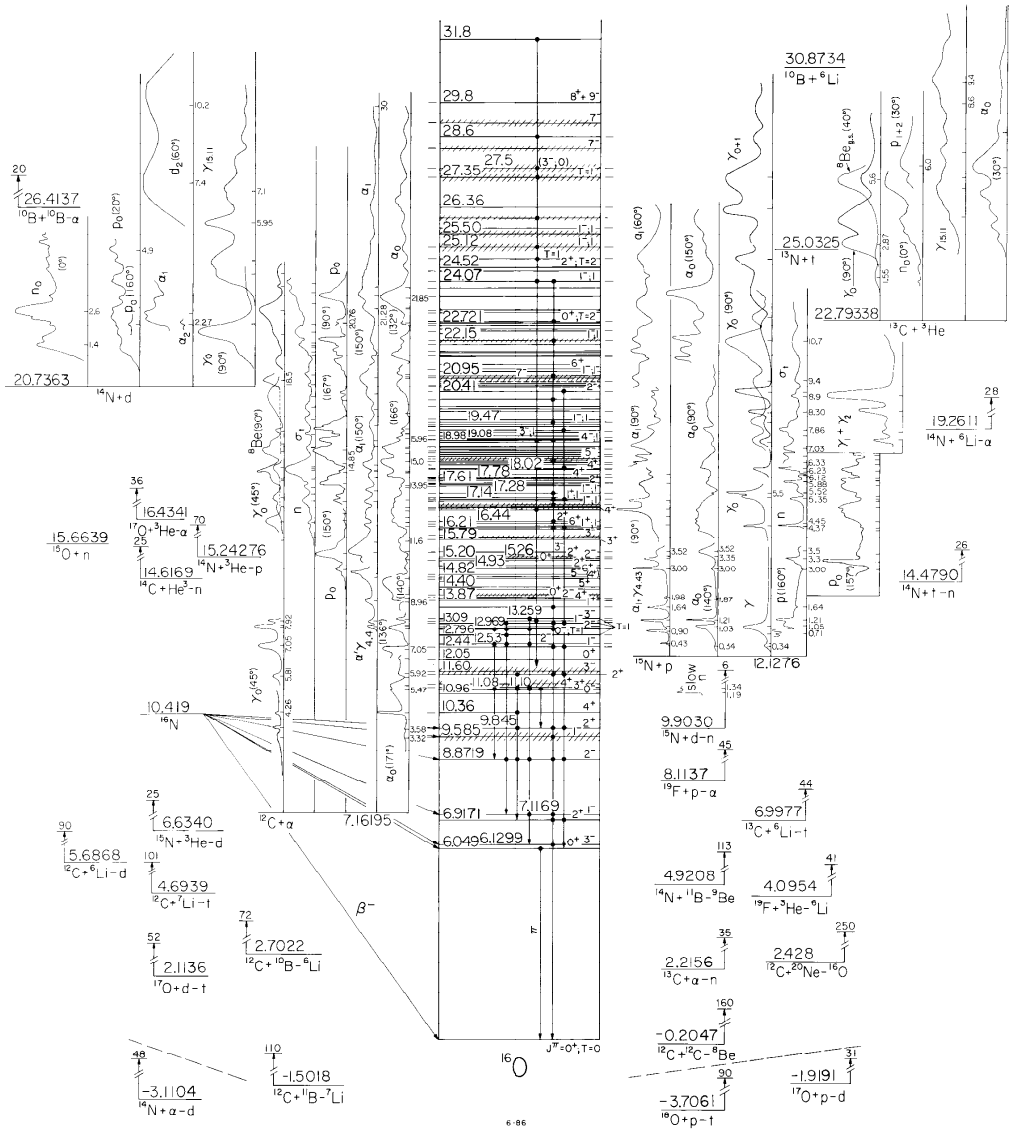

Figure D.2: Decay scheme for ^{16}O [94]

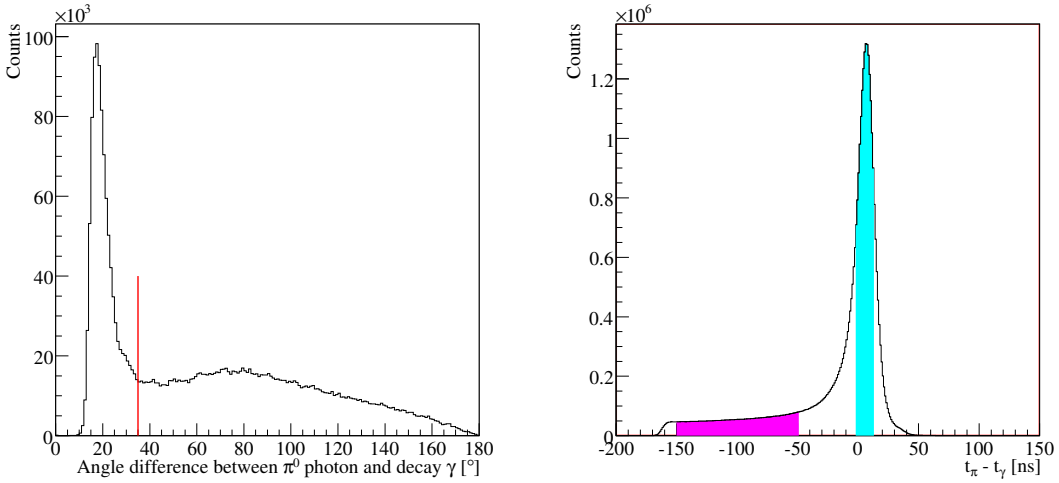

(a) Angle between π^0 decay photon and coincident low energy photons. The red line at 35° indicates the cut placed on the data to eliminate split offs.

(b) Time difference betweeen π^0 and a low energy photon.

Figure D.3:

4.4 MeV corresponding to a gamma decay from its first excited state. In ^{16}O there are 4 energy levels between 6 MeV and 7 MeV, 3 of which gamma decay. A clear peak can be seen in the ^{16}O spectra at the average of these energies. For the ^{40}Ca data there is a small peak at ∼4MeV consistent with a population of the first excited state at 3.7 MeV. but the relative contribution of the peak to the approximately exponential background is much smaller than for ^{12}C or ^{16}O. This is also true for ^{208}Pb: any peak due to the lowest excited state of ^{208}Pb has a negligible area compared to the background.

This remaining low energy electromagnetic background could arise from a variety of sources including split-off photons from the π^0 photon clusters that are not removed by the angular cut, Compton background in the Crystal Ball or the detection of electrons/photons from interactions of the photon beam in the target.

The shape of the uncorrelated background was investigated by cutting on the timing between the π^0 and the low energy photons away from the coincident peak. This timing spectrum is plotted in figure D.5 with the chosen uncorrelated area shown by the pink shaded area. The shape of this uncorrelated background is shown in figure D.5. The background is compared with the experimental data in figure D.6. In this comparison the background was scaled up by a factor of 10. This discrepency may indicate that the majority of the background arises from prompt events. The uncorrelated background

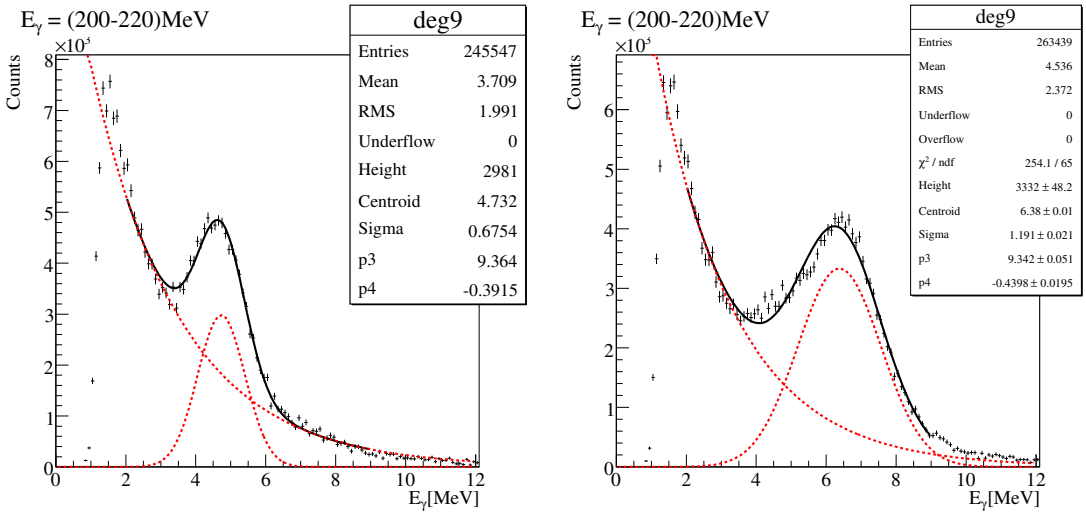

(a) ^{12}C (b) ^{16}O

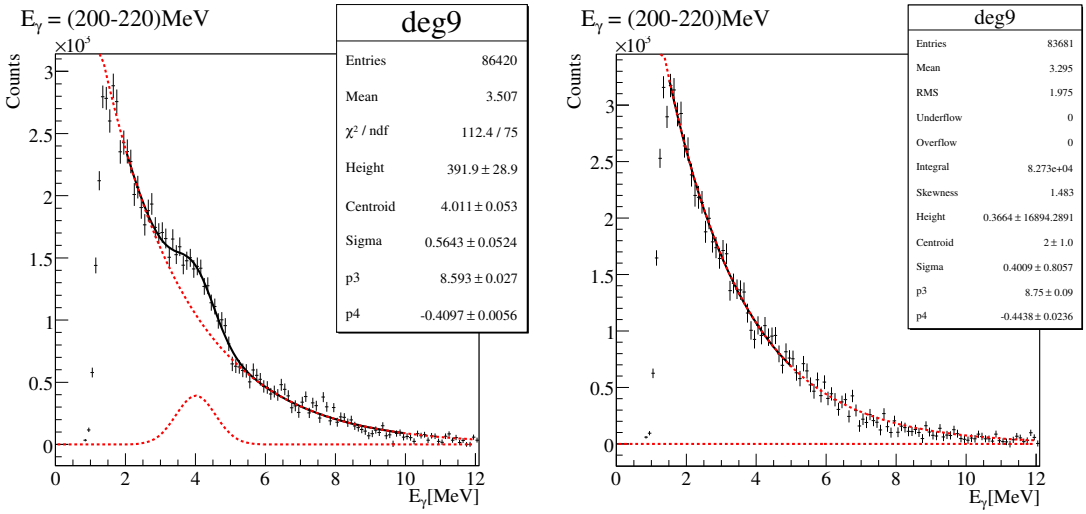

(c) ^{40}Ca (d) ^{208}Pb

Figure D.4: Energy deposition spectra for low energy photons detected in the CB in coincidence with a π^0 .

does not show the simple exponential shape assumed in the fits of figure D.4.

Clearly a full and detailed study of the sources of the background in the Crystal Ball as well as the response of the Crystal Ball to low energy photons are the necessary next step. However, this study represents the first proof of principle for $\sim 4\pi$ detection of nuclear decay photons in the same detector as the high energy products from photonuclear reactions. With a better understanding of the source of the background, the information from the nuclear decay photons can be used to isolate the incoherent strength to discrete states or groups of states in the residual nucleus. As well as obtaining some of the first information on the incoherent process, with understanding of the low energy detection efficiency the incoherent strength could be assesed and subtracted to obotain improved samples of the coherent process. This work is presently under way.

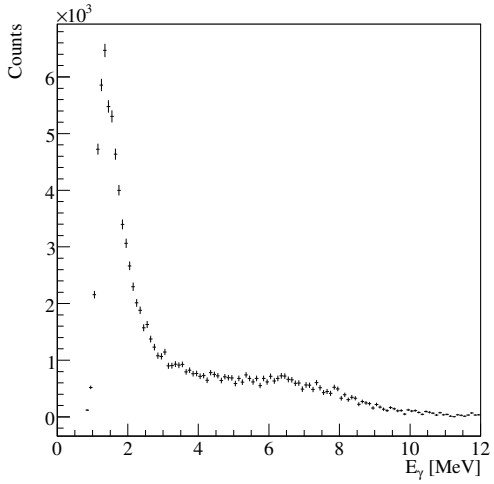

Figure D.5: Low energy background in the Crystal Ball - uncorrelated in time with the π^0 .

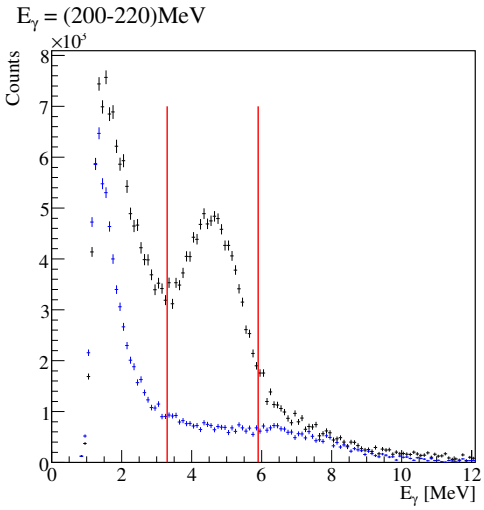

Figure D.6: ^{12}C data, cut on decay gammas. Black markers: decay gammas correlated in time with the π^0 . Blue markers: decay gammas uncorrelated in time with the π^0 .

References

1. H. de Vries *et al.*, Nuclear Charge-Density-Distribution Parameters from Elastic Electron Scattering, *At.Dat.Nuc.Tab.* **36** 495-536 (1987).

2. G. Fricke *et. al. At. Nuc. Dat. Nuc. Dat. Tab.* **60**, 177-285 (1995).
3. S. Schadmand, Two Pion Production in Photon Induced Reactions. *Pramana* **53** 6 (1999).
4. A. Nagl *et. al.*, Nuclear Pion Photoproduction *Springer Tracts in Modern Physics* **201** (1991).
5. D.E. Groom *et al.*, Review of Particle Physics. *The European Physical Journal* **C15** 1 (2000).
6. T. Ericsson, W. Weise, Pions and Nuclei.
7. M. Gmitro, S. Kamalov *et. al. Phys. Rev. C* **36**, (1987) 3.
8. D. Dreschel, L. Tiator, S.S. Kamalov, Shin Nan Yang, Medium effects in coherent pion photo- and electroproduction on ^{4}He and ^{12}C *Nuc. Phys. A* **660** 423-438 (1999).
9. D. Dreschel, O. Hanstein, S.S. Kamalov, L. Tiator, A unitary isobar model for pion photo- and electroproduction on the proton up to 1 GeV *Nuc. Phys. A* **645** 145-174 (1999).
10. G.F. Chew, M. L. Goldberger, F.E. Low, Y. Nambu, Relativistic Dispersion Relation Approach to Photomeson Production *Phys. Rev* **106** 1345 (1957).
11. K. Watson *Phys. Rev.* **95** (1954) 228.
12. F.A. Berends *et. al.*, *Nuc. Phys. B* **4**, (1967) 54.
13. K. Blomqvist and J. Laget, *Nuc. Phys. A* **280**, (1977) 405.
14. B. Krusche *et. al.*, Coherent π^0 Photoproduction from atomic nuclei. *Phys.Lett.B* **526** 287 (2002).
15. L.C. Liu and C.M. Shakin, Pion-nucleus elastic scattering : theory and applications. *Prog. Part. Nucl. Phys.* **5** 207 (1981).

16. G.J. Miller and R.O. Owens, The treatment of data from a neutral meson spectrometer. *Nuc. Inst. and Meth.* **390** (1997) 257-266.

17. S. Kamalov.*Private communication.*

18. J. E. Leiss and R. A. Schrack, Nuclear Matter Distributions from Coherent Neutral Pion Photoproduction. *Rev. Mod. Phys* **30** 456 (1958).

19. R. A. Schrack *et. al.*, Neutral Meson Photoproduction from Complex Nuclei. *Physical Review* **127** 1772 (1962).

20. R. Sanderson, Coherent Neutral Pion Photoproduction on ^{16}O and ^{208}Pb. *Ph.D Thesis, University of Glasgow* (2002).

21. B. Krusche *et. al.*, Photoproduction of π^0 mesons from nuclei. *Eur.Phys.J.A* **22** 277 (2004).

22. T.E Rodrigues *et al.* Incoherernt π^0 photoproduction from complex nuclei. *Phys.Rev.C* **71** 051603 (2005).

23. T. Takaki *et. al.* Photoproduction of Neutral Pions to Discrete Nuclear States.*Nuclear Physics A.* **443** 570-588 (1985).

24. S. Pieper *et. al.* Quantum Monte Carlo calculations of A=9,10 nuclei. *Phys. Rev. C.* **66** 044310 (2002).

25. C.J. Horowitz *et al.*, Parity violating measurements of neutron densities, *Phys.Rev.C* **63** 025501.

26. K. Pomorski, P. Ring *et al.*, Ground state properties of the β stable nuclei in various mean field theories, *Nuc.Phys.A* **624** 349-369 (1997).

27. Report of the 'Nuclear Structure and Astrophysics Town Meeting', Oakland, CA, Nov 2000. http://snohp1.lbl.gov/∼lpr2000/oakland.wp.pdf

28. C. A. Bertulani, Nuclear Physics in a Nutshell. *Princeton University Press.* (2007) .

29. A.W. Steiner *et al.*, Isospin Asymmetry in Nuclei and Neutron Stars. *Phys.Rept.* **411** 325-375 (2005).

30. J. Lattimer, M. Prakash, Neutron star structure and the equation of state, *Astrophys J.* **550** 426 (2001)

31. P.E. Haustein, An overview of the 1986-1987 atomic mass predictions. *At.Data Nucl. Data Tables* **39**, 185 (1988).

32. R.J. Furnstahl, Neutron radii in mean-field models, *Nuc.Phys.A* **706** 85-110(2002).

33. M. Prakash, *et al.*, Equation of State and the Maximum Mass of Neutron Stars. *Phys. Rev. Lett* **61**, 22 (1988).

34. C.-H. Lee, *et al.*, Nuclear Symmetry Energy. *Phys. Rev. C* **57**, 6 (1998).

35. J. Lattimer, *et al.*, A generalized equation of state for hot, dense matter. *Nuc.Phys.A* **535**, 331-376 (1991).

36. J.M. Lattimer, M. Prakash, The Physics of Neutron Stars, *Science* **304** 536.

37. C. Alcock, A. Olinto, Exotic Phases of Hadronic Matter and their Astrophysical Application, *Ann.Rev.Nucl. and Part.Phys.* **38** 161-184 (1988).

38. S. Typel, B.A. Brown, Neutron radii and the neutron equation of state in relativistic models, *Phys.Rev.C* **64** 027302.

39. C.J. Horowitz, J. Piekarewicz, Neutron Star Structure and the Neutron radius of ^{208}Pb, *Phys.Rev.Lett* **86** 25 (2001).

40. J. Carriere *et al.*, Low Mass Neutron Stars and the Equation of State of Dense Matter, *Astrophys. J.* **593** 463-471 (2003).

41. M. Alford, *hep-ph/0209287*

42. B.A. Brown, Neutron Radii in Nuclei and the Neutron Equation of State, *Phys.Rev.Lett* **85** 25.

43. C.J. Horowitz, J. Piekarewicz, Constraining URCA cooling of neutron stars from the neutron radius of ^{208}Pb. *Phys.Rev.C* **66** 055803 (2002).

44. A.W. Steiner, B. Li, Isospin diffusion in heavy-ion collisions and the neutron skin thickness of lead, *Phys.Rev.C* **72** 041601 (2005).

45. C.S. Wood, *et al.*, Measurement of Parity Nonconservation and an Anapole moment in Cesium, *Science* **275** 1759 (1997).

46. E.N. Fortson, *et al.*, Nuclear-Structure Effects in Atomic Parity Nonconservation, *Phys. Rev. Lett.* **65** 23 (1990).

47. S.J. Pollock, M.C. Welliver, Effects of neutron spatial distributions on atomic parity nonconservation in cesium, *Phys.Lett.B* **464** (1999) 177-182.

48. L. Ray, G.W. Hoffman, Relativistic and nonrelativistic impulse approximation descriptions of 300-1000MeV proton + nucleus elastic scattering, *Phys.Rev.C* **31** 2 (1985).

49. R.C. Clark, *et al.*, *nucl-th/0209052*.

50. J. Piekerawicz. Insensitivity of the elastic proton-nucleus reaction to the neutron radius of ^{208}Pb. *Nuc.Phys.A* **778** 10-21 (2006).

51. C. Olmer. Elastic and inelastic scattering of 291 MeV pions by ^{9}Be, Si,^{58}Ni and ^{208}Pb. *Phys.Rev.C* **23** 6 (1981).

52. S.J. Pollock *et al.* Atomic parity nonconservation: Electroweak parameters and nuclear structure. *Phys.Rev.C* **46** 2587 (1992).

53. L. Ray and G.W. Hoffman, Relativistic and nonrelativistic impulse approximation descriptions of 300-1000MeV proton + nucleus elastic scattering, *Phys.Rev.C* **31** 2 (1985).

54. H. Herminghaus *et al.*, The design of a cascaded 800 MeV normal conducting C.W. race track microtron.*Nuc. Inst. Meth.* **138** (1976) 1-12.

55. T. Walcher, Physics at the Electron Accelerator MAMI. *Prog. Part. Nucl. Phys* **34** (1995) 1-15.

56. I. Anthony, Design of a tagged photon spectrometer for use with the Mainz 840 MeV microtron. *Nuc. Inst. Meth A* **301** (1991) 230-240.

57. S.J. Hall *et al.*, A focal plane system for the 855 MeV tagged photon spectrometer at MAMI-B. *Nuc. Inst. Meth. A* **368** (1996) 698-708

58. E. D. Bloom, Scaling, Duality and the Behaviour of Resonances in Inelastic electron-proton Scattering. *Phys.Rev.Lett.* **25** (1970) 1140.

59. R. Hofstadter, Electron Scattering and Nuclear Structure. *Rev.Mod.Phys* **28** (1956) 214-254.

60. K. Aulenbacher *et al. Nuc. Inst. Meth. A* 403:263 (1998).

61. National Institute of Standards and Technology, *http://physics.nist.gov*.

62. M. Oreglia *et al.*, Study of the reaction $\psi' \to \gamma\gamma \mathrm{J}\psi$ *Phys. Rev. D.* **25** 9 (1982).

63. H. Marsiske *et al.*, Measurement of $\pi^0\pi^0$ production in two-photon collisions. *Phys. Rev. D.* **41** 11 (1990).

64. S. Prakhov *et al.*, Search for the CP forbidden Decay $\eta \rightarrow 4\pi^0$ *Phys. Rev. Lett.* **84** 21 (2000).

65. A. Starostin *et. al.*, Measurement of $K^-p \rightarrow \eta\lambda$. *Phys.Rev.C* **64** (2001) 055205.

66. E. Downie, University of Glasgow, Ph.D Thesis.

67. G. Audit *et al.*, DAPHNE: a large-acceptance tracking detector for the study of photoreactions at intermediate energies. *Nuc. Inst. Meth.* **A301** (1991) 473-481.

68. J. Albert, Test Measurements for the Crystal Ball Detector at MAMI . *Diploma Thesis.* (2003) .

69. R. Novotny, The BaF_2 Photon Spectrometer TAPS *IEEE Trans. Nucl. Sci.* **38** 2 (1991).

70. A. Starostin *Private communication.*

71. J.R.M. Annand and D. Drambrick, DAQ for CB@MAMI. *Technical Report CB@MAMI*, November 2002.

72. D. Watts, Calorimetry with the Crystal Ball and TAPS. *Calorimetry in Particle Physics, Proceedings of the Eleventh International Conference, Perugia*, (2004).

73. J.R.M.Annand *AcquRoot manual: http://nuclear.gla.ac.uk/∼acqusys/doc/AcquRoot.pdf.*

74. *Root manual: http://root.cern.ch.*

75. K. Livingston *AcquTagger Manual: http://nuclear.gla.ac.uk/∼acqusys/doc/AcquTagger.pdf.*

76. D. Krambrich, University of Mainz, Ph.D Thesis.

77. M. Rost *Private communication.*

78. M.Unverzagt, University of Mainz, *Diploma thesis.*

79. J.Brudvik, University of California, Los Angeles, *Ph.D Thesis.*

80. G.F. Knoll, Radiation Detection and Measurement, *John Wiley and Sons*

81. R.Codling, University of Glasgow, *Ph.D in preparation.*

82. S.Schumann, University of Bonn, *Ph.D in preparation.*

83. B.Boillat, University of Basel, *Ph.D in preparation.*

84. F. Zehr, University of Basel, *Ph.D in preparation.*

85. R. Gregor, University of Giessen, *Ph.D in preparation.*

86. S. Lugert, University of Giessen, *Ph.D in preparation.*

87. M. Goosens. GEANT - Detector Description and Simulation Tool, *CERN Program Library Long Writeup W5013, CERN* (1994)

88. C. Allgower. Getting Started with the Crystal Ball Geant3 simulation. *CB@BNL analysis note.*

89. B. Krusche *et. al.*, Nuclear mass form factors from coherent photoproduction of π^0 mesons. *Eur.Phys.J.A* **26** 76 (2005).

90. R.H. Helm. Inelastic and Elastic Scattering of 187-MeV Electrons from Selected Even-Even Nuclei. *Phys. Rev* **104** 1466 (1956).

91. B. Dreher. The Determination of the Nuclear Ground State and Transition Charge Density from Measured Electron Scattering Data. *Nuc. Phys. A* **235** 219 (1974).

92. H. Ströher, Neutral Pion Photoproduction Experiments Near Threshold,*Ph.D Thesis, University of Giessen*, Unpublished (1990)

93. J.R.M. Annand *Private communication.*

94. Triangle Universities Nuclear Laboratory, Nuclear Data Group. *http://www.tunl.duke.edu/nucldata/.*